DISSERTATION

Titel der Dissertation

„On the Quaternary Systems Ce-Ni-Zn {B, Si}“

Verfasserin

Zahida Malik

angestrebter akademischer Grad

Doktorin der Naturwissenschaften (Dr. rer. nat)

Wien, 2012

Dedicated to,

My daughters Eeshah & Roshaan I care the most

My parents without them I couldn't accomplish this work

Table of Contents

9.   Phase Equilibria and Crystal Structures in the System Ce-Zn-Si   **154**

Acknowledgements

All praises to Almighty Allah the beneficent the merciful. This thesis is the end of my journey in obtaining my doctorate degree. This journey was not in a vacuum due to the support, guidance and encouragement of the Supervisor, Colleagues and the Family I had. It was a great privilege to spend several years at the Institute of Physical Chemistry at University of Vienna, my group members and this city will always remain dear to me.

My first debt of gratitude must go to my advisor, Prof. Peter Franz Rogl, for providing me the vision, encouragement and guidance along with all necessary infrastructure and resources, throughout the doctoral program. I warmly thank Dr. A. Grytsiv, for his valuable advice, constructive criticism and his extensive discussions around my work. I am great full to Dr. O. Sologub as she spent a lot time in the beginning this study for introducing me to the field of Solid State Chemistry. I am thankful to Dr. Gerda Rogl for unforgettable care she gave to me and my daughter during our stay in Austria. I am thankful to my colleagues Matthias, Dr. Yan, Izolde, and Fainan for their cooperation and for the creations of such a peaceful working environment.

I am thankful to Dr. Stephan Puchegger for EPM analysis, Prof. H. Michor and all group of Prof. E. Bauer for the physical properties measurements of my samples at the technical University of Vienna. I am grateful to Prof. G. Giester and Prof. H. Effenbergger for the measurement of my single crystals at the Institute of Mineralogy and Crystallography, University of Vienna.

I wish to thank my parents, Malik Sakhawat Husain and Tazeem Akhtar and my brothers and sisters. Their love was an inspiration and a driving force for me. I owe them everything and wish I could show them just how much I love and appreciate them. Special thanks are due to my husband, Arshad Mahmood Malik, who insisted me to be independent all the way and encouraged me to finish this work. Finally, I would like to dedicate this work to my daughters Eeshah Arshad and Roshaan Arshad and my Parents; 'I hope that this work will make you proud'.

My friends in Austria, Germany, Pakistan, Spain and other parts of the World were sources of laughter, joy, and support. Special thanks go to Anjum Saleem, Navida Nasir, Tania Jabbar, Saira Arif, and Uzma Nisar.

I take this opportunity to sincerely acknowledge the Higher Education commission (HEC),of Pakistan and the Austrian Exchange Service (ÖAD), Austria, for providing me financial assistance which buttressed me to perform my work comfortably.

Abstract

Zn-based alloys with rare-earth metals are an important part of the high strength lightweight multinary Mg-based alloy system Mg-Zn-Mn(Ni)-RE for automotive applications. Rare earths (RE) improve the mechanical performance, tensile strength, hardness and also the corrosion resistance by removing impurities from the grain boundaries of their alloys with zinc. The present work provides detailed information on phase relations and crystal structures in the quaternary systems Ce-Ni-Zn-(B,Si) at 800°C backed by light optical microscopy, electron microprobe analysis and x-ray powder and single crystal diffraction.

The isothermal sections at 800°C have been established for the systems Ce-Zn-B, Ni-Zn-B, Ce-Ni-Zn and Ce-Zn-Si. In the system Ni-Zn-B six ternary compounds were found, which in some cases exhibit considerable mutual solid solubilities mostly as an exchange of Ni-Zn at constant B-content, but in the case of the so-called τ-phase τ_1-$(Ni_{1-x}Zn_x)_{21}[Zn_{1-y-z}\square_y(B_4)_z]_2B_6$ (1.5<x<2.25, 0.07<y<0.53, 0<z<0.3) also with Zn/B substitution. Whereas Ni/Zn exchange (at constant B-content) ranges at about 4 to 5 at. % for τ_4-Ni_3ZnB_2 and τ_5-$Ni_{48}Zn_{32}B_{20}$, it is below 3 at. % for τ_2-$Ni_{12}ZnB_{8-x}$ (x=0.43), τ_3-$Ni_{21}Zn_2B_{20}$ and τ_6-$Ni_{47}Zn_{23}B_{30}$. Phase relations in the system Ce-Ni-Zn are characterized by a large region for the liquid phase in the Ce-rich part and a continuous solution of the phase $Ce(Ni_{1-x}Zn_x)_5$ with CaCu$_5$-type through the entire section for the full temperature region from 400 to 800°C. Zn/Ni substitution has found to stabilize the structure of CeZn$_{11}$ at 800°C appearing as a ternary solution phase $Ce(Zn_{1-x}Ni_x)_{11}$(0.03≤x≤0.22) and a rather extended solution of $Ce_2(Ni_xZn_{1-x})_{17}$(0≤x≤0.53). No ternary compound exists in the ternary system Ce-Zn-B and no significant mutual solid solubilities of binary phases have been observed. For the low temperature modification $\alpha CeZn_7$ ($Ce_{1-x}Zn_{5+2x}$; x~0.33) up to 750°C the TbCu$_7$-type could be assigned in this work.

X-ray single crystal and x-ray powder diffraction were employed to study the precise site occupation and site preferences in the crystal structures of more than 18 compounds. The crystal chemistry of the rhombohedral β boron solid solution co-doped by Ni,Zn metal atoms has been studied on a $Ni_{0.19}Zn_{1.24}B_{34.22}$ single crystal. Zn atoms were found in the E void (occupancy of 28%) whilst random mixtures of Ni, Zn atoms (ratio 15.5:84.5) occupy the sites A$_1$, D and D$_d$. Among the new crystal

structures determined a new boron-metal cluster was found in $Ni_{21}Zn_2B_{20}$ (*I4/mmm*) with characteristic isolated B_{20}- cages nesting six nickel atoms in the form of an octahedron. Ni_3ZnB_2 (*C2/m*) was found to form B_4 zigzag chains, $Ce_7Zn_{23-x}Si_x$, x=0.14 (*Pbam*) consists of $AuCu_3$ and disordered $BaAl_4$ structural units and $Ce(Ni_{1-x}Zn_x)_2Si_2$, x=0.39 (Pnmm) is $CaBe_2Ge_2$-type.

Physical properties including thermal expansion, hardness, elastic properties, resistivity, specific heat and magnetization were studied for the borides $Ni_{21}Zn_2B_{20}$ and Ni_3ZnB_2.

Kurzfassung

Zinklegierungen mit Seltenerdmetallen sind ein wichtiger Bestandteil des hochfesten und ultraleichten Legierungssystems Mg-Zn-Mn(Ni)-Seltenerden für Anwendungen in der Automobilbranche. Seltenerdmetalle verbessern die mechanischen Eigenschaften wie die Zugfestigkeit, Härte oder die Beständigkeit gegen Korrosion indem sie mit Hilfe von Zink Verunreinigungen an den Korngrenzen der Legierungen beseitigen. Die hier vorgelegte Arbeit gibt detaillierte Informationen über die Phasenbeziehungen und Kristallstrukturen des quaternären Systems Ce-Ni-Zn-(B,Si) bei 800°C, unterstützt durch optische Mikroskopie, Elektronenmikrosondenanalysen, Röntgenpulver- und Einkristallbeugung.

Für die Systeme Ce-Zn-B, Ni-Zn-B, Ce-Ni-Zn und Ce-Zn-Si wurden sotherme Schnitte bei 800°C erstellt. Im System Ni-Zn-B wurden sechs ternäre Verbindungen gefunden die in einigen Fällen beträchtliche homogene Bereiche (Mischkristalle) aufweisen meist als Austausch von Ni-Zn bei einem konstanten B-Gehalt, nur im Fall der sogenannten τ-Phase τ_1-$(Ni_{1-x}Zn_x)_{21}[Zn_{1-y-x}\square_y(B_4)_z]_2B_6$ kam es auch zu einem Zn/B Ersatz. Während der Ni/Zn Austausch (bei konstantem B-Gehalt) ungefähr 4 bis 5 at. % für τ_4-Ni_3ZnB_2 und τ_5-$Ni_{48}Zn_{32}B_{20}$ beträgt, liegt er für τ_2-$Ni_{12}ZnB_{8-x}$ (x = 0.43), τ_3-$Ni_{21}Zn_2B_{20}$ und τ_6-$Ni_{47}Zn_{23}B_{30}$ unter 3 at. %. Phasenbeziehungen im System Ce-Ni-Zn werden durch einen großen Bereich einer flüssigen Phase im Ce-reichen Teil und durch eine vollständige Lösung der $Ce(Ni_{1-x}Zn_x)_5$ Phase mit $CaCu_5$-Typ im gesamten Konzentrationsschnitt und dem ganzen Temperaturbereich von 400 bis 800°C charakterisiert. Zn/Ni Austausch konnte (i) die Struktur von $CeZn_{11}$ bei 800°C stabilisieren, die somit als ternäre Lösungsphase $Ce(Zn_{1-x}Ni_x)_{11}$ ($0.03 \leq x \leq 0.22$) erscheint, sowie auch (ii) die ziemlich ausgedehnte Lösung von $Ce_2(Ni_xZn_{1-x})_{17}$ ($0 \leq x \leq 0.53$). Im ternären System Ce-Zn-B existiert keine ternäre Verbindung und es wurden keine wesentlichen gemeinsamen Löslichkeiten von binären Phasen festgestellt. Für die Tieftemperatur-Modifikation $\alpha CeZn_7$ ($Ce_{1-x}Zn_{5+2x}$; $x\sim0.33$) konnte in dieser Arbeit bis zu 750°C der $TbCu_2$-Typ zugeordent werden.

Um die genaue atomare Verteilung in den Kristallstrukturen zu studieren wurden für mehr als 18 Verbindungen Röntgenpulver- und Einkristallbeugung angewendet. An einem $Ni_{0.19}Zn_{1.24}B_{34.22}$ Einkristall wurde die Kristallchemie des rhomboedrischen β Bormischkristalls, dotiert mit Ni, Zn-Atomen, untersucht. Zinkatome wurden in der E Fehlstelle (Besetzung: 28%) gefunden während statistische Mischungen von Nickel und

Zinkatomen (Verhältnis 15.5:84.5) die A_1, D und D_d Stellen besetzen. Unter den neu bestimmten Kristallstrukturen wurde im $Ni_{21}Zn_2B_{20}$ (*I4/mmm*) ein neuer Bor-Metall Cluster gefunden, der als charakteristischer B_{20}-Käfig einen Oktaeder aus sechs Nickelatomen umsachliesst. Es wurde weiters entdeckt, dass Ni_3ZnB_2 (*C2/m*) B_4 Zickzackketten ausbildet, dass $Ce_7Zn_{23-x}Si_x$, x = 0.14 (*Pbam*) aus $AuCu_3$ und ungeordneten $BaAl_4$ Struktureinheiten besteht und dass $Ce(Ni_{1-x}Zn_x)_2Si_2$, x = 0.39 ($P\overline{4}2_1m$) eine Variante des $CaBe_2Ge_2$-Typs ist.

Physikalische Eigenschaften, einschließlich thermischer Ausdehnung, Härte, elastische und magnetische Eigenschaften sowie spezifische Wärme wurden an den Boridverbindungen $Ni_{21}Zn_2B_{20}$ und Ni_3ZnB_2 untersucht

1

Introduction

Anthropologists characterize the different stages of the human cilivilizations development, as the Stone Age, Bronze Age, Iron Age and the Modern Age. The Modern Age can be called as called Nuclear Age, Space Age or the Age of Science. In this Modern Age materials and the knowledge about the materials has a pivot role [1]. Technology of the present time is based on the knowledge of properties of the materials. Phase diagrams are one of the most important sources of information about the behavior of the phases, compounds and solutions. In the present work equilibrated alloys mainly, Borides and Silicides have been used for the construction of '*Isothermal Secti*ons/*Phase Diagrams*' along with the structure elucidation of the new compounds via *Single Crystal Studies*. It is hoped that a better understanding of the borides and silicides will emerge.

1.1.Borides

Elemental boron is well known to form three-dimensional framework of covalently bonded boron atoms in the structure resulting in the formation of a series of voids (see figure 1), which can accommodate metal (M) atoms [2]. Due to the strong covalent bonds in β-rhombohedral-boron high temperature modification ($T_m(\beta B)$ = 2072°C [3]) and its solid solutions with transition metals exhibit high (Vickers) hardness around 40 GPa as well as high resistance against corrosion and acid [4]. The strong covalent bonding of most borides is responsible for their high melting points, moduli, and hardness values. Borides generally have high negative free energies of formation, which gives them excellent stability under many conditions [5].

The B/M ratio and the number of *d*- and *f*-electrons of the metal atoms determine crystal structure and the properties of the transition metal borides. In case of metal-rich borides, M≥2B the electron transfer is directed toward the metal, and the metal states play the main part in the electronic structure of the compounds. In boron-rich borides, such as MB≥2, the electron transfer is directed toward the boron [6]. Ferroboron has been observed to be grain refiner for steel, CaB is reported to be a strong deoxidizer/defluxing agent for nonferrous metals such as Cu [5]. Zinc-based

alloys with rare-earth metals are used in several engineering applications and are often employed to replace cast iron because of similar properties and better machinability [7]. Rare earths (RE) improve the mechanical performance, tensile strength, hardness and also the corrosion resistance by removing impurities from the grain boundaries of their alloys with zinc [8]. Zinc alloys with about 15 mass % boron or even less exhibit high tensile strength, high degree of hardness, high resistance to oxidation and corrosion, low shrinkage factor and low specific gravity [9]. Multi-component zinc and boron alloys containing various amounts of elements such as aluminum, copper or calcium can be used for the production of bearings, bars, rods, sheets, tubes, plates, for the production of ingots, or other finished or semi-finished articles [9]. Generally, additions of boron and borides act as grain refiners in many metals and alloys increasing cohesive strength but also may clean grain boundaries for superplasticity [10].
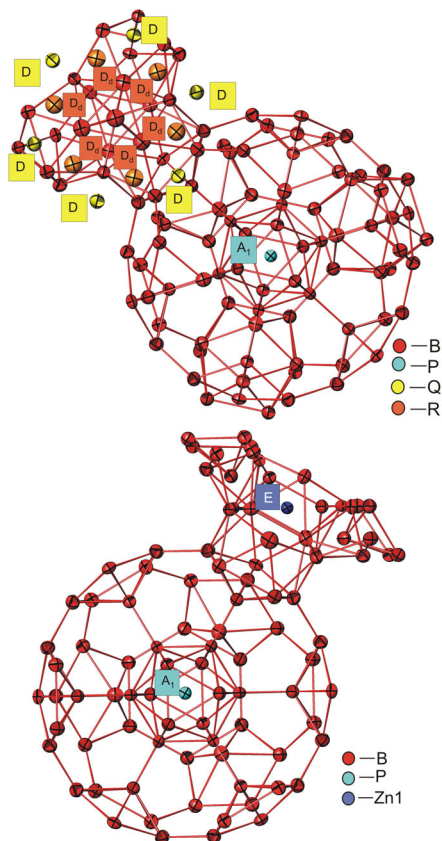
Figure 1. E, A_1, D, and D_d holes in β boron structure [11].

1.2. Silicides

2

Transition metal Silicides have been reported to have outstanding electrical, thermal and structural properties [12]. Silicides may find applications in the contact materials or in optoelectronic devices or simply as grain refiners [13]. The resistivity of silicides is most important criterion for considering them for metallization in integrated circuits. Investigations of certain metal-silicon systems have resulted in silicide resistivities that are routinely obtainable [14].

A majority of (TM) transition metal silicides show metallic properties. Usually Si-rich phases with TM from semiconducting materials, nine such semiconducting silicides are known: $CrSi_2$, $MnSi_x$, β-$FeSi_2$, Ru_2Si_3, $ReSi_{1.75}$, $OsSi$, Os_2Si_3, $OsSi_2$, and lr_3Si_5. In the recent years numerous research has been observed in the growth of epitaxial layers and single crystals of semiconducting silicides. This offers a deeper understanding of the fundamental electronic and electrical properties and of silicides and their prospects in various applications [15, 16]. As far as high strength lightweight alloys for automotive applications are concerned [17], the Ce-Zn system is an important part of the multinary Mg-based alloy system Mg-Zn-Mn-RE-(Si).

1.3. Task of the Present Work

In this thesis phase equilibria, crystal structure and physical properties in the ternary systems, making the boundaries of the Ce-Ni-Zn(B, Si) quaternary systems, have been presented. The keen literature review demanded the detailed study in the systems Ce-Zn-B, Ce-Ni-Zn, Ni-Zn-B and Ce-Zn-Si. This thesis includes the crystal structure and the properties of the binary, ternary and quaternary compounds along with the binary and ternary isothermal sections. The work was planed on the bases explained below,

1.   To investigation the phase equilibria, presence of ternary phases and homogeneity ranges of the binaries at 800°C for the system Ce-Zn-B. During this study a low temperature modification of Ce_2Zn_{17} phase and problem in the Ce-Zn binary phase relations led this work to include Ce-Zn system in the process of investigation.

2.   Phase equilibria at 800°C for the Ni-Zn-B ternary system has been reported by [18] for the Ni rich corner with five ternary phases, out of which structure of only one was reported [19].

i. The aim of the present work was to reconstruct an isothermal section at 800°C for the Ni-Zn-B ternary system covering the entire range of the phase diagram.

ii. To determine the crystal structures of all the hitherto unknown phases in the Ni-Zn-B system. So the structure of τ_1, τ_2, τ_3, τ_4, τ_5 and τ_6 was aimed to investigate with help of X-ray single crystal and TEM analysis.

iii. After determination of novel Ni-Zn-B compounds; τ_3 and τ_4 with infinite nets of metal atoms, interesting physical properties were expected to arise from the metal features arising from the covalently bonded metal atoms and ceramic like boron aggregations. Therefore it was aimed to study the electrical, magnetic and mechanical properties of the τ_3 and τ_4 compounds, which reveal a rather different boron-boron aggregation due to their different boron/metal ratio.

iv. Consequently in the present work it was intended to employ X-ray single crystal structure and EPM analyses in order to elucidate details on the site occupation and the void-filling mechanism of combined Ni-Zn in the solid solution of β rhombohedral boron and the self-compensation of the solid solution of Ni-Zn co-doped β boron.

3. An investigation of the isothermal section at 800°C seemed to be necessary in order to link phase relations to our investigation of the multicomponent system Ce-Ni-Zn-{B,Si}. As a further task, thermal stability, crystal symmetry and atom distribution was needed to be checked/established for the solution phases $Ce(Ni_{1-x}Zn_x)_5$, $Ce_2(Ni_xZn_{1-x})_{17}$ and $Ce(Ni_xZn_{1-x})_{11}$.

4.   Besides the compound CeZnSi, which has been reported [20] to be paramagnetic within the temperature range of 77-300K, no phase diagram was reported for the system Ce-Zn-Si. Therefore the present work intends to provide detailed information on phase equilibria and crystal structures in the Ce-Zn-Si system.

Arc melting, sintering or melting in the quartz ampoules have been employed for sample preparation for all the investigations. X-ray Powder diffraction and X-ray single crystal diffraction were used to solve the crystal structure. Light optical microscope, Scanning electron microscope and EPM analysis were used for characterization of materials. (Details given: Chapter 2).

1.4. References

[1]   J.F. Smith, Methods for Phase Diagram Determination, Chapter 1, Elsevier Ltd., 2007.

[2]   T. Mori, D. Berthebaud, T. Nishimura, A. Nomura, T. Shishido, K. Nakajima, Dalton Trans. 39(2010) 1027–1030.

[3]   T.B. Massalski, Binary Alloy Phase Diagrams, 2nd Ed., ASM International, Ohio, 1990.

[4]   T. Mori, Handbook on the Physics and Chemsitry of Rare Earths, ed. K.A. Gschneidner Jr., J-C. Bunzli and V. Pecharsky, North-Holland, Amsterdam, 2008.

[5]   R A Cutler, Engineered Materials Handbook, ASM International, USA, 4 (1991) 787-803

[6]   G V Samsonov, I U M. Goria, B A. Kovenskaia, Journal of the Less-Common Metals 47 (1976) 147-156.

[7]   S. Murphy, Wear, 98 (1984) 151-161

[8]   X.Tao, G.Wenguan, G.Pinlin, Zhongguo Xitu Xuebao, 16(3) (1998) 230-233.

[9]   A.G.De Golyer, United State Patent Office. 1490696 (1923)

[10]   S.P. Chen, A.F. Voter, R.C. Albers, A.M. Boring, P.J. Hay. J Mater. Res 5 (1990) 955-970.

[11]   Z. Malik, O. Sologub, G. Giester and P. Rogl, Submitted to the J. Alloys Compounds, 2012.

[12]   S. Mantl, '*Ion-beam synthesis of epitaxial silicides—fabrication, characterization and applications*', Mater. Sci. Rep., 1992.

[13]   J.Y. Duboz, P.-A. Badoz, A. Perio, J.C. Oberlin, F. Arund d'Avitaya, Y. Campidelli, J.A. Chroboczek, Appl.Surf.Sci. 38(1989) 171.

[14]   S. P.Murarka, M. H.Read, C. J.Doherty, D. B.Fraser,. J. Electrochem. Soc.129 (1982) 293-301.

[15]   H. Lange, phys. stat. sol. (b) 201 (1997) 3.

[16]   K. Meax and M. Van Rossum (Eds.), Properties of Metal Silicides, INSPEC, London 1995.

[17]   I.J. Polmear, Light Alloys, third ed., Arnold London, 1995.

[18]   H.H. Stadelmaier, J.-D. Schöbel, L.T. Jordan, Metall. 16 (1962) 752-754.

[19]   H.H.Stadelmaier, T.S. Yun, Z. Metallkde 53 (1962) 754-756.

[20]   H. Kido, T. Hoshikawa, M. Shimada and M. Koizumi, Phys. Stat. Sol. (a) 80 (1983) 601-605.

2

Experimental Techniques

2.1. Synthesis Details and Characterization Procedure

Alloys have been prepared either by Arc melting or sintering of the high purity, i.e, 99.9% elements. In sintering pieces of rare earth metals, Zn filings or Ni powders were used. In case of Arc melting procedure, powders of the arc melted mater alloys were cold compacted with the Zn filings and then were sealed in quartz tubes along with the Al_2O_3 crucibles. After heating or melting to the desired temperatures samples were water-quenched. These samples were either used for (single crystal) SC selection or were further annealed. After synthesis, in some cases, samples were powdered for the assurance of the homogeneity, inside the glove box or under cyclohexane in order to avoid the oxidation. Re-powdered samples were again cold compacted and annealed in the quartz tubes and after water quenching were subjected to the XPD and EPMA analysis.

Single crystals have also been grown through flux method by using Zn in excess to act as a matrix. In this case sample's melts were boiled with the 15% aqueous solution of HCl in a water bath. Residues of the samples were separated with the help of the filter paper, after washing many times crystals were dried up.

For the physical properties measurements sample cylinders of 0.8 cm height and 1 cm diameter were prepared by arc melting of their master alloys. These master alloys were powderized either by ball milling or hand milling, in case of hand milling process was carried out in the glove box. The Zn filings were cold compacted with the powders of master alloys and process of synthesis was carried out in the quartz tubes. After synthesis samples were again powdered in the glove box and loaded to the graphite die for hot pressing. Hot pressed materials were grinded from the surface to get rid of the attached carbon, after density measurement small parts were cut down to use in the XPD and EPM analysis. Flow sheet diagram of the general synthesis procedure has been described in Fig. 1.
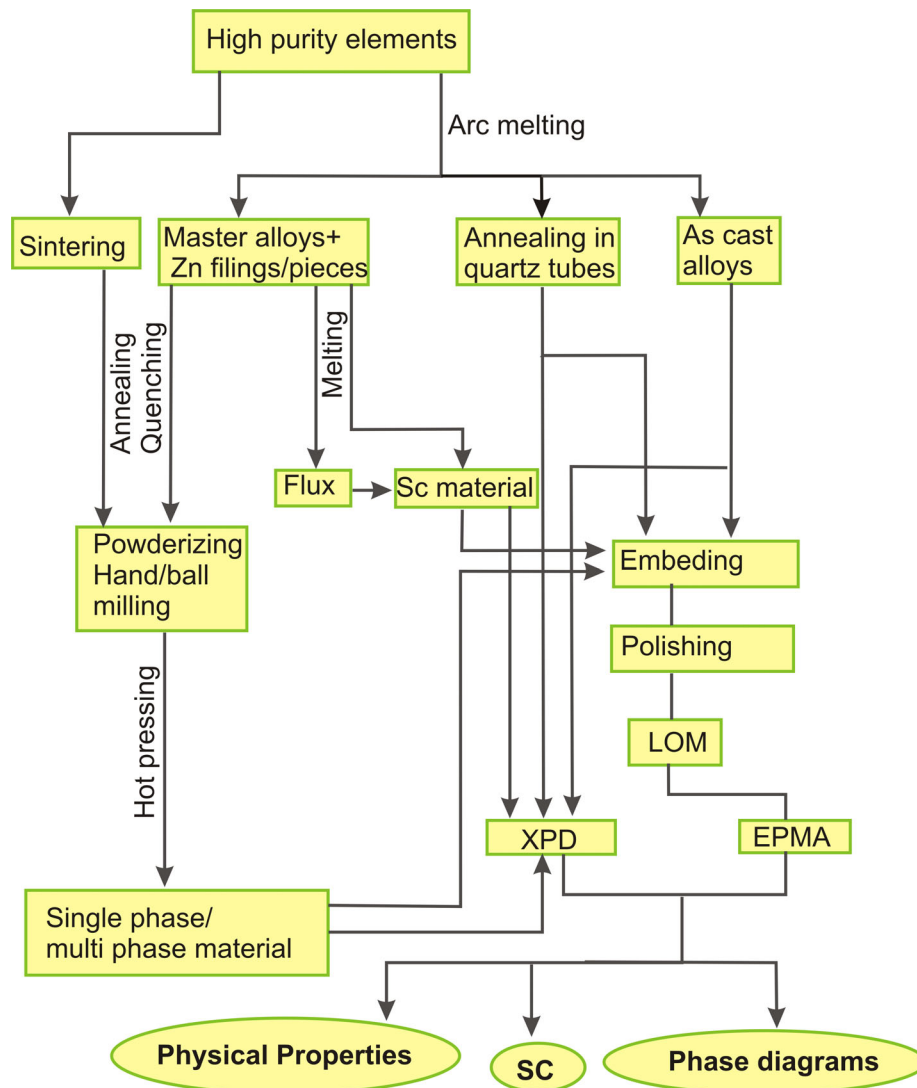
Figure 1. Flow sheet diagram for the synthesis procedure.

2.2. Instruments

2.2.1. Arc Furnace

Arc melting has been performed on the elemental ingots on a water-cooled Cu hearth under argon atmosphere in the presence of Ti getter. Prior to the melting with W electrode arc melting chamber is evacuated to 0 bar and then flush Ar up to 07-0.8 bar three times. After this Ti getter is melt first in order to ensure the burning of all air if it is there in small quantities. Then sample was melted three times after turning its sides, in order to ensure its homogeneity. Power is switched off, during complete diminishing of the flam it is kept on the Ti getter again. At the end the Ar is flushed to the full scale in order to open the chamber for taking the sample out. Schematic view of our arc melting chamber is given in Fig.2

Figure 2. The arc-melting furnace.

2.2.2. *Hot Pressing*

In order to densify the materials (HP W 200/250-2200-200KS) HP from FCT System GmbH has been used, an overall view of the equipment is shown in Fig. 3. System has high-density graphite heater with a limit of 2200°C and the maximum 14 kN pressure is possible to be exerted on the material. Process of hot pressing can be carried out in the presence of Argon or Nitrogen or in the vacuum. The experimental parameters such as temperature, heating/cooling rate, pressure and dewel time had to be optimized according to the nature of the material going to be hot pressed. In case of volatile material HP was cleaned before and after its application. In present work 800°C temperature and 56 MP pressure for 1 hour has been employed on both: the bulk sample powders loaded in 1 cm graphite die or the 6mm sample pellets loaded in two layers by putting three pellets in each layer with a separator, the Al_2O_3 powder (Al_2O_3 powder was pre heated and cooled down at 800°C in order to get rid water vapors).

Figure 3. An overall view of FCT Hot Press.

2.2.3. **X-Ray Diffraction**

2.2.3.1. *IP (Image Plate) and XPD (X-ray Powder Diffraction)*

The IP (Huber Gunier Image Plate Camera G 670) with CuKα radiation (λ=0.154051 nm) has been used for X-ray powder diffraction analysis. In the Guinier camera a monochromatic beam (at the angle of 45° to sample normal) is being transmitted through the powder sample and the diffracted beams is being recorded on the circular focusing detecting film (Fig. 5b). The diameter of the focal circle of the monochromator is 360 mm while that of the focal circle of the camera is 180 mm (covering the 2θ range from 0 to 100°).

The aluminum camera housing has two main parts (see Fig. 5a):

a) The upper inner part of the camera cylinder has the,

    i.   Image Plate.

    ii.   Halogen lamp (for erasing).

    iii.   X-ray entrance window.

b) The lower part has,

    i.   Electromechanical device to actuate the readout unit.

The red beam (λ=635nm) from the diode laser is focused on the surface of the IP. The diffusely scattered blue *photo-stimulated luminescence* light enters a *photomultiplier*

tube through a blue transmitting filter. The step motor clock triggers the A/D converter, i.e. each step of the driving motor generates the corresponding signal value of the PMT. One complete diffractogram of a sample within 2θ range (0-100°) consists of 20,000 data points for a step resolution of 0.005° 2θ. More details about the IP Guinier camera G670 are possible to obtain from the web site: [1]
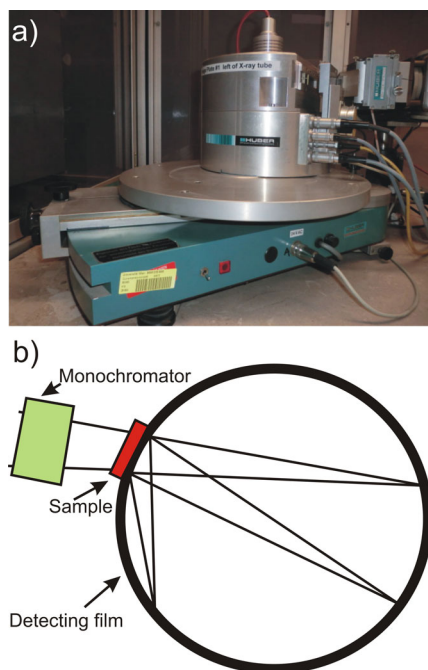
Figure 5. a) An overall view of Huber G670 Image Plate, b) schematic view of geometry.

2.2.3.2. AXS GADDS

The morphology, any of kind disorder and twinning in the crystal have been analyzed with the help of D8 Discover with GADDS (General Area Detector Diffraction System) by Brucker Axs GmbH. Main feature of this instrument is the presence of 2D detector as it collects the data in two dimensions.
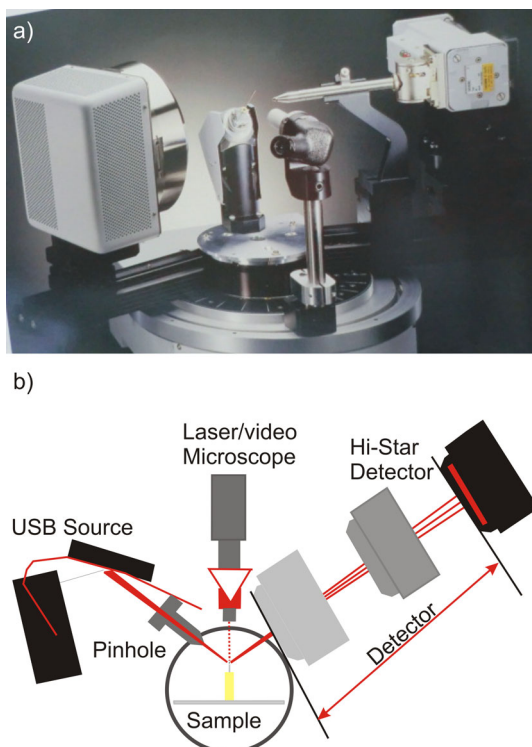
Figure 5. a) View of D8 discover with GADDS, b) Schematic of SC mounted.

GADDS has various applications but we use it to ensure the good quality of the crystal and its unit cell dimensions. Single crystal is mounted with the transparent glue on the tip o f glass fiber mounted inside the brass holder with help of wax as shown in the figure 5b. Sample holder is mounted on a *xyz* stage. Hi –Star area detector intercepts the X-rays scattered from the sample finally displays the pattern in the 2 dimensional image frames. (Details can be found in the D8 discover with GADDS manual).

2.2.3.2. Nonius Kappa diffractometer and area detector CCD

The Bruker's four-circle diffractometer has been used for (single crystal) SC studies. The instrument is equipped with,

    i.   Kappa goniometer,

    ii. MoK_α X-rays source and

    iii.   2 dimensional CCD detector.

Position of the SC sample is adjusted with the help of its image on the computer screen attached. HV (high voltage) and the rotating anode generators produce MoK_α X-rays. These X-rays are controlled with the help of main shutter, fast shutter, monochromator and collimator before interfering with the sample. X-rays diffracted

through the sample hit the detector through the Be window, where these X-rays are transferred to the light photons. These photons are converted to the electrons by the CCD camera. Detector reads the signals and amplifier, amplifies them. In the controller system these signals are digitalized and appear on the computer (Technical detail scan be found in the manual). Figure 6a and b are showing the schematic view of the instrument.
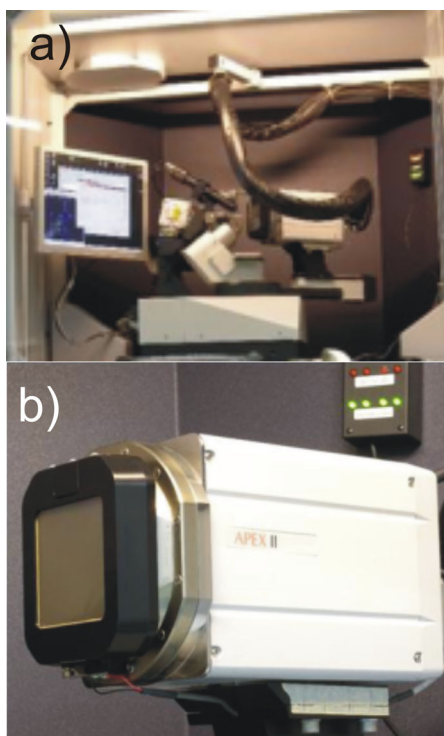
Figure 6. a) KAPPA APEX II CCD X-Ray diffractometer of the manufacturer Bruker AXS, b) detector in bigger view.

2.2.4. EPMA (Electron Microprobe Microanalysis)

In case of compact, solid and hard samples the pieces were embedded inside the conducting resin by using AOMPLIMET 3 molding press (Buehler, Lake Bluff: Illinoise USA with 2150°C and $9*10^7$ Pa). In some cases the samples were embedded inside the Technovit with a conducting rim around when samples were required to cut in a specific direction. The powder samples were mixed with the conducting glue to form the 5 mm molds, after drying, these moulds were embedded inside the conducting resin. Samples were grinded on sand papers of different SiC grit size and then polished with water, glycerin, ethanol or oil as per requirement of the material. Polishing was performed in the presence of 0.05-0.3 μ fine alumina powder on fine polishing cloth.

Electron microscope Zeiss Supra 55 VP by Oxford Instruments has been used for the characterization of composition in the samples (see Fig. 7 L.H.S) its working principle is shown in the Fig. 7 (R.H.S). The instrument is equipped with the four detectors, working partly under vacuum and partly under low pressure conditions. Out of these four detectors, three are sensitive to the secondary electrons, and one is to the backscattered electrons.

Electron beam is bombarded on the polished surface of the sample. These electrons can excite the inner shell electrons of the specimen leaving a vacancy in the inner shell. This vacancy is filled by the outer shell electrons with a consequence of crharacteristics X-rays are emitted. From these characteristic X-rays qualitative (from λ) and quantitative (from I) analysis is possible.

As a result of sample and electron beam interaction heat, X-rays, Bremstrahlung, secondary and backscattered electrons are liberated. Secondary electrons are used for the topological analysis while backscattered electrons are used to differentiate the phases in the sample due to enhanced contrast.
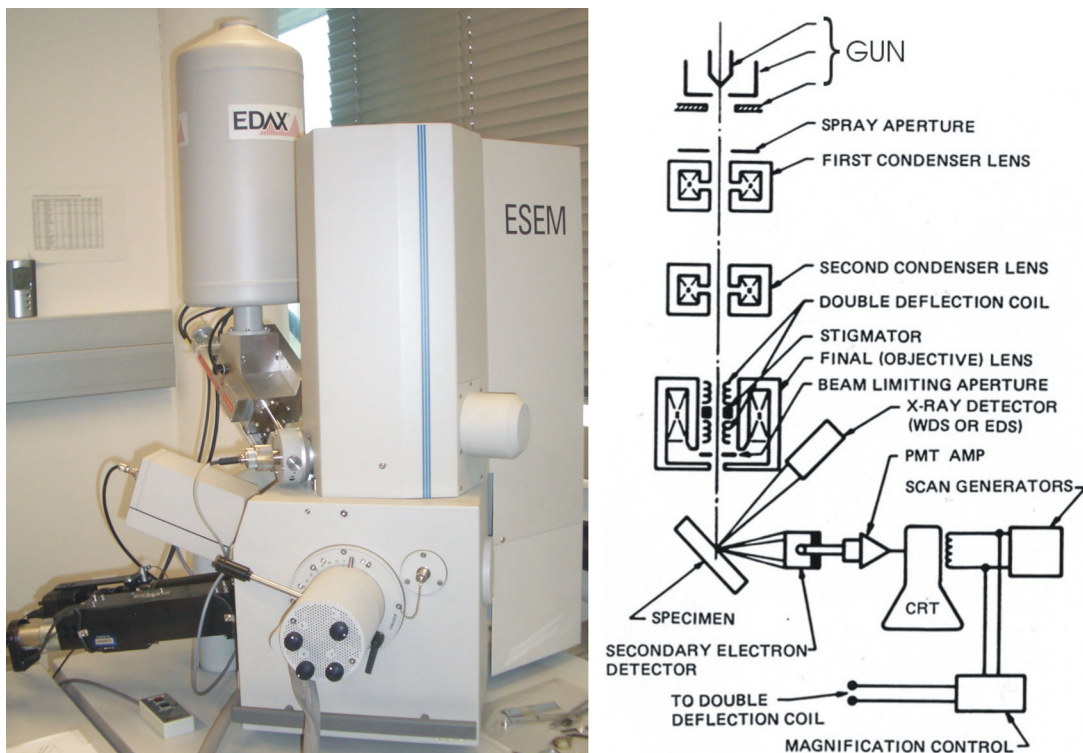
Figure 7. Over all view of (L.H.S) SEM-EPMA, schematic drawing (R.H.S) of electron and X-rays optics of a combined Sem and EDX. (Fig. (R.H.S): [2]

Electron microprobe set up mainly consists of the following parts:

i) Electron gun (commonly W-filament).

ii) Series of electromagnetic lenses (to have condense and focused electron beam).

iii) *xyz* - sample stage in a vacuum chamber.

iv) Light microscope (to observation the sample).

v) The detectors (around the sample chamber).

2.3. Data Analysis
2.3.1. XPD Data

X-ray powder diffraction data of single or multi phase sample powders have been recorded on a Huber G670 IP in the Guinier geometry both with and without the Ge as an internal standard.

2.3.1.1. PCW (Powder Cell)

The program PCW (Powder Cell) [3] has been used for the comparison of experimental XPD data with the patterns of known structures created through the cell files.

2.3.1.2. STRUKTURE

X-ray powder diffraction data collected with the Ge as an internal standard are used for the calculation of the lattice parameters of the phases present in the single or multiphase samples. The peaks of the XPD data of the sample with Ge standard are marked at the certain theta positions in the program STRUCTURE [4] form where a correction curve for Ge peaks is obtained. After employing this correction to all peaks of the pattern, lattice parameters of the phases in the sample are calculated by comparing the theoretical and observed peaks in the program X15. LAZY PULVARIX and GITTER are present in the package of MENU program. The input data for known structures have been provided by the help of LAZY PULVARIX while the GITTER program creates a git file from where we can estimate the correctness of the lattice parameter values calculated.

2.3.1.3. Rietveld Refinement
Rietveld refinement is a technique devised by the Hugo Rietveld for the characterisation of crystalline materials [5]. The neutron and X-ray diffraction of

powders result in the patterns characterised by peaks with the intensities at certain positions. Rietveld refinement solves the following system of equations by means of least squares minimization, $y_1^{calc} = s y_1^{obs}$ $y_2^{calc} = s y_2^{obs}$ $y_i^{calc} = s y_i^{obs}$ where Y_i^{calc} and Y_i^{obs} are the calculated and observed intensities at a pont i, respectively. s is the pattern scale factor [6].

The quantity minimized in the least squares refinement is the residual, S_y: Where y_{ci}

$$S_y = \sum_i w_i (y_i - y_{ci})^2$$

and y_i are the calculated and observed intensities at the ith point.

A powder diffraction pattern of the crystalline material is a collection of individual reflection profiles, each of which has a certain intensity,

$$I_k \propto |F_k|^2$$

I_k is the Bragg intensity (k stands for the Miller indicies, *h, k, l*).and $|F_k|$ is the absolute value of the structure factor. The calculated intensities (y_{ci}) are determined from the $|F_k|^2$: calculated from the structural model by summing the calculated contributions from neighbouring Bragg reflections and the background, Wher s is the scale factor, k represents the Miller indicies, L_k the Lorentz, polarization and

$$y_{ci} = s \sum_k L_k |F_k|^2 \phi(2\theta_i - 2\theta_k) P_k A + y_{bi}$$

multiplicity factor, Ø is the reflection profile function, P_k is for the preferred rientation function, A is an absorption function, F_k is the structure factor for the k th Bragg reflection and y_{bi} is the background at the *ith* step. Structure factor is calculated by the following equation,

$$F_k = \sum_j N_j f_j \exp\left[2\pi i \left(hx_j + ky_j + lz_j\right)\right]\exp\left[-M_j\right]$$

where *hkl* are the Miller indicies, *xj, yj, zj* are the position parameters, f_j is the scattering power of the jth atom it is a fuction of $\sin\theta/\lambda$, $\overline{U_j}^2$ stands for the root mean square thermal displacement, N_j is the site occupation and B_j is its thermal displacement parameter. $M_j = 8\pi^2 \overline{\mu_s^2} \sin^2\theta / \lambda$

$\overline{\mu_s^2}$, is the root mean square thermal displacement of the jth atom parallel to the diffraction vector. Certain parameters, i.e, scale factor, background, lattice parameters, shape parameters, temperature factors, site occupation, atomic coordinates, asymmetry and preferred orientation are refined in the FULPROF [7] until the difference between observed and calculated is reached to its minimum. Mathematically following equations are the criteria for a best fit,

$$R_F = \frac{\sum \left| (I_k(obs))^{1/2} - (I_k(obs))^{1/2} \right|}{\sum \left(|I_k(obs)| \right)^{1/2}} \_\_\_\_\_ R - structure - factor$$

$$R_B = \frac{\sum |I_k(obs) - I_k(calc)|}{\sum (I_k(obs))} _____ R - Bragg\_factor$$

$$R_P = \frac{\sum |y_i(obs) - y_i(calc)|}{\sum (y_i(obs))} _____ R - Pattern$$

$$R_{wp} = \left\{ \frac{\sum w_i (y_i(obs) - y_i(calc))^2}{\sum w_i (y_i(obs))^2} \right\}^{1/2} \_\_\_ R - Weighted - Pattern$$

R- weighted pattern is more meaningful among all as is because it has the residual being minimized in the munerator. So it best reflects the quality of the refinement process.

2.3.2. SC (Single Crystal) Data

An X-ray SC measurement through Nonius Kappa diffractometer and area detector CCD gives an *hkl* file and the unit cell dimensions of the crystal. From the analysis of systematic extinctions space group is assigned. According to the electron density map of the crystal, atom positions are assigned finally the structure is calculated by using the WINGIX [8] program, which has SHLEXL97 [9], SHLEXL-97-2 [10], Fourier MAP and many other programs in its package. Crystal structure and the polyhedra are drawn in the pictorial from by using either DIAMOND and / ATOMS.

2.4. References

[1]   www.xhuber.com/er/diffractometer/guinier/ 670/670.htm
[2]   http://serc.carleton.edu/research_education/geochemsheets/techniques/SEM.html)
[3]   W. Kraus, G. Nolze, Federal Institute of Materials Research and Testing Rudower Chaussee 5, 1289 Berlin, Germany (version: 1990-2000).
[4]   W. Wacha, Diploma Thesis, TU Wien, 1989.
[5]   H. M. Rietveld, Acta Cryst. 22 (1967) 151.
[6]   Young,R.A. Ed., Teh Rietveld Method,Oxfor University Press, Oxford, New York, 1995.
[7]   J. Rodríguez-Carvajal, Satellite Meeting on Powder Diffraction of the XV IUCr Congress, 127 (1990).

[8]   L.J. Farrugia, J. Appl. Cryst. 32 (1999) 837-838.

[9]   G.M.Sheldrick, SHELXS-97, Program for Crystal Structure Refinement University of Göttingen, Germany Windows version by McArdle, Natl. Univ. Ireland, Galway, 1997.

[10]   G.M.Sheldrick, Acta Crystallogr. A64 (2008) 112-122.

3

The System Ce-Zn-B at 800°C

3.1.   Introduction

Zinc-based alloys with rare-earth metals are used in several engineering applications and are often employed to replace cast iron because of similar properties and better machinability [1]. Rare earths (RE) improve the mechanical performance, tensile strength, hardness and also the corrosion resistance by removing impurities from the grain boundaries of their alloys with zinc [2]. Zinc alloys with about 15 mass% boron or even less exhibit high tensile strength, high degree of hardness, high resistance to oxidation and corrosion, low shrinkage factor and low specific gravity [3]. Multi-component zinc and boron alloys containing various amounts of elements such as aluminium, copper or calcium can be used for the production of bearings, bars, rods, sheets, tubes, plates, for the production of ingots, or other finished or semi-finished articles [3].

As far as high strength lightweight alloys for automotive applications are concerned [4], the Ce-Zn system is an important part of the multinary Mg-based alloy system Mg-Zn-Mn-RE, however, nothing is yet known on the influence of boron additions and no phase diagrams have yet been reported for systems RE-Zn-B. Therefore the present work tries to provide detailed information on phase equilibria and crystal structures in the Ce-Zn-B system.

3.2.   Experimental

Samples in a total amount of ca. 0.5 g each were prepared from cerium ingots (Alfa Aesar, purity >99.9 mass%), zinc granules (Alfa Aesar, purity >99.9 mass%) and boron pieces (ChemPur, Karlsruhe, purity 98 mass%). Zinc drops were purified in an evacuated quartz tube by heating them below the boiling temperature of Zn (907°C). Cerium was mechanically surface cleaned before use.

> ***Binary alloys:*** Ce cuttings and Zn filings in various stiochiometric ratios were cold pressed, sealed in quartz tubes under vacuum and then slowly heated to 420 °C. Samples were kept at this temperature for 12h before heating up to the melting range (about 100°C above T_m) at the rate of 1°C/min. prior to cooling down to 800°C at the same rate. The reguli were annealed at 800°C for 7 days and

quenched by immersing the quartz ampoules in cold water. Selected alloys were annealed at various temperatures in the range of 420 °C to 850 °C for 7 days. CeB_6 and CeB_x master alloys were prepared by arc melting cerium cuttings and boron pieces under argon.

Ternary alloys: Two procedures were used for the evaluation of ternary phase relations: (i) samples were prepared from intimate blends of powders of arc melted CeB_x master alloy and fine Zn-filings in proper compositional ratios. The blends were cold compacted in a steel die without lubricant, vacuum sealed in quartz tubes and heat treated and quenched as described for the binary alloys.

(ii) samples were prepared from mixtures of arc melted CeB_6 and binary Ce_xZn_y master alloys prepared like described in (i). Melting and heat treatment was performed as for alloys (i).

X-ray powder diffraction data were collected from each alloy in as cast and annealed state employing a Guinier-Huber image plate system with monochromatic $CuK_{\alpha 1}$ radiation ($8º<2\theta<100º$). Quantitative Rietveld refinements of the X-ray powder diffraction data were performed with the FULLPROF program [5].

Single crystals were mechanically isolated from crushed as cast alloys. Inspections on an AXS-GADDS texture goniometer assured high crystal quality, unit cell dimensions and Laue symmetry of the specimens prior to the X-ray intensity data collections on a four-circle Nonius Kappa diffractometer equipped with a CCD area detector employing graphite monochromated Mo Kα radiation ($\lambda=0.071069$ nm). Orientation matrices and unit cell parameters were derived using the program DENZO [6]. No absorption corrections were performed because of the rather regular crystal shapes and small dimensions of the investigated specimens. The structures were solved by direct methods and were refined with the SHELXL-97 program [7,8] within the Windows version WINGX [9]. The as cast and annealed samples were polished using standard procedures and microstructures and compositions were examined by light optical microscopy (LOM) and scanning electron microscopy (SEM) via Electron Probe Micro-Analyses (EPMA) on a Zeiss Supra 55 VP equipped with an EDX system operated at 20 kV. For binary compounds $ßCe_2Zn_{17}$ was used as EPMA standard. The differences between measured and nominal compositions were found to be <1 at %.

3.3. Results and Discussion

3.3.1. Binary Boundary Systems

The binary systems Zn-B and Ce-B were used in the version presented by Massalski [10]. In agreement with literature data, we observed no evidence of chemical interaction between zinc and boron. The formation and crystal structures of compounds CeB_4 and CeB_6 were confirmed. Although several critical assessments have been recently published on the phases and phase relations in the Ce-Zn binary [11, 12], our work on the ternary Ce-Zn-B system revealed several structural inconsistencies for the binary Ce-Zn compounds [10, 13, 14], which made a reinvestigation of the crystal structures in the Ce-Zn binary system necessary (see below).

The crystal data relevant to the unary and binary boundary phases in the Ce-Zn-B system, including results of our reinvestigation of the Ce-Zn system, are presented in Table 1.

3.3.2. The System Ce-Zn

Crystal structure Rietveld refinements for all those binary compounds, which have been already reported earlier, namely $CeZn_{11}$ [15], $CeZn_5$, $CeZn_3$, $CeZn_2$ and $CeZn$ [10, 13], were found to be consistent with data in the literature. Therefore, the reinvestigation of crystal structures and phase relations in the Ce-Zn system essentially focused on the determination of crystal symmetry, precise atom site distribution and positional parameters for those compounds (*hexagonal*-$CeZn_{\sim 7}$, *rhombohedral*-Ce_2Zn_{17}, Ce_3Zn_{22}, $Ce_{13}Zn_{58}$, and Ce_3Zn_{11}), for which crystal structure data hitherto have only been derived from X-ray diffraction photographs or have not been evaluated (*hex*-$CeZn_{\sim 7}$).

3.3.3. Structural Chemistry

3.3.3.1. X-ray single crystal intensity data refinement of Ce_3Zn_{11} and Ce_3Zn_{22}

Ce₃Zn₁₁: The X-ray intensity spectrum of a single crystal selected from the crushed sample $Ce_{23.35}Zn_{76.65}$ (at.%) was fully indexed with an orthorhombic lattice (a=0.45242(2) nm, b=0.88942(3) nm, c=1.34754(4) nm). Systematic extinctions only

observed for a body-centered Bravais lattice (*hkl*), *h+k+l=2n+1* indicated the space groups *Immm, I222, Imm2* and *I2₁2₁2₁*. *Immm* with highest symmetry was used to solve the crystal structure employing direct methods. Composition, lattice parameters, crystal symmetry, Wyckoff sequence *2a, 2d, 4h, 4i, 8l²* and atom parameters prompted isotypism with the structure type of La$_3$Al$_{11}$. The structure solution converged at $R_{F^2} = 2.6$ yielding a residual electron density less than ±2.8 e⁻/Å³. Crystal data and interatomic distances are presented in Table 2a. and 2b. The characteristic stacking of face-connected units...AuCu$_3$-BaAl$_4$ ...is documented in Fig. 1 including the polyhedra of the individual atom sites. Although the structure solution provides positional and thermal atom parameters of significantly higher precision it confirms the early structure determination of Ce$_3$Zn$_{11}$ by Lott and Chiotti [16] performed on the basis of X-ray Weissenberg and precession photographs.
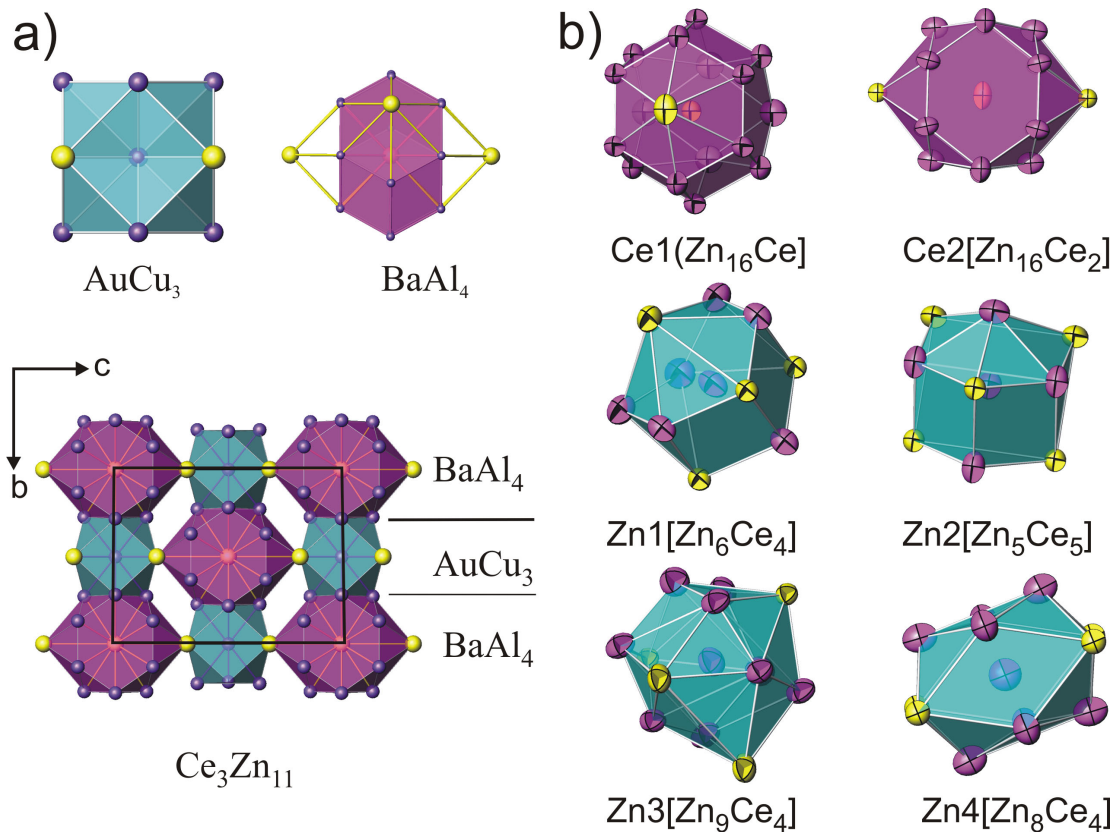
Figure 1. a. Crystal structure of Ce$_3$Zn$_{11}$ (La$_3$Al$_{11}$-type) as an arrangement of building blocks of AuCu$_3$-and BaAl$_4$-type, b. Coordination polyhedra for all crystallographic sites in Ce$_3$Zn$_{11}$ with anisotropic displacement ellipsoids from single crystal refinement.

Ce₃Zn₂₂. A first analysis of the crystal structure of Ce_3Zn_{22} from essentially steric considerations is due to Kripyakevich et al. [17] providing a set of atom parameters. Johnson and Wood [18] compared observed and calculated X-ray powder data for Ce_3Zn_{22} and reported isotypism with the structure of Pu_3Zn_{22} for which they solved the structure on the basis of single crystal Weissenberg and precession photographs (reliability factor $R_F = 0.096$). In order to provide a precise set of atom parameters and to check on defects or random distributions, a full structure determination was performed on a crystal selected from a crushed sample with nominal composition $Ce_{12}Zn_{88}$ (at.%). X-ray intensity data depicted systematic extinctions, (*hkl*) for *h+k+l=2n+1*, (*hk0*) for *h,k=2n+1* and (*hhl*) for *2h+l=4n+1* prompted space group *I4₁/amd* as the one with highest symmetry. Structure analysis employing direct methods ended up at $R_{F^2} = 2.1$ and residual electron densities less than, ± 2.4 e⁻/Å³. The refinement with anisotropic ADPs revealed a fully ordered structure without any defect atom sites. Crystal data and interatomic distances are presented in Table 2a. and 2c, respectively. The crystal structure of Ce_3Zn_{22} is shown in Fig. 2 in three-dimensional view on the *bc* plane emphasizing on the interconnectivity of the Ce-centered polyhedra (Ce1 polyhedra with coordination number 18 and Ce2 polyhedra with coordination number 20). Description of the structure, coordination polyhedra and interatomic distances are consistent with the description earlier presented for isotypic Pu_3Zn_{22} [18].
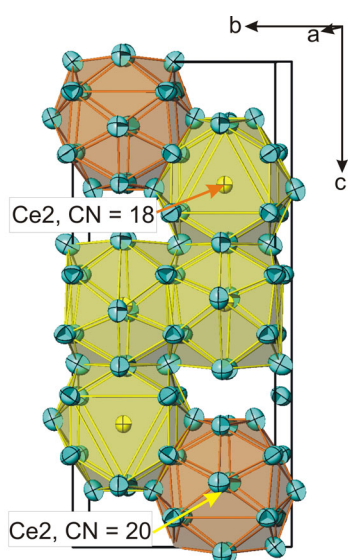
Figure 2. Unit cell of Ce_3Zn_{22} revealing the coordination polyhedra around atom sites for Ce1 and Ce2. Anisotropic displacement parameters comply with single crystal refinement.

3.3.3.2. Rietveld refinement of $Ce_{13}Zn_{58}$, rhombohedral $ßCe_2Zn_{17}$ (*hT*) and of hexagonal $\alpha CeZn_7$ (*lT*).

$Ce_{13}Zn_{58}$: Recently single crystal studies were reported for the $RE_{13}Zn_{58}$ family of hexagonal quasicrystals derived from $Gd_{13}Cd_{58}$ (RE = Ce, Pr, Nd, Sm, Gd, Tb, Dy) [19]. Whereas the Ce and Pr structures were reported to be identical to the prototype, different types of disorder were detected for the other members of the series. Our X-ray powder refinement of $Ce_{13}Zn_{58}$ revealed significant defects for several atom positions e.g. for the sites Ce3, Zn3 and Zn9. With respect to the formation of periodic structures for the later members of the rare earth series, we assume that the structure of $Ce_{13}Zn_{58}$ may exhibit a similar variability in local ordering rendering the general formula $Ce_{13}Zn_{58}$.

Rhombohedral $ßCe_2Zn_{17}$: Polymorphism was reported for the compound Ce_2Zn_{17} with a rhombohedral structure at high temperatures but a hexagonal structure at low temperature [20,21]. In agreement with the findings in the literature our X-ray powder spectra obtained from samples annealed at 800°C were fully indexed on the basis of a rhombohedral lattice (a=0.90916(4) nm, c=1.3286(1) nm) prompting isotypism with the structure type of Th_2Zn_{17} (space group $R\overline{3}m$; No. 166). The results of the Rietveld refinement confirm the Th_2Zn_{17}–type as defined earlier for a single crystal study of the high temperature modification of Ce_2Zn_{17} [22].

Hexagonal $\alpha CeZn_7$ (αCe_2Zn_{17}). As already observed by Iandelli et al. [21], it seems extremely difficult to obtain the low temperature form from the high temperature modification ($ßCe_2Zn_{17}$) by long term annealing at 500°C. $ßCe_2Zn_{17}$ however, can easily be formed by heating the low temperature modification above ~775°C. Slow heating of the mixture of components $Ce_{10.5}Zn_{89.5}$ (at.%) up to 500 °C and annealing at this temperature for 5 days produced an alloy with an X-ray powder diffraction pattern yielding a majority of the low-temperature phase. Although the X-ray pattern was completely indexed with a hexagonal cell (a=0.52424(2) nm, c=0.44274(1) nm) for the low temperature form and small amounts of $ßCe_2Zn_{17}$ ($P6_3/mmc$) and $CeZn_{11}$ ($BaCd_{11}$-type), the small unit cell parameters do not correspond to the Th_2Ni_{17}-type

structure as reported for "αCe$_2$Zn$_{17}$" by Iandelli et al. [21] and Veleckis et al. [23]. Much better correspondence between the observed and calculated X-ray powder diffraction pattern was achieved applying the atomic model of the TbCu$_7$ type structure [24]. The TbCu$_7$-type adopts the CaCu$_5$-type unit cell and is a member of a structure family A$_{1-s}$B$_{5+2s}$ where a fraction s of the A-atoms is randomly or in ordered fashion replaced by a dumbbell of B-atoms covering a range of stoichiometries AB$_5$ to AB$_{9.5}$ [25]. Rietveld refinement of the "αCe$_2$Zn$_{17}$" pattern on the basis of this model prompted a low residual value R$_F$=0.045 with a random distribution of 0.67 Ce in the 1a site of space group *P6/mmm*, the holes around the vacancies being filled by 0.33 Zn-dumbbells (Zn2) in site 2*e*. Accordingly the overall formula is close to Ce$_{0.7}$Zn$_{5.6}$ (Ce$_{1-x}$Zn$_{5+2x}$; x~0.33). The Rietveld refinement profile for αCeZn7 is shown in Fig. 3.
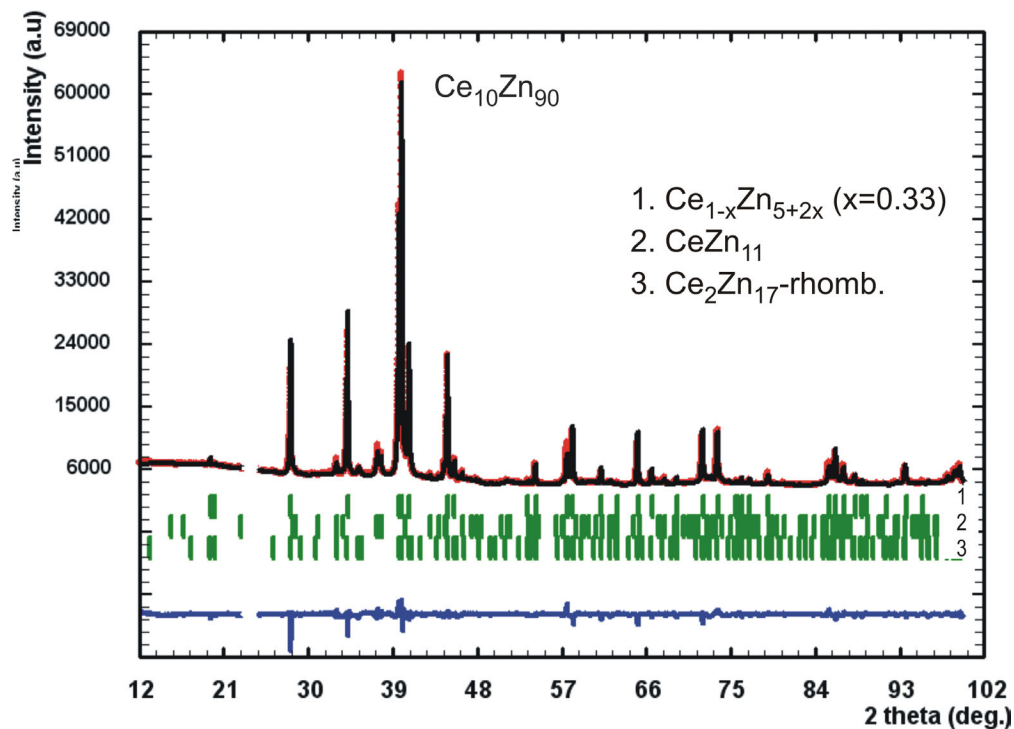
Figure 3. X-ray powder spectrum of alloy Ce$_{10}$Zn$_{90}$ and Rietveld refinement of the low temperature phase: hexagonal CeZn$_7$ (Ce$_{1-x}$Zn$_{5+2x}$, x=0.33) with TbCu$_7$-type. (Excluded region contains a small peak from sample holder).

Interatomic distances are depicted in Table 3a, 3b and Fig. 4a. A Fourier map (Fig. 5b) shows the presence of the electron density, which refers to the Zn2 atoms. Formally short distances d$_{Ce-Zn2}$=0.133 nm and d$_{Zn2-Zn2}$=0.174 nm appear for the random occupation of Ce and Zn2 atoms. However, either a Ce-atom or a Zn2-

dumbbell may exist with an acceptable distance $d_{Ce-Zn2}=0.300$ nm and $d_{Zn2-Zn2}=0.260$ nm.
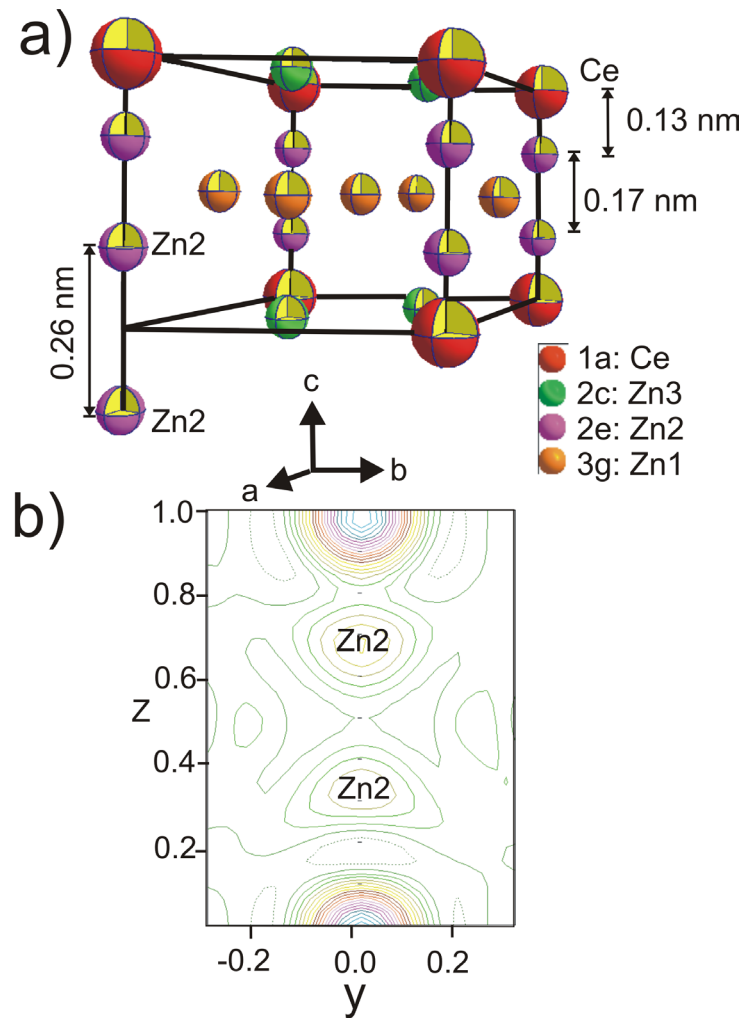
Figure 4. a. Crystal structure of hexagonal CeZn$_7$ [Ce$_{1-x}$Zn$_{5+2x}$ (x=0.33)] with TbCu$_7$-type. A Zn-dumbbell replaces the Ce-atom site in the left lower front corner. b. Fourier map for hexagonal CeZn$_7$ projected onto the yz plane revealing the Zn-dumbbells.

3.3.4. The Phase Diagram Ce-Zn

Knowledge on the binary Ce-Zn phase diagram is summarized in two recent critical assessments and Calphad-type thermodynamic modelings of the binary system [11, 12], both relying on the experimental solidus and liquidus data and the reaction isotherms determined by Chiotti and Mason [26]. In accordance with the published Ce-Zn phase diagram our X-ray reinvestigation confirmed the existence of all

compounds hitherto reported. For a listing of crystal data of compounds (unit cell parameters, space group and structure type) see Table 1. Whereas the crystal structures of $CeZn_{11}$, $CeZn_5$, $CeZn_3$, $CeZn_2$ and $CeZn$, were found to be consistent with data in the literature (Table 1), precise structural data on atom site distribution, atom order and defect formation were provided for *hexagonal*-$CeZn_7$, Ce_3Zn_{22}, $Ce_{13}Zn_{58}$, and Ce_3Zn_{11} (for details see section 3.1.1). We also confirm the irreversible character of the transition (about 750 to 800°C on heating) between the low temperature form *$CeZn_7$* ($Ce_{10}Zn_{90}$ at.%) and the high temperature form *βCe_2Zn_{17}* ($Ce_{10.6}Zn_{89.4}$ at.%), both existing at practically identical composition. Once *βCe_2Zn_{17}* has formed it is impossible to revert to *$\alpha CeZn_7$* (*αCe_2Zn_{17}*), an observation already reported in earlier studies [21].

Evaluation of homogeneity regions of the binary compounds with respect to lattice parameter and EPMA data generally confirmed the various Ce-zincides as practically line-compounds without significant phase regions. Figure 5 documents the two-phase regions for the boundary phases. There was no difference between the refined and reported lattice parameters of Zn [27] suggesting no solubility of Ce in Zn.
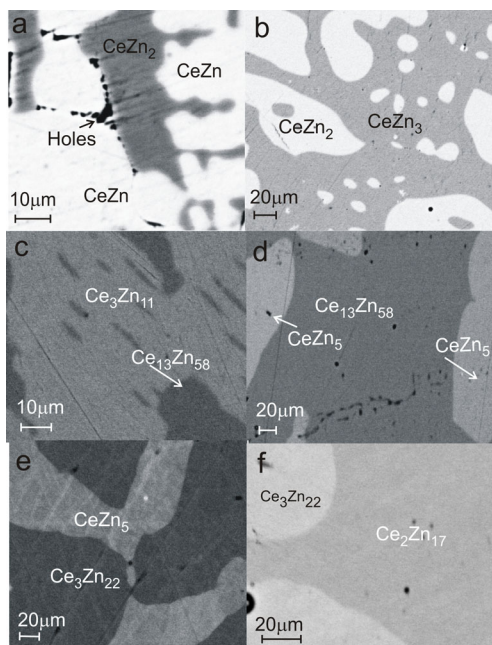
Figure 5. Microstructures for selected Ce-Zn samples annealed at 800°C for 7 days: (a) 40 at.%Ce, (b) 29 at.% Ce, (c) 20 at% Ce, (d) 17.6 at%, (e) 14.3 at.% Ce and, (f), 11.27 at.% Ce.

3.3.5. The System Ce-Zn-B (<50 at. % Ce)

About 20 ternary alloys were prepared and were analyzed by x-ray powder diffraction combined with EPMA. The analysis of the isothermal section at 800°C did not reveal the formation of ternary compounds and all three-phase equilibria derived are documented in Table 4. Two-phase equilibria between Ce_xZn_y binaries and CeB_4 range from CeZn to Ce_3Zn_{22}, whereas Ce_2Zn_{17} and $CeZn_{11}$ tie to CeB_6 (see Fig.6).

1. $CeZn_3$
2. Ce_3Zn_{11}
3. $Ce_{13}Zn_{58}$
4. $CeZn_5$
5. Ce_3Zn_{22}
6. Ce_2Zn_{17}
7. $CeZn_{11}$

Ce - Zn - B
Isotherm 800°C
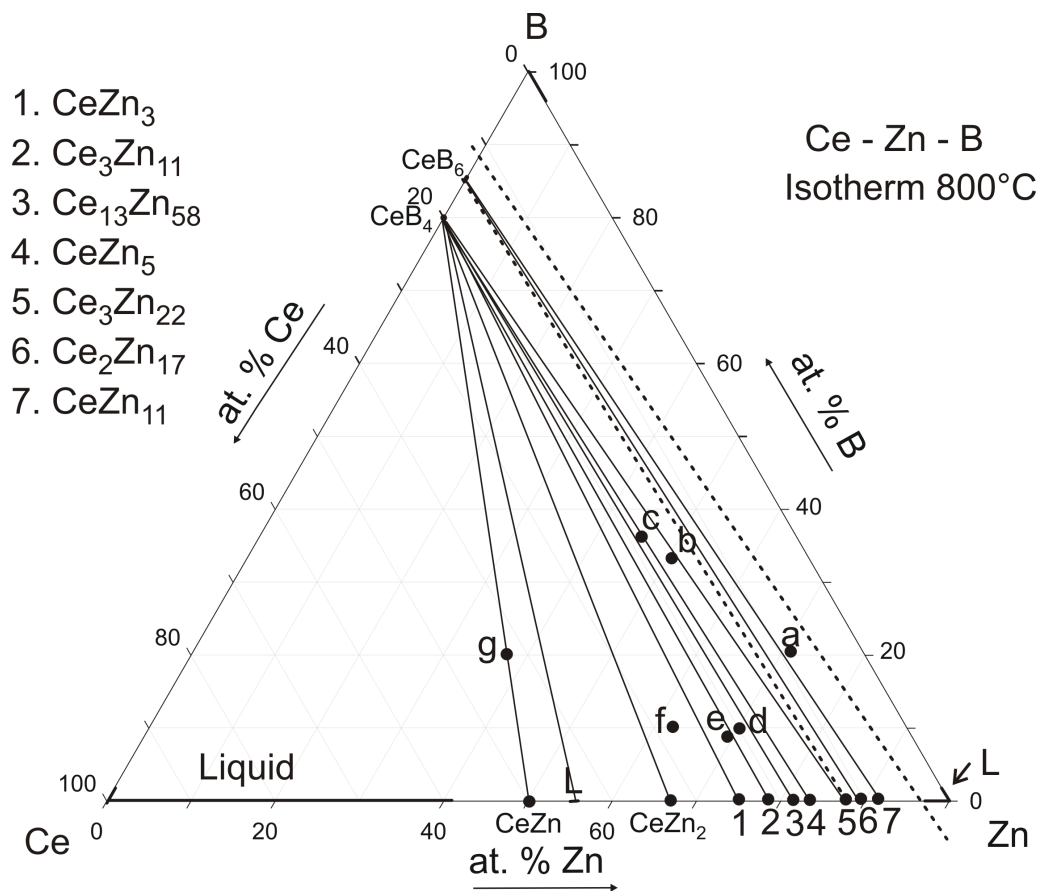
Figure 6. Ce-Zn-B. Isothermal section at 800°C.

In order to verify the equilibria a set of samples was made from CeB_6 + $CeZn_x$ master alloys, which on formation of CeB_4 for (2<x<7) confirmed the triangulation in Fig. 6. Rietveld refinements of representative alloys are summarized in Fig. 7 and document that no ternary Ce-Zn-borides were observed in the alloys investigated. It is, however, still unclear whether Ce_2Zn_{17} ties to CeB_4 or Ce_3Zn_{22} ties to CeB_6 (dashed line in Fig. 6).

In analogy to carbon incorporation in the Th_2Zn_{17} type structure of $Pr_2Mn_{17}C_{3-x}$ [28] we tested the solubility of boron as interstitial in Ce_2Zn_{17} for alloy $Ce_{8.6}Zn_{70.7}B_{20.7}$ (in at%). Rietveld refinement of the powder pattern, however, revealed no change in the lattice parameters with respect to binary Ce_2Zn_{17} as well as the absence of B in the octahedral voids $[Ce_2Zn_4]$. The interatomic distances $d_{B-Ce}=0.262$ and $d_{B-Zn}=0.189$ nm are unfavourable to form $Ce_2Zn_{17}B_{3-x}$. The evaluation of the Rietveld refinement is shown in Table 3a and Fig. 7d.
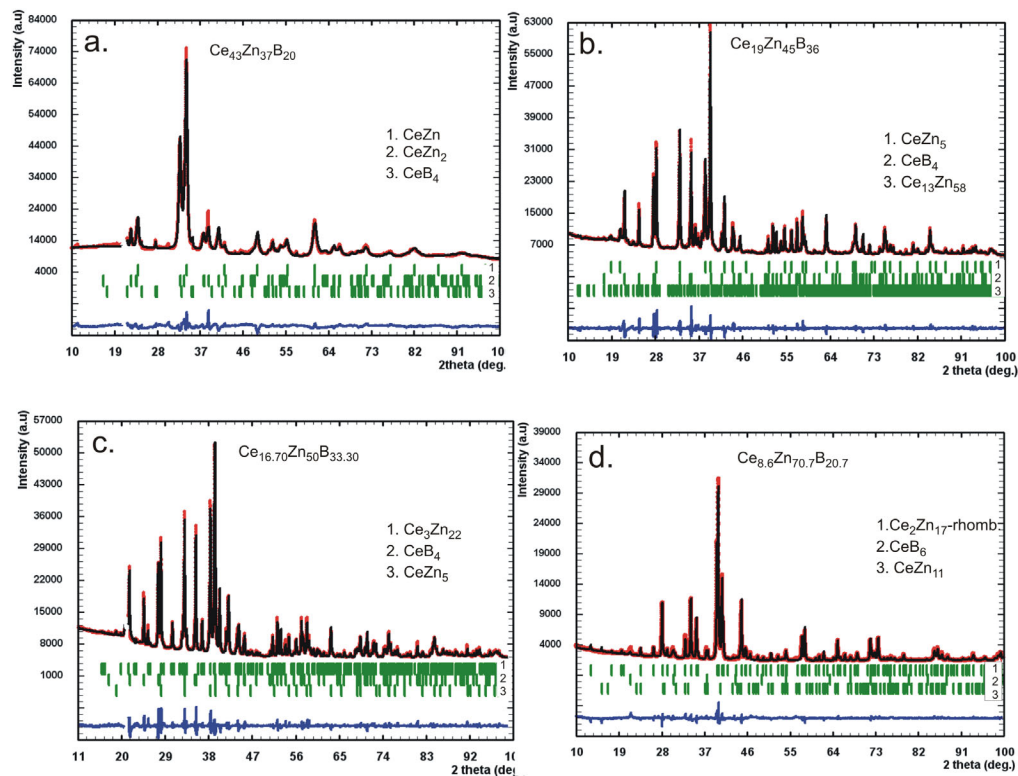
Figure.7. Rietveld refinement for alloys a. $Ce_{43}Zn_{37}B_{20}$, b. $Ce_{19}Zn_{45}B_{36}$ c. $Ce_{16.7}Zn_{50}B_{33.3}$, and, d. $Ce_{8.6}Zn_{70.7}B_{20.7}$. (Excluded regions in 7a ad c contain a small peak from sample holder).

3.4. Conclusion

With EDX and WDX-electron microprobe analysis and x-ray powder diffraction we have derived the isothermal section for the system Ce-Zn-B at 800°C. The section is characterized by the absence of ternary compounds and the absence of significant mutual solid solubilities of binary phases. In the course of the ternary system investigation the binary Ce-Zn system was re-evaluated on about 20 alloys. In the concentration range of 10-10.5 at.% Ce two structural modifications have been

confirmed, which show irreversible transformation behaviour: high temperature ßCe$_2$Zn$_{17}$ exists above ~750 °C with the Th$_2$Zn$_{17}$ type ($R\bar{3}m$, a=0.90916(4) nm, c=1.3286(1) nm) and low temperature CeZn$_7$ (Ce$_{1-x}$Zn$_{5+2x}$; x~0.33) adopts the TbCu$_7$ type (Rietveld refinement of X-ray powder data; $P6/mmm$, a=0.52424(2), c=0.44274(1) nm) which irreversibly transfers to the hT phase on heating above 750°C. X-ray single crystal refinements have been carried out for several compounds, for which crystal structure data hitherto have only been derived from X-ray diffraction photographs. Thus precise data on atom site distribution and positional parameters have been provided for Ce$_3$Zn$_{11}$ (*Immm*, a=0.45242(2), b=0.88942(3) and c=1.34754(4) nm) and Ce$_3$Zn$_{22}$ (*I4$_1$/amd*, a=0.89363(2) and c=2.1804(5) nm).

3.5. References

[1]   S. Murphy, Wear, 98 (1984) 151-161

[2]   X.Tao, G.Wenguan, G.Pinlin, Zhongguo Xitu Xuebao, 16(3) (1998) 230-233.

[3]   A.G.De Golyer, United State Patent Office. 1490696 (1923)

[4]   I.J. Polmear, Light Alloys, third ed., Arnold London, 1995.

[5]   T.Roisnel and J.Rodriguez-Carvalaj, Materials-Science-Forum, (1) 118 (2010) 378-381.

[6]   Nonius Kappa CCD Program Package COLLECT, DENZO, SCALEPACK, SORTAV, Nonius Delft, The Netherlands, 1998.

[7]   G.M.Sheldrick, SHELXS-97, Program for Crystal Structure Refinement University of Göttingen, Germany Windows version by McArdle, Natl. Univ. Ireland, Galway, 1997.

[8]   G.M.Sheldrick, Acta Crystallogr. A64 (2008) 112-122.

[9]   L.J. Farrugia, J. Appl. Crystallogr, 32 (1999) 837-838.

[10]   T.B.Massalski, Binary Alloy Phase Diagrams, second ed., ASM International, Materials Park, OH, 1990.

[11]   P.J.Spencer, A.D.Pelton, Y-B. Kang, P.Chartrand and C.D. Fuerst, Calphad, 32 (2008) 423-431.

[12]   C.P.Wang, X.Chen, X.J.Liu, F.S.Pan and K.Ishida, Journal of Alloys and Compounds, 458 (2008) 166-173.

[13]   P.Villars, K.Cenzual, Pearson's Crystal Data-Crystal Structure Database for Inorganic compounds (on CD-ROM), Release 2010/11, ASM International, Materials Park, Ohio, USA.

[14]   H. Okamoto, Desk Handbook: Phase Diagram for Binary Alloys, ASM International: Materials Park, OH, 2000.

[15]   O.Zelinska, M.Conrad and B.Harbrecht, Z. Kristallogr., NCS, 219 (2004) 357-358.

[16]   B.G.Lott and P.Chiotti, Acta Crystallogr., 20(1966), 733-738.

[17]   P.I.Kripyakevich, Y.B.Kuz'ma and N.S.Ugrin, Journal of Structural Chemistry, Translated from Zhural Strukturnoi Khimmi, 8 (1967) 632-633.

[18]   Q.Johnson, D.H.Wood and G.S.Smith, Acta Crystallogr., B24 (1968) 480-484.

[19]   S Piao, C.P.Gomez and S.Lidin, Z. Kristallogr. 221 (2006) 391-401.

[20]   E. Veleckis, C. L. Rosen and H. M. Feder, A Recording Effusion For Phase Diagram Investigation, (1961) 2127-2131

[21]   A.Iandelli and A.Palenzona, J. Less-Common Metals, 12 (1967) 333-343.

[22]   T.Siegrist and Y.L. Page, J. Less-Common Metals, 127 (1987) 189-197.

[23]   E.Veleckis, R.V.Schablaske, I.Johnson and H.M.Feder, Transactions of the Metallurgical Society of AIME, 239 (1967) 58-63

[24]   K.H.J.Buschow and A.S.Van der Goot, Acta Crystallogr, B27 (1971) 1085-1088

[25]   R.Cerny. Y.Filinchuk and S.Brühne, Intermetallics, 17 (2008) 818-825.

[26]   P.Chiotti and J. T.Mason, Transactions of the Metallurgical Society of AIME, 233 (1965), 786-795.

[27]   R.W.Lynch and H.G.Drickamer. J. Phy. Chem. Solids, 26 (1965) 36-38.

[28]   G.Block and W.Jeitschko, Inorg. Chem., 25 (1986) 279-282.

[29]   M.M. Korsukova, V.N.Gurin, Y.B.Kuz'ma, A.Y.Kiskachi and N.E.Solov'ev, Sov. Phys. Crystallogr, 22 (6), (1977)

[30]   Y.B.Kuz'ma, V.N.Gurin, M.M.Korsukova, A.L.G.Akselrud, Inorganic Materials, Izvestiya Akademii Nauk SSSR, 23 (1987) 500-503.

[31]   E.Parthé, L.Gelato, B.Chabot, M.Penzo, K.Censual and R.Gladyshevskii, TYPIX—Standardized Data and Crystal Chemical Characterization of Inorganic Structure Types, Berlin, Springer, 1994.

Table 1. Crystallographic data of unary and binary boundary solid phases of the system Ce–Zn–B

Phase, Temperature range (°C)	Space group, Prototype	Lattice parameters (nm)			Comments
		a	b	c	
(δCe), 798-700[10]	$Im\bar{3}m$, W	0.412	-	-	[10]
					0≤x≤0.014 at 722 °C [10]
(γCe), <726[10]	$Fm\bar{3}m$, Cu	0.51610	-	-	[10]
		-	-	-	-
(Zn), <420	$P6_3/mmc$, Mg	0.2665	-	0.4947	[10]
		0.2667(1)	-	0.4951(1)	From alloy Ce7Zn93, 600°C^a
(βB), <2092[10]	$R\bar{3}m$, βB	1.09251	-	2.38143	[13]
Zn_xB_{1-x}	-	-	-	-	-
	-	-	-	-	0≤x≤0.042 at 907 °C [29]
	-	1.093	-	2.374	x=0 at 907 °C [29]
	-	1.100	-	2.404	x=0.042 at 907 °C[29]
	-	1.09862(2)	-	2.4016(4)	x=0.039 at 907 °C[30]
CeZn, <825[10]	$Pm\bar{3}m$, CsCl	0.3704(1)	-	-	[13]
		0.37125(2)	-	-	850 °C^a [This work]
		0.37059(2)	-	-	830°C^a Ce poor [This work]
CeZn$_2$, <875[10]	$Imma$, CeCu$_2$	0.4633(5)	0.7538(5)	0.7499(5)	[13]
		0.46393(8)	0.7544(1)	0.7506(1)	700 °C^a Ce-rich [This work]
		0.46356(4)	0.75375(7)	0.75525(6)	850 °C^a Ce-poor [This work]
CeZn$_3$, <820[10]	$Cmcm$, CeZn$_3$	0.4620(5)	1.0440(5)	0.6640(5)	[13]
		0.46324(5)	1.0452(1)	0.66557(6)	850 °C^a Ce-rich [This work]
		0.4635(1)	1.0439(3)	0.6641(2)	850 °C^a Ce-poor [This work]
Ce$_3$Zn$_{11}$, <840[10]	$Immm$, Ce$_3$Zn$_{11}$	0.45215	0.88855	1.3463	[13]
		0.45242(2)	0.88942(3)	1.34754(4)	Single crystal [This work]
		0.45222(1)	0.88898(2)	1.34649(4)	820 °C^a Ce-rich [This work]
		0.45175(6)	0.8894(1)	1.3447(2)	820 °C^a Ce-poor [This work]
Ce$_{13}$Zn$_{58}$, <870[10]	$P6_3/mmc$, Gd$_{13}$Zn$_{58}$	1.4638(1)		1.4158(1)	[19]
		1.4616(1)		1.4173(1)	820 °C^c [19]
		1.4635(5)		1.4176(5)	820 °C^a Ce-rich [This work]
					820 °C^a [This work]
CeZn$_5$, <885[10]; CeZn$_{5+y}$	$P6/mmm$, CaCu$_5$	0.54163(5)	-	0.42647(5)	[13]
		0.54082(1)	-	0.42798(1)	800 °C^a Ce poor [This work]
		0.54163(5)	-	0.42647(5)	0.017≤y≤0.046 <885 °C [16]
Ce$_2$Zn$_{22}$, <960[10]	$I4_1/amd$, Ce$_2$Zn$_{22}$	0.897(1)	-	2.133(5)	[17]
		0.8936(2)	-	2.1380(5)	Single crystal [This work]
		0.89331(2)	-	2.13701(6)	800 °C^a Ce-rich [This work]
		0.89286(1)	-	2.13599(2)	850 °C^a Ce-poor [This work]

Phase, Temperature range (°C)	Space group, Prototype	Lattice parameters (nm)			Comments
		a	b	c	
β Ce$_2$Zn$_{17}$	$R\bar{3}m$	0.9090(5)	-	1.32844(7)	827 °C [13]
<980[10]	Th$_2$Zn$_{17}$	0.90916(4)	-	1.32861(1)	850°C^a [This work]
980~750		0.90884(7)	-	1.3300(1)	850°C^a Ce-rich [This work]
[This Work]		0.90947(1)	-	1.32955(2)	750°C^a Ce-poor [This work]
α Ce$_2$Zn$_{17}$	$P6_3/mmc$ Th$_2$Ni$_{17}$	0.9088(4)	-	0.8856(5)	[21]
<~750[This work]	TbCu$_7$	0.52424(2)	-	0.44274(1)	700°C^a [This work]
CeZn$_{11}$	$I4_1/amd$	1.0658(6)	-	0.6862(8)	497 °C [15
<795[10]	BaCd$_{11}$	1.06630(1)	-	0.686644(7)	480°C^a [This work]
-	-	1.0666(1)	-	0.68645(1)	600°C^a Ce rich [This work]
-	-	1.06689(2)	-	0.68680(2)	600°C^a Ce poor [This work]
CeB$_4$	$P4/mbm$ ThB$_4$	0.7208(1)	-	0.4091(1)	[13]
<2380[10]		-	-	-	-
<2165[14]		-	-	-	-
CeB$_6$	$Pm\bar{3}m$ CaB$_6$	0.4139(4)	-	-	[13]
<2550[10]		-	-	-	-
<2330[14]	-	-	-	-	-

^{a} Quenching temperature of samples while the lattice parameters are measured at room temperature.

Table 2a. Crystal structure data from X-ray single crystal evaluation of Ce_3Zn_{11} and Ce_3Zn_{22}

Compound	Ce_3Zn_{11}	Ce_3Zn_{22}
Composition[c] (at. %)	$Ce_{23.35}Zn_{76.65}$	$Ce_{12}Zn_{88}$
Space group	*Immm*; No. 71	*I4₁/amd*; No. 141, origin at $\bar{1}$
Structure type	La_3Al_{11}	Ce_3Zn_{22}
Formula from refinement	Ce_3Zn_{11}	Ce_3Zn_{22}
θ Range [deg]	$2.74 < \theta < 36.16$	$2.47 < \theta < 36.26$
Crystal size [µm]	20×30×45	25×30×45
a [nm]	0.45242(2)	0.89363(2)
b [nm]	0.88942(3)	0.89363(2)
c [nm]	1.34754(4)	2.13804(5)
Reflections in refinement	615 $F_o > 4\sigma(F_o)$ of 759	875 $F_o > 4\sigma(F_o)$ of 1131
Mosaicity	0.55	0.6
Number of variables	28	39
$R_F^2 = \Sigma|F_0^2-F_c^2|/\Sigma F_0^2$	0.026	0.021
R_{Int}	5.6	6.7
GOF	1.059	1.061
Extinction (Zachariasen)	0.0009(1)	0.00011(1)
M1; Occ. U_{11}^{b}; U_{22}; U_{33}; U_{23}; U_{13}; U_{12}	2*a* (0, 0, 0); 1.00 Ce2 0.0139(3); 0.0239(3); 0.0096(2); 0; 0; 0	8*e* (0, ¼, z); z=0.25343(2); 1.00 Ce1 0.0084(1); 0.0065(1); 0.0076(1); 0; 0; 0
M2; Occ. U_{11}^{b}; U_{22}; U_{33}; U_{23}; U_{13}; U_{12}	4*i* (0, 0, z); z= 0.29571(2); 1.00 Ce1 0.0089(2); 0.0103(2); 0.0103(2); 0; 0; 0	4*a* (0, ¾, 1/8); 1.00 Ce2 0.0066(1); 0.006(1); 0.0069(1); 0; 0; 0
M3; - Occ. U_{11}^{b}; U_{22}; U_{33}; U_{23}; U_{13}; U_{12}	8*l* (0, y, z); y= 0.35869(7), z=0.34366(4); - 1.00 Zn2 0.0119(3); 0.0109(3); 0.0166(3); 0; 0.002(2); 0	32*i (x, y, z)*; x=0.23223(4), y=0.00749(4), z=0.1889(2); 1.00 Zn1 0.0122(2); 0.0111(2); 0.0096(2); 0.0017(1); 0.0002(1); 0.0009(1)
M4; Occ. U_{11}^{b}; U_{22}; U_{33}; U_{23}; U_{13}; U_{12}	8*l* (0, y, z); y= 0.28363(7), z=0.14007(4); 1.00 Zn1 0.0107(3); 0.0144(3); 0.0211(3); -0.0006(2); 0	16*h* (0, y, z) y=0.02584(6), z=0.37681(2); 1.00 Zn2 0.0091(2); 0.0147(2); 0.0119(2); -0.0021(2); 0; 0;
M5; Occ. U_{11}^{b}; U_{22}; U_{33}; U_{23}; U_{13}; U_{12}	4*h* (0, y, ½); z=0.18232(10); 1.00 Zn3 0.0193(4); 0.0180(4); 0.0118(3); 0; 0; 0	16*h* (0, y, z) y=0.10292(6), z=0.11676(2); 1.00 Zn3 0.0112(2); 0.0094(2); 0.0114(2); -0. 0012(2); 0; 0;
M6; Occ. U_{11}^{b}; U_{22}; U_{33}; U_{23}; U_{13}; U_{12}	2*d* (½, 0, ½); 1.00 Zn4 0.0187(6); 0.0187(6); 0.0173(5); 0; 0; 0	16*h* (0, y, z) y=0.59875(6); z=0.26315(2); 1.00 Zn4 0.0092(2); 0.0099(2); 0.0130(2); 0. 0017(2); 0; 0;
M7; Occ. U_{11}^{b}; U_{22}; U_{33}; U_{23}; U_{13}; U_{12}		8*c* (0, 0, 0); 1.00 Zn5 0.0083(3); 0.0104(3); 0.0111(3); -0.0021(3); 0; 0
Residual electron density; max; min in [electrons/nm³] x10³	2.83; -1.85	2.37; -1.33

[a]crystal structure data are standardized using the program Structure Tidy [31].
[b]anisotropic atomic displacement parameters U_{ij} in $[10^2 nm^2]$.
[c]nominal composition of the alloy from which a single crystal was isolated.

Table 2b. Interatomic distances in Ce$_3$Zn$_{11}$

Atom	Distance (nm)	Atom	Distance (nm)	Atom	Distance (nm)
Ce1 – 4Zn1	0.30935(4)	Zn1 – 2Zn2	0.26014(4)	Zn3 – 2Zn2	0.26266(7)
Ce1 – 2Zn3	0.31950(5)	Zn1 – Zn4	0.26956(6)	Zn3 – 2Zn4	0.27833(5)
Ce1 – 4Zn2	0.31975(4)	Zn1 – Zn2	0.28236(7)	Zn3 – 4Zn1	0.29616(4)
Ce1 – 2Zn2	0.32550(6)	Zn1 – 2Zn3	0.29616(4)	Zn3 – Zn3	0.32432(13)
Ce1 – 2Zn1	0.32806(6)	Zn1 – 2Ce1	0.30935(4)	Zn3 – 2Ce1	0.31950(5)
Ce1 – 2Zn4	0.35631(3)	Zn1 – Ce2	0.31506(6)	Zn3 – 2Ce2	0.36195(7)
Ce1 – Ce2	0.39848(3)	Zn1 – Ce1	0.32807(6)	Zn4 – 4Zn1	0.26956(6)
Ce2 – 4Zn1	0.31506(6)	Zn2 – Zn2	0.25137(12)	Zn4 – 4Zn3	0.27833(5)
Ce2 – 8Zn2	0.33369(4)	Zn2 – 2Zn1	0.26014(4)	Zn4 – 4Ce1	0.35631(3)
Ce2 – 4Zn3	0.36195(7)	Zn2 – Zn3	0.26266(7)		
Ce2 – 2Ce1	0.39848(3)	Zn2 – Zn1	0.28236(7)		
		Zn2 – 2Ce1	0.31975(4)		
		Zn2 – Ce1	0.32550(6)		
		Zn2 – 2Ce2	0.33369(4)		

Table 2c. Interatomic distances in Ce$_3$Zn$_{22}$

Atom	Distance (nm)	Atom	Distance (nm)	Atom	Distance (nm)
Ce1 – 2Zn4	0.3124(1)	Zn2 – 2Zn1	0.2571(1)	Zn4 – 2Zn5	0.2626(1)
Ce1 – 2Zn3	0.3204(1)	Zn2 – Zn4	0.2673(1)	Zn4 – Zn2	0.2673(1)
Ce1 – 2Zn2	0.3251(1)	Zn2 – 2Zn1	0.2779(1)	Zn4 – Zn4	0.2703(1)
Ce1 – 4Zn1	0.3303(1)	Zn2 – 2Zn3	0.2802(1)	Zn4 – 2Zn1	0.2771(1)
Ce1 – 2Zn2	0.3312(1)	Zn2 – 2Zn2	0.2834(1)	Zn4 – 2Zn1	0.2780(1)
Ce1 – 4Zn1	0.3456(1)	Zn2 – Ce1	0.3251(1)	Zn4 – 2Zn3	0.2909(1)
Ce1 – 2Zn2	0.3661(1)	Zn2 – Ce1	0.3312(1)	Zn4 – Ce1	0.3123(1)
Ce2 – 4Zn3	0.3159(1)	Zn2 – Ce1	0.3661(1)	Zn4 – Ce2	0.3218(1)
Ce2 – 4Zn4	0.3248(1)	Zn3 – Zn3	0.2629(1)	Zn4 – Zn3	0.3611(1)
Ce2 – 8Zn1	0.3386(1)	Zn3 – Zn5	0.2660(1)	Zn5 – 4Zn4	0.2626(1)
Ce2 – 4Zn5	0.3483(1)	Zn3 – 2Zn1	0.2722(1)	Zn5 – 4Zn1	0.2651(1)
Zn1 – Zn2	0.2571(1)	Zn3 – 2Zn2	0.2802(1)	Zn5 – 2Zn3	0.2660(1)
Zn1 – Zn1	0.2633(1)	Zn3 – 2Zn1	0.2806(1)	Zn5 – 2Ce2	0.3483(1)
Zn1 – Zn5	0.2651(1)	Zn3 – 2Zn4	0.2909(1)		
Zn1 – Zn3	0.2722(1)	Zn3 – Ce2	0.3158(1)		
Zn1 – Zn1	0.2750(1)	Zn3 – Ce1	0.3204(1)		
Zn1 – Zn4	0.2771(1)	Zn3 – Zn4	0.3611(1)		
Zn1 – Zn2	0.2779(1)				
Zn1 – Zn4	0.2780(1)				
Zn1 – Zn3	0.2805(1)				
Zn1 – Ce1	0.3303(1)				
Zn1 – Ce2	0.3386(1)				
Zn1 – Ce1	0.3456(1)				

Table 3a. Rietveld Refinement data for $Ce_{13}Zn_{58}$, $Ce_{1-x}Zn_{5+2x}$-hex; (x=0.33; $\alpha CeZn_7$) and alloy $Ce_{8.6}Zn_{70.7}B_{20.7}$ (all from Guinier-Huber Image Plate, $CuK_{\alpha1}$)

Compound	$Ce_{13}Zn_{58}$	$Ce_{1-x}Zn_{5+2x}$-hex; (x=0.33)	Ce_2Zn_{17}-rhombohedral
Nominal composition (at.%)	$Ce_{18.31}Zn_{81.69}$	$Ce_{10}Zn_{90}$	$Ce_{8.6}Zn_{70.7}B_{20.7}$
Composition from EPMA	$Ce_{18.0}Zn_{82.0}$	-	$Ce_{11.08}Zn_{88.92}$
Space group	$P6_3/mmc$; No. 194	$P6/mmm$; No. 191	$R\bar{3}m$; No. 166
Structure type	$Ce_{13}Zn_{58}$	$TbCu_7$	Th_2Zn_{17}
Composition from refinement	$Ce_{16.3}Zn_{82.7}$	$Ce_{10.6}Zn_{89.4}$	$Ce_{10.5}Zn_{89.5}$
Theta range	8°<2θ<100°	8°<2θ<100°	8°<2θ<100°
a [nm]	1.4616(1)	0.52424(2)	0.90872(1)
c [nm]	1.418(1)	0.44274(1)	1.32825(2)
Reflections in refinement	606	39	146
No. of parameters refined	103	26	39
Reliability factors $R_F=\Sigma\vert F_o-F_c\vert/\Sigma F_o$ $R_{exp}=[(N-P+C)/\Sigma w_i y^2_{oi})]^{1/2}$ $\chi^2=(R_{wP}/R_e)^2$	- 0.032 0.032 11.2	- 0.045 0.035 5.84	- 0.038 0.024 4.15
R1; - Occ., B_{iso}	12k ($x,2x,z$); x=0.2031(4), z=0.0529(3); - 0.888(2) Ce1; 0.85(5)	1a (0,0,0); - 0.67(3)Ce1; 0.29(2)	6c (0,0,z); z=0.33561(7); - 1.00Ce1; 0.32(2)
R2 in 6h ($x,2x,$ ¼); Occ.; B_{iso}	x=0.5057(9); 0.448(2) Ce2; 0.4(1)	-	-
R3 in 6h ($x,2x,$ ¼); Occ.; B_{iso}	x=0.875(4); 0.486(1) Ce3; 0.8(1)	-	-
R4 in 2a (0,0,0); Occ., B_{iso}	0.924(2)Ce4; 0.7(2)	-	-
M1; - Occ., B_{iso}	24l (x,y,z); x=0.3725(4), y=0.0374(5), z=0.0992(5); 0.948(8) Zn1; 0.9(1)	3g (½,0, ½); - 1.00Zn1; 0.15(3)	18h ($x\bar{x}$,z); x=0.5052(4), z=0.15512(7); 1.00Zn1; 0.20(2)
M2; - Occ., B_{iso}	12k ($x,2x,z$); x=0.0923(7), z=0.1548(6); 0.868(6) Zn2; 0.9(1)	2e (0,0,z); z=0.2995(5); - 0.33(1)Zn2; 0.43(2)	18f (x,0,0); x=0.29213(9); - 1.00Zn2; 0.20(3)
M3; - Occ., B_{iso}	12k ($x,2x,z$); x=0.247(2), z=0.6724(6); 0.858(8) Zn3; 0.8(2)	2c (⅓,⅔,0); - 1.00(1)Zn3; 0.46(3)	9d (½,0, ½); - 1.00Zn3; 0.53(4)
M4 Occ., B_{iso}	12k ($x,2x,z$); x=0.549(2), z=0.6332(7); 1.00 Zn4; 0.3(2)	-	6c (0,0,z); z=0.0988(1); 1.00 Zn4; 0.67(4)
M5 in 12k ($x,2x,z$); Occ., B_{iso}	x=0.5995(9), z=0.0521(7); 1.00 Zn5; 0.8(1)	-	9e (½,0, 0); 0.15(4)B; 0.8(-)
M6 in 12j ($x,y,$ ¼); Occ., B_{iso}	x=0.0910(7), y=0.3728(7); 0.958(5) Zn6; 0.2(1)	-	-
M7 in 12i ($x,0,$ 0); Occ., B_{iso}	x=0.194(3); 0.552(5); 0.3(3)	-	-
M8 in 6h ($x,2x,$ ¼); Occ., B_{iso}	x=0.2701(5), 1.00 Zn8; 0.4(2)	-	-
M9 in 6g (½,0,0); Occ., B_{iso}	0.640(4) Zn9; 0.9(3)	-	-
M10 in 4f (⅓,⅔, z); Occ., B_{iso}	z=0.095(1); 0.882(3) Zn10; 0.3(3)	-	-
M11 in 2d (⅓,⅔,¾); Occ., B_{iso}	0.912(2) Zn11; 0.08(48)	-	-
M12 in 2b (0,0,¼); Occ., B_{iso}	0.924(2) Zn12; 0.3(5)	-	-

Table3b. Interatomic distances for $Ce_{1-x}Zn_{5+2x}$-*hex*; (x=0.33)

Atom	Distance (nm)	Atom	Distance (nm)
Ce1 – 2Zn2	0.13234	Zn2 – Ce1	0.13234
Ce1 – 6Zn3	0.30258	Zn2 – Zn2	0.17793
Ce1 – 2Zn2	0.31027	Zn2 – Zn2	0.26468
Ce1 –12Zn1	0.34299	Zn2 – 6Zn1	0.27673
Zn1 – 4Zn1	0.26204	Zn2 – Ce1	0.31027
Zn1 – 4Zn3	0.26807	Zn2 – 6Zn3	0.33025
Zn1 – 4Zn2	0.27673	Zn3 – 6Zn1	0.26807
Zn1 – Ce1	0.34299	Zn3 – Ce1	0.30258
		Zn3 – Zn3	0.30258
		Zn3 – 2Ce1	0.30258
		Zn3 – 2Zn3	0.30258
		Zn3 – 6Zn2	0.33025

Table 4. Phase analyses (EPMA and XPD) of Ce-Zn-B alloys, annealed at 800°C

Code	Nominal composition Ce-Zn-B, at %	Experimental	Phase	Space Group	Structure type	Lattice Parameters, nm		
						a	b	c
a	8-72-20	Ce_xB_y	$CeZn_{11}$	$I4_1/amd$	$BaCd_{11}$	1.06589(6)	-	0.68602(9)
		(ArcMelted)+	Ce_2Zn_{17}	$R\overline{3}m$	Th_2Zn_{17}	0.908727(6)	-	1.32822(1)
		Zn	CeB_6	$Pm\overline{3}m$	CaB_6	0.4149(1)	-	
b	17-50-33	Ce_xB_y	Ce_3Zn_{22}	$I4_1/amd$	Ce_3Zn_{22}	0.89339(2)	-	2.13793(6)
		(ArcMelted)+	$CeZn_5$	$P6/mmm$	$CaCu_5$	0.541078(9)	-	0.42778(1)
		Zn	CeB_4	$Pm\overline{3}m$	ThB_4	0.72085(1)	-	0.409173(8)
c	19-45-36	Ce_xB_y	$CeZn_5$	$CeZn_5$	$CaCu_5$	0.541716(7)	-	0.427091(8)
		(ArcMelted)+	$Ce_{13}Zn_{58}$	$P6_3/mmc$	$Gd_{13}Cd_{58}$	1.46306(9)	-	1.4171(1)
		Zn	CeB_4	CeB_4	ThB_4	0.72076(1)	-	0.409129(8)
d	20-70-10	CeB_6	$Ce_{13}Zn_{58}$	$P6_3/mmc$	$Gd_{13}Cd_{58}$	1.46278(2)	-	1.4163(2)
		(ArcMelted)+	Ce_3Zn_{11}	$Immm$	La_3Al_{11}	0.45210(2)	0.88854(5)	1.34685(8)
		Ce_xZn_y	CeB_4	$Pm\overline{3}m$	ThB_4	0.7209(1)	-	0.4048(1)
e	22-69-9	CeB_6	Ce_3Zn_{11}	$Immm$	La_3Al_{11}	0.45260(2)	0.89027(4)	1.34753(7)
		(ArcMelted)+	$CeZn_3$	$Cmcm$	$CeZn_3$	0.46338(4)	1.0460(1)	0.66440(6)
		Ce_xZn_y	CeB_4	$Pm\overline{3}m$	ThB_4	0.72564(4)	-	0.40312(4)
f	43-37-20	CeB_4	$CeZn_2$	$Imma$	$CaCu_2$	0.46422(3)	0.75427(6)	0.75080(6)
		(ArcMelted)+	$CeZn$	$Pm\overline{3}m$	$CsCl$	0.37087(2)	-	-
		Ce_xZn_y	CeB_4	$Pm\overline{3}m$	ThB_4	0.72022(6)	-	0.40860(6)

4

Phase relations and crystal structures in
the system Ce-Ni-Zn at 800°C

4.1. Introduction

Addition of rare earths (RE) to Ni-Zn alloys results in local distortion and disorder inducing a softening of the metal network [1]. RE furthermore improve the mechanical performance, tensile strength, hardness and also the corrosion resistance by removing impurities from the grain boundaries of their alloys with zinc [2]. In order to thoroughly understand the alloying behaviour of rare earth metals in Ni-Zn alloys, the formation of ternary compounds, their crystal structure and particularly the phase relations have to be known. For the Ce-Ni-Zn isothermal section at 200°C (see Fig. 1) Opainych [3] reported five ternary compounds and some quite extensive solid solutions by substitution of Ni and Zn in the Ce-Ni and Ce-Zn binary phases (i.e. particularly for the phases $Ce(Ni_{1-x}Zn_x)_5$ ($0 \leq x \leq 0.41$) and $Ce(Ni_xZn_{1-x})_5$ ($0 \leq x \leq 0.35$) [4]).
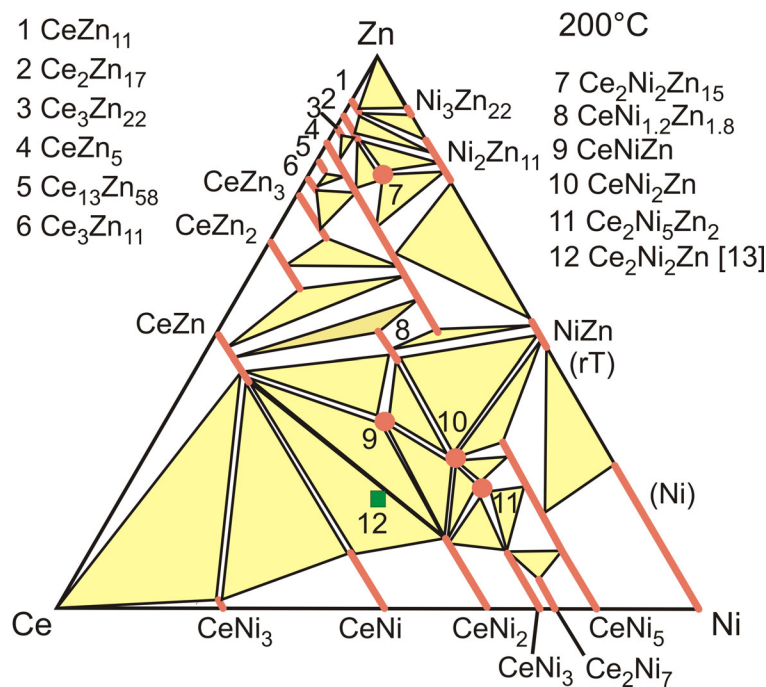
Figure 1. Isothermal section at 200°C after Opainych et al. [3]. The green square denotes the position for Ce_2Ni_2Zn, a ternary phase reported by Solokha et al [13]**.** (For interpretation of the references to colour in this figure legends, the reader is referred to the web version of this article.)

The crystal structures of known compounds have been determined and details are given in Table 1: CeNiZn [5, 3, 6], CeNi$_2$Zn [7], Ce$_2$Ni$_5$Zn$_2$ [7], and CeNi$_{1.2}$Zn$_{1.8}$ [8]. Whereas binary Ce$_2$Zn$_{17}$ (for which a hexagonal low temperature form Ce$_{1+x}$Zn$_{5+2x}$ has recently been established by Malik et al. [9]) was shown [3] to form a limited solid solution Ce$_2$(Ni$_x$Zn$_{1-x}$)$_{17}$ at 200°C (x<0.05), a structural change was noted [10] for higher Ni-concentrations forming the ternary compound Ce$_2$Ni$_2$Zn$_{15}$, which was observed with an ordered version of the rhombohedral Th$_2$Zn$_{17}$-type. It should be mentioned that although Ce$_2$Ni$_3$Zn$_{14}$ [11] was described at 400°C with the Th$_2$Zn$_{17}$ type, the Ni/Zn atom order assigned differs from Ce$_2$Ni$_2$Zn$_{15}$. A recent investigation of the La-Ni-Zn system at 400°C revealed seven ternary compounds in the region from 16.7 to 100 at.% La [12], among which La$_2$Ni$_2$Zn and corresponding isotypes for Ce and Tb have been determined by Solokha et al. [13] to crystallize with the Pr$_2$Ni$_2$Al-type. Some further controversy concerns the structure of the compound CeNiZn. Although two research groups [5, 6], confirmed the ordered ZrNiAl type (space group $P\bar{6}2m$) for CeNiZn on alloys heat treated at 750°C [5] and 647°C [2008Her], using powder photographs and x-ray single crystal analysis, respectively, Opainych [3] claimed the LiYSn-type (space group $P6_3mc$) for CeNiZn powders annealed at 200°C. Magnetic susceptibility data for CeNiZn (ZnNiAl type) showed intermediate-valent cerium [6].

As a preliminary study of a few alloys in the Ce-Ni-Zn system along the section with 10 at.% Ce revealed phase relations different from those described at 200°C [3], an investigation of the isothermal section at 800°C seemed to be necessary in order to link phase relations to our investigation of the multicomponent system Ce-Ni-Zn-{B,Si} [14,15]. As a further task, thermal stability, crystal symmetry and atom distribution need to be checked/established for the solution phases Ce(Ni$_{1-x}$Zn$_x$)$_5$, Ce$_2$(Ni$_x$Zn$_{1-x}$)$_{17}$ and Ce(Ni$_x$Zn$_{1-x}$)$_{11}$.

4.2. Experimental

Samples in a total amount of ca. 0.5 g each were prepared from cerium ingots (Alfa Aesar, purity >99.9 mass%), zinc granules (Alfa Aesar, purity >99.9 mass%), nickel foil (Alfa Aesar, purity >99.8 mass%) and nickel powder (-100 mesh; 99.9 mass%; PCR Inc. USA). Zinc drops were purified in an evacuated quartz tube by heating them

below the boiling temperature of Zn (907°C). Cerium was mechanically surface cleaned before use.

Two procedures of sample preparation were used for the evaluation of ternary phase relations and single crystal investigation: (i) samples were prepared by mixing the powders of arc melted $CeNi_x$ master alloys and fine Zn-filings in proper compositional ratios. The blends were cold compacted in a steel die without lubricants, were inserted into Al_2O_3 crucibles, vacuum-sealed in quartz tubes and then slowly heated to 420°C and kept at this temperature for 12h. The samples were then heated up to 800°C at the rate of 1°C/min and finally were annealed at 800°C for 7 days and quenched by immersing the quartz ampoules in cold water. (ii) In the concentration range up to15 at. % Ce, samples were prepared from ground $Ce_{16}Ni_{84}$ master alloy by adding Zn filings and Ni powders. These blends were cold compacted and heat-treated as described above. After quenching, samples were powderized under cyclohexane and then hot pressed under Ar in a uniaxial hotpress system (HP W 200/250-2200-200-KS) operated at 800°C and 56 MPa for 1 hour.

X-ray powder diffraction data were collected from each alloy in as cast, annealed and hot pressed state employing a Guinier-Huber image plate system with monochromatic $CuK_{\alpha 1}$ radiation (8º<2θ<100º). Quantitative Rietveld refinements of the X-ray powder diffraction data were performed with the FULLPROF program [16]. Precise lattice parameters were calculated by least-square fits to indexed 2θ values using Ge as an internal standard (a_{Ge}=0.565791 nm).

Single crystals were mechanically isolated from crushed alloys which were melted in Al_2O_3 crucibles and then slowly cooled at 0.5°C/min. Inspections on an AXS-GADDS texture goniometer assured high crystal quality, unit cell dimensions and Laue symmetry of the specimens prior to the X-ray intensity data collections on a four-circle Nonius Kappa diffractometer equipped with a CCD area detector employing graphite monochromated Mo Kα radiation (λ=0.071069 nm). Orientation matrices and unit cell parameters were derived using the program DENZO [17]. No absorption corrections were performed because of the rather regular crystal shapes and small dimensions of the investigated specimens. The structures were solved by direct methods and were refined with the SHELXL-97 program [18,19] within the Windows version WINGX [20]. The hot pressed samples were polished using standard procedures and microstructures and compositions were examined by light

optical (LOM) and scanning electron microscopy (SEM) via Electron Probe Micro-Analyses (EPMA) on a Zeiss Supra 55 VP equipped with an EDX system operated at 20 kV. Ni_2Zn_{11} at the Zn-rich boundary (15.4 at.% Ni [21]) and βCe_2Zn_{17} (89.5 at.% Zn) were used as EPMA standard. Error bars on the measured compositions are <1 at. %.

4.3. Results and Discussion

4.3.1. Binary Boundary Systems

The binary systems Ce-Zn, Ni-Zn and Ce-Ni are based on the versions presented by Massalski [22]. Several critical assessments have hitherto been published on the phases and phase relations in the Ce-Zn binary [9, 23, 24]. Although the Ni-Zn phase diagram listed by Massalski [22] essentially relies on the experimental data derived by Nash et al. [25] and comprises four intermediate compounds with extended homogeneity regions: cubic β-NiZn (sometimes in literature named as β'-NiZn), tetragonal β_1-NiZn, cubic γ-Ni_2Zn_{11} (including orthorhombic or triclinic γ_1-$NiZn_3$, which formerly was considered to be an independent phase) and monoclinic δ-Ni_3Zn_{22}. More recent investigations of the systems Ni-Zn-Sb and Ni-Zn-Ge [26, 27] at 297°C reported that γ_1-$NiZn_3$ phase does not exist at this temperature, whereas the examination of Mn-Ni-Zn [28] at 400°C and Ni-Si-Zn [29] at 600°C claimed the existence of this phase. In the present work we therefore checked on the formation of γ_1-$NiZn_3$ and δ-Ni_3Zn_{22} at the temperature of concern (800°C), employing x-ray powder and EPMA analysis. The phases we observed were essentially consistent with the phase diagram of Nash and Pan [25]: (Ni), tetragonal low temperature modification β_1-NiZn (also labeled as NiZn(rT)) and cubic γ-Ni_2Zn_{11}. The extension of the homogeneity regions of these phases determined by EPMA agrees within 1 at. % with the literature data [25], however, due to the heat content of the protective Al_2O_3 crucibles we were unable to quench the cubic high temperature modification of β'-NiZn in binary as well as in ternary alloys. Crystal structure data on unary, binary and ternary phases have been summarized in Table 1.

4.3.2. Structural Chemistry

4.3.2.1. Crystal Structure of Ce$_2$(Ni$_x$Zn$_{1-x}$)$_{17}$, x=0.49: A single crystal was selected from the crushed sample with composition Ce$_{22}$Ni$_{42}$Zn$_{36}$ (in at. %). The X-ray intensity pattern of this crystal was completely indexed on the basis of a hexagonal lattice, a=0.87541(3) nm and c=1.25410(4) nm. The observed systematic extinctions *hkil (–h+k+l=3n), hh$\overline{2h}$l (l=3n), h$\overline{h}$0l (h+l=3n), 000l (l=3n)* and *h$\overline{h}$00 (h=3n)* were consistent with the rhombohedral space groups $R\overline{3}m$, $R\overline{3}$ and $R3$, $R3m$ and $R32$. Structure solution with direct methods in the space group of highest symmetry, $R\overline{3}m$, disclosed one position for Ce and four positions for Ni and Zn atoms. A first refinement was run with Zn atoms at all four metal atom positions. As the coordination figures around the sites 6*c* and 9*d* revealed the largest (d$_{6c\text{-ligands}}$ = 0.27341(7) nm) and the shortest distances (d$_{9d\text{-ligands}}$ = 0.25047(1) nm) to the ligands, we felt inclined to locate the larger Zn-atom in the 6*c* site and the smaller Ni-atom in the 9*d* site. For the remaining Ni, the average distances for the coordination figures around the sites 18*f* (d$_{18f\text{-ligands}}$ = 0.258 nm) and 18*h* (d$_{18h\text{-ligands}}$ = 0.265 nm) are less decisive, but favour Ni in 18*f*: 0.88 Ni + 0.12 Zn. Refinement with anisotropic atom displacement parameters (ADP) converged to $R_{F^2} = 0.06$, however prompted a residual electron density of about 7 electrons/Å^3 at site 3*a* (0, 0, 0), which lies exactly between two Zn1 atoms at d$_{Zn1\text{-}3a}$= 0.1353(1) nm, as shown in the difference Fourier synthesis map (Fig. 2).
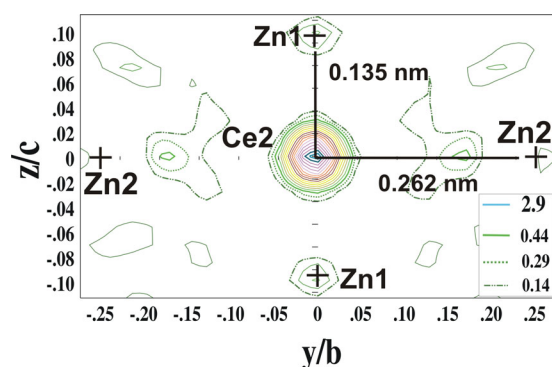
Figure 2. Difference Fourier synthesis map ΔF(0,y,z) showing the residual density of 7 electrons/Å^3 residing between two Zn1 atoms. This density was covered in the refinement by a Ce2-atom (Occ=0.02) alternating with Zn1 (Occ.=0.98).

Refinement in the lower symmetry space group $R\bar{3}$ neither revealed any further atom ordering nor removed the residual density at site 3a (0, 0, 0). Thus $R\bar{3}m$ was kept as the proper space group. Mutual replacement of rare earth atoms by a dumbbell of small metal atoms was encountered to be a special feature in many compounds deriving from the structure types $CaCu_5$ - Th_2Zn_{17} - Th_2Ni_{17} [30] and similar cases were reported for $Ce_{1+x}Zn_{5+2x}$ [9] and $GdFe_{7.7}Si_{1.3}$ [31]. Therefore, we decided to introduce a Ce atom at the 3a site, which alternately but randomly shares the space with the Zn1-dumbbell atoms in the 6c-site. Refinement yielded an occupancy of only 2% of Ce2 in 3a (alternatively 4% of a Ni atom could cover the residual density). Final refinement in space group $R\bar{3}m$ arrived at $R_{F^2} = 0.018$ with a residual electron density less then $\pm1.3/Å^3$ and led to the formula $Ce_{2+y}(Ni_xZn_{1-x})_{17}$, y=0.02, x=0.49, $(Ce_{10.6}Ni_{43.7}Zn_{45.7})$ in perfect consistency with the composition measured by EPMA: $Ce_{10.8}Ni_{44.1}Zn_{45.1}$.
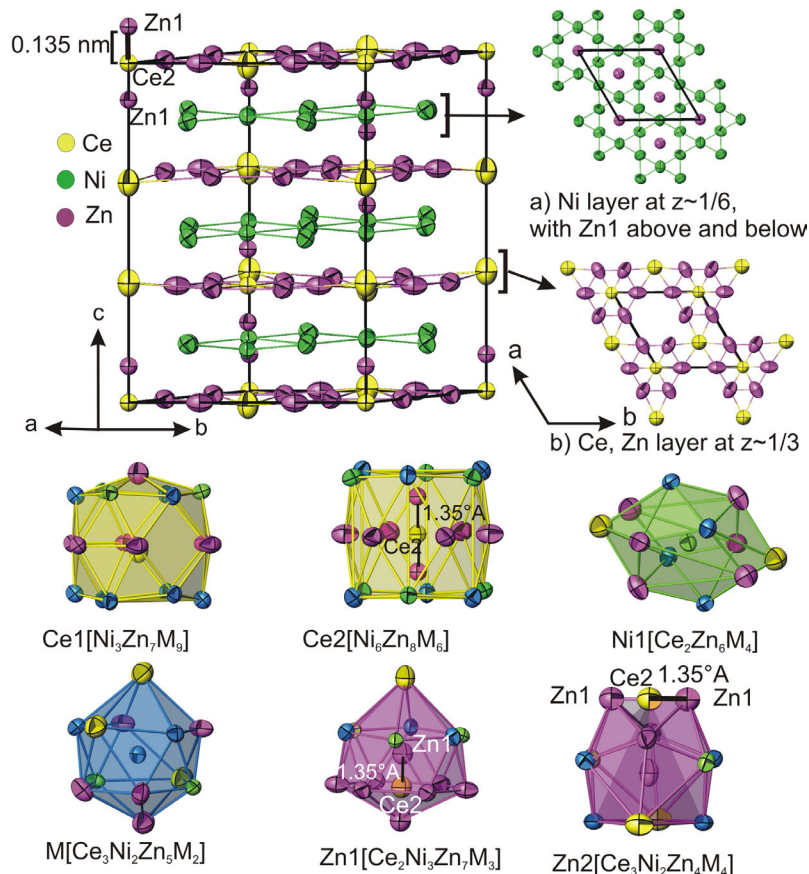
Figure 3. Unit cell of $Ce_{2+y}(Ni_xZn_{1-x})_{17}$, y=0.02, x=0.49 ($Th_2Zn_{17}$-type) showing the layered architecture in three-dimensional view; a) Ni atom layer at z~1/6 with Zn1 atoms above and below; b) Ce-Zn layer at z ~1/3 with a small amount (~2%) of Ce2-atoms randomly substituting for Zn1-atom dumbbells. All atoms are presented with

anisotropic displacement parameters from single crystal refinement. Polyhedra for the atoms of $Ce_{2+y}(Ni_xZn_{1-x})_{17}$, y=0.02, x=0.49 with anisotropic displacement parameters from single crystal refinement.
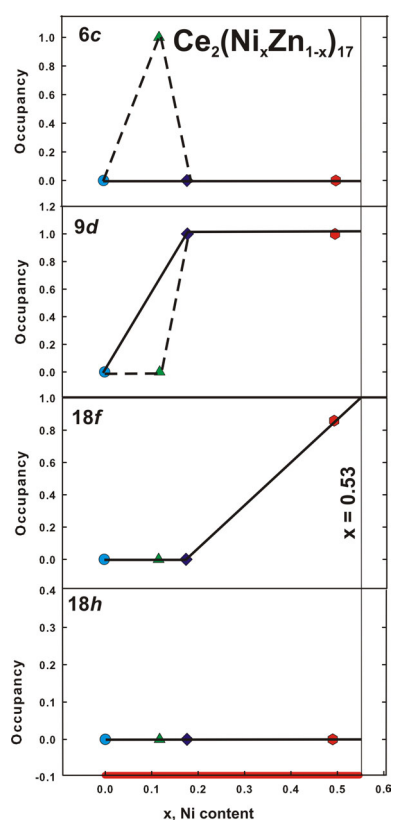
Figure 4. Ni-occupancies for the four atom sites 6*c*, 9*d*, 18*f* and 18*h* as a function of Ni content in the unit cell of $Ce_{2+y}(Ni_xZn_{1-x})_{17}$, y=0.02, x=0.49 (red circle-this work, purple tilted square-[11], green triangle-[10] and blue circle-[33]). The solid lines follow the atom site occupation model derived in this work. The dashed lines are according to [10].

Crystal data along with the interatomic distances are summarized in Table 2 and 3 and are consistent with the structure type Th_2Zn_{17} in which a small fraction of Zn-dumbbells is substituted by Ce (or Ni) atoms. The crystal structure is shown in Figure 3 in three-dimensional view emphasizing the layer-type building principle as well as indicating the statistical replacement of Zn1-dumbbells by Ce2-atoms. The low residual density at site 9*e* (½, 0, 0) as well as the corresponding distances $d_{9e\text{-}Zn} = 0.1756$, $d_{9e\text{-}Ni} = 0.1954$ and $d_{9e\text{-}Ce} = 0.25383$ nm in the distorted octahedron around 9*e* [$Ce_2Ni_2Zn_2$] rule out any significant occupation by small interstitial atoms as was for instance reported for isotypic $Pr_2Mn_{17}C_{1.77}$ [32].

Coordination polyhedra for $Ce_{2+y}(Ni_xZn_{1-x})_{17}$, y=0.02, x=0.49 are outlined in Figure 3. Whereas the substitution of Zn1-dumbbells by Ce2-atoms is shown for Ce2 as the central atom, the polyhedron around the mixed site M (88%Ni+12%Zn) excludes the Ce2 atoms. The mode of filling the sites $6c$, $9d$, $18f$ and $18h$ by Ni-atoms in $Ce_2(Ni_xZn_{1-x})_{17}$ is plotted in Fig. 4 as a function of Ni content in the unit cell, including data for $Ce_2Ni_2Zn_{15}$ [10], $Ce_2Ni_3Zn_{14}$ [11] and Ce_2Zn_{17} [33]. In contrast to the observations of Opainych [10] for $Ce_2Ni_2Zn_{15}$ (Ni atoms in 6, $R_{F^2} = 0.118$), our model seems to confirm that Ni-atoms first replace Zn in the $9d$ sites as observed for $Ce_2Ni_3Zn_{14}$ ($R_{F^2} = 0.017$) [11]. At higher Ni-concentrations Ni-atoms enter the $18f$ site, which will be filled exclusively by Ni at the solubility limit at $Ce_2Ni_9Zn_8$ at 800°C (i.e. $Ce_2(Ni_xZn_{1-x})_{17}$, x=0.53).

4.3.2.2. Crystal Structure of $Ce(Ni_xZn_{1-x})_{11}$, x=0.18:

A single crystal was selected from a sample with the nominal composition $Ce_6Ni_{20}Zn_{74}$ (in at. %), which was heated up to 990°C and kept at this temperature for 30 min. and was then cooled down to 810°C at the rate of 1°C/min. The single crystal X-ray intensity spectrum was fully indexed on a tetragonal unit cell and extinctions were consistent with the space group with the only possible space group; $I4_1/amd$. Structure solution employing direct methods revealed one position for Ce and three positions for Ni and Zn atoms. A first refinement was made with Ce atoms in $4b$, but with Zn in the remaining positions. The analysis of average distances around these sites, $4a$, $32i$, and $8c$ (i.e. 0.2773(1), 0.2664(1) and 0.2572(1) nm), suggested the larger Zn1 atoms at site $4a$, the small Ni2 atoms at $8c$ and a random mixture Ni1/Zn1 at $32i$. Refinement converged at $R_{F^2} = 0.049$ for a random occupation of 0.98Zn+0.02Ni in the 32i site and a residual electron density of less then $\pm 2.86 \ /Å^3$. This yields the formula $Ce(Ni_xZn_{1-x})_{11}$, x=0.18 ($Ce_{8.3}Ni_{18}Zn_{73.7}$), close to the composition found by EPMA, $Ce_{8.5}Ni_{18.5}Zn_{73}$. Crystal structure data and interatomic distances are summarized in tables 4 and 5 and reveal consistency with the $BaCd_{11}$ type. The low residual density at site $8d$ (0, 0, ½) as well as the corresponding distances $d_{8d-M} = 0.186$ and $d_{8d-Ce} = 0.274$ nm in the distorted octahedron around $8d$

[Ce₂M₄] rule out any significant occupation by small interstitial atoms as was for example observed for isotypic $La_2Mn_{11}C_{2-x}$ and [34] $RFe_9(Fe,Si)_2C_{0.5}$ [35].

The architecture of the crystal structure and the atom coordination polyhedra are shown in Fig. 5. The structural model of this phase was ~~is~~ confirmed by Rietveld XPD refinement. It is interesting to mention here, that for $NdZn_{11}$ a high temperature modification (> 635°C) was reported [36], for which the hexagonal $Sm_{1.1}Zn_{11.8}$-type [37] was tentatively assigned from X-ray rotation and Weissenberg photographs. Our search for a corresponding Ce-Ni-Zn phase at 800°C did neither reveal a compound with $Sm_{1.1}Zn_{11.8}$-type nor with $ThMn_{12}$-type.
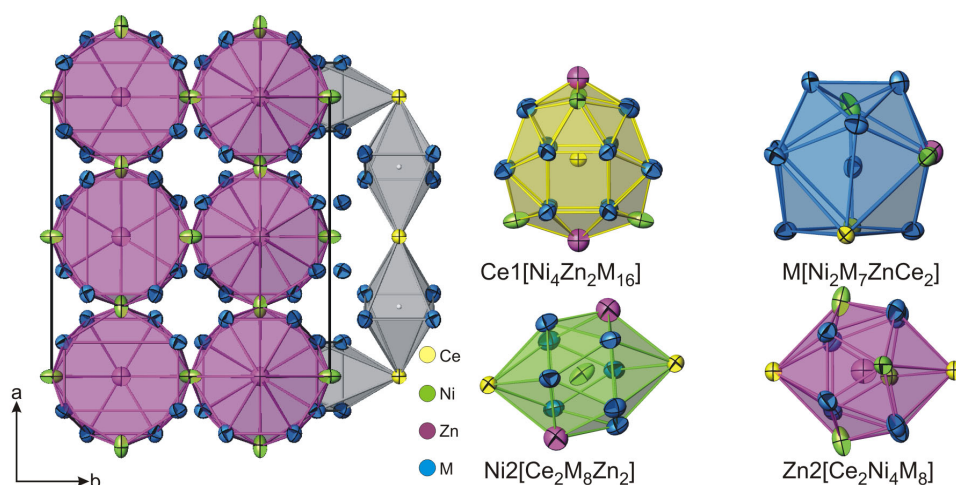
Fig. 5.The crystal structure of $Ce(Ni_xZn_{1-x})_{11}$ (x=0.18, $BaCd_{11}$-type) along [001] with polyhedra drawn for Zn2 and the void in (0, 0, ½) forming distorted octahedra with CN=6 (4M+2Ce). Coordination polyhedra are shown for the independent atom sites with anisotropic displacement parameters from single crystal refinement.

4.3.3. Phase relations in the isothermal section of the system Ce-Ni-Zn

The isothermal section for the Ce-Ni-Zn system at 800°C (see Fig. 6) has been constructed from x-ray powder diffraction analyses combined with EPMA on about 50 ternary alloys. The results are summarized in Table 6. Phase relations at 800°C are characterized by a large region for the liquid phase covering most of the Ce-rich part

of the diagram, whereas a Zn-rich liquid is confined to a small region near the Zn-corner of the Gibbs triangle. The Ce-rich liquid completely surrounds at 800°C the binary phases CeZn, which dissolves 3.5 at. % Ni, and $CeNi_2$, which dissolves 10 at. % Zn in equilibrium with the liquid. A second characteristic concerns the solid solution between the isotypes $CeNi_5$ and $CeZn_5$, which at 800°C form a continuous solid solution $Ce(Ni_{1-x}Zn_x)_5$ (details are given in the section below).
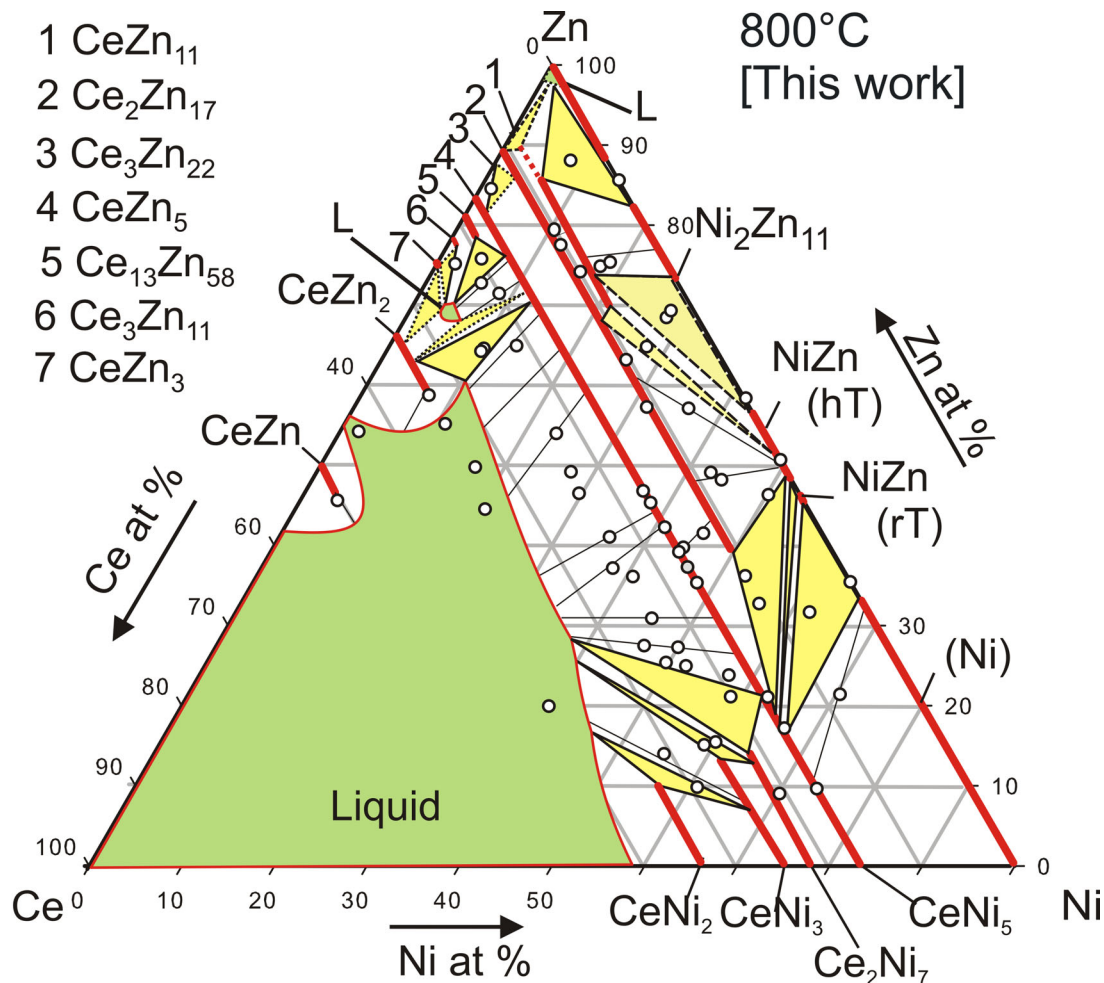
Fig. 6. Ce-Ni-Zn isothermal section at 800°C.

Micrographs in Fig. 7 reveal that the Ce-rich liquid forms tie lines to the $Ce(Ni_{1-x}Zn_x)_5$ phase for a large part of the diagram (see Fig. 7 a to h). In the Zn-poor part three-phase equilibria exist among $L+Ce_2(Ni_{1-x}Zn_x)_7+ Ce(Ni_{1-x}Zn_x)_5$ (Fig.7a), $L+Ce_2(Ni_{1-x}Zn_x)_7+Ce(Ni_{1-x}Zn_x)_3$ (Fig.7b) and $L+Ce(Ni_{1-x}Zn_x)_3+Ce(Ni_{1-x}Zn_x)_2$ (Fig.7c). Similarly, equilibria with a liquid were identified near the Ce-Zn boundary: $L+Ce_3Zn_{11}$ (practically no Ni dissolved) and $L+Ce_{13}Zn_{58}+Ce(Ni,Zn)_5$ (Fig.7d). This liquid region exists as an "island" in the phase diagram. For the solid region of the

isothermal section, micrographs in Fig. 7e, Fig. 7f and 7g document the three-phase equilibria: $Ni_{48}Zn_{52}(rT)+Ni_2Zn_{11}+Ce(Ni_{1.6}Zn_{7.9})_{11}$ (Fig.7e), $Ni_{48}Zn_{51.8}(rT)+Ce(Ni_{1.91}Zn_{6.36})_{11}+Ce_2(Ni_{1.24}Zn_4)_{17}$ (Fig.7f) and the tie-line $Ni_{50}Zn_{50}(rT)+Ce_2(Ni_{2.6}Zn_{2.82})_{17}$ (Fig.7g). It should be noted, that due to insufficiently fast quenching of the alloys (inside protective Al_2O_3 crucibles within sealed quartz-walls) we were unable to retain the cubic high temperature modification of β'-NiZn, which transfers on cooling to the low temperature form NiZn(rT). Therefore the dashed lines in Fig 6 refer to the low temperature form of NiZn(rT). This is particularly true for the phase triangle observed with the vertices $Ce(Ni_{13.9}Zn)_5+Ni_{54.45}Zn_{45.41}(\beta_1$-NiZn (NiZn(rT))$+Ni_{69.53}Zn_{33.23}$ (solid solution of Zn in Ni) (Fig.7h).
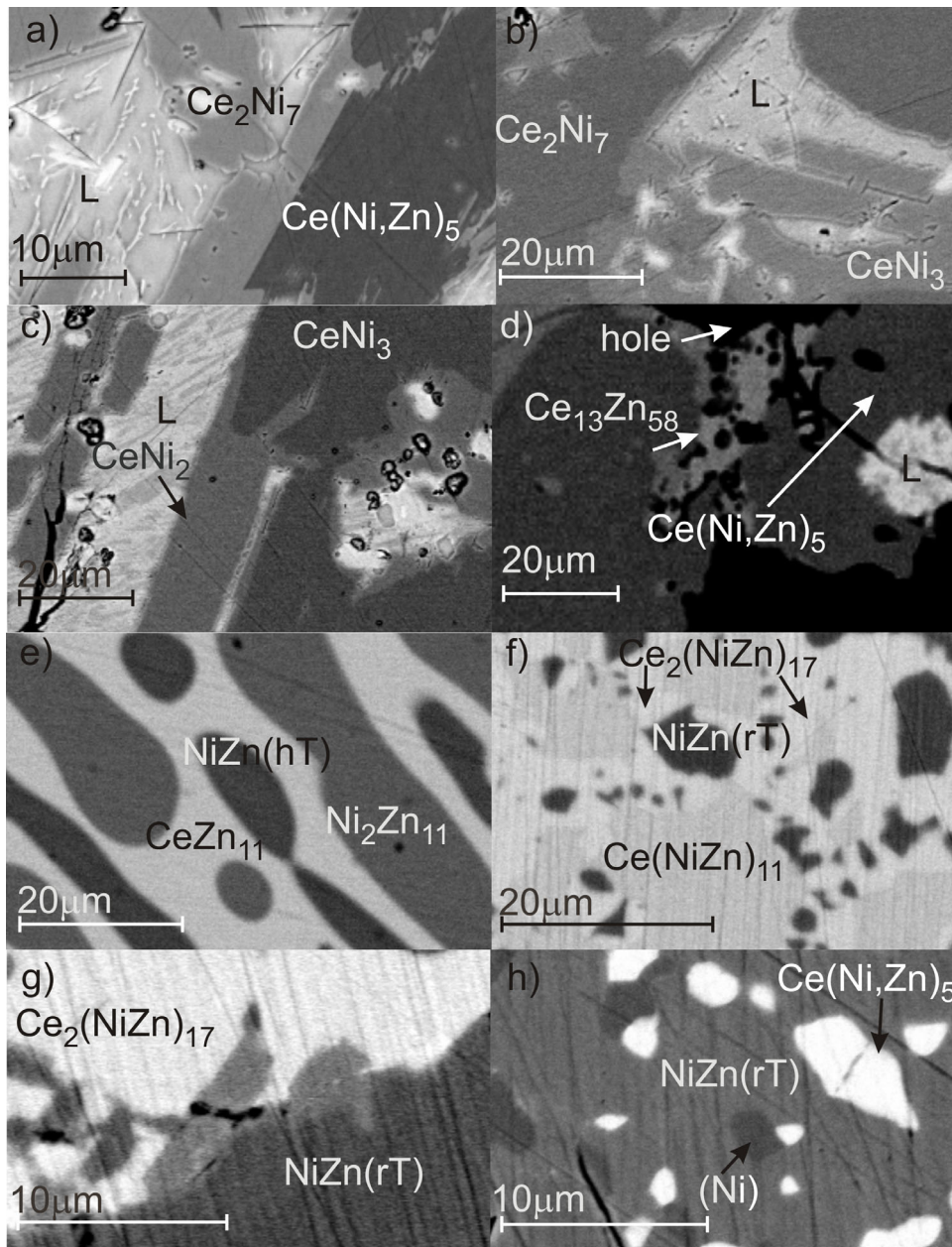
Fig. 7. Micrographs for Ce-Ni-Zn samples annealed at 800°C a) $Ce_{20}Ni_{58}Zn_{22}$
b) $Ce_{24}Ni_{62}Zn_{14}$, c) $Ce_{30}Ni_{60}Zn_{10}$, d) $Ce_{19}Ni_3Zn_{78}$, e) $Ce_4Ni_{28}Zn_{68}$, f) $Ce_6Ni_{33}Zn_{61}$, g) $Ce_9Ni_{45}Zn_{46}$ and h) $Ce_6Ni_{62}Zn_{32}$ (all compositions given in at. %).

The phase equilibria determined in Fig. 7 show that the ternary compounds observed at 200°C (for comparison see Fig.1, [3]), namely: $CeNi_{1.2}Zn_{1.8}$, $CeNiZn$, $CeNi_2Zn$, $Ce_2Zn_5Ni_2$ as well as $CeNi_2Zn_2$ (observed at 400°C [13]) are all submersed by the liquid at 800°C. From the extent of the solid solution phase $Ce_2(Ni_xZn_{1-x})_{17}$ (0≤x≤0.53) we note that nickel has a strong stabilizing influence although no compound Ce_2Ni_{17} exists. The inclusion of Ni replacing Zn leads to a decrease in the unit cell volume as shown in figure 8.
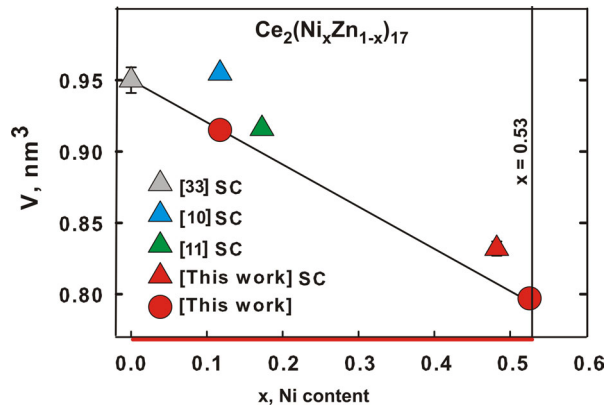
Fig. 8.Cell volume versus Ni content in $Ce_2(Ni_xZn_{1-x})_{17}$ (Th_2Zn_{17} type). Data taken from single crystal (SC) and powder samples. The solid line is a guide to the eye. The solid bar at the abscissa outlines the homogeneity range at 800°C.

Similarly, $CeNi_{11}$ with $BaCd_{11}$-type has not been reported in literature [9, 23, 24] and although $CeZn_{11}$ already decomposes on heating at 795°C, $Ce(Ni_xZn_{1-x})_{11}$ is stabilized by Zn/Ni substitution as a ternary phase for the region $0.03 \leq x \leq 0.22$ at 800°C. The lattice parameters and unit cell volume decrease linearly with the Ni addition as shown in figure 9.
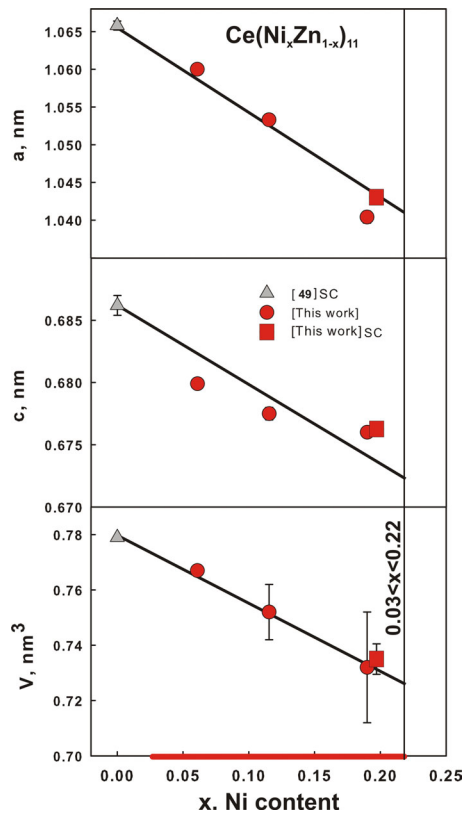
Fig. 9.Lattice parameters and cell volume versus Ni content in $Ce(Ni_xZn_{1-x})_{11}$ ($BaCd_{11}$-type) for alloys annealed at 800°C. Data taken from single crystal (SC) and

powder samples. The solid line is a guide to the eye. The solid bar at the abscissa outlines the homogeneity range at 800°C.

4.3.4. Homogeneity range of $Ce(Ni_{1-x}Zn_x)_5$

Solid solution ranges along the section $CeNi_5$-$CeZn_5$ have been reported at 200°C with the limiting compositions $CeNi_{3.24}Zn_{1.76}$ for $CeNi_{5-x}Zn_x$ and $CeNi_{2.03}Zn_{2.97}$ for $CeZn_{5-x}Ni_x$ [4]. At 800°C, however, we observed a continuous solid solution range extending from $CeNi_5$ to $CeZn_5$. Figure 10 reveals the lattice parameter variation with respect to the Ni, Zn substitution in $Ce(Ni_{1-x}Zn_x)_5$ as a function of x at 800°C including data from the literature. A single-phase sample with composition $Ce_{16.5}Ni_{43.75}Zn_{39.76}$ (in at. %) has been annealed at different temperatures, i.e. 800, 750, 700, 600 and 400°C up to 350 h in order to trace a possible miscibility gap in the continuous solid solution, but at all temperatures the sample remained single-phase and showed no signs of decomposition.

51
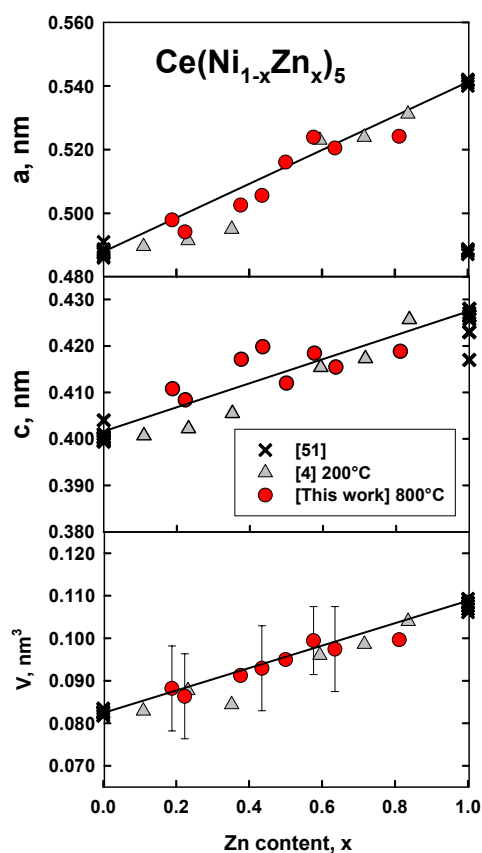
Fig. 10.Lattice parameter variation with respect to the Ni, Zn substitution in $Ce(Ni_{1-x}Zn_x)_5$ (CaCu$_5$-type). Data from powder samples (this work and from the literature [51]). The solid line is a guide to the eye.

4.4. Conclusion

Employing EDX electron microprobe analyses and x-ray single crystal and powder diffraction, phase relations in the isothermal section and crystal structures have been established for the system Ce-Ni-Zn at 800°C. Phase equilibria at 800°C are characterized by a large region for the liquid phase covering most of the Ce-rich part of the diagram, whereas a Zn-rich liquid is confined to a small region near the Zn-corner of the Gibbs triangle. For the solid part of the diagram, large mutual solubilities of Ni and Zn at a constant Ce content have been observed at 800°C for most Ce-Zn and Ce-Ni compounds, whereas solubility of Ce in the binary Ni-Zn compounds is negligible. A further characteristic feature of the Ce-Ni-Zn isotherm at 800°C is the continuous homogeneity region of $CeZn_5$ and $CeNi_5$ phases. Nickel is found to stabilize the structure of $CeZn_{11}$ to higher temperatures and at 800°C $Ce(Zn_{1-x}Ni_x)_{11}$ ($0.03 \leq x \leq 0.22$) appears as a ternary solution phase. Similarly, a rather extended solution forms for $Ce_2(Ni_xZn_{1-x})_{17}$ ($0 \leq x \leq 0.53$). Detailed data on atom site occupation and atom parameters were derived from X-ray structure analyses for single crystals of $Ce_{2+y}(Ni_xZn_{1-x})_{17}$, y=0.02, x=0.49 (Th$_2Zn_{17}$ type; $R_{F^2} = 0.018$) and $Ce(Ni_{0.18}Zn_{0.82})_{11}$ (BaCd$_{11}$ type, $R_{F^2} = 0.049$).

In comparison to the ternary compounds observed by Opainich at 200°C [3] and Solokha at 400°C [13], the phase relations determined at 800°C show that the phases $CeNi_{1.2}Zn_{1.8}$, CeNiZn, $CeNi_2Zn$, $Ce_2Zn_5Ni_2$ and $CeNi_2Zn_2$ appear submersed by the Ce-rich liquid.

4.5. References

[1] S.E. Jacobo, S. Duhalde, H.R. Bertorello, Journal of Magnetism and Magnetic Materials 272 – 276 (3) (2004) 2253–2254.

[2] X. Tao, G. Wenguan, G. Pinlin, Zhongguo Xitu Xuebao (Chinese Rare Earth Society). 16(3) (1998) 230-233.

[3] I.M. Opainych, M. PhD Thesis. University of L'viv. Ukraine. (1996).

[4] I.M. Opainych, V. Pavlyuk, I.O. Bodak, Inorganic Materials (translated from Neorgan. Materialy Akad. Nauk Ukr. RSR). 32 (1996) 625–626.

[5] A. Iandelli, Journal of Alloys and Compounds. 182 (1992) 87–90.

[6] W. Hermesa, R. Mishra, U.C. Rodewald, and R. Pöttgen, Z. Naturforsch. 63B (2008) 537–542.

[7] V.V. Pavlyuk, I.M. Opainych, and I.O. Bodak, Acta Crystallogr. C51 (1995) 2464–2466.

[8] I.M. Opainych, V. Pavlyuk, I.O. Bodak, Inorg Mater. (translated from Neorgan. Materialy Akad. Nauk Ukr. RSR). 32 (1996) 627–628.

[9] Z. Malik, O. Sologub, G. Giester, P. Rogl, J. Solid State Chemistry. 184 (2011) 2840–2848.

[10] I.M. Opainych, V. Pavlyuk. I.O. Bodak, R. Cherny, K. Yvon, Crystallogr. Rep. (translated from Krystallografiya). 41 (1996) 809–812.

[11] N. Gross, G. Block, W. Jeitschko, Chem. Mater. 14 (2002) 2725–2731.

[12] S. De Negri, P. Solokha, A.Saccone, V. Pavlyuk, Intermetallics. 16 (2008) 168–178.

[13] P. Solokha, S. De Negri, A. Saccone, V. Pavlyuk and J. -C. Tedenac, Z. Anorg. Allg. Chem. 633 (2007) 482–489.

[14] Z. Malik, Ni-Zn-B, 800°C Isothermal Section, J. Solid State Chemistry. (to be published).

[15] Z. Malik, Ce-Zn-Si, 800°C Isothermal Section, J. Solid State Chemistry. (to be published).

[16] T. Roisnel, J. Rodriguez-Carvalaj, Materials-Science-Forum. (1) 118 (2010) 378–381.

[17] Nonius Kappa CCD Program Package COLLECT, DENZO, SCALEPACK, SORTAV, Nonius Delft, The Netherlands, 1998.

[18] G.M. Sheldrick, SHELXS-97, Program for Crystal Structure Refinement University of Göttingen, Germany Windows version by McArdle, Natl. Univ. Ireland, Galway, 1997.

[19] G.M. Sheldrick, Acta Crystallogr. A64 (2008) 112–122.

[20] L.J. Farrugia, J. Appl. Crystallogr. 32 (1999) 837–838.

[21] A. Jonnasson, H. Ljung, S. Westman, Acta Chemica Scandinavica. 22(1968) 2743–2753.

[22] T.B. Massalski, Binary Alloy Phase Diagrams, second ed., ASM International, Materials Park, OH, 1990.

[23] P.J. Spencer, A.D. Pelton, Y.-B. Kang, P. Chartrand, C.D. Fuerst, Calphad. 32 (2008) 423–431.

[24] C.P. Wang, X. Chen, X.J. Liu, F.S. Pan, K. Ishida, Journal of Alloys and Compounds. 458 (2008) 166–173.

[25] P. Nash, Y.Y. Pan, Bull. Alloy Phase Diagrams. 8 (5) (1987) 422-430.

[26] I. Chumak, V. Pavlyuk, J. Alloys Compounds. 367 (2004) 85–88.

[27] I. Chumak, V. Pavlyuk, G. Dmvtriv, Intermetallics. 13 (2005) 109–112.

[28] J. I. Liang, Y. Du, S. Z. Liao, Y.Y. Tang, L.Q. Nong, F. Zheng, H. H. Xu, J. Alloys Compounds. 489 (2010) 362–368.

[29] H. Xu, B. Hu, W. Sun, P. Wang, Y. Du, X. Xiong, J.L. Liang, Z. Jin, Intermetallics. 19 (2011) 1089–1095.

[30] K.H.J. Buschow, A.S. van der Goot, Acta Crystallogr. B27 (1971) 1085 –1088.

[31] V. Svitlyk, Y. Yin, J. Cheung, Y. Mozharivskyj, J. Solid State Chem. 182 (2009) 2543–2548.

[32] G. Block, W. Jeitscjko, Inorg. Chem. 25 (1986) 279–282.

[33] T. Siegrist, Y.Le Page, JCOMAH. 127 (1987) 189–197.

[34] W. Jeitschko, G. Block, Z. Anorg. Chem. 528 (1985) 61-68.

[35]   J. Le Roy, J.M. Moreau, C. Bertrand, J. of Less-Common Met. 136 (1987) 19-24.

[36]   J.T. Mason, P.Chiotti, Metall. Trans. 3 (1972) 28-51–2855.

[37]   J.T. Mason, K.S. Harsha, P. Chiotti, Acta Crystallogr. B26 (1970) 356–361.

[38]   R.P. Anantatmula, D.B. Masson, Metallurgical Transactions. 5 (1974) 605–613.

[39]   W.B. Pearson, L.T. Thompson, Canadian J. Physics. 35 (1957) 349–357.

[40]   W. Heike, J. Schramm, O. Vaupel, Metallwirtsch Metallwiss Metalltech. 51 (1936) 655–662.

[41]   J.K. Critchley, S. Denton, Journal of the Institute of Metals. 99 (1971) 26–27.

[42]   G. Novar, K. Shubert, J. of Less-Common Met. 75 (1980) 51–63.

[43]   P. Villars, L.D. Calvert, Person's Handbook of Crystallographic Data for Intermetallic Phases; second ed., ASM International: Materials Park, OH, 1991.

[44]   V. Paul-Boncour, A. Percheron-Guegan, M. Diaf , J.C. Achard, Journal of the Less common Metals. 131 (1987), 201–208.

[45]   S. Piao, C.P. Gomez, S. Lidin, Z. Kristallogr. 221 (2006) 391–401.

[46]   B.G. Lott, P. Chiotti, Acta Crystallogr. 20(1966), 733–738.

[47]   P.I. Kripyakevich, Y.B. Kuz'ma, N.S. Ugrin, Journal of Structural Chemistry (Translated from Zhural Strukturnoi Khimmi). 8 (1967) 632–633.

[48]   A. Iandelli, A. Palenzona, J. Less-Common Metals. 12 (1967) 333–343.

[49]   O. Zelinska, M. Conrad, B. Harbrecht, Z. Kristallogr., NCS. 219 (2004) 357–358.

[50]   E. Parthé, L. Gelato, B. Chabot, M. Penzo, K. Censual, R.Gladyshevskii, TYPIX—Standardized Data and Crystal Chemical Characterization of Inorganic Structure Types, Berlin, Springer, 1994.

[51]   P. Villars, K.Cenzual, Pearson's Crystal Data CD-ROK, Release 2011/12, ASM International, Ohio, USA.

Table 1. Crystallographic data of solid phases of the system Ce –Ni–Zn.

Phase, Temperature range (ºC)	Space group, Prototype	Lattice parameters (nm) a	b	c	Comments
(δCe) 798-700	$Im\bar{3}m$ W	0.412	-	-	[22]
		-	-	-	-
(γCe) <726	$Fm\bar{3}m$ Cu	0.51610	-	-	[22]
		-	-	-	-
(Ni) <1455	$Fm\bar{3}m$ Cu	0.35240	-	-	[22]
$Ni_{1-x}Zn_x$		-	-	-	$0 \leq x \leq 0.24$ at 1000°C[a] [38]
		0.35269	-	-	$x=0$ at 1000°C[a] [38]
		0.35791	-	-	$x=0.24$ [38]
		-	-	-	$0 \leq x \leq 0.30$ [39]
(Zn) <420	$P6_3/mmc$ Mg	0.2665	-	0.4947	[22]
		0.2667(1)	-	0.4951(1)	From alloy Ce_7Zn_{93}, 600°C[a]
β NiZn / $Ni_{1-x}Zn_x$ 1040-675[22]	$Pm\bar{3}m$ CsCl	0.29083	-	-	[40]
		--	-	-	-
$β_1$ NiZn / $Ni_{1-x}Zn_x$ <810 [22]	$P4/mmm$ CuTi	0.27487	-	-	$0.46 \leq x \leq 0.51$ at 600°C[a] [38]
		-	-	0.31768	$x=0.46$
	$I4/mmm$	0.27504	-	0.32006	$x=0.51$
		0.2754	-	0.3214	$x=0.5$ [40]
$Ni_{2+x}Zn_{11-x}$ <881 [22]	$I\bar{4}3m$ Cu_5Zn_8	0.8920(2)	-	-	$0.32 \leq x \leq 1.55$ at 800°C[a] [22]
		-	-	-	$0.80 \leq y \leq 0.85$ at 600°C[a] [38] $Ni_{1-y}Zn_y$
		0.89069	-	-	$x=0.6$
		0.89186	-	-	$x=-0.04$
Ni_3Zn_{22} <490 [22]	$C2/m$ Ni_3Zn_{22}	1.337(1)	0.747(2)	0.765(1)	[41]
		-	$\beta=111.3(2)°$	-	-
$Ni_{16}Zn_{53}$ or $NiZn_3$	$Aem2$ $Ni_{16}Zn_{53}$	3.3326(8)	1.2499(4)	0.8869(1)	Orthorhombic variant of Cu_5Zn_8 [42]
		-	-	-	-
<600		-	-	-	$x=74.5-80.2$ at. % [38]
Ce_2Ni_7	$P6_3/mmc$	0.498(2)	-	2.452(8)	[43]

55

Phase, Temperature range (°C)	Space group, Prototype	Lattice parameters (nm) a	b	c	Comments
<1065 [22]	Ce₂Ni₇		-		$0 \leq x \leq 0.064^{c}$ at 200°C^{a} [3]
Ce₂(Ni₁₋ₓZnₓ)₇	-		-		$x=0$ at [3]^{c}
-	-	0.4980	-	2.452	$x=0.064$ [3]^{c}
-	-	0.5075	-	2.504	$0 \leq x \leq 0.10$ at 800°C^{a} [This work]
CeNi₃	P6₃/mmc	0.498(2)	-	1.654(6)	[43]
<930 [22]	CeNi₃				$0 \leq x \leq 0.13$ at 200°C^{a} [3]^{c}
Ce(Ni₁₋ₓZnₓ)₃	-	0.4980	-	1.654	$x=0$ [3]^{d}
-	-	0.5045	-	1.696	$x=0.13$ [3]^{c}
-	-	-	-	-	$0 \leq x \leq 0.17$ at 800°C^{a} [This work]
CeNi₂	$Fd\bar{3}m$	0.7194	-	-	-
<830 [22]	MgCu₂	-	-	-	-
CeNi₂₊ᵧ	-	-	-	-	$y=0.08$ at 650°C^{a} [44]
Ce(Ni₁₋ₓZnₓ)₂	-	-	-	-	$0 \leq x \leq 0.15$ at 200°C^{a} [3]^{c}
-	-	0.72224	-	-	$x=0$ [3]^{d}
-	-	0.7242	-	-	$x=0.15$ [3]^{c}
-	-	-	-	-	$0 \leq x \leq 0.15$ at 800°C^{a} [This work]
CeNi	$Cmcm$	0.3788(1)	1.0556(1)	0.4366(1)	[43]
<680 [22]	CrB	-	-	-	$0 \leq x \leq 0.28$ at 200°C^{a} [3]^{c}
Ce(Ni₁₋ₓZnₓ)	0.3783		1.0372	0.4286	$x=0$ [3]^{c}
-	-	0.3791	1.0420	0.4350	$x=0.28$ [3]^{c}
Ce₇Ni₃	$P6_3mc$	0.9926(2)		0.6311(2)	[43]
<500 [22]	Th₇Fe₃	-		-	-
CeZn	$Pm\bar{3}m$	0.3704(1)		-	[43]
<825 [22]	CsCl	0.37059(2)	-	-	[9]
CeZn₁₋ₓNiₓ	-	-	-	-	$0 \leq x \leq 0.07$ at 800°C^{a} [This work]
CeZn₂	$Imma$	0.4633(5)	0.7538(5)	0.7499(5)	[43]
<875 [22]	CeCu₂	0.46393(8)	0.7544(1)	0.7506(1)	[9]
Ce(Zn₁₋ₓNiₓ)₂	-	-	-	-	$0 \leq x \leq 0.15$ at 800°C^{a} [This work]
CeZn₃	$Cmcm$	0.4620(5)	1.0440(5)	0.6640(5)	[43]
<820 [22]	CeZn₃	0.46324(5)	1.0452(1)	0.66557(6)	[9]

Phase, Temperature range (°C)	Space group, Prototype	Lattice parameters (nm) a	b	c	Comments
Ce₃Zn₁₁	Immm	0.45215	0.88855	1.3463	[43]
<840 [22]	La₃Al₁₁	0.45242(2)	0.88942(3)	1.34754(4)	[9] SC
Ce₁₃Zn₅₈	P6₃/mmc	1.4638(1)	-	1.4158(1)	820°C^b [45]
<870 [22]	Gd₁₃Zn₅₈	1.4616(1)	-	1.4173(1)	[9]
Ce₁₃(Zn₁₋ₓNiₓ)₅₈		-	-		0≤x≤0.04 at 800°C^a [This work]
CeZn₅	P6/mmm	0.54163(5)	-	0.42647(5)	[43]
<885 [22]	CaCu₅	0.54082(1)	-	0.42798(1)	[9]
CeZn₅₊ᵧ		0.54163(5)	-	0.42647(5)	0.017≤y≤0.046 <885°C^a [46]
CeNi₅		0.4875(5)	-	0.4010(5)	[41]
<1360 [22]		-	-	-	-
Ce(Ni₁₋ₓZnₓ)₅		-	-	-	0≤x≤0.35 and 0.59≤x≤1 at 200°C [4]
-	-	-	-	-	-
-	-	0.4896(1)	-	0.4007(1)	x=0.11 [4]
-	-	0.4914(6)	-	0.4022(5)	x=0.23 [4]
-	-	0.4950(3)	-	0.4280(4)	x=0.35 [4]
-	-	0.4896(1)	-	0.4007(1)	x=0.41 [This work]
-	-	0.5030(1)	-	0.4154(1)	x=0.59 [4]
-	-	0.5239(4)	-	0.4173(3)	x=0.72 [4]
-	-	0.5213(3)	-	0.4257(4)	x=0.84 [4]
-	-		-		For details see Fig 10.
-	-	0.4914(6)	-	0.4022(5)	x=0.23 [4]SC^d
Ce₃Zn₂₂	I4₁/amd	0.897(1)	-	2.133(5)	[47]
<960 [22]	Ce₃Zn₂₂	0.8936(2)	-	2.1380(5)	[9] SC^d
-	-	-	-	-	-
-	-	-	-	-	-
-	-	-	-	-	-
β Ce₂Zn₁₇	R$\bar{3}$m	0.9090(5)	-	1.32844(7)	827°C^a [41]
<980 [22]	Th₂Zn₁₇	-	-	-	-
980~750 [9]	-	0.90916(4)	-	1.32861(1)	[9]

Phase, Temperature range (ºC)	Space group, Prototype	Lattice parameters (nm)			Comments
		a	b	c	
Ce$_{2+y}$(Ni$_x$Zn$_{1-x}$)$_{17}$		0.87541(3)	-	1.254410(4)	y=0.02, x=0.49[This work]
-	-		-		0≤x≤0.53, Fig. 8
-	-	0.8964(2)	-	1.3165(3)	Ce$_2$Ni$_3$Zn$_{14}$ [11]
α Ce$_2$Zn$_{17}$	P6$_3$/mmc	0.9088(4)	-	0.8856(5)	[48]
αCe$_{1-x}$Zn$_{5+2x}$ <~750 [9]	TbCu$_7$	0.52424(2)	-	0.44274(1)	x=0.33[9]
CeZn$_{11}$ <795 [22]	I4$_1$/amd BaCd$_{11}$	1.0658(6)	-	0.6862(8)	[49]
		1.06630(1)	-	0.686644(7)	[9]
Ce(Ni$_x$Zn$_{1-x}$)$_{11}$		1.043022(2)	-	0.67624(3)	x=0.18[This work] SC^d
			-		0.03≤x≤0.22 at 800°C Fig. 9
Ce$_2$Ni$_2$Zn	Immm Pr$_2$Ni$_2$Al	0.4365(1)	0.5430(1)	0.8279(2)	400°C^a [13]
-	-		-		-
Ce$_2$Ni$_2$Zn$_{15}$	R$\bar{3}$m Ce$_2$Co$_{15}$Al$_2$	0.9080(3)	-	1.3294(3)	200°C^a [10]
-	-		-		-
Ce$_2$Ni$_5$Zn$_2$	R$\bar{3}$m Er$_2$Co$_7$	0.49445(2)	-	3.678(1)	[7]
-	-		-		-
CeNi$_{1.2}$Zn$_{1.8}$ Ce(Ni$_{1-y}$Zn$_{1+x}$)	Pm$\bar{3}$m AuCu$_3$	0.5417(2)	-		[8]
-	-		-		0.80≤x≤0.88 at 200°C
-	-		-		0.53≥y≥0.44 at 200°C [8]
CeNi$_2$Zn	P6$_3$/mmc YRh$_2$Si	0.5045(3)	-	1.6434(7)	200°C^a [7]
CeNiZn	P$\bar{6}$2m ZrNiAl	0.7141(1)	-	0.3888(1)	[5]
-		0.7133(3)	-	0.3887(1)	[6] SC^d
-	P6$_3$mc LiYSn	0.8599(3)	-	0.7378(2)	[3]
-			-		-

^{a} Quenching temperature of samples, but lattice parameters measured at room temperature. ^{b}Temperature from which sample was cooled, but lattice parameters measured at room temperature. ^{c}values scaled from graph. ^{d}SC stands for Single Crystal Studies

58

Table 2. X-ray single crystal data[a,b] for $Ce_{2+y}(Ni_xZn_{1-x})_{17}$, y=0.02, x=0.49; Th_2Zn_{17}-type(MoK$_\alpha$ radiation)

Compound	$Ce_{2+y}(Ni_xZn_{1-x})_{17}$, y=0.02, x=0.49
Nominal composition [at. %][c]	$Ce_{22}Ni_{42}Zn_{36}$
Composition fro EPMA [at. %]	$Ce_{10.8}Ni_{44.1}Zn_{45.1}$
Formula from refinement [at. %]	$Ce_{10.64}Ni_{43.62}Zn_{45.73}$
Space group	$R\overline{3}m$; No. 166
θ Range [deg]	$3.14 < \theta < 36.02$
a [nm]	0.87541(3)
c [nm]	1.25410(4)
Reflections in refinement	456 Fo > 4σ (Fo) of 500
Unit cell volume [nm^3]	0.832(5)
Z, Calculated density [g/cm^3]	3, 7.99
Crystal size [μm]	20×30×45
Number of variables	25
$R_F^2 = \Sigma|F_0^2-F_c^2|/\Sigma F_0^2$	0.018
R_{Int}	0.056
GOF	1.10
Extinction (Zachariasen)	0.00048 (6)
Ce1 in 6c (0, 0, z); Occ. $U_{11}{}^b$= U_{22}; U_{33}; U_{23} = U_{13} = 0; U_{12}	z = 0.35233(3); 1.00(1) 0.0131(1); 0.0206(2); 0.0065(1)
Ce2 in 3a (0, 0, 0); Occ. $U_{11}{}^b$= U_{22}; U_{33}; U_{23} = U_{13} = 0; U_{12}	0.02(1) 0.0145(2); 0.0160(3); 0.0073(1)
Zn1 in 6c (0, 0, z); Occ. $U_{11}{}^b$= U_{22}; U_{33}; U_{23} = U_{13} = 0; U_{12}	z = 0.10792(6); 0.98(-) 0.0145(2); 0.0160(3); 0.0073(1)
Zn2 in 18h (x, 0, 0); Occ. $U_{11}{}^b$; U_{22}; U_{33}; U_{23} U_{13}; U_{12}	x = 0.29942(6); 1.00(1) 0.0174(2); 0.0096(2); 0.0101(2); -0.0008(1) ; -0.0004(1); 0.0048(1)
M in 18f ($x.y,z$) Occ. $U_{11}{}^b$= U_{22}; U_{33}; U_{23}= -U_{13}; U_{12}	x = 0.50184(3); y = 0.49816(3); z = 0.15578(3) 0.88 Ni2+ 0.12 Zn3^d 0.0077(1); 0.0105(2); 0.0005(1); 0.0027(1)
Ni1 in 9d ($^-$, 0, $^-$); Occ. $U_{11}{}^b$; U_{22}; U_{33}; U_{23} U_{13}; U_{12}	1.00(1) 0.0083(2); 0.0111(3); 0.0081(3); 0.0013(2) 0.0006(1); 0.0056(1)
Residual electron density; max; min in [electrons/nm^3] x 10^{-3}	1.24; -1.35

[a]crystal structure data are standardized using the program Structure Tidy [50].
[b]anisotropic atomic displacement parameters U_{ij} in [10^2 nm^2].
[c]nominal composition of the alloy from which a single crystal was isolated.
[d]fixed from EMPA.

Table 3. Interatomic distances for $Ce_{2+y}(Ni_xZn_{1-x})_{17}$, y=0.02, x=0.49

Bonds	Distance (nm)	Bonds	Distance (nm)
Ce1 – Zn1	0.30653(8)	M – 2Ni1	0.25170(2)
Ce1 – 6Zn2	0.30865(3)	M – 2M	0.25695(4)
Ce1 – 3M	0.30776(4)	M – 2Zn2	0.25938(5)
Ce1 – 3M	0.32375(4)	M – 2Zn2	0.26271(5)
Ce1 – 3M	0.33243(4)	M – Ce1	0.30776(4)
Ce1 – 3Ni1	0.34362(3)	M – Ce1	0.32375(4)
		M – Ce1	0.33243(4)
Ce2 – 2Zn1	0.13533(8) [a]	M – Zn1	0.26473(5)
Ce2 – 6Zn2	0.26212(5)		
Ce2 – 6M	0.32794(3)	Zn2 – 2Ni1	0.24804(1)
Ce2 – 6Ni1	0.32795(5)	Zn2 – 2M	0.25938(5)
		Zn2 – 2Zn2	0.26212(5)
Zn1 – Ce2	0.13533(8) [a]	Zn2 – Ce2	0.26212(5)
Zn1 – 3Ni1	0.26323(2)	Zn2 – 2M	0.26271(5)
Zn1 – 3M	0.26473(5)	Zn2 – 2Zn1	0.29500(6)
Zn1 – Zn1	0.2707(2)	Zn2 – 2Ce1	0.30865(3)
Zn1 – 6Zn2	0.29500(6)		
Zn1 – Ce1	0.30653(8)		
Ni1 – 4Zn2	0.24804(1)		
Ni1 – 4M	0.25170(2)		
Ni1 – 2Zn1	0.26323(2)		
Ni1 – 2Ce1	0.34362(3)		

[a] $d_{Zn1 - Ce2}$ =0.13533(8) not bonding distance, for description see figure 3 and text.

Table 4. Crystal structure data[a] for Ce(Ni$_x$Zn$_{1-x}$)$_{11}$, x=0.18; BaCd$_{11}$ type (Nonius KappaCCD diffractometer, MoK$_\alpha$ radiation)

Compound	Ce(Ni$_x$Zn$_{1-x}$)$_{11}$, x=0.18
Nominal composition [at. %][c]	Ce$_6$Ni$_{20}$Zn$_{74}$
Composition from EPMA [at. %]	Ce$_{8.52}$Ni$_{18.48}$Zn$_{73}$
Formula from refinement	Ce$_{8.31}$Ni$_{18.3}$Zn$_{73.66}$
Space group	$I4_1/amd$; No. 141
θ Range [deg]	$3.59 < \theta < 38.95$
a [nm]	1.04302(2)
c [nm]	0.67624(3)
Reflections in refinement	477 Fo > 4σ (Fo) of 568
Unit cell volume [nm^3]	0.735(5)
Z, Calculated density [gm/cm^3]	8, 9.55
Crystal size [μm]	25×30×30
Number of variables	20
$R_F^2 = \Sigma|F_0^2-F_c^2|/\Sigma F_0^2$	0.049
R_{Int}	0.06
GOF	0.94
Extinction (Zachariasen)	0.0008(4)
Ce1 in 4b (0, ¼, ⅜); Occ. U$_{11}$[b]= U$_{22}$; U$_{33}$; U$_{23}$ = U$_{13}$ = U$_{12}$ = 0	1.00(1) 0.0063(3); 0.0050(4)
M in 32i (x, y, z) Occ. U$_{11}$[b]; U$_{22}$; U$_{33}$; U$_{23}$ U$_{13}$; U$_{12}$	x = 0.20451(6); y = 0.12756(6); z = 0.06183(9) 0.98(1) Zn1 + Ni1 0.02 0.0095(3); 0.0071(3); 0,0069(3); 0.0015(2) 0.0014(2); 0.0003(2)
Zn2 in 4a (0, ¾, ⅛); Occ. U$_{11}$[b]= U$_{22}$; U$_{33}$; U$_{23}$= U$_{13}$= U$_{12}$=0	1.00(1) 0.0104(5); 0.0113(8)
Ni2 in 8c (0, 0, 0); Occ. U$_{11}$[b]; U$_{22}$; U$_{33}$; U$_{23}$; U$_{13}$ = U$_{12}$ = 0	1.00(1) 0.0058(6); 0.0152(7); 0.0060(6); 0.0021(5)
Residual electron density; max; min in [electrons/nm^3] x 10^{-3}	2.86; -3.15

[a]crystal structure data are standardized using the program Structure Tidy [50].
[b]anisotropic atomic displacement parameters U$_{ij}$ in [10^2 nm^2].
[c]nominal composition of the alloy from which a single crystal was isolated.

Table 5. Interatomic distances for $Ce(Ni_xZn_{1-x})_{11}$, x=0.18

Bonds	Distance (nm)	Bonds	Distance (nm)
Ce1 – 8M	0.32653(5)	M – 2Ni2	0.25105(5)
Ce1 – 8M	0.33635(5	M – M	0.25531(7)
Ce1 – 2Zn2	0.33812(2)	M – 2M	0.26177(8)
Ce1 – 4Ni2	0.36373(2)	M – M	0.26929(7)
		M – M	0.27162(8)
Zn2 – 4Ni2	0.27411(1)	M – M	0.27883(5)
Zn2 – 8M	0.27883(5)	M – Zn2	0.27903(8)
Zn2 – 2Ce1	0.33812(5)	M – M	0.28022(8)
		M – Ce1	0.32653(5)
Ni2 – 4M	0.25105(5)	M – Ce1	0.33635(5
Ni2 – 4M	0.25485(5)		
Ni2 – 2Zn2	0.27411(1)		
Ni2 – 2Ce1	0.36373(2)		

M=98% Zn1+ 2%Ni1

Table 6. Ce-Ni-Zn system: Phase equilibria and Lattice Parameters of alloys annealed at 800°C

Phase regions at 800°C	Phase	EPMA Composition, at. %			Lattice Parameters, nm		
		Ce	Ni	Zn	a	b	c
$Ce(Ni_{1-x}Zn_x)_5 + Ce_2(Ni_xZn_{1-x})_{17}$ +NiZn (rT)	$CeZn_5$ / $CeNi_5$	16.7	54	29.3	0.50225(8)		0.41705(7)
	$Ce_2(Ni_xZn_{1-x})_{17}$	11	49.1	39.9	0.8703(2)		1.252(1)
	NiZn (rT)	0	50.5	49.5	0.27484(1)		0.31878(1)
$L + Ce(Ni_xZn_{1-x})_{11} + Ni_2Zn_{11}$	L^1				0.2667(1)		0.4939(1)
	$Ce(Ni_xZn_{1-x})_{11}$	9.1	6.1	84.8	1.0649(1)		0.6842(1)
	Ni_2Zn_{11}	0.1	17.7	82.2	0.89184(7)		
$Ce(Ni_xZn_{1-x})_{11} + Ni_2Zn_{11} + NiZn(hT)$ Figure 7e	$Ce(Ni_xZn_{1-x})_{11}$	8.6	17.8	73.6	1.0529(2)		0.6776(2)
	Ni_2Zn_{11}	0.2	25.5	74.3	0.8865(6)		
	$NiZn(rT)^2$	0.5	47.5	52	0.2944(5)		
$NiZn(rT) + Ce(Ni_xZn_{1-x})_{11}$ $+Ce_2(Ni_xZn_{1-x})_{17}$ Figure 7f	$NiZn(rt)^2$	0.3	47.9	51.8			
	$Ce(Ni_xZn_{1-x})_{11}$	8.5	21.3	70.2	1.0448(2)		0.67729(4)
	$Ce_2(Ni_xZn_{1-x})_{17}$	10.5	21.1	68.4	0.89123(8)		1.2956(4)
$Ce(Ni_{1-x}Zn_x)_5 + NiZn$ (rT) - (Ni) Figure 7h	$CeZn_5$ / $CeNi_5$	17	68.6	14.4	0.4918(1)		0.4074(8)
	NiZn (rT)	0.1	54.5	45.4			
	(Ni)	0.2	66.6	33.2			
$L + Ce_2(Ni_{1-x}Zn_x)_7 + Ce(Ni_{1-x}Zn_x)_5$ Figure 7a	L	33	28	39			
	Ce_2Ni_7	22	62	16			
	$CeZn_5$ / $CeNi_5$	17	61.3	21.7			
$L + Ce_2(Ni_{1-x}Zn_x)_7$ - $Ce(Ni_{1-x}Zn_x)_3$ Figure 7b	L	25	35	40			
	Ce_2Ni_7	22	64	14			
	$CeNi_3$	25	62	13			
$L + Ce(Ni_{1-x}Zn_x)_3 + Ce(Ni_{1-x}Zn_x)_2$ Figure 7c	L	39	43	18			
	$CeNi_3$	26	64	10			
	$CeNi_2$	34	56	10			
$L + Ce_{13}Zn_{58} + Ce(Ni_{1-x}Zn_x)_5$ Figure 7d	L	26.3	4.4	69.3			
	$Ce_{13}Zn_{58}$	18.4	3.3	78.3		———	————
	$CeZn_5$ / $CeNi_5$	17	7.3	75.7			
$NiZn$ (rT) $+ Ce_2(Ni_xZn_{1-x})_{17}$ Figure 7g	$NiZn (rT)^2$	0.3	49.9	49.8			
	$Ce_2(Ni_xZn_{1-x})_{17}$	10.8	41.4	47.8	0.8747(2)		1.2560(6)
$L + CeZn_2 + Ce(Ni_{1-x}Zn_x)_5$	L	29.2	10.2	60.6			
	$CeZn_2$	34.2	3.9	61.9			
	$CeZn_5$ / $CeNi_5$	16.8	13.5	69.7			

[1] Lattice parameter calculation of the liquid formed during quenching appear as that of Zn.
[2] low temperature modification NiZn(rt) (due to insufficiently fast quenching of NiZn (hT).

Phase Relations and Structural Chemistry
In the System Ni-Zn-B

5.1. Introduction

Alloys with 65-99 mass % zinc, 0.05-25 mass % nickel and 0.01-15 mass % boron were noticed to be suitable for casting, forging, stamping, for manufacturing wires, rods, bars, sheets, tubes and other articles: they exhibit high tensile strength, high degree of hardness, high resistance to oxidation and corrosion, low shrinkage factor and low specific gravity [1]. Generally, additions of boron and borides act as grain refiners in many metals and alloys increasing cohesive strength but also may clean grain boundaries for superplasticity [2].

Stadelmaier et al. [3] reported on the Ni-Zn-B phase equilibria at 800°C along with a liquidus projection in the composition range up to ~55 at. % Zn and up to ~43 at.% B identifying four congruently melting ternary compounds (Figure 1, see table 1).
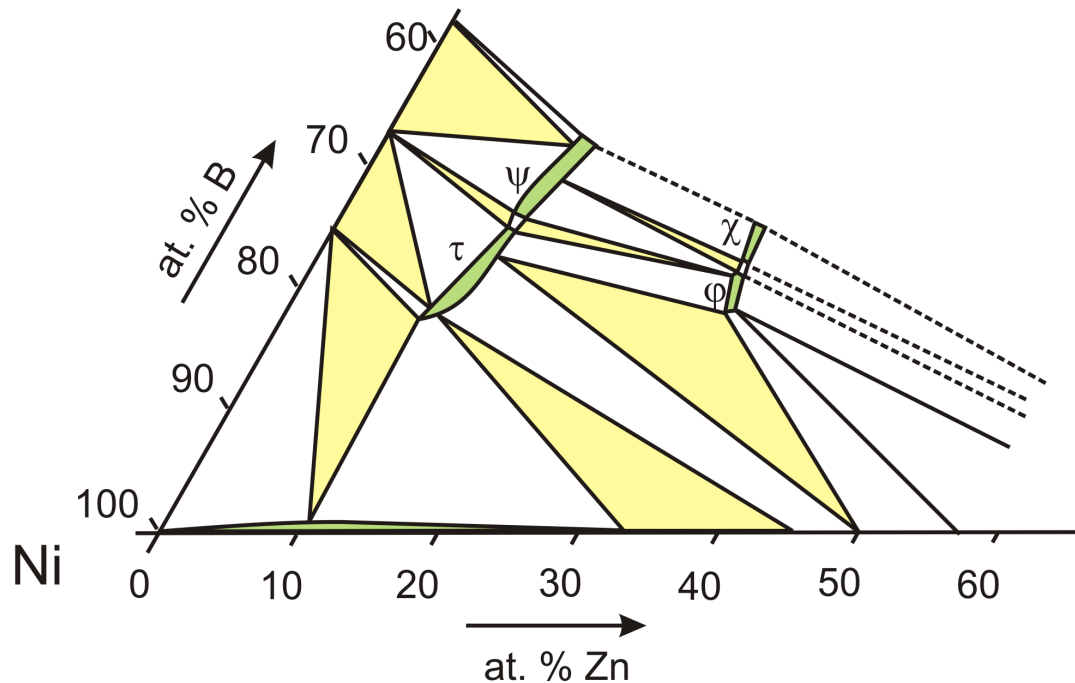

Figure 1. Ni-Zn-B phase equilibria at 800°C with four ternary phases (compositions given in table 1), as reported by Stadelmaier [3].

Whereas the structure type of the so-called τ-phase $Ni_{72-61}Zn_{10-13}B_{18-26}$ (in at.%; $Cr_{23}B_6$-type) has been studied from X-ray powder and single crystal rotation photographs, merely the compositions have been derived for the remaining three phases (labeled φ, ψ and χ) from metallography and X-ray powder inspection [3, 4, 5]. The findings of Stadelmaier [3, 4, 5] were later used by Bhan et al. [6] in a review of the Ni-Zn-B system. More recently, the crystal structures and particularly the boron-aggregation in two crystals from the $Cr_{23}C_6$-type homogeneity region (τ-phase) have been determined: $Ni_{21.4}Zn_{1.6}B_6$ and $Ni_{20}Zn_{2.4}B_{7.75}$ [7]. In a foregoing paper, we have determined the crystal structures of three ternary compounds: τ_2-$Ni_{12}ZnB_{8-x}$ (x=0.43), τ_3-$Ni_{21}Zn_2B_{20}$[1] and τ_4-Ni_3ZnB_2 [8]. Although the composition of τ_4 (Ni_3ZnB_2) is near that of the ψ-phase ($Ni_{57}Zn_{13}B_{30}$ [1962Sta1]), the phase relations observed by [3] and this work, indicate that the ψ-phase ($Ni_{57}Zn_{13}B_{30}$, shown to be in equilibrium with τ_1) rather corresponds to τ_2-$Ni_{12}ZnB_{8-x}$ (x=0.43). The other two compounds (τ_3 and τ_4) have to be considered as new compounds in this system. Therefore, in view of the new compounds detected, the present work attempts (i) to reconstruct the phase equilibria at 800°C covering the entire range of the Ni-Zn-B phase diagram and (ii) to determine the crystal structures of all the hitherto unknown phases in the Ni-Zn-B system.

5.2. Experimental

Samples in a total amount of ca. 0.5 g each were prepared from Ni foil (Alfa Aesar, purity >99.8 mass%), boron pieces (ChemPur, Karlsruhe, 98 mass%), nickel powder (-100 mesh; 99.9 mass%; PCR Inc. USA) and zinc granules (Alfa Aesar, >99.9 mass%), which were purified in an evacuated quartz tube by heating them at 800°C, below the boiling temperature of Zn (907°C).

Binary alloys: Ni-borides were prepared from Ni-cuttings and B-pieces in various stiochiometric ratios by arc melting with an inconsumable tungsten electrode under an argon atmosphere on a water-cooled copper hearth. To assure the homogeneity of the master alloy arc melting has been performed three times.

---

[1] In our previous study we have reported on the crystal structure of $Ni_{21}Zn_2B_{24}$. [2011Mal]. However, the boron positions were incorrectly summed up and thus the correct chemical formula is $Ni_{21}Zn_2B_{20}$.

Ternary alloys: Ternary samples were prepared from intimate blends of powders of Ni_yB_x master alloys and fine Zn-filings in proper compositional ratios. The blends were compacted at room temperature in a steel die without lubricants at a pressure of 130 MPa and then sealed in quartz tubes under vacuum. After slow heating to 420°C, the samples were kept at this temperature for 12h before temperature was raised to 800°C at the rate of 1°C/min. Samples were annealed at 800°C for 7 days. For further reaction the pre-annealed samples were powderized and again cold compacted in steel dies submersed in Al_2O_3-powder in graphite cartridges and hot pressed under argon at 800°C for 1 hour and under a pressure of 56 MPa. All samples were finally subjected to an annealing of 7 days at the temperature of 800°C after sealing them in quartz tubes along with the Al_2O_3 crucibles (protecting the alloy from attack by the hot quartz walls).

X-ray powder diffraction data were collected from each alloy in hot pressed and annealed state employing a Guinier-Huber image plate system with monochromatic $CuK_{\alpha1}$ radiation (8°<2θ<100°). Quantitative Rietveld refinements of the X-ray powder diffraction data were performed with the FULLPROF program [9].

Single crystals: specimens of Ni_4B_3 for single crystal analysis were mechanically isolated from the crushed reguli $Ni_{50}Zn_{15}B_{35}$ and $Ni_{56}Zn_6B_{38}$ (both in at.%) respectively, prepared as described (heated to 990°C at the rate of 1°C/min and slowly cooled). Single-phase crystalline material of τ_5 was obtained from an alloy $Ni_{48}Zn_{37}B_{15}$ (in at. %), prepared in same manner as discussed above, heated to 1100°C from 420°C at the rate of 1°C / min, then cooled to 880°C and annealed for 5 days. After water-quenching the sample was boiled in 15 % aqueous solution of HCl, in order to dissolve the Ni-Zn binary phases. Undissolved τ_5 material was washed several times with 5% dilute aqueous solution of HCl and finally with distilled water and dried.

Inspections on an AXS-GADDS texture goniometer assured high crystal quality, unit cell dimensions and Laue symmetry of the single crystal specimens prior to X-ray intensity data collections on a four-circle Nonius Kappa diffractometer equipped with a CCD area detector employing graphite-monochromated MoKα radiation (λ=0.071069 nm). Orientation matrices and unit cell parameters were derived using the program DENZO [10]. No special absorption corrections were performed because of the rather regular crystal shapes and small dimensions of the investigated

specimens. The structures were solved by direct methods and were refined with the SHELXL-97 program [11, 12] within the Windows version WINGX [13].

EPMA Measurements: Samples were polished using standard procedures, microstructures and compositions were examined by light optical microscopy (LOM) and scanning electron microscopy (SEM) via Electron Probe Micro-Analyses (EPMA) on a Zeiss Supra 55 VP equipped with an EDX system operated at 20 kV. For Ni:Zn ratios the binary compound Ni_2Zn_{11} at the Zn-rich boundary (15.0 at.% Ni after [14]) was used as EPMA standard. The differences between measured and nominal compositions were found to be less than ±1 at. %. Whereas Ni:Zn ratios were taken from EPMA, the boron content of the alloys relies upon the single crystal studies reported in this work and published previously [8].

Transmission Electron Microscopy (TEM) was employed to get information about crystal symmetry and lattice parameters of the major phase (τ_5) extracted from the sample of composition $Ni_{48}Zn_{37}B_{15}$. A Philips CM12 STEM transmission electron microscope was used working at acceleration voltage of 120 kV, with an EDAX energy dispersive X-ray (EDX) analyzer and Phoenix software [15]. The sample for TEM study was prepared in form of a thin lamella (lateral dimensions about 10×7 μm) roughly perpendicular to the long axis of a needle-like crystal using a focused ion beam (FIB) technique in a TESCAN LYRA 3 XMU FEG/SEM×FIB scanning electron microscope.

5.3. Results and Discussion.
5.3.1. Binary Boundary Systems

The binary systems Ni-Zn, Zn-B and Ni-B were used in the version presented by Massalski [16]. A critical assessment and thermodynamic calculation of the Ni-B system has been recently published [17]. Crystal structure Rietveld refinements for all those binary compounds, which have been already reported earlier, namely, βB [18], Zn_xB_{1-x} 0≤x≤0.043 ($ZnB_{\sim22}$) [19, 20], Ni_xB_{1-x}, x=0.020 ($NiB_{48.5}$) [21], NiB, m-Ni_4B_3, o-Ni_4B_{3-x} [22], Ni_2B [18], Ni_3B [23], were found to be consistent with the literature. Therefore the reinvestigation of crystal structures in the Ni-B system essentially focused on the determination of crystal symmetry, precise atom site distribution and positional parameters for the compounds, m-Ni_4B_3, o-Ni_4B_{3-x}, for which crystal

structure data hitherto have only been derived from X-ray Weissenberg and precession photographs. The Ni-Zn phase diagram at 800°C has been corroborated in our previous work on Ce-Ni-Zn [24] and was found to be essentially consistent with the data derived by Nash and Pan [25]. However, due to the heat content of the protective Al_2O_3 crucibles we were unable in our samples to quench the cubic high temperature form NiZn(hT). The crystal data relevant to the unary, binary boundary and ternary phases in the Ni-Zn-B system, including results of our reinvestigation of the binaries, are presented in Table 1.

5.3.2. Structural Chemistry

X-ray single crystal structure determination of o-Ni$_4$B$_{3-x}$ and of m-Ni$_4$B$_3$

o-Ni$_4$B$_{3-x}$. The X-ray intensity spectrum of a single crystal selected from the crushed regulus $Ni_{50}Zn_{15}B_{35}$ (at.%) was fully indexed with an orthorhombic lattice (a=1.19665(4), b=0.29852(1) and c=0.65750(2) nm). No traces of Zn have been detected in this boride phase by EPMA. Systematic extinctions prompt the space group types *Pnma* or *Pna2$_1$* and the highest symmetry was used to solve the crystal structure employing the direct methods. The structure solution with anisotropic thermal atom displacement parameters (ADPs) for the nickel atoms but isotropic temperature factors for the boron atoms converged at $R_{F^2} = 0.015$ yielding a residual electron density less than ±0.97 e$^-$/Å^3 with small but significant defects at two of the boron sites (B1 and B3). Crystal data are presented in table 2. The refined composition, Ni$_4$B$_{3-x}$ (x=0.19), lattice parameters, crystal symmetry, atom positions and Wyckoff sequence $4c^7$ essentially confirm the early structure determination of *o-*Ni$_4$B$_{3-x}$ by Rundqvist at R_F = 0.083 [26] performed on the basis of Weissenberg and precession X-ray photographs. As stated before [26], the crystal structure of o-Ni$_4$B$_{3-x}$ is characterized by (i) isolated boron atoms B2 in tetrakaidekahedral metal surrounding [Ni$_9$]B and (ii) by infinite B1-B1 and B3-B3 chains running parallel to the *b* direction with B-B distances d_{B1-B1}= 0.1797 nm and d_{B3-B3}= 0.1778 nm, respectively (see Fig. 2). It should be pointed out here, that the appearance of about 10% vacancies in the sites of B1 and B3 cuts the boron chains into fragments. Conclusions on possibly defect ordering may come from future neutron diffraction experiments. Coordination polyhedra for all crystallographic sites are presented in Fig. 2.
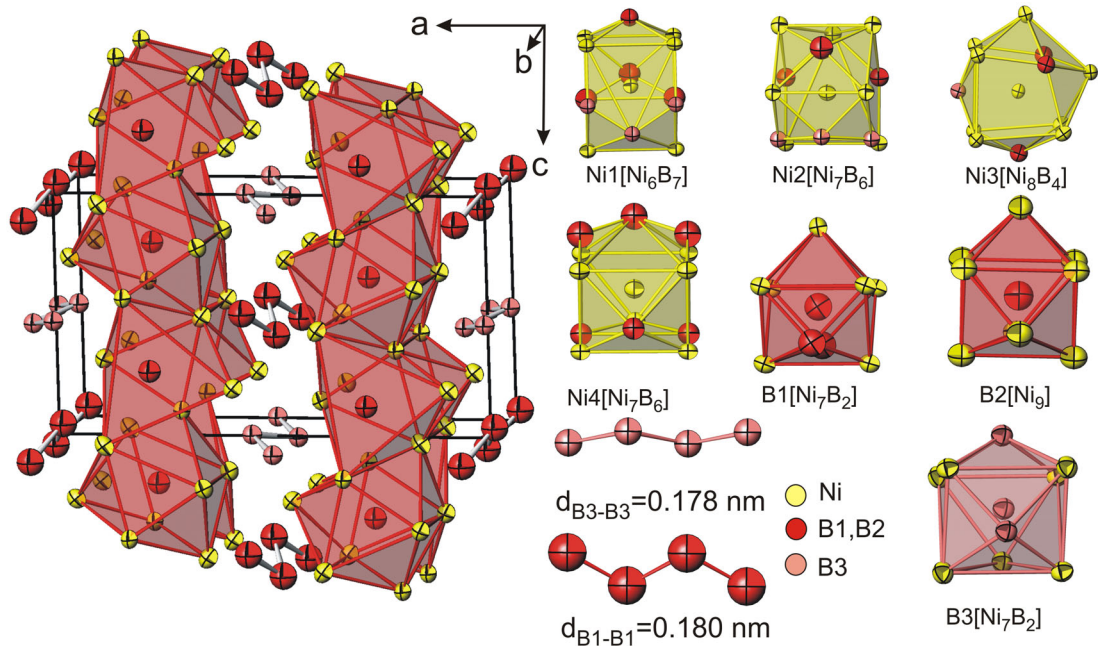
Figure 2. Crystal structure of o-Ni_4B_{3-x} (x=0.19) in three-dimensional view along the b-axis. Nickel atoms are presented with ADPs from single crystal refinement; boron atoms are shown with isotropic temperature factors. The Ni-polyhedra around the B2 atoms and the infinite B1-B1 and B3-B3 chains are highlighted.

B3 atoms occupy the centers of triangular Ni-prisms capped by 1Ni + 2B atoms and Ni atoms have 6, 7 or 8 next nearest Ni-neighbors, respectively. Supplementary material (Table I) provides a comparison of interatomic distances from Rundqvist [26] and this work. Despite of the higher precision of our data, B-B distances perfectly correspond to those derived earlier. Taking a metal atomic radius of nickel, R_{Ni}=0.124 nm [27], and a covalent radius for boron, R_B=0.088 nm [1988Sla], the Ni-B distances ($0.2066<d_{Ni-B1}<0.2147$, $0.2042<d_{Ni-B2}<0.2424$, $0.2039<d_{Ni-B3}<0.2197$) are centered around the ideal sum $R_{Ni}+R_B$=0.212 nm and also B-B distances are close to the ideal covalent B-B bond of 0.176 nm, but still typical for metal borides with a ratio B/M≤1 [28]. The calculation of Voronoi coordination polyhedra around the four individual Ni-atoms using program DIDO 95 [29] resulted in 6 to 8 bonding Ni atoms excluding those with Ni-Ni bonds longer than 0.26 nm forming a '*Dirichlet area smaller than 20% of the largest.* 'The average Ni-Ni bonding distance in the structure is $d_{av(Ni-Ni)}$ = 0.2556 nm.

m-Ni₄B₃. A single crystal of prismatic shape was selected from the crushed regulus with nominal composition $Ni_{56}Zn_6B_{38}$ (at.%). No traces of Zn have been detected in

this phase by EPMA. The X-ray diffraction pattern was indexed completely on the basis of a monoclinic unit cell (a=0.64356(3), b=0.48867(3), 0.78267(3) nm, β=103.288(3)°). Systematic absences were consistent with the space group types *C2/c* and *Cc*. Direct methods for structure solution in the centrosymmetric space group *C2/c* yielded R_{F^2}=0.021 and residual electron densities smaller than $\pm 1.2 e^-/\text{Å}^3$ employing ADPs for the metal atoms and isotropic temperature factors for the boron sites. The final refinement is summarized in Table 2 and confirms the early structure determination of *m*-Ni$_4$B$_3$ by Rundqvist [26] performed on the basis of X-ray Weissenberg and precession photographs (R_F=0.108). The crystal structure of stoichiometric *m*-Ni$_4$B$_3$ is characterized by infinite chains of boron atoms in a sequence B1-B2-B1-B1-B2-B1 and distances d_{B1-B1}= 0.1879 and d_{B1-B2}= 0.1862 nm (see Figure 3). The structure combines two different next nearest neighbor coordinations around B1 and B2, respectively, which alternate along the boron chains: a three-capped triangular prism B1[Ni$_7$B$_2$] and a distorted B-bicapped Archimedean antiprism B2[Ni$_8$B$_2$] (see Fig. 3). From a comparison of interatomic distances presented earlier [26] and in this work (see Table II of supplementary material) we find a slightly narrower distribution for B-B distances, 0.1862<d_{BB}<0.1879 nm, as well as for Ni-B distances, 0.2072<d_{Ni-B1}<0.2163, 0.2112<d_{Ni-B2}<0.2366. The Ni-B distances are centered around the ideal sum R_{Ni}+R_B=0.212 nm, whereas the B-B distances are slightly longer than the ideal covalent B-B bond of 0.176 nm, but are still typical for metal borides with a ratio B/M≤1 [28]. Coordination polyhedra around the Ni atoms adopt rather distorted shapes (see Fig. 3).

Therefore Voronoi coordination polyhedra around Ni1 and Ni2 were calculated with the aid of program DIDO 95 [29] and resulted in 9 Ni atoms for both cases, wherefrom two appear at almost equal and rather long distances of 0.2812 nm from the central atom but with a significantly different '*Dirichlet area*'. In figure 3 these two atoms are differentiated by asterisks. As the atom with a single asterisk has a *Dirichlet area* = 1.164 (50 % of the highest value) it has been kept in the coordination polyhedron, whereas the atom with the double asterisk (*Dirichlet area* = 0.5 i.e. 20 % of the highest value) was excluded from the coordination figure. The average Ni-Ni bonding distance in the structure is $d_{av(Ni-Ni)}$ = 0.2605 nm.
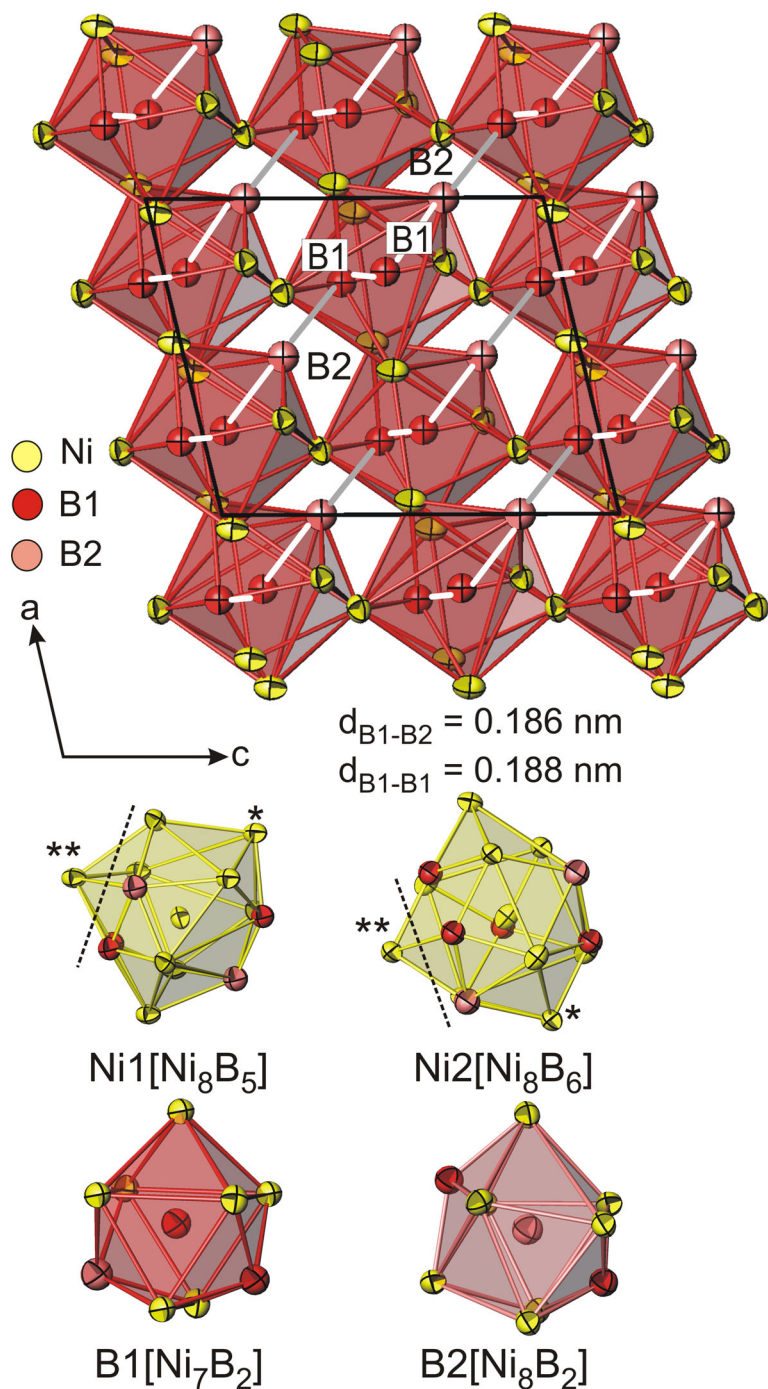
Figure 3. Crystal structure of m-Ni$_4$B$_3$ in three-dimensional view along the b-axis with polyhedra around B1 atoms. Nickel atoms are presented with ADPs from single crystal refinement; boron atoms are shown with isotropic temperature factors. The infinite boron chains with distances d_{B1-B1}= 0.188 nm d_{B1-B2}= 0.186 nm are highlighted. The Ni-atom with a single asterisk has been kept in the coordination polyhedron, whereas the atom with the double asterisk was excluded from the Voronoi coordination figure because of its small *Dirichlet area* = 0.5 i.e. 20 % of the highest value.

5.3.3. X-ray single crystal structure determination of ternary borides

5.3.3.1. Crystal structure of the τ_1-phase τ_1-$(Ni_{1-x}Zn_x)_{21}[Zn_{1-y-z}\square_y(B_4)_z]_2B_6$ (x=0.07, y=0.125, z=0.30) with $Cr_{23}C_6$-type

Stadelmaier and coworkers reported a large homogeneity region for the $Cr_{23}C_6$-type phase in the Ni-Zn-B system (τ_1 at 800°C from $Ni_{20}Zn_3B_5$ to $Ni_{19}Zn_4B_8$; a = 1.050 to 1.055 nm [3, 4, 5]), and particularly noted a significant extent in direction of boron contents higher than the stoichiometric 20.7 at.% B. More recently crystal structure solutions have been reported for $Ni_{21.4}Zn_{1.6}B_6$ and $Ni_{20}Zn_{2.4}B_{7.75}$ with Ni : Zn atomic ratios 93 : 7 and 88 : 12, respectively, [7] with a minor difference in lattice parameters (a = 1.05409(17) and a = 1.05521(17) nm; in both cases space group type was $Fm\bar{3}m$). Whereas the crystal structure of $Ni_{21.4}Zn_{1.6}B_6$ was isotypic with the $Cr_{23}C_6$-type, for the crystal $Ni_{20}Zn_{2.4}B_{7.75}$, however, tetrahedral boron clusters (B in site $32f$ forming a B_4-tetrahedron centered around site $8c$) were reported to share the space with Zn-atoms that partially occupy the $8c$ site. It should be emphasized, that the single crystal of Kotzot et al. [7] was selected from an alloy $Ni_{20}Zn_3B_8$ heated at 1450°C for 1 hour, whilst the crystal we selected from an alloy of same composition, which was heated at 1000°C and annealed at 800°C for 7 days, exhibits a much bigger lattice parameter a = 1.05800(3) nm at the ratio of Ni : Zn = 88 : 12 defined by EPMA. This may indicate an extended homogeneity with respect to boron content at the same metal atom ratio and thus warrants a single crystal X-ray investigation. The X-ray diffraction pattern of the single crystal was completely indexed with cubic face centered symmetry. Systematic extinctions led to the space groups $Fm\bar{3}m$, $F\bar{4}3m$, $F432$, $F23$ and $Fm\bar{3}$. The structure was solved from Patterson syntheses in centrosymmetric $Fm\bar{3}m$ prompting four metal atom positions consistent with the $Cr_{23}C_6$-type. For atoms in $8c$ (¼,¼,¼) the thermal parameter was rather high i.e. 5-6 times larger than for the other atoms, suggesting a partial occupancy of ~60% Zn yielding an R-value R_{F^2} =0.067. An additional electron density of ±13.59 e/Å^3 was found from the Fourier synthesis at a distance of 2.09 Å from the metal atom in 8c prompting boron occupation. Analysis of difference Fourier maps revealed the presence of boron tetrahedra formed by borons in the $32f$ site with an occupancy level of 30 %. The corresponding refinement smoothly proceeded to R_{F^2} =0.014 revealing a

residual electron density of less than ± 0.73 e/Å^3 and a formula $Ni_{63.9}Zn_{8.6}B_{27.5}$ (at. %). From this refinement the Ni to Zn ratio was 88.2 : 11.8 in fine agreement with the ratio 88:12 defined by EPMA on bulk samples. In accordance with the typical behaviour of τ-phases formed by two metals with close atomic radii and similar electronegativities, the refinement of occupancies of all metal atom sites showed that the larger and more electropositive atoms (Zn) are located in site $8c$ (¼,¼,¼) and site $4a$ (0,0,0), whereas the $48h$ site is filled with the more electronegative Ni atoms. A small part of Zn atoms also enters the $32f$ metal site displaying an extended homogeneity range as reported for $((M, Ir)_{23}B_6, M = Cr, Fe, Mn, Co; (M, Re)_{23}B_6, M = Mn, Fe, Co, Ni)$ [28, 30].

In order to check for possible ordering among metal atom/boron tetrahedra, the crystal structure was also explored in the lower symmetry space group $F\bar{4}3m$ taking the atomic coordinates reported for τ-$(Co_{0.64}Ir_{0.36})_{21}Co_{0.16}B_4B_6$ [30] as initial values for structure refinement. Refinement in this space group revealed no further ordering. Therefore the atom arrangement in the centrosymmetric space group was considered to represent the proper structure with the final formula τ_1-$(Ni_{1-x}Zn_x)_{21}[Zn_{1-y-z}\square_y(B_4)_z]_2B_6$ (x=0.07, y=0.125, z=0.30). Results are summarized in tables 3 and 4. Rietveld refinement of an X-ray powder spectrum of alloy $Ni_{70}Zn_5B_{25}$ at. % annealed at 800°C is presented in Fig.5 confirming the structure model derived from our single crystal data.

$Ni_{70}Zn_5B_{25}$
800°C
$R_F=0.0284$
$R_I=0.0328$

$(Ni_{1-x}Zn_x)_{21}[Zn_{1-y-z}\square_y(B_4)_z]_2B6$
(x=0.07, y=0.125, y=0.30)
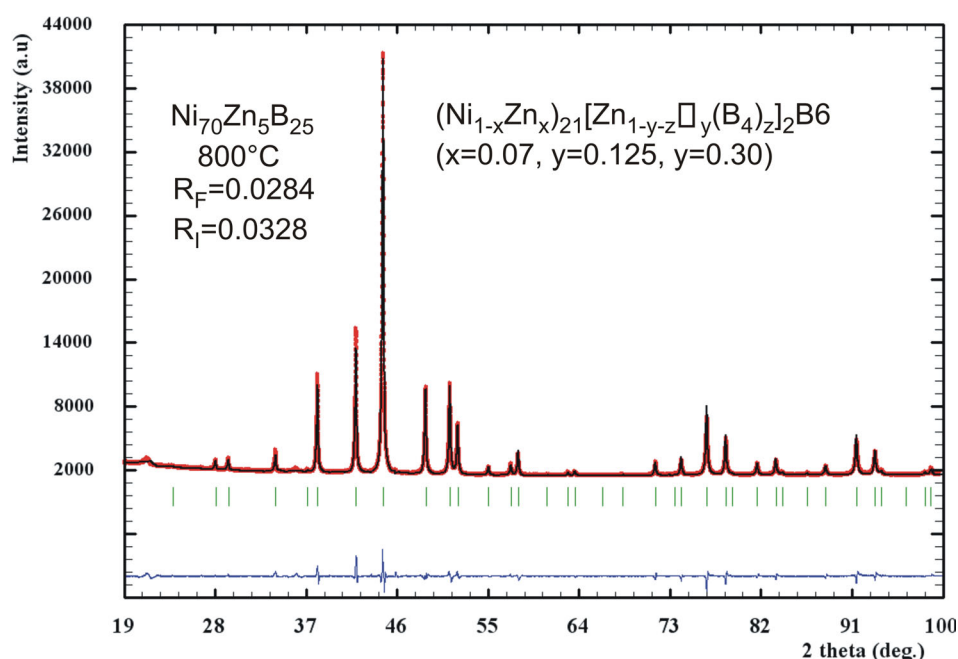
Figure 4. Rietveld refinement for the alloy $Ni_{70}Zn_5B_{25}$ (τ_1-phase).

Comparing the obtained structure solution with that reported by Kotzot et al. [7] (table 3) we found good agreement in atom order and positional parameters whilst a significant difference concerns the occupancy of B at 32f (22 % [7]) and 30 % for the crystal investigated in the current work. This change of boron content form 22 to 30 at % at the same metal ratio may be held responsible for a significant increase in lattice parameter. Despite the difference concerns only the boron occupancy on one crystallographic site (32f) all interatomic distances in the structure expand by 0.24 % proportionally to the increase in lattice parameter.

5.3.3.2. *The τ_5-phase*

The crystalline τ_5 material obtained by acid leaching from Zn-flux (alloy $Ni_{48}Zn_{37}B_{15}$, in at. %; see X-ray powder spectrum in Fig.5) showed single crystals of a needle like morphology.
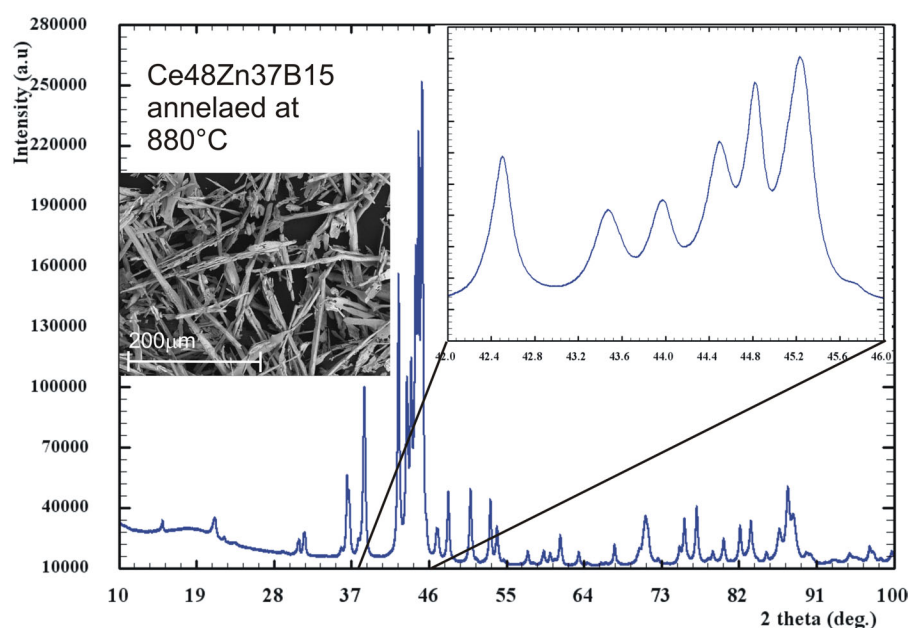
Figure 5. X-ray powder pattern of the τ_5-phase grown from Zn-flux from alloy $Ni_{48}Zn_{37}B_{15}$ (at. %), an elaborated area with dense peaks 42<2θ<46.

These needles, however, appeared severely intergrown along the needle axis and proved improper for X-ray single crystal structure determination. Therefore TEM was employed to gain information on symmetry and unit cell dimensions. TEM diffraction patterns were collected from a thin lamella roughly perpendicular to the needle axis

and were processed in the following way: Fig. 6a shows the high symmetry selected area diffraction (SAD) pattern obtained with the electron beam along the needle axis.
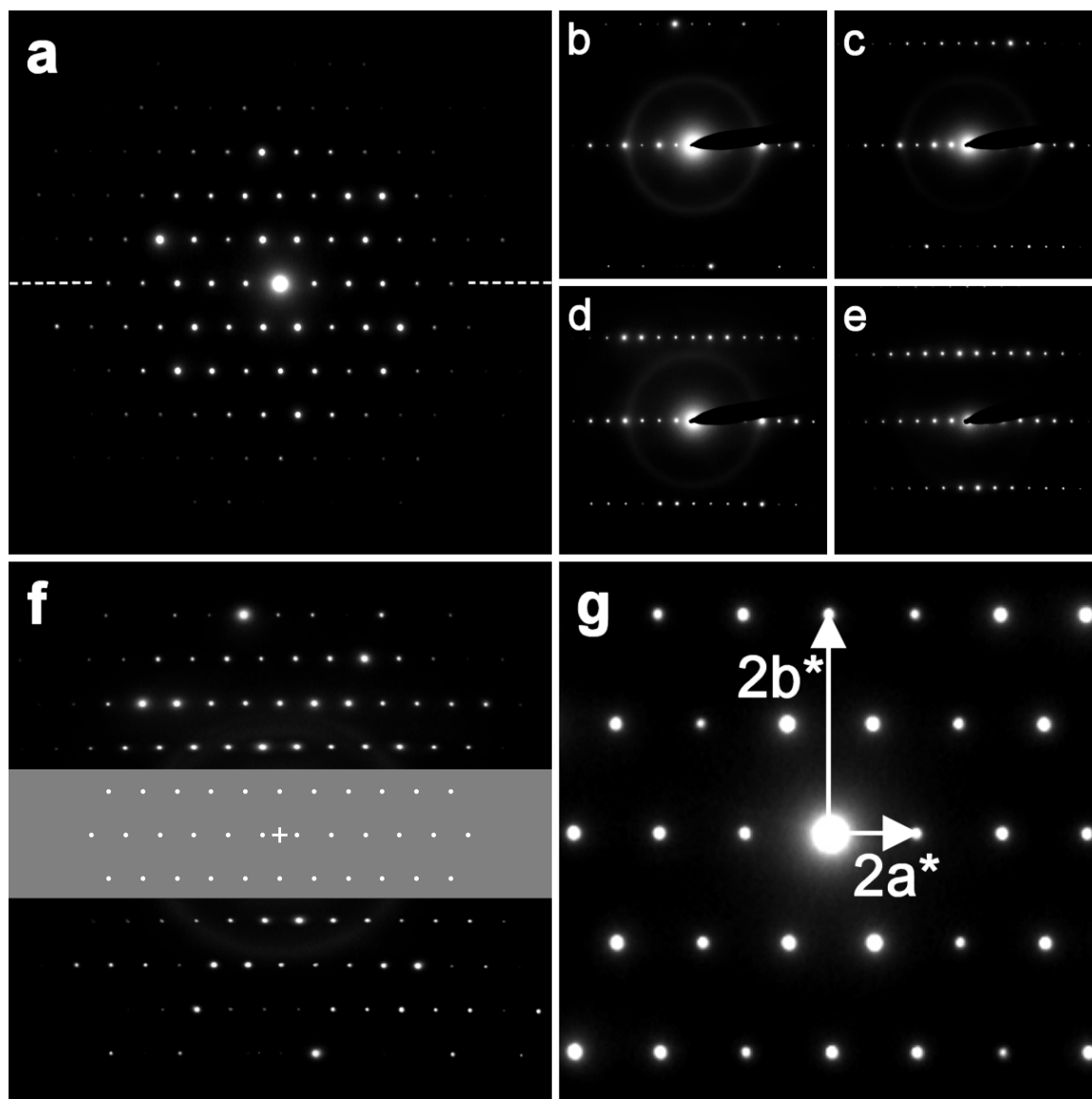
Figure 6. TEM analysis of a thin lamella prepared from needle-like crystals of the τ_5-phase. Diffraction pattern obtained with electron beam along the needle axis (tilt 0°). The dashed line marks the tilt axis for the following tilt series: (a) tilt series from the lamella tilted by 25.15° (b), 30.25° (c), 38.10° (d) and 49.8° (e). Reconstructed parallel reciprocal plane (f), where the horizontal region along the tilting axis (in gray) cannot be reached by sample tilt, however it can be filled in unambiguously according to what is found above and below it. Enlarged central part of the zero tilt diffraction (evaluated as [001] zone axis pattern) with two perpendicular reciprocal vectors marked (g).

This SAD was taken as the reference one with zero sample tilt and a series of diffraction patterns from the sample tilted by different angles around the axis marked in Fig 6a was obtained (Fig. 6b-e). From this tilt series we can reconstruct the intensity distribution in the reciprocal space. Fig. 6f (as a combination of tilt-corrected SADs from Fig. 6b-e) shows the next reciprocal plane parallel to the one shown in Fig. 6a. By combining the information from the two parallel planes, we arrive at a face centered orthorhombic distribution of diffraction spots in the reciprocal space. Fig. 6g shows the enlarged central part of Fig. 6a with two reciprocal lattice vectors marked and the third reciprocal lattice vector being equal to the distance of the two parallel planes. Finally we can conclude that the crystal structure of the τ_5 phase is body-centered orthorhombic with unit cell parameters a=1.6(2), b=0.63(7), c=0.27(0) nm. The needle-like crystals grow along the shortest (c) axis. An estimated error of lattice parameters evaluated by this method is ±3%.

5.3.3.3. The τ_6-phase

No single crystals could so far be obtained for this phase. Its composition has been defined to be $Ni_{47}Zn_{23}B_{30}$ (in at. %) from the EPMA Ni:Zn ratio in combination with the phases in equilibrium (Fig 8) Figs. 9a and 9b show the micrographs of alloys with nominal compositions $Ni_{42}Zn_{44}B_{14}$ (at. %) and $Ni_{50}Zn_{30}B_{20}$ (at. %), respectively with nicely shaped crystals of τ_5 and τ_6. However, we were unable to select crystals suitable for X-ray single crystal diffraction due to enhanced adhesion of a eutectic matrix around the τ_5 and τ_6 crystals and because of numerous micro-cracks caused by the hair-like morphology of these phases. The XPD pattern characteristic for the τ_6 phase is shown in Fig. 7.
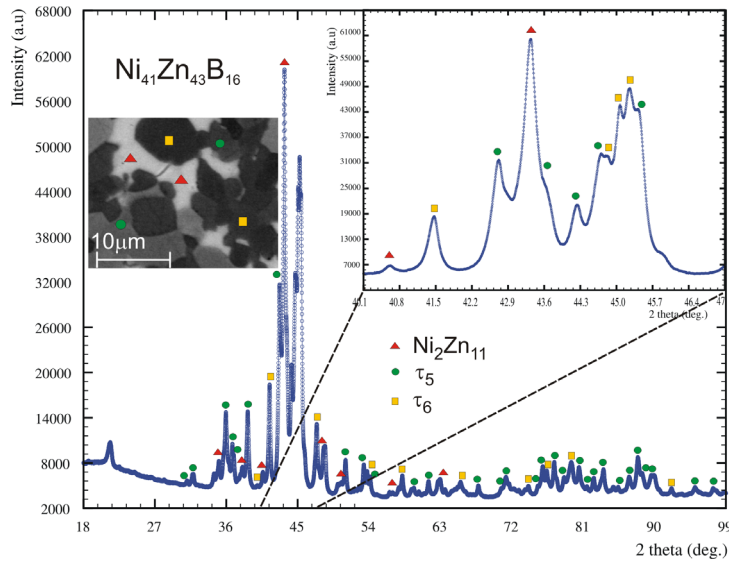
Figure 7. Three-phase equilibrium ($Ni_2Zn_{11}+\tau_5+\tau_6$) confirmed by X-ray powder diffraction and EPMA, showing Ni_2Zn_{11} as light gray phase, τ_5 as medium gray and τ_6 as dark gray grains.

5.3.4. Phase equilibria in ternary system Ni-Zn-B

Due to the large differences in the melting temperatures of the constituents, thermodynamic equilibrium at 800°C was difficult to achieve for samples prepared by melting. However preparation performed from powdered Ni_xB_y precursors cold-pressed with Zn filing by slow heating, annealing at 800°C, re-powderization and hot pressing and repeated annealing at 800°C for 60 samples proved sufficient to establish the phase eqilibria in this system (see Fig. 8. Table 5 summarizes the XPD and EPMA analyses of hot pressed ternary alloys before and after annealing at 800°C.
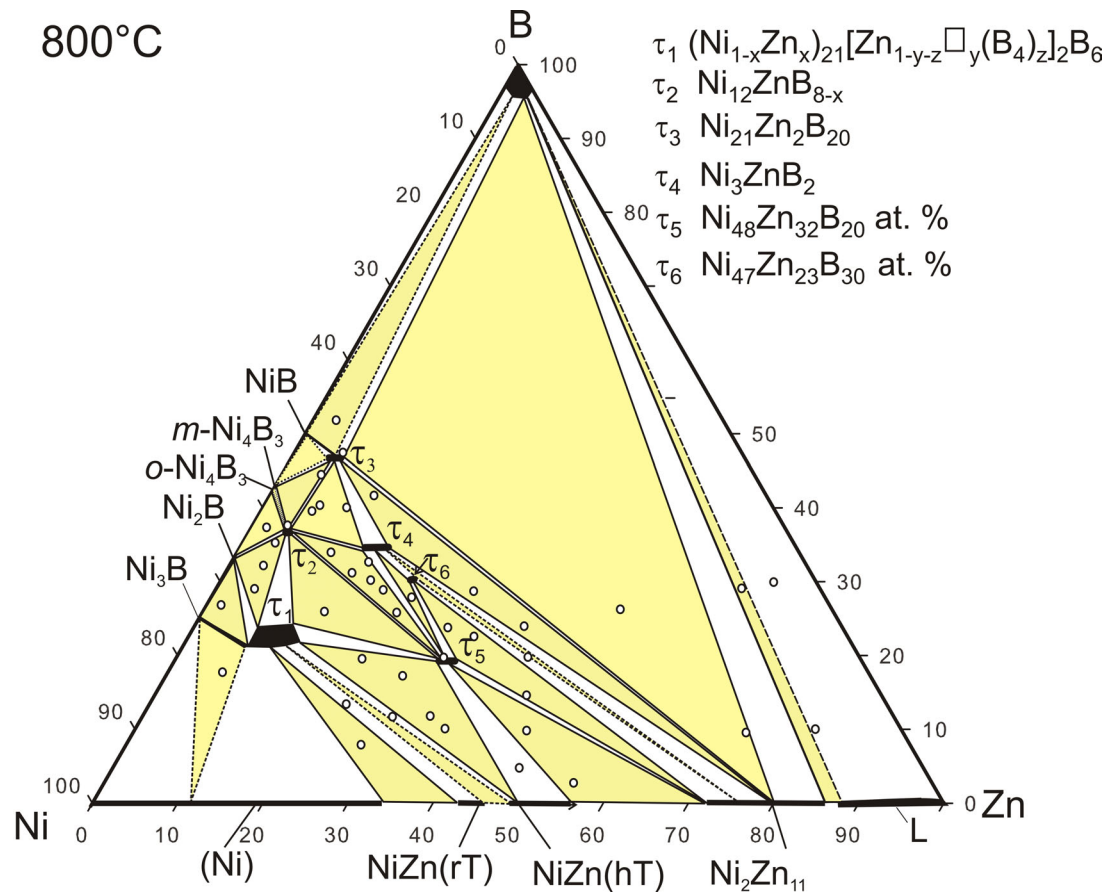
Figure 8. System Ni-Zn-B: isothermal section at 800°C.

$\beta B + Ni_2Zn_{11} + \tau_3$, documented by the microstructure of the alloy with composition $Ni_{25}Zn_{49}B_{26}$ (at. %).

The low melting point of Zn implies a liquid phase at 800°C near the Ni-Zn binary: the alloy with $Ni_{10}Zn_{80}B_{10}$ (at. % nominal composition), shows a narrow three-phase field $L + Ni_2Zn_{11}$(Ni:Zn=17.61: 82.39)$+\beta B$, where boron appears segregated revealing no interaction with Ni and Zn at this composition. The isothermal section Ni-Zn-B is dominated by a large three-phase region between $\beta B + Ni_2Zn_{11} + \tau_3$, documented by the microstructure of the alloy with composition $Ni_{25}Zn_{49}B_{26}$ (at. %). Prior to annealing the micrograph in figure $8c_1$ (inset of 8c) reveals the presence of boron, which is obvious from the particular shape of grains with sharp edges and its characteristic colour in LOM. After powderizing and annealing Zn losses have shifted the alloy composition to the two-phase region of $Ni_2Zn_{11} + \tau_3$ (see Fig. 9c). The micrographs of Figs. 9d and 9e prove the three-phase equilibrium: $\tau_3 + \tau_4 + Ni_2Zn_{11}$ in the alloy $Ni_{37}Zn_{39}B_{24}$ (at. %) and a narrow three-phase region $\tau_4 + \tau_5 + \tau_6$ is obvious from the alloy with composition $Ni_{49}Zn_{31}B_{20}$ (at. %) as shown in Fig. 9e.
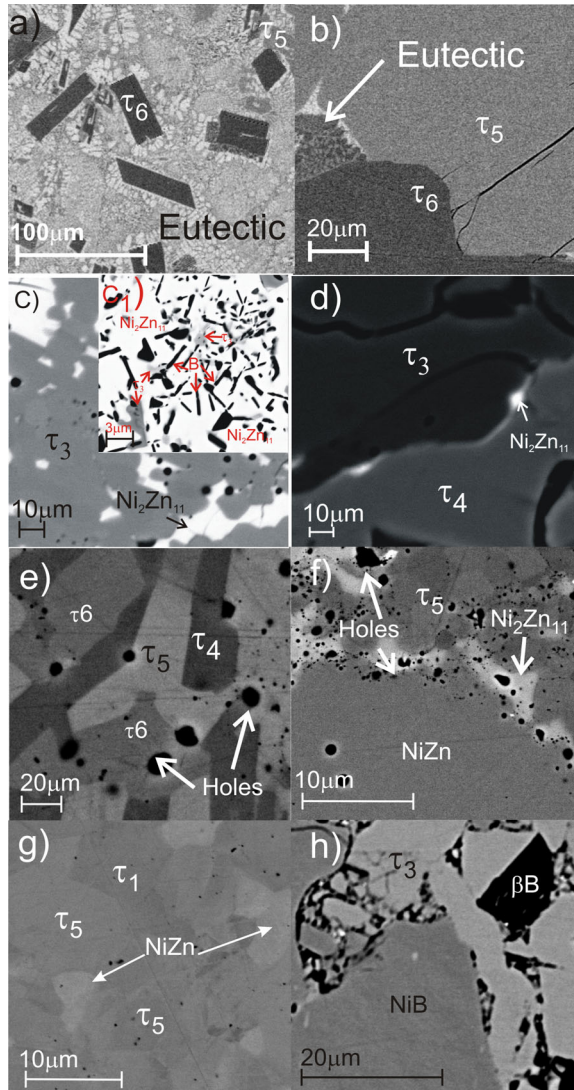
Figure 9. Samples $Ni_{42}Zn_{44}B_{14}$ (a) and $Ni_{50}Zn_{30}B_{20}$ (b) at. %, melted at 990°C, cooled at the rate 1°C/min to 990°C and annealed for 5 days at 880°C. Selected micrographs of Ni-Zn-B alloys: $Ni_{25}Zn_{49}B_{26}$ (at. %) hot pressed (c_1) and annealed at 800°C (c). Alloys annealed at 800°C: $Ni_{37}Zn_{39}B_{24}$ (d), $Ni_{49}Zn_{31}B_{20}$ (e), $Ni_{44}Zn_{46}B_{10}$ (f), $Ni_{56}Zn_{28}B_{16}$ (g) and $Ni_{56}Zn_6B_{38}$ (h) (at. %).

Further three-phase regions define the tie-lines of τ_5 to the Ni-Zn binary: $Ni_2Zn_{11}+\tau_5+NiZn$ (rT) (see Fig. 9f, alloy $Ni_{44}Zn_{46}B_{10}$), $\tau_1+\tau_5+NiZn$ (rT) (alloy $Ni_{56}Zn_{28}B_{16}$) and $\tau_5+\tau_6+Ni_2Zn_{11}$ (alloy $Ni_{41}Zn_{43}B_{16}$, for microstructure see the insert in Fig. 7). XPD has been employed to distinguish between the solid solution of (Ni) and NiZn (rT), which reveal insufficiently clear contrast in the micrograph (alloy $Ni_{63}Zn_{24}B_{13}$ at. %). It should be noted, that due to insufficiently fast quenching of the alloys (inside the protective Al_2O_3 crucibles sealed in quartz-walls) we were not able

to retain the cubic high temperature modification of β'-NiZn, which transfers on cooling to the low temperature form NiZn(rT). In the Ni-rich part of the diagram the phase τ_1 exists at 800°C in a large homogeneity region (see section below) and dominates the phase equilibria: the three-phase field $\tau_1+\tau_2+\tau_3$ has been determined by X ray powder and microprobe analysis of the alloy $Ni_{53}Zn_7B_{40}$. Tie lines between τ_2+o-Ni_4B_3 and τ_1+Ni_2B, respectively, are provided by the samples $Ni_{56}Zn_6B_{38}$ and $Ni_{64}Zn_4B_{32}$ at. % and the three-phase triangle $\tau_1+Ni_2B+Ni_3B$ is backed by the alloy $Ni_{72}Zn_4B_{24}$ at. % (see Rietveld refinement and micrograph in Fig. 10).
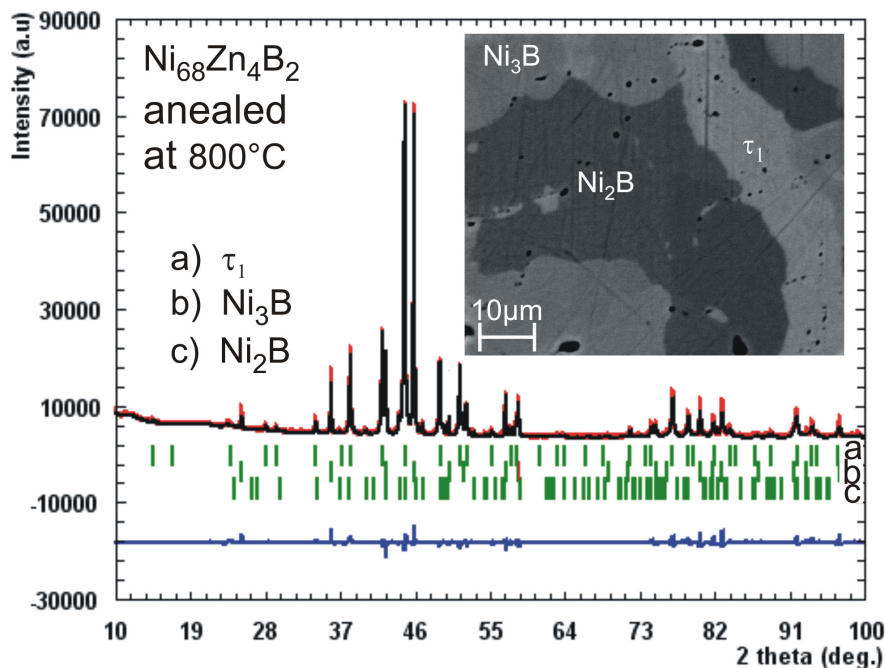
Figure 10. a) Rietveld refinement and b) micrograph of alloy $Ni_{72}Zn_4B_{24}$ (at. %) annealed at 800°C.

Most of the ternary compounds show at 800°C rather limited solution ranges and mainly in form of Ni/Zn exchange at constant B-content i.e. about 4 to 5 at. % for τ_4-Ni_3ZnB_2 [8] and τ_5-$Ni_{48}Zn_{32}B_{20}$, but below 3 at. % for τ_2-$Ni_{12}ZnB_{8-x}$ (x=0.43), τ_3-$Ni_{21}Zn_2B_{20}$ [8] and τ_6-$Ni_{47}Zn_{23}B_{30}$.

5.3.5. *Homogeneity range of the τ_1- phase*

Fig. 11 shows the composition dependence of the average atomic volume (unit cell/metal atom) for Ni-Zn binary phases as well as for the Ni-Zn side of the τ_1-phase.

Interestingly the slope of the dependence for the τ_1-phase is the same as that for the Ni-Zn binaries. This prompts us to conclude that the increase in lattice parameters of the τ_1-phase is due to a simple Ni-Zn substitution.
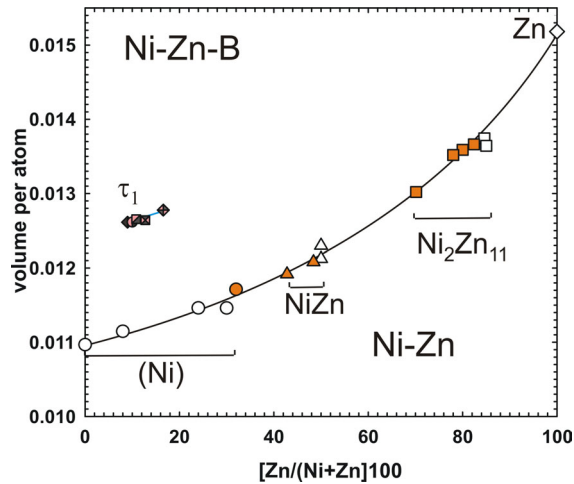
Figure 11. Compositional dependence of atomic volume for Ni-Zn binaries and ternary τ_1 (pink-gray half-shaded symbols) on the Ni-Zn side of the homogeneity range. Literature data for the binary system are presented by open symbols [18]; filled symbols represent the data from this work.

However, the lattice parameters of the τ_1-phase on the boron-rich side of the homogeneity region are significantly higher (Fig. 12b), which thus explains by the substitution of Zn-atoms in the 9c sites by B-tetrahedra (for details see chapter 3.3.1). This observation was employed to sketch the shape of the homogeneity region for the τ_1-phase as shown in Fig. 12a.

Comparing the phase relations derived in this work with those of Stadelmaier et al. [3], we see not only a larger number of ternary compounds (labeled τ_1 to τ_6), but also significant changes in phase triangulation. Phase correspondence with those of Stadelmaier et al. [3] (given in brackets) can be inferred for τ_1 (τ) and τ_2 (ψ), but correlation between τ_4, τ_5, τ_6 and φ, χ is rather speculative, τ_3 being out of the range investigated by Stadelmaier et al. [3].
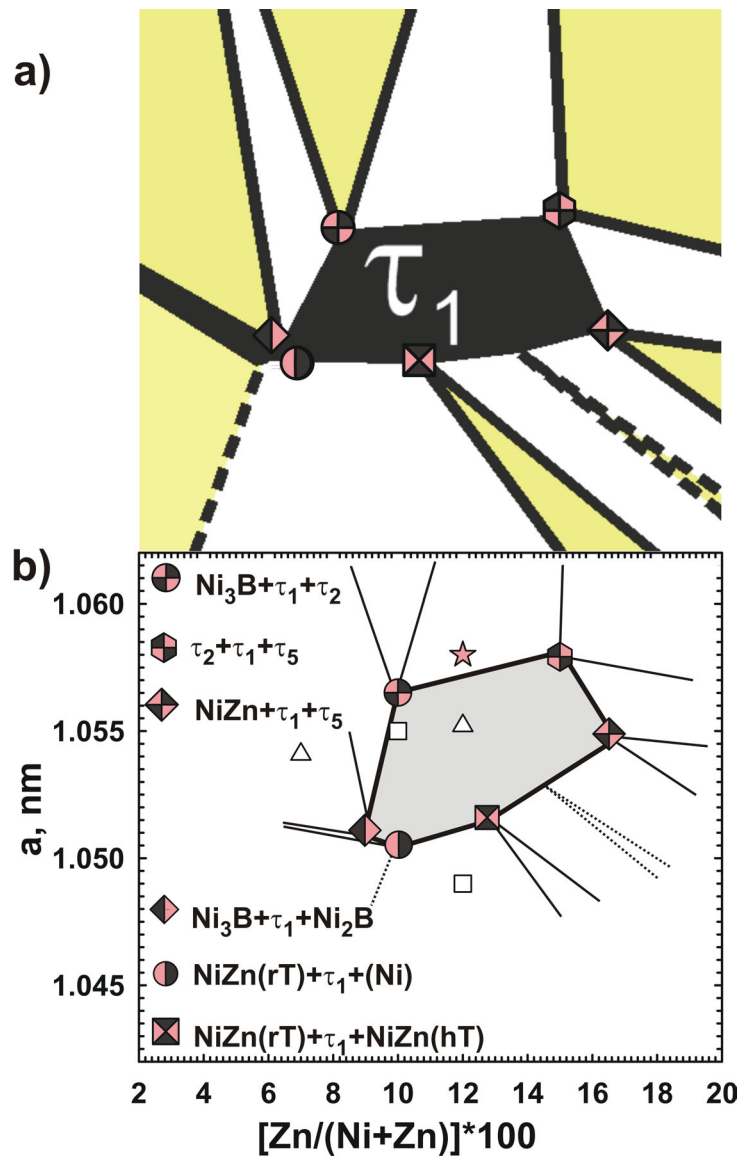
Figure 12. a) Partial isothermal section at 800°C around τ_1 phase, b) lattice parameters versus Zn fraction [Zn/(Ni+Zn)]*100 at. % after EPMA). Pink-gray half shaded symbols and pink star are the data points of powder samples and of the single crystal in this work, respectively. Open symbols are the data points from literature, i.e, open triangles [7] and open squares [3].

5.4. Conclusion

Phase equilibria in the isothermal section at 800°C have been established for the system Ni-Zn-B using X-ray powder diffraction and electron microprobe analyses and were found to be characterized by the formation of six ternary compounds (labeled τ_1 to τ_6). Phase relations at 800°C are dominated by a large three-phase field

(βB)+Ni$_2$Zn$_{11}$+τ_3, as practically all ternary compounds form at concentrations <50 at. %Ni. The Ni-rich part is dominated by the so-called τ-phase τ_1-(Ni$_{1-x}$Zn$_x$)$_{21}$[Zn$_{1-y-z}\square_y$(B$_4$)$_z$]$_2$B$_6$, which exhibits a large homogeneity region ($0.07<x<0.11$, $0.07<y<0.53$, $0<z<0.3$ at 800°C). Whereas B-poor compositions are isotypic with the Cr$_{23}$C$_6$ type (space group $Fm\bar{3}m$), single crystal X-ray data analysis for the composition x=0.07, y=0.125, z=0.30, a=1.05800(3) nm revealed partial replacement of Zn-atoms by B$_4$-tetrahedra (R$_F^2$=0.014, space group $Fm\bar{3}m$). The crystal structures of τ_2-Ni$_{12}$ZnB$_{8-x}$ (x=0.43; Ni$_{12}$AlB$_8$ type), τ_3-Ni$_{21}$Zn$_2$B$_{20}$ (own type) and τ_4-Ni$_3$ZnB$_2$ (own type) have been determined in our foregoing paper [8]. Due to bad crystals, the crystal structures of τ_5-Ni$_{48}$Zn$_{32}$B$_{20}$ (*oI,* a=1.6(2) nm, b=0.63(7) nm, c=0.27(0) nm, determined from TEM) and of τ_6-Ni$_{47}$Zn$_{23}$B$_{30}$ have not been elucidated yet. Most of the ternary compounds show at 800°C rather limited solution ranges and mainly in form of Ni/Zn exchange at constant B-content: about 4 to 5 at. % for τ_4-Ni$_3$ZnB$_2$ [8] and τ_5-Ni$_{48}$Zn$_{32}$B$_{20}$, but solubilities are below 3 at.% for τ_2-Ni$_{12}$ZnB$_{8-x}$ (x=0.43), τ_3-Ni$_{21}$Zn$_2$B$_{20}$ [8] and τ_6-Ni$_{47}$Zn$_{23}$B$_{30}$.

As a side product of the ternary investigation, precise data on atom site distribution and positional parameters have been provided with higher reliability factors from X-ray single crystal refinements for Ni-borides, for which crystal structures hitherto have only been derived from X-ray diffraction photographs: *o*-Ni$_4$B$_3$ (*Pnma,* a=1.9665(4) nm, b=0.29852(1) nm, c=0.65750(2) nm; R$_F^2$=0.015) and *m*-Ni$_4$B$_3$ (*C2/c*, a=0.64356(3) nm, b=0.48867(3) nm, c=0.78267(3) nm, β=103.288(3)°; R$_F^2$=0.021).

5.5.Associated Content
Supporting Information. X-ray crystallographic file in CIF format, tables on interatomic distances. This material is available free of charge via the Internet at http://pubs.acs.org.

5.6. References

[1]   A.G. De Golyer, United State Patent Office 1490696 (1924).

[2]   S.P. Chen, A.F. Voter, R.C. Albers, A.M. Boring, P.J. Hay. J Mater. Res. 5 (1990) 955-970.

[3]   H.H. Stadelmaier, J-D. Schöbel, L.T. Jordan, Metall. 16 (1962) 752-754.

[4]   H.H. Stadelmaier, T.S. Yun, Z Metallkde. 53 (1962) 754-756.

[5]   H.H. Stadelmaier, R.A. Draughn, G. Hofer, Z Metallkde. 54 (1963) 640-644.

[6]   S. Bhan, S. Singh, A. Lal, J Alloy Phase Diagrams (India) 6 (1990) 147-152.

[7]   D. Kotzot, M. Ade, H. Hillebrecht, J Solid State Chem. 183 (2010) 2281-2289.

[8]   Z. Malik, O. Sologub, A. Grytsiv, G. Giester, P. Rogl, Inorg Chem. 50 (2011) 7669-7675.

[9]   J. Rodríguez-Carvajal, Satellite Meeting on Powder Diffraction of the XV IUCr Congress, (1990) 127.

[10]   Nonius Kappa CCD Program Package COLLECT, DENZO, SCALEPACK, SORTAV, Nonius Delft, The Netherlands, 1998.

[11]   G.M. Sheldrick, SHELXS-97, Program for Crystal Structure Refinement University of Göttingen, Germany Windows version by McArdle, Natl. Univ. Ireland, Galway, 1997.

[12]   G.M. Sheldrick, Acta Crystallogr. A64 (2008) 112–122.

[13]   L.J. Farrugia, J. Appl. Crystallogr. 32 (1999) 837–838.

[14]   A. Jonnasson, H. Ljung, S. Westman, Acta Chem Scand. 22(1968) 2743–2753.

[15]   EDAX Phoenix software, TEM Quant Materials, (version 3.2.), Mahwah(NJ): EDAX Inc., 2000.

[16]   T.B. Massalski, Binary Alloy Phase Diagrams, 2nd ed., ASM International, Materials Park, OH, USA, 1990.

[17]   W-H. Sun, Y. Du, Y. Kong, H-H. Xu, W. Xiong, S-H. Liu, Int J Mat Res. (formerly Z. Metallkd) 100(1) (2009) 59-67.

[18]   P. Villars, K Cenzual, Pearson's Crystal Data CD-ROM, AMS International,Ohio, Release 2011/12.

[19]   M.M. Korsukova, V.N. Gurin, Y.B. Kuz'ma, A.Y. Kiskachi, N.E. Solov'ev, Sov. Phys. Crystallogr. 22(6) (1977) 690-692.

[20]   Y.B. Kuz'ma, V.N. Gurin, M.M. Korsukova, A: L.G. Akselrud, Inorganic Materials Izvestiya Akademii Nauk SSSR. 23 (1987) 500-503.

[21]   T. Lundstrom, l. Tergenius, Zeitschrift für Kristallogr. 167 (1984) 235-246.

[22]   S. Rundqvist, Chem Scand. 13 (1959) 1193-1208.

[23]   S. Rundqvist, Chem Scand. 12 (1958) 658-662.

[24]   Z. Malik, A. Grytsiv, P. Rogl, G. Giester, DIO: 10.1016/j.jssc.2012.07.032

[25]   P. Nash, Y.Y. Pan, Bull. Alloy Phase Diagrams. 8 (5) (1987) 422-430.

[26]   S. Rundqvist, S. Pramatus, Acta Chem Scand. 21 (1967) 191-194.

[27]   E. Teatum, K. Gschneidner, J. Waber, LA-2345, U.S. Department of Commerce: Washington D.C., 1960.

[28]   P. Rogl, Borides with Boron Chains, in Inorganic Reactions and Methods: Formation of Bonds to Group-I, -II, and -IIIB Elements, Volume 13 (eds J. J. Zuckerman and A. P. Hagen), N.J. Hoboken, John Wiley & Sons, 1991.

[29]   E. Koch, W. Fischer, Z. Kristallogr. 211 (1996) 251-253.

[30]   O. Sologub, P. Rogl, G. Giester, Intermetallics. 18 (2010) 694-701.

[31]   R.P. Anantatmula, D.B. Masson, Metallurgical Trans. 5 (1974) 605-613.

[32]   W.B. Pearson, L.T. Thompson, Canadian J. Physics. 35 (1957) 349–357.

[33]   W. Heike, J. Schramm, O. Vaupel, Metallwirtsch Metallwiss Metalltech. 51 (1936) 655–662.

[34]   J.K. Critchley, S. Denton, Journal of the Institute of Metal.s 99 (1971) 26–27.

[35]   G. Novar, K. Shubert, J. Less-Common Met. 75 (1980) 51–63.

[36]   G.A. Slack, C.I. Hejna, M.F. Garbauskas, J.S. Kasper, J. Solid State Chem. 76 (1988) 64-86

[37]   Z. Malik, O. Sologub, G. Giester, P. Rogl, (submitted) J. Alloys Compounds. (2012).

[38]   T. Weissbach, D.C. Meyer, T. Leisegang, A. Kreyssig, M. Frontzek, J.U. Hoffmann, D. Souptel, A. Köhler, G. Behr, P. Paufler, Journal of Applied Crystallogr. 41 (2008) 738-746.

[39]   R. Gumeniuk, H. Borrmann, A. Leithe-Jasper, Z. Kristallog.r 221 (2006) 425-426.

[40]   E. Parthé, L. Gelato, B. Chabot, M. Penzo, K. Censual, R. Gladyshevskii, TYPIX—Standardized Data and Crystal Chemical Characterization of Inorganic Structure Types, Berlin:Springer; 1994.

Table 1. Crystallographic data of solid phases of the system Ni–Zn–B.

Phase	Temp. range, °C	Space group, Prototype	a	b	c	Comments
(Ni)	<1455 [16]	$Fm\bar{3}m$ Cu	0.35240	-	-	[16]
$Ni_{1-x}Zn_x$						$0 \leq x \leq 0.24$ at 1000°Cᵃ [31]
-		-	0.35269	-	-	x=0 at 1000°Cᵃ [31]
-		-	0.35791	-	-	x=0.24 [31]
						$0 \leq x \leq 0.30$ [32]
(Zn)	<420 [16]	$P6_3/mmc$ Mg	0.2665	-	0.4947	[16]
			0.2667(1)	-	0.4951(1)	From alloy Ce_7Zn_{93}, 600°Cᵃ
β NiZn / $Ni_{1-x}Zn_x$	1040-675 [16]	$Pm\bar{3}m$ CsCl	0.29083	-	-	[33]
β₁ NiZn / $Ni_{1-x}Zn_x$	<810 [16]	$P4/mmm$ CuTi	0.27487	-	0.31768	$0.46 \leq x \leq 0.51$ at 600°Cᵃ [31]
-			0.27504	-	0.32006	x=0.46
-		$I4/mmm$	0.2754	-	0.3214	x=0.51
						x=0.5 [33]
$Ni_{2+x}Zn_{11-x}$		$I\bar{4}3m$ Cu_5Zn_8	0.8920(2)	-	-	$0.6 \leq x \leq 1.5$ at 800°Cᵃ [25]
<[16]						$-0.1 \leq x \leq 0.6$ at 600°Cᵃ [31]
-		-	0.89069	-	-	x=0.6
-		-	0.89186	-	-	x=-0.1
Ni_3Zn_{22}	<490 [16]	$C2/m$ Ni_3Zn_{22}	1.337(1)	0.747(2) β=111.3(2)°	0.765(1)	[34]
$Ni_{16}Zn_{53}$ ($NiZn_3$)		$Aem2$ $Ni_{16}Zn_{53}$	3.3326(8)	1.2499(4)	0.8869(1)	Orthorhombic variant of Cu_5Zn_8 [35]
(βB)	<2092 [16]	$R\bar{3}m$ βB	1.09251	-	2.38143	[18]
Ni_xB_{1-x}						-
-			1.09615(5)	-	2.38544(7)	x=0.021 at 1700°C [21]
-			1.0955(8)	-	2.3865(22)	for $Ni_{0.95}B_{106.1}$ [36]
-			1.0950(3)	-	2.3851(10)	For $Ni_{0.78}B_{106.3}$ [36]
Zn_yB_{1-y}			-	-	-	$0 \leq y \leq 0.042$ at 907°C [19]
-			1.093	-	2.374	y=0 [19]
-			1.100	-	2.404	y=0.042 [19]

Phase, Temp. range, °C	Space group, Prototype	Lattice parameters, nm			Comments
		a	b	c	
$Ni_xZn_yB_{1-x-y}$					
-	-	1.0986(2)	-	2.4016(4)	y=0.039 at 907°C [20]
-	-	1.10182(2)	-	2.40534(5)	x=0.005, y=0.034
-	-	-	-	-	$Ni_{0.19}Zn_{1.24}B_{34.22}$ [37] SC
NiB	$Cmcm$	0.2928	0.7391	0.2964	[22]
<1043 [2009Sun]	CrB	-	-	-	[18]
m-Ni_4B_3	$C2/c$	0.64282(5)	0.48795(4)	0.78190(6)	[26]
<1031 [16]	m-Ni_4B_3	-	β=103.32(1)°	-	-
-	-	0.64356(3)	0.48867(3)	0.78267(3)	[This work] SC
-	-	-	β=103.29(1)°	-	-
o-Ni_4B_{3-x}	$Pnma$	1.1954	0.29815	0.65684	x=0.17 [22]
<1025 [16]	o-Ni_4B_3	1.1953	0.2981	0.6569	Ni-rich [22]
-	-	1.1973	0.2985	0.6584	B-rich [22]
-	-	1.19540(8)	0.29815(3)	0.65684(5)	[22]
-	-	1.1966(4)	0.2985(1)	0.6575(2)	x=0.20 [This work] SC
Ni_2B	$I4/mcm$	0.4991(3)	-	0.4247(3)	[18]
<1125 [16]	$CuAl_2$	0.4995(2)	-	0.4238(2)	[38]
Ni_3B	$Pnma$	0.52105(5)	0.66174(6)	0.43904(4)	[26]
<1165 [2009Sun]	Fe_3C	0.52219(2)	0.66171(2)	0.43918(1)	[39]
τ_1-$(Ni_{1-x}Zn_x)_{21}[Zn_{1-y-z}\square_y(B_4)_z]_2B_6$	$Fm\bar{3}m$ $Cr_{23}C_6$	1.05800(3)	-	-	x=0.07, y=0.125, z=0.30, [This work] SC
-	-	1.055	-	-	τ-phase [5]
-	-	1.050-1.055	-	-	$Ni_{20}Zn_3B_5$-$Ni_{19}Zn_4B_8$ [4]
-	-	1.049-1.055	-	-	$Ni_{72}Zn_{10}B_{18}$-$Ni_{61}Zn_{13}B_{26}$ [3]

Phase, Temp. range , °C	Space group, Prototype	Lattice parameters, nm			Comments
		a	b	c	
-	-	1.05409(17)	-	-	$Ni_{21.4}Zn_{1.6}B_6$ [7]
-	-	1.05521(17)	-	-	$Ni_{20}Zn_{2.4}B_{7.75}$ [7]
τ_2-$Ni_{12}ZnB_{8-x}$	*Cmca* $Ni_{12}AlB_8$	1.05270(2)	1.45236(3)	1.45537(3)	x=0.43, [8] SC;
-		-	-	-	likely to be identical with phase ψ [b] $Ni_{57}Zn_{13}B_{30}$ [3]
τ_3-$Ni_{21}Zn_2B_{20}$	*I4/mmm* $Ni_{21}Zn_2B_{20}$	0.72103(1)	-	1.42842(5)	[8] SC
-		-	-	-	-
τ_4 -Ni_3ZnB_2	*C2/m* Ni_3ZnB_2	0.95101(4)	0.2892(4) $\beta=101.097(3)°$	0.84366(3)	[8] SC
-		-	-	-	-
τ_5	*ol**	1.621	0.637	0.270	$Ni_{48}Zn_{32}B_{20}$ TEM [This work]; likely to be identical with phase φ [d] at $Ni_{49}Zn_{31}B_{20}$ [3]
τ_6	*unknown*	-	-	-	$Ni_{47}Zn_{23}B_{30}$ [This work]
χ		-	-	-	$Ni_{45}Zn_{30}B_{25}$ [3]: not observed in the present investigation

[a] Quenching temperature of samples, but lattice parameters measured at room temperature.

[b] ψ reported by [1962Sta] likely to be identical with τ_2 in this paper.

[c] τ reported by [1962Sta] is abbreviated by τ_1 in this paper.

[d] φ reported by [1962Sta] has composition near to that of τ_5 in this paper.

Table 2. Crystal structure data for o- Ni_4B_{3-x} (x=0.19) and m-Ni_4B_3 (Nonius KappaCCD, MoK$_\alpha$)

Compound	o-Ni_4B_{3-x}	m-Ni_4B_3
Alloy composition [c] (at. %)	$Ni_{50}Zn_{15}B_{35}$	$Ni_{56}Zn_6B_{38}$
Space group	$Pnma$; No. 62	$C2/c$; No. 15
Formula from refinement	Ni_4B_{3-x} (x=0.19)	Ni_4B_3
Structure type	o-Ni_4B_{3-x}	m-Ni_4B_3
θ Range [deg]	$3.40 < \theta < 36.50$	$5.29 < \theta < 36.15$
Crystal size [μm]	25×30×42	20×30×45
a, b, c [nm]	1.19665(4), 0.29852(1), 0.65750(2)	0.64356(3), 0.48867(3), 0.78267(3)
β [deg]	-	103.288(3)
Reflections in refinement	591 $F_o > 4\sigma(F_o)$ of 636	493 $F_o > 4\sigma(F_o)$ of 561
Mosaicity	0.57	0.52
Number of variables	37	27
$R_F^2 = \Sigma|F_0^2 - F_c^2|/\Sigma F_0^2$	0.015	0.021
R_{Int}	5.8	6.4
GOF	1.075	1.008
Extinction (Zachariasen)	0.0169(8)	0.0055(5)
M1; Occ. U_{11}[b]; U_{22}; U_{33}; U_{23}; U_{13}; U_{12}	$4c$ (x, ¼, z); x= 0.04998(2), z=0.75077(4); 1.00(1) Ni1 0.0050(1); 0.0050(1) 0.0055(1); 0; -0.0007(1); 0	$8f$ (x, y, z); x= 0.20283(4), y= 0.43020(6), z= 0.28639(4); 1.00(1) Ni1 0.0066(2); 0.0059(2); 0.0047(1); 0.0006(1); 0.0010(1), -0.0007(1)
M2; Occ. U_{11}[b]; U_{22}; U_{33}; U_{23}; U_{13}; U_{12}	$4c$ (x, ¼, z); x= 0.12402(2), z=0.33323(4); 1.00(1) Ni2 0.0050(1); 0.0062(1); 0.0054(1); 0; 0.0003(1); 0	$8f$ (x, y, z); x= 0.45551(4), y= 0.25201(5), z= 0.01675(4); 1.00(1) Ni2 0.0051(2); 0.0049(2); 0.0082(1); 0.0001(1); 0.0009(1), -0.0002(1)
M3; Occ. U_{11}[b]; U_{22}; U_{33}; U_{13}; U_{23}= U_{12}=0	$4c$ (x, ¼, z); x= 0.30006(6), z=0.12129(4); 1.00(1) Ni3 0.0039(1); 0.0058(1); 0.0049(1); 0.; -0.0000(1); 0	$8f$ (x, y, z); x= 0.23303(39), y= 0.08048(49), z= 0.44187(31); 1.00(1) B1 U_{iso}[b]=0.0068(4)
M4; Occ.; U_{iso}[b] U_{11}[b]; U_{22}; U_{33}; U_{13}; U_{23}= U_{12}=0	$4c$ (x, ¼, z); x= 0.35175(2), z=0.50899(4); 1.00(1) Ni4 0.0056(1); 0.0058(1); 0.0060(1); 0.0014(1)	$4e$ (0, y, ¼); y= 0.0708(7); 1.00(1) B2; 0.0078(6)
B1 in $4c$ (x, ¼, z); Occ.; U_{iso}[b]	x= 0.0245(2), z=0.0616(4); 0.89(1); 0.0075(6)	
B2 in $4c$ (x, ¼, z); Occ.; U_{iso}[b]	x=0.2420(2), z=0.8189(4); 1.00(1) ; 0.0075(4)	
B3 in $4c$ (x, ¼, z); Occ.; U_{iso}[b]	x= 0.4616(2), z=0.0226(3); 0.92(1); 0.0040(6)	-
Residual electron density; max; min in [electrons/nm^3] x1000	0.85; -0.97	1.161; -1.21

[a]crystal structure data are standardized using the program Structure Tidy [40].

[b]anisotropic atomic displacement parameters U_{ij} and isotropic U_{iso} in [10^2 nm^2].

[c]nominal composition of the alloy from which the single crystal was isolated.

Table 3. Structural data [a] for τ_1-$(Ni_{1-x}Zn_x)_{21}[Zn_{1-y-z}\square_y(B_4)_z]_2B_6$ (x=0.07, y=0.125, z=0.30) with $Cr_{23}C_6$-type (space group $Fm\overline{3}m$; No. 225, MoK_α radiation)

Alloy composition (at %)[b]	$Ni_{65}Zn_{10}B_{25}$
Ni:Zn atomic ratio, EPMA/refinement	**88 : 12**/ 88.2 : 11.8 [88 : 12][d]
Composition from refinement (at %)	$Ni_{63.9}Zn_{8.6}B_{27.5}$ [$Ni_{66.6}Zn_8B_{25.4}$] [d]
Formula from refinement	$Ni_{19.52}Zn_{2.62}B_{8.4}$
θ-range; sets; frames; time/frame	$3.34 < \theta < 36.12$, 5, 212, 180 sec
a [nm]	1.05800(3) [1.05521(17)][d]
Crystal size (μm)	30x30x35
Mosaicity	0.55
Reflections in refinement	169 F_o >4σ(F_o) of 186
Number of variables	20
$R_F^2 = \Sigma|F_0^2-F_c^2|/\Sigma F_0^2$	0.014
R_{Int}	0.058
GOF	1.06
Extinction (Zachariasen)	0.00201(7)
Ni1 in 48h (0,y,y); Occ. U_{11}[c]; U_{22}=U_{33}; U_{23}; U_{13}=U_{12}=0	y =0.16987(2) [0.16994(3)][d]; 1.00(1) 0.00784(2); 0.0062(1);0. 0004(1)
Ni2+Zn1 in 32f (x,x,x) Occ. U_{11}=U_{22}=U_{33}; U_{23}=U_{13}=U_{12}	x=0.3819(9) [0.38242(3)] [d] 0.94(3)Ni2+0.06Zn1 [0.99+0.01][d] 0.0083(1); 0.0023(1)
Zn2 8c (¼,¼,¼); Occ. U_{11}=U_{22}=U_{33}; U_{23}=U_{13}=U_{12}=0	0.57(4) [0.68(5)][d] 0.0109(4)
Zn3 in 4a (0,0,0); Occ. U_{11}=U_{22}=U_{33}; U_{23}=U_{13}=U_{12}=0	1.00(1) [0.99(1)][d] 0.0068(2)
B1 in 24e (x,0,0); Occ; U_{iso}	x = 0.2745(4) 1.00(1) [1.00][d] 0.0098(7)
B2 in 32f (x,x,x); Occ; U_{iso}	x = 0.1943(9) [0.166][d]; 0.30(1) [0.22(16)][d]; 0.019(4) [0.025(fixed)][d]
Residual electron density; max; min in [electrons/nm³] x1000	0.73; -0.70

[a] crystal structure data are standardized using the program Structure Tidy [40].

[b] nominal composition of the alloy from which a single crystal was isolated.

[c] atomic displacement parameters U_{ij} and U_{iso} in [10^2 nm^2].

[d] structural parameters after [7] are presented in square brackets.

Table 4. Interatomic distances (nm) for τ_1-$(Ni_{1-x}Zn_x)_{21}[Zn_{1-y-z}\square_y(B_4)_z]_2B_6$.

Bonds	Distance	Bonds	Distance
Ni1 – 2B2	0.2088(1)	M2 – 3B1	0.2101(2)
Ni1 – 2B1	0.2111(2)	M2 – 3B2	0.2289(20)
Ni1 – Ni1	0.2398(1)	M2 – Zn2	0.2417(20)
Ni1 – 4Ni1	0.2542(1)	M2 – 4M2	0.2499(2)
Ni1 – Zn3	0.2542(1)	M2 – 6M2	0.2626(1)
Ni1 – 4M2	0.2626(1)	B1 – 4M2	0.2101(2)
		B1 – 4Ni1	0.2111(2)
Zn2 – 4M2	0.2417(20)	B2 – 3B2	0.1668(25)
Zn2 – 12Ni1	0.2904(1)	B2 – 3Ni1	0.2088(1)
Zn3 – 12Ni1	0.2542(1)	B2 – 3M	0.2289(20)

M2=94(3) % Ni2+6(3)%Zn1

Table 5. Ni-Zn-B system: Phase equilibria and lattice parameters for alloys annealed at 800°C.

Ni-Zn-B, at. % (Nominal)	3- and 2-phase regions	Phases	EPMA, at. %		Lattice parameters (nm)		
			Ni	Zn	a	b	c
10-80-10	L+Ni$_2$Zn$_{11}$+βB	L[1]	-	100	0.2680(8)	-	0.4942(1)
-	-	Ni$_2$Zn$_{11}$	17.6	82.4	0.89229(2)		
-	-	B	-	-			
25-49-26	τ$_3$+Ni$_2$Zn$_{11}$	τ$_3$	91.0	9.0	0.7208(1)	-	1.4281(4)
-	Figure 8c	Ni$_2$Zn$_{11}$	20.0	80.0	0.8907(1)		
-	-	β boron	13.3	86.7	-		
37-39-24	τ$_4$+τ$_3$+Ni$_2$Zn$_{11}$	τ$_4$	75.1	24.9	0.951(3)	0.2892(1)	0.8434(3)
-	Figure 8d	-	-	-	-	β=101.03°	
-	-	τ$_3$	91.9	8.2	0.7198(2)		1.455(9)
-	-	Ni$_2$Zn$_{11}$	22.0	78.0	0.8892(3)		
49-31-20	τ$_4$+τ$_5$+τ$_6$	τ$_4$	74.7	25.3	-	-	-
-	Figure 8e	τ$_5$	60.6	39.4	-	-	-
-	-	τ$_6$	67.4	32.6		-	-
44-46-10	Ni$_2$Zn$_{11}$+τ$_5$+ NiZn (rT)[2]	Ni$_2$Zn$_{11}$	28.0	72.0	0.8842(3)	-	-
-	Figure 8f	τ$_5$	61.0	39.0	-	-	-
-	-	NiZn (rT)[2]	51.0	49.0	-	-	-
56-28-16	τ$_1$+τ$_5$+NiZn (rT)	τ$_1$	83.4	16.6	1.05659(6)	-	-
-	Figure 8g	τ$_5$	63.8	36.2	-	-	
-	-	NiZn (rT)	51.6	48.4	0.27536(4)	-	0.31865(9)
56-6-38	τ$_3$+NiB+β Boron	τ$_3$	91.0	9.0	0.7207(2)		1.42770(7)
	Figure 8h	NiB	-	-	0.2936(5)	0.7396(2)	0.2967(5)
-	-	β boron	-	-	-	-	-
41-43-16	Ni$_2$Zn$_{11}$+τ$_5$+τ$_6$	Ni$_2$Zn$_{11}$	28.0	72.0	0.884(1)	-	-
-	Figure-10	τ$_5$	61.0	39.0		-	-
-	-	τ$_6$	67.0	33.0		-	-
72-4-24	τ$_1$+Ni$_2$B+Ni$_3$B	τ$_1$	90.0	10.0	1.05088(3)	-	-
-	Figure 11	Ni$_2$B	-	-	0.4990(2)	-	0.4248(2)
-	-	Ni$_3$B	-	-	0.5233(2)	0.66170(7)	0.43844(9)
53-7-40	τ$_1$+τ$_2$+τ$_5$	τ$_1$	88.7	11.3	1.045(1)		
-	-	τ$_2$	92.1	7.9	1.0576(4)	1.456(1)	1.460(1)
-	-	τ$_5$	62.1	37.9	-	-	-
56-6-38	τ$_2$+o-Ni$_4$B$_3$	τ$_2$	92.0	8.0	1.0581(1)	1.4565(2)	1.4603(2)
		o-Ni$_4$B$_3$	100	-	1.2104(2)	0.1074(1)	0.656(1)
64-4-32	τ$_1$+Ni$_2$B	τ$_1$	90.0	10.0	1.0578(9)		
-	-	Ni$_2$B	100	-	0.4996(1)	-	0.4251(5)
74-4-22	τ$_1$+Ni$_3$B	τ$_1$	91.0	9.0	1.0508(9)		
-	-	Ni$_3$B	100	-	0.5226(9)	0.661(1)	0.4391(9)
63-24-13	(Ni)+τ$_1$+NiZn (rT)	(Ni)	67.9	32.1	0.3605(2)	-	-
-	-	τ$_1$	87.3	12.8	1.0516(2)	-	-
-	-	NiZn (rT)	57.2	42.8	0.2727(3)	-	0.3205(4)
52-3-45	τ$_2$+τ$_3$+o-Ni$_4$B$_3$	τ$_2$	91	9	-	-	-
-	-	τ$_3$	89	11	-	-	-
-	-	o-Ni$_4$B$_3$	100	-	-	-	-
58-5-37	m-Ni$_4$B$_3$+τ$_2$+Ni$_2$B	m-Ni$_4$B$_3$	100	-			
-	-	τ$_2$	90.4	9.6	1.0538(8)	1.4522(2)	1.4543(2)
-	-	Ni$_2$B	100	-	0.4995(4)	-	0.4249(1)

[1]Lattice parameter of Zn formed during quenching.
[2] low temperature modification NiZn(rT) (due to insufficiently fast quenching of NiZn (hT)).

Appendix:
Supporting Information. X-ray crystallographic file in CIF format, tables on interatomic distances. This material is available free of charge via the Internet at http://pubs.acs.org.

Table I. Comparison of interatomic distances for o-Ni$_4$B$_{3-x}$ (x=0.19) in this work and literature [26]

Bonds	Distance range, nm [1967Run]	Distance range, nm [This work]
Ni1-7B	0.2056(3)-0.236(3)	0.2086(2)-0.2341(2)
-10Ni	0.2482(4)-0.2981(-)	-
-6Ni	-	0.2485(2)- 0.26208(3)
Ni2-6B	0.207(2)-0.220(2)	0.2047(2)-0.2197(2)
-11Ni	0.2515(5)-0.2981(-)	-
-7Ni	-	0.2526(4)-0.26208(3)
Ni3-4B	0.205(2)-0.208(3)	0.2042(1)-0.2106(2)
-10Ni	0.2458(4)-0.2981(-)	-
-8Ni	-	0.24644(3)- 0.2623(1)
Ni4-6B	0.208(2)-0.242(3)	0.2119(2)-0.2247(2)
-11Ni	0.2458(4)-0.2981(-)	-
-7Ni	-	0.2464(3)-0.2623(4)
B1 -5B	0.180(3)-0.301(4)	-
-2B	-	0.1797(2)
-7Ni	0.206(2)-0.221(2)	0.2066(3)-0.2147(3)
B2 -4B	0.2981(-)-0.301(4)	-
-9Ni	0.205(2)-0.242(3)	0.2042(2)-0.2424(2)
B3 -6B	0.173(3)- 0.2981(-)	-
-2B	-	0.1778(2)
-7Ni	0.205(3)-0.220(2)	0.2039(2)-0.2197(2)

Table II. Comparison of interatomic distances for *m*-Ni_4B_3 in this work and literature [26]

Bonds	Distance range, nm [1967Run]	Distance range, nm [This work]
Ni1 -5B	0.204(1)-0.219(2)	0.2059(2)-0.2168(2)
-10Ni	0.2515(3)-0.3074(3)	-
-7Ni	-	0.2520(4)- 0.2638(4)
- Ni*	-	0.2813(4)
- Ni**	-	0.28099(4)
Ni2 -6B	0.207(2)-0.234(1)	0.2081(3)-0.2366(2)
-10Ni	0.2514(5)-0.3074(3)	--
-7Ni	-	0.2518(4)-0.2638(4)
- Ni*	-	0.2813(4)
- Ni**	-	0.28099(4)
B1 -3B	0.185(1)-0.316(2)	-
-2B	-	0.1862(2)-0.1879(3)
-7Ni	0.2037-0.217(1)	0.2072(2)-0.2163(3)
B2 -3B	0.185(1)-0.316(2)	-
-2B	-	0.1862(2)
-8Ni	0.2102(9)-0.235(2)	0.2112(1)-0.2366(2)

Crystal Structure of Novel Ni-Zn Borides;
First Observation of a Boron–Metal Nested Cage Unit: $B_{20}Ni_6$

6.1. Introduction

The system Ce-Ni-Zn-B is part of the multinary Mg-based alloy system Mg-Zn-Mn(Ni)-RE used as high strength lightweight alloys for automotive applications (RE stands for a rare earth element)[1,2]. Although, little is yet known on the influence of nickel-boron additions in these multinary alloys, phase diagram information in terms of an isothermal section at 800°C and a liquidus projection has been provided for the Ni-rich corner of the Ni-Zn-B sub-system by Stadelmaier[3]. The findings of Stadelmaier[3-5] were used in a review of the Ni-Zn-B system by Bhan et al[6]. From the four ternary compounds identified[3, 4], only the crystal structure of the so-called tau-phase with $Cr_{23}C_6$-type ($Ni_{19.5}Zn_{3.5}B_6$) has been defined from X-ray powder and single crystal rotation photographs[5]. Metal borides hitherto are known to form a large variety of compounds, which are characterized by a large diversity of boron to boron bonds, reaching from isolated boron atoms in metal-rich compositions to boron clusters in "high"-boron compounds. Based on the classification of borides with respect to boron-boron aggregation as a function of the boron to metal ratio B/M, boron clusters and frameworks have commonly been observed only at ratios M/B>4 and comprise a quite large variety of regular and/or distorted boron clusters, cages and frameworks such as (i) B_5-pentagonal pyramids in MgB_4[7], (ii) B_4-square units connected by weak B-B bonds to a channel like framework in CrB_4[8] and MnB_4[9] hosting the metal atoms, (iii) B2-units connecting B_6-octahedra in Sm_2B_5[10] (Gd_2B_5[11]-type) borides, (iv) corner-connected boron octahedra B_6 in hexaborides forming a cage accepting large metal atoms[12], (v) corner-linked B_{12} icosahedra through carbon atoms in $Mg_2B_{24}C$[13], (vi) interconnected B_{12} cubooctahedra forming a B_{24} cage centered by metal atoms in dodecaborides[14,15], (vii) eight super-icosahedra $[B_{12}(B_{12})_{12}]$ per unit cell of the hectoborides MB_{66}[16,17] forming a framework that accepts metal atoms as well as additional borons. Icosahedra bonded via

intericosahedral boron bonds create a series of structures such as MgB_7, $Mg_{\sim 5}B_{44}$[18], $MgAlB_{14}$[19] (viii). Four icosahedra of boron atoms are linked by B-B bonds and carbon bridges in $AlB_{24}C_4$[20] (ix). A linear C-B-C chain (B at the centre of symmetry) links B_{12} icosahedra in $Al_{2.1}B_{51}C_8$[21, 22]. The present work intends to elucidate the hitherto unknown crystal structures of the ternary Ni-Zn-B compounds.

6.2. Experimental

Samples in a total amount of ca. 1 g each were prepared from Ni foil (Alfa Aesar, purity >99.8 mass%), zinc granules (Alfa Aesar, purity >99.9 mass%) and boron pieces (ChemPur, Karlsruhe, purity 98 mass%). Zinc drops were purified in an evacuated quartz tube by heating them 50°C below the boiling temperature of Zn (907°C). Samples were prepared from intimate blends of powders of arc melted NiB_x master alloys and fine Zn-filings in proper compositional ratios. The blends were compacted at room temperature in a steel die without lubricants at a pressure of 62 MPa, and were subsequently sealed in quartz tubes under vacuum. Samples were heated to 1150°C, kept at this temperature for 10 minutes, cooled to 800°C at the rate of 1°C/min, annealed at 800°C for 7 days and subsequently quenched in water.

X-ray powder diffraction data were collected from each alloy in as cast and annealed state employing a Guinier-Huber image plate system with monochromatic $CuK_{\alpha 1}$ radiation (8°<2θ<100°). Quantitative Rietveld refinements of the X-ray powder diffraction data were performed with the FULLPROF program[23].

Single crystals were mechanically isolated from crushed alloys. Inspections on an AXS-GADDS texture goniometer assured high crystal quality, unit cell dimensions and Laue symmetry of the specimens prior to the X-ray intensity data collections on a four-circle Nonius Kappa diffractometer equipped with a CCD area detector employing graphite monochromated MoKα radiation (λ=0.071069 nm). Orientation matrices and unit cell parameters were derived using the program DENZO[24]. No absorption corrections were performed because of the rather regular crystal shapes and small dimensions of the investigated specimens. The structures were solved by direct methods and were refined with the SHELXL-97 program[25, 26] within the Windows version WINGX[27].

The as cast and annealed samples were polished using standard procedures and microstructures and compositions were examined by light optical microscopy (LOM) and scanning electron microscopy (SEM) via Electron Probe Micro-Analyses (EPMA) on a Zeiss Supra 55 VP equipped with an EDX system operated at 20 kV. For Ni : Zn ratios the binary compound Ni_2Zn_{11} at the Zn-rich boundary (15 at.% Ni [28]) was used as EPMA standard. The differences between measured and nominal compositions were found to be less than ±1 at. %.

6.3. Results and Discussion

6.3.1. Structural Chemistry

6.3.1.1. Crystal structure of $Ni_{21}Zn_2B_{24}$ – a novel structure type with a metal nested cage $B_{20}Ni_6$

A single crystal suitable for X-ray structure determination was selected from the alloy $Ni_{30}Zn_{40}B_{30}$ (in at %) annealed at 800°C for 7 days. The observed extinctions are consistent with the body centred tetragonal space groups $I4$, $I\bar{4}$, $I4/m$, $I422$, $I4mm$, $I\bar{4}2m$ and $I4/mmm$. Structure solution was possible in space group $I\bar{4}2m$, however, search for missing symmetry prompted the space group $I4/mmm$. Structure refinement in $I4/mmm$ resulted in seven fully occupied metal atom positions and three boron positions yielding a structure formula $Ni_{21}Zn_2B_{24}$. With anisotropic atomic displacement parameters (ADPs) for the metal atoms and isotropic temperature factors for the boron sites the final refinement converged to $R_F^2=0.017$ and residual electron densities smaller than ±1.62e$^-$/Å^3. Structure data are summarized in table 1 and the crystal structure is shown in figures 1 and 2.

The ratio Ni : Zn obtained from the refinement is 91.22 : 8.77 in good agreement with the ratio 91.0 : 9.0 derived from EPMA on the bulk sample. Rietveld refinement of the X-ray powder spectrum confirmed the structure model. The crystal structure of $Ni_{21}Zn_2B_{24}$ - shown in figure 1a in three-dimensional view along [001] - is characterized by B_{20}-units (Figure 1a, c, d) made of two eight-membered corrugated boron rings consisting of B1 and B2 atoms. Two such rings are linked at the four B2 positions via a B3-atom forming a clamp B2-B3-B2 and thereby building a cage around an empty Ni octahedron [Ni_6] (figure 1d), which is nested within the B_{20} unit. The cage as well as the Ni-octahedron is centred at site 2b (½,½,0). These cages

appear to have eight-membered boron rings on all six sides like the faces of a cube. The cages are stacked along [100] directly on top of each other. The boron-boron distances within the ring as well as the B2-B3 distances are 0.177 nm close to the sum of the covalent radii of two boron atoms (R_B=0.088 nm). The distances between the centre of the cage and the surrounding Ni atoms are d_{2b-Ni2} =0.187 nm and d_{2b-Ni6} =0.196 nm and are too short for metal-metal bonds.
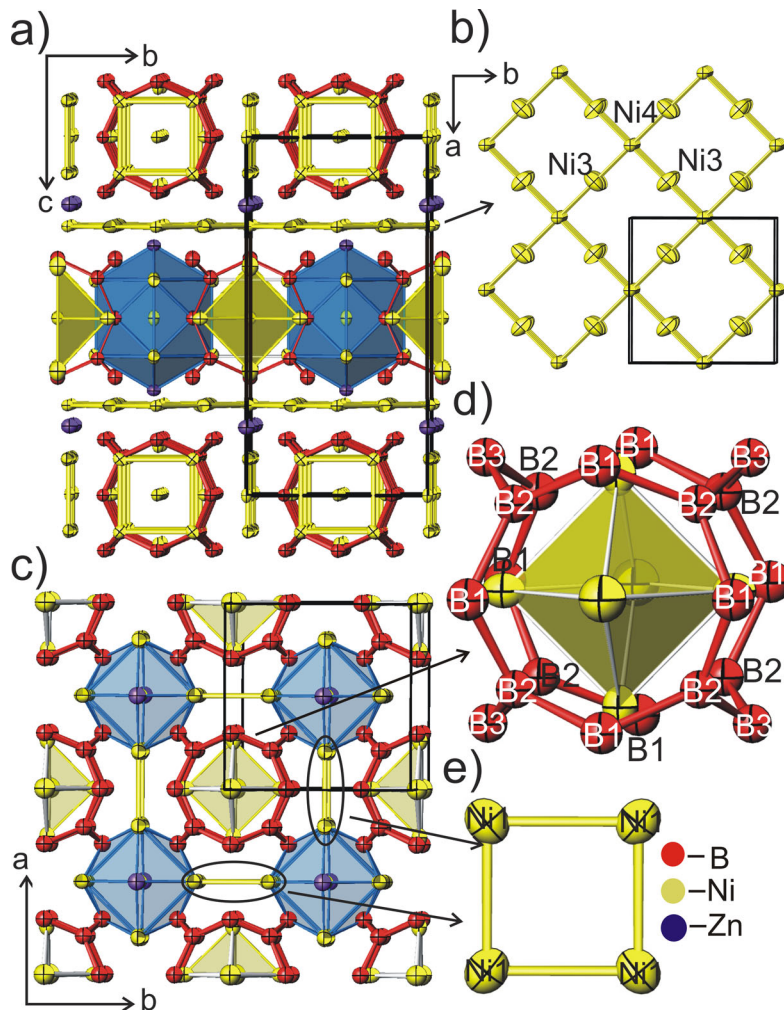
Figure 1. Crystal structure of $Ni_{21}Zn_2B_{24}$; a) perspective view along [100] with anisotropic displacement parameters (for metal atoms) from single crystal refinement; b) infinite Ni layer formed of -Ni3-Ni4-Ni3-atoms parallel (001); c) $Ni_{21}Zn_2B_{24}$ structure as arrangement of i) B_{20}-units nesting empty octahedra [Ni_6], and ii) $Ni5[Ni_8Zn_2B_4]$ polyhedra (for better visualization only the slab within ¼<z<¾ is shown); d) enlarged view of B_{20}-units in combination with empty octahedra [Ni_6]; e) Ni_4 squares around B_{20} unit.

It may be noted here, that stabilities of hyper-coordinated d-block metal atoms centred in planar boron rings MB_n (n = 7, 8, 9, and 10) have recently been explored by density-function theory (DFT) computations[29]. Whereas the B_{20}-units are flanked by squares of Ni1 atoms parallel to (100) and (010) (see figure 1b), a square net formed by Ni3 and Ni4 atoms at a distance of 0.255 nm is attached to B1 (Ni4) and to B1 and B2 (Ni3). The unit cell contains 2 blocks of [Ni_6] nested B_{20}-units, which are linked via B2-B3 bonds to a hexa-capped square prism around Ni5. These blocks are connected by shared infinite planar nets formed of inter-crossed-Ni4-Ni3-Ni4-chains (figure 1b). Along the z-direction, the structure can be viewed as composed of Ni-atom chimneys, which accommodate the columns formed by alternating [Ni_6B_{20}] and $Ni5[Ni_8Zn_2B_4]$ units (figure 1c).

Ni1[Ni_8ZnB_6]   Ni2[Ni_8B_8]   Ni3[$Ni_6Zn_2B_6$]   Ni4[Ni_8B_4]

Ni5[$Ni_8Zn_2B_4$]   Ni6[Ni_4ZnB_8]   Zn1[Ni_{10}]

● — B
● — Ni
● — Zn

B1[Ni_7B_2]   B2[Ni_6B_3]   B3[Ni_7B_2]
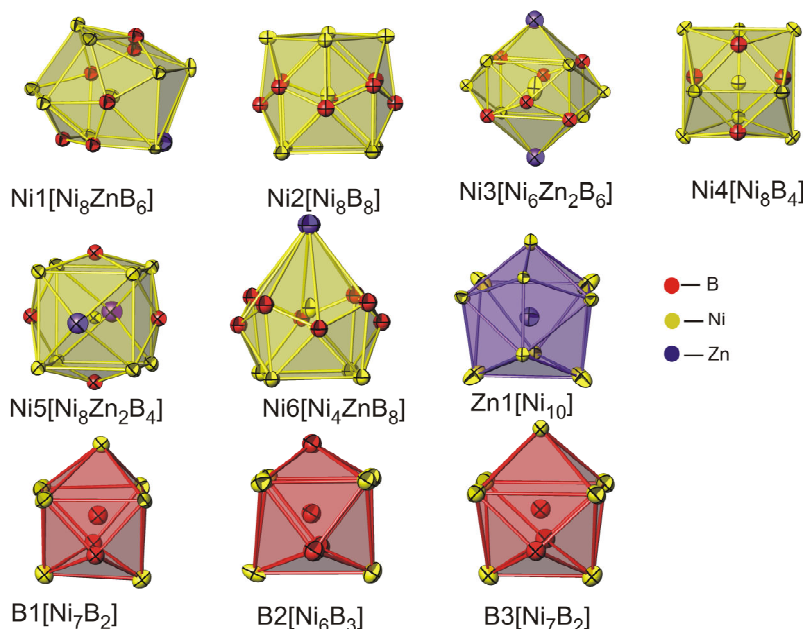
Figure 2. Coordination polyhedra of atoms in $Ni_{21}Zn_2B_{24}$.

The atomic environment for every atom site is depicted in figure 2. Boron atoms are in tricapped trigonal prismatic coordination (CN=9) in which we encounter seven metal atoms (B1 and B3) or six nearest metal neighbours (B2). Due to the smaller affinity of Zn to B with respect to Ni-B, the coordination figures around the boron atoms include only Ni atoms. The range of metal-boron distances from 0.199 to 0.228 is typical for nickel borides[30]. Metal atoms have coordination numbers ranging from 10 to 16, which in some cases form irregularly shaped coordination figures. For instance the coordination polyhedron around the Ni2-atom is a slightly distorted Archimedian

99

antiprism of metal atoms with a zigzag chain of eight boron atoms around its waist. Similarly Zn is at the centre of a bi-capped Archimedian antiprism of metal atoms. Ni3 resides inside a hexa-capped square prism revealing distorted rhombic and triangular faces. The atomic environment of Ni4 is a distorted cuboctahedron. Ni5 is at the centre of a square prism of eight Ni-atoms, with the six faces capped by four B and two Zn atoms. Ni6 atoms reside in a basket formed by a square Ni atom base and a zigzag ring of eight boron atoms capped by a Zn atom. It should be emphasized, that the B_{20}-units are a unique boron aggregation that has never been encountered before in metal-boron chemistry[31].

In view of borides classification, the crystal structure of $Ni_{21}Zn_2B_{24}$, although its boron / metal ratio it only slightly higher than 1, is a new and first example of the combination of a boron cage with a nested empty metal octahedron forming a $B_{20}Ni_6$ unit linking the electron deficient boron atoms in the cage to the metal framework of the crystal structure. It is somewhat surprising that the nested metal octahedron is formed by Ni-atoms, which themselves need to fill their d-shell. In order to fully elucidate this particularly interesting bonding situation, a current investigation focuses on the physico-chemical properties of $Ni_{21}Zn_2B_{24}$ in combination with a DFT calculation of the electronic structure.

6.3.1.2. Crystal structure of $Ni_{12}ZnB_{8-x}$ (x=0.43) with $Ni_{12}AlB_8$ structure type

A single crystal was selected from a crushed as cast sample $Ni_{58.34}Zn_{4.86}B_{36.79}$ (in at %). Systematic extinctions for a C-centered orthorhombic unit cell (a=1.05270(2) nm, b=1.45236(3) nm and c=1.45537(3) nm) resulted in two possible space group types, $C2cb$ (standard setting $Aba2$) and $Cmca$. Structure solution with direct methods was successful in centrosymmetric $Cmca$, the space group of highest symmetry. Refinement - employing anisotropic atomic displacement parameters (ADPs) for the metal atoms and isotropic temperature factors for the boron atoms - converged to R_F^2=0.028 with residual electron densities less than ±2.0 e$^-$/Å^3. With Zn and Ni atoms in thirteen independent and fully occupied positions and nine sites for boron atoms of which the sites for B8 and B9 were occupied at 70% and 65%, respectively, the refinement yielded the composition $Ni_{12}ZnB_{8-x}$ (x=0.43). The ratio Ni : Zn = 92.3 : 7.7 is in accordance with the value 91.6 : 8.4 found by EPMA. Unit cell parameters, crystal symmetry and atom distribution reveal isotypism with the structure type of

$Ni_{12}AlB_8$[32]. Crystallographic data including occupancy, thermal parameters for individual atomic positions are summarized in table 2. Figure 3 portrays the crystal structure of $Ni_{12}ZnB_{8-x}$ in three-dimensional view along [100].
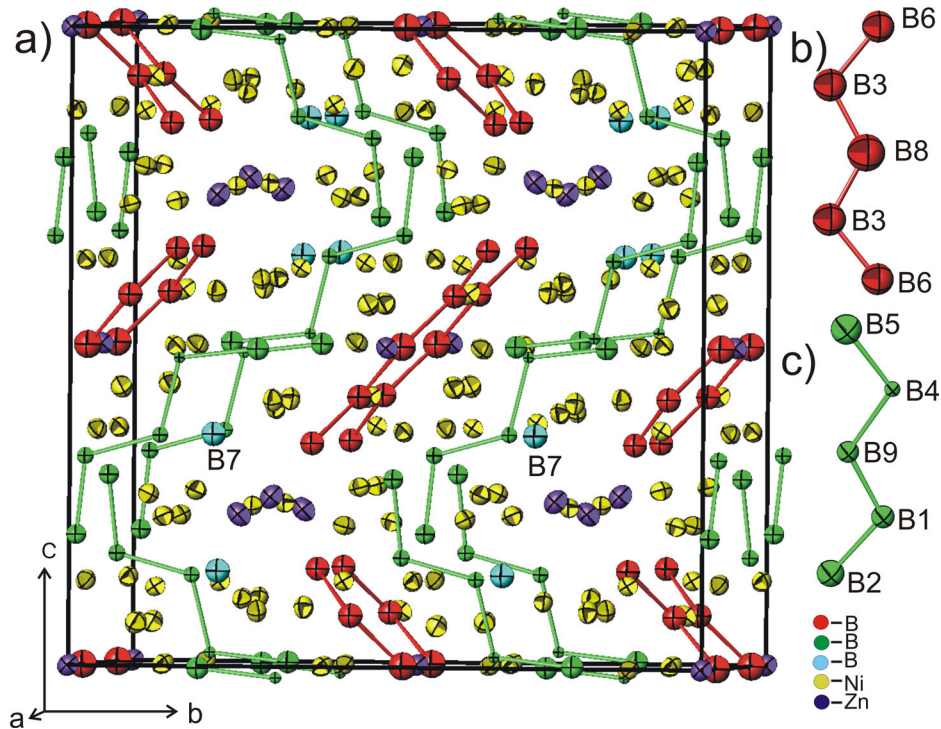
Figure 3. Unit cell of $Ni_{12}ZnB_{8-x}$ (x=0.43), a) showing two types of isolated five-membered boron zigzag chains, b) B6-B3-B8-B3-B6 chain with B-B equidistance 0.180 nm, c) B6-B4-B9-B1-B2 chain with different B-B distances.

As described earlier[32]the structure type of $Ni_{12}AlB_8$ is characterized by a stacking of two layer units alternating along [100]. Both layers are characterized by five-membered boron zig-zag chains running along [011] and [01-1]. Whereas the boron zig-zag orientation is in the bc plane for the layer at x=0, the zig-zag orientation for the layer x=0.5 changes to the plane a - $b\sqrt{2}$. Besides the B-B chains, isolated boron atoms exist in the layer at x=0.5.

B-B distances in the chain $(B_6-B_3-B_8-B_3-B_6)$ parallel to the bc plane are uniformly 0.180 nm, but B-B distances in the chain $(B_5-B_4-B_9-B_1-B_2)$ parallel to the a - $b\sqrt{2}$ plane range from 0.178 to 0.181 nm, all close to the sum of covalent boron radii. The site for B9 is occupied by 65% only and is further bonded to 6 Ni + 1 Zn + 2 B. Whereas Ni1 centres a cube of 8 Ni atoms capped by 4 boron atoms, Ni2 has a waist of boron atoms B3-B8-B3 and B1-B9-B4 (both from the middle part of two different 5-

membered zigzag chains); above and below are squares of metal atoms one of which is capped by a B7-atom (isolated boron atom in the unit cell). Ni3, Ni6 and Ni11 are at the centres of a rather distorted cube with Ni atoms at 8 corners and all 6 faces are capped (by 2 Zn + 4 B atoms). Polyhedra of Ni4, Ni5, Ni7 Ni8, Ni9 and Ni10 form triangular and square faces with 5 boron and 10 metal atoms. Ni11 has 10 metal and 4 B atoms in its polyhedron. Zn1 and Zn2 reside in cuboctahedra with additional boron atoms. For Zn1, one square is capped by one B atom while for Zn2, two boron atoms cap squares (see figure 4a).
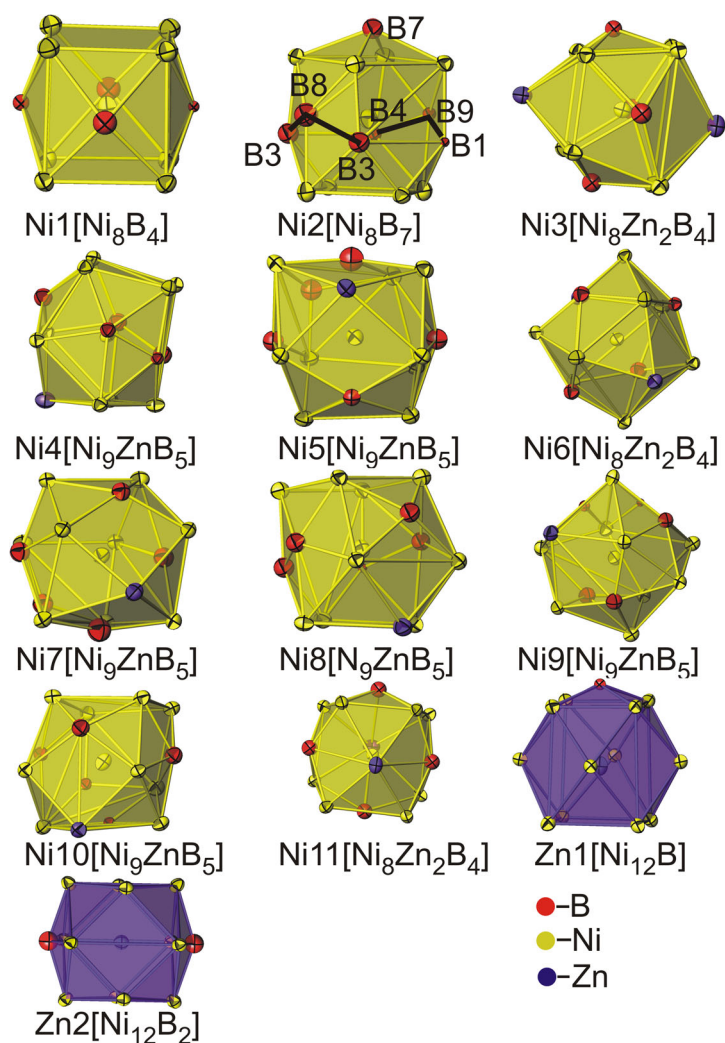
Figure 4a. Coordination polyhedra around Ni and Zn atoms in $Ni_{12}ZnB_{8-x}$ (x=0.43).

For boron coordination see figure. 4b. Whilst B1, B3, B4, B8 and B9 form tricapped trigonal prisms bonding to two boron atoms at a total coordination number 9, atoms B2, B5, B6 and B7 are inside square antiprisms, where one square face is capped by a boron atom for B2, B5, B6 but by a metal atom in case of B7. Isolated boron atoms

(B7) in tetrakaidecahedral metal coordination in combination with boron chain fragments are consistent with the low boron to metal ratio in the structure (B : M = 8 : 13) as a typical feature seen in low-boron structure types[33].
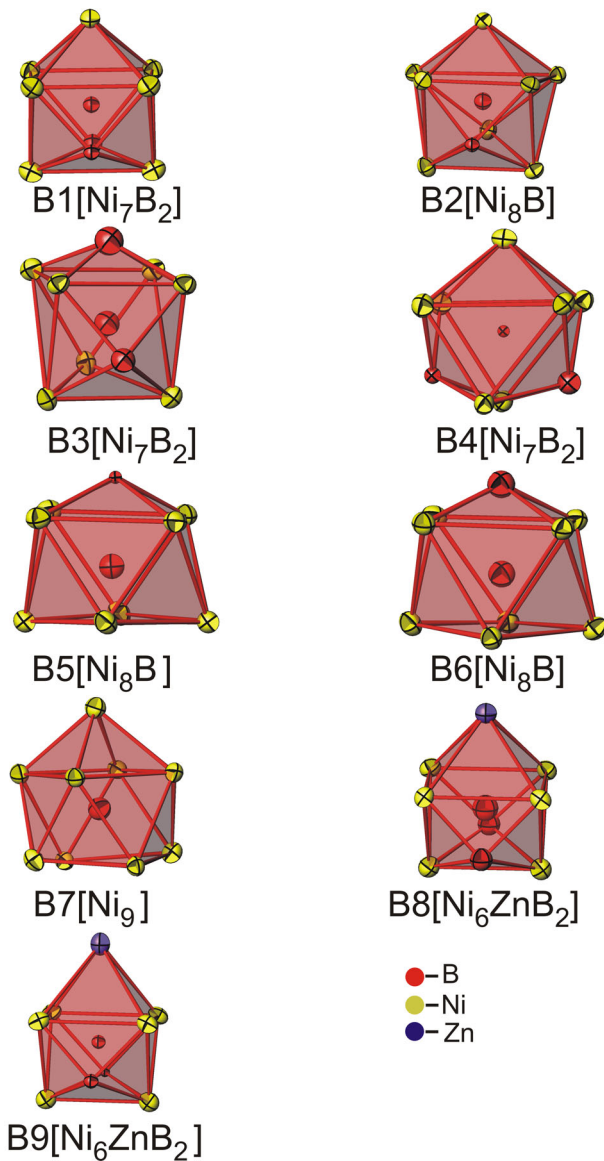
Figure 4b. Coordination polyhedra around B atoms in $Ni_{12}ZnB_{8-x}$ (x=0.43).

6.3.1.3. Crystal structure of Ni_3ZnB_2 – a novel structure type

Single crystals of Ni_3ZnB_2 were grown from an alloy of composition $Ni_{23}Zn_{67}B_{10}$ (in at %) melted at 1150°C, slowly cooled at 0.5°C/min to 970°C and water quenched. The excess of Zn was dissolved in dilute HCl. The observed extinctions are consistent with the C-centred monoclinic space groups $C2/m$, $C2$ and Cm. Structure refinement in $C2/m$ resulted in four fully occupied metal atom positions and two boron positions yielding a new and unique structure type Ni_3ZnB_2. With anisotropic atomic

displacement parameters (ADPs) for the metal atoms and isotropic temperature factors for the boron atoms the final refinement converged to $R_F^2=0.020$ and residual electron densities smaller than ± 1.6 e$^-$/Å^3. X-rays cannot distinguish well between Ni and Zn because both differ by only two electrons; therefore positions of Zn and Ni atoms in the unit cell have been defined with respect to interatomic distances. Structure data are summarized in table 3. The ratio Ni : Zn obtained from the refinement is 75 : 25 in good agreement with the experimental ratio 75 : 25 derived from EPMA on the bulk sample.
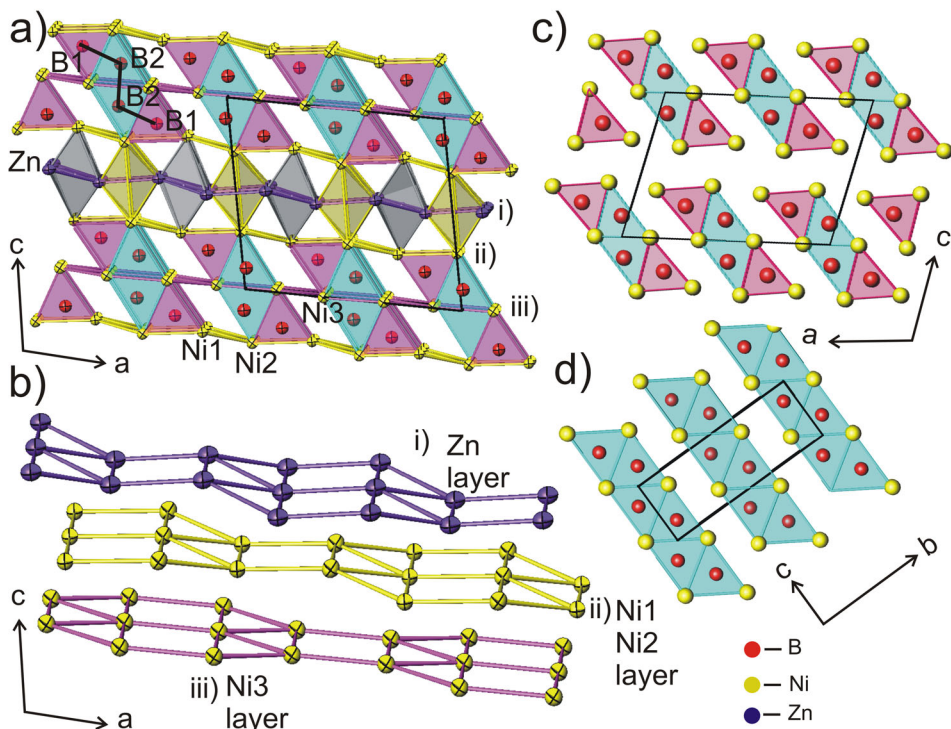
Figure 5. Crystal structure of Ni$_3$ZnB$_2$. a) AlB$_2$-type fragments and four-membered zigzag chains of boron atoms with octahedra around (0,0, ½), and (¾,¾, ½); b) slightly puckered 3^34^2 layers of metal-atoms, c) Dy$_3$Ni$_2$ structure along [010] projection with outlined AlB$_2$-type fragments and four-membered zigzag chains of Ni atoms, d) CrB structure along [100] with AlB$_2$-type fragments containing infinite zigzag chains of B atoms.

Figure 5a shows the unit cell drawn along the *b* axis. Whereas Zn atoms form a continuous and slightly puckered 3^34^2 grid of triangles and rectangles (see figure 5b), coupled triangular prisms around boron atoms resemble the AlB$_2$ structural fragments. Four face-connected triangular prisms form a B$_4$-zigzag chain unit (figure 5a). The B-B distances (d$_{B1-B2}$ = 0.1833 nm and d$_{B2-B2}$ = 0.1855 nm) are consistent with the sum of B-B atomic radii. The same kind of B4-units have been observed in the structure types of Mo$_2$IrB$_2$[34] and αCr$_2$IrB$_2$[35]. The coordination figures of all crystallographic sites are

summarized in figure 6. The polyhedron for the Zn-site has one boron and 12 metal atoms in a distorted penta-capped square prism remotely reminding the shape of a rhombododecahedron with one missing atom. The Ni1 atom has three boron and 11 metal atoms forming a distorted cube-octahedron. Ni2 has four boron and 11 metal atom neighbors resulting in a polyhedron with triangular and square faces. The atom environment of Ni3 accounts 7 boron and 10 Ni atoms. B1 and B2 atoms center a tricapped prism (CN=9, see figure 6).

$Ni1[Ni_8Zn_3B_3]$ $Ni2[Ni_7Zn_4B_4]$

$Ni3[Ni_{10}B_7]$ $Zn1[Ni_7Zn_5B]$

$B1[Ni_7ZnB]$ $B2[Ni_7B_2]$

     — B
     — Ni
     — Zn
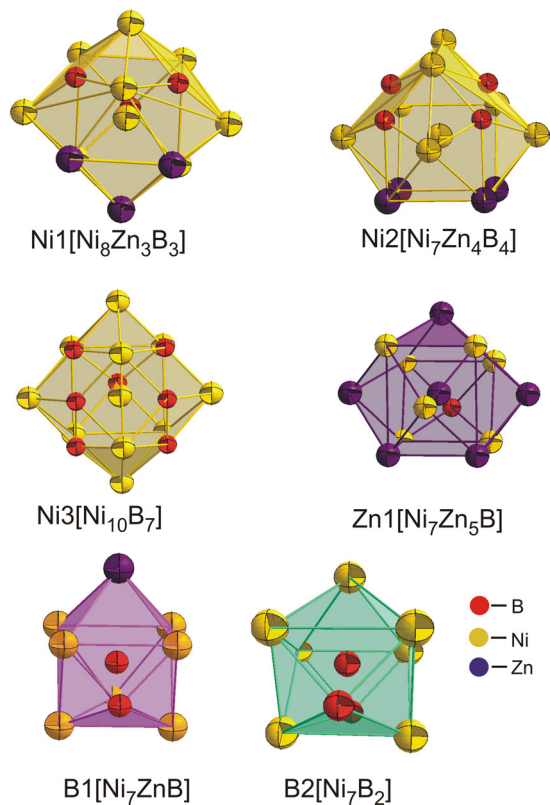
Figure 6. Coordination polyhedra for the Ni_3ZnB_2 structure.

The Ni_3ZnB_2 structure is related to Dy_3Ni_2[36] where infinite columns of face-sharing mono-caped triangular prisms $Ni[Dy_6]$ are running along the *b*-direction. Both structures, Dy_3Ni_2 and Ni_3ZnB_2 originate from the CrB-type structure which in turn is an intergrowth structure of AlB_2 and W fragments consisting of infinite planar layers of face-connected triangular prisms alternating with the columns of face-linked empty tetrahedra and empty tetragonal pyramids. In case of Ni_3ZnB_2, due to insertion of the puckered 3^34^2 layers of metal atoms, their rectangular prism faces are coupled by empty octahedra. The shortest distances between octahedral centers and metal ligands

are only 0.13 - 0.14 nm and therefore these void are too small to accommodate any interstitial atom.

6.4. *Conclusion*

The crystal structures of three ternary Ni-Zn borides have been elucidated by means of X-ray single crystal and powder diffraction techniques assisted by electron microprobe analyses defining the Ni/Zn ratio. B-B bonds manifest unique structure formations in the Ni-Zn borides. The structure of $Ni_{21}Zn_2B_{24}$ is the first example for characteristic isolated cages of B_{20}-units composed of two octogonal boron rings that are fused at four positions by boron atoms. All boron atoms are at a distance of 0.177 nm from one another. As a new feature, a Ni_6-octahedron is nested within the B_{20}-cage. The crystal structure of $Ni_{12}ZnB_{8-x}$ (x=0.43) is isotypic with $Ni_{12}AlB_8$ and reveals finite zigzag chains of five boron atoms. Ni_3ZnB_2 adopts a unique structure type with fragments of B_4-zig-zag chains with B-B bond lengths of 0.180 nm. The compound Ni_3ZnB_2 crystallizes in a unique structure type with characteristic B_4 zig-zag chain fragments at a B-B bond distance of 0.180 nm.

6.5. Associated Content

Supporting Information. X-ray crystallographic file in CIF format, tables on interatomic distances. This material is available free of charge via the Internet at http://pubs.acs.org.

6.7. References

(1)   Moreno, I.P.; Nandy, T.K.; Jones, J.W.; Allison, J.E.; Pollock, T.M. Scripta Mater. **2003**, 48, 1029-1034.

(2)   Kang, Y.-B.; Pelton, A.D.; Chartrand, P.; Spencer, P.; Fuerst, C.D. Journal of Phase Equilibria Diffusion **2007**, 28, 242.

(3)   Stadelmaier, H.H.; Schöbel J.-D.; Jordan, L.T. Metall. **1962**, 16, 752-754.

(4)   Stadelmaier, H.H.; Yun, T.S. Z. Metallkde **1962**, 53, 754-756.

(5)   Stadelmaier, H.H.; Draughn, R.A.; Hofer G. Z. Metallkde **1963**, 54, 640-644.

(6)   Bhan, S.; Singh, S.; Lal, A. J Alloy Phase Diagrams (India) **1990**, 3, 147-152.

(7)   Guette, A.; Naslain, R.; Galy, J. C. R. Acad. Sc. Paris **1972**, 275, 41-44.

(8)   Ansersson, S.; Lundström, T. Acta Chem. Scand. **1968**, 24, 1791-1799.

(9)   Ansersson, S, Carlsson, J-O. Acta Chem. Scand. **1970**, 22, 3103-3110.

(10)   Zavalii, L.V.; Kuz'ma, Y.B.; Mikhalenko, S.I. Translated from Poroshkova Metallurgiya **1990**, 6(330), 61-63.

(11)   Schwarz, S.; Simon, A. Z. Naturforsch. **1987**, 42b, 935-939.

(12)   Schell, S.; Winter, H.; Riestschel, H.; Gompf, F. Physical Review B **1982**, 25, 1589-1599.

(13)   Adasch, V.; Hess, K-U.; Ludwig, T.; Vojteer, N.; Hillebrecht, H. Journal of Solid State Chemistry **2006**, 179, 2150-2157.

(14)   Leithe-Jasper, A.; Sato, A.; Tanaka. T. Z. Kristallogr. NCS **2002**, 217, 319-320.

(15)   Matkovich, V.I.; Economy, J.; Giese, R.F.; Barrett, R. Acta Crystallogr. **1965**, 19, 1056-1058.

(16)   Richards, S.M.; Kasper, J.S. Acta Crystallogr. **1969**, B25, 237-251.

(17)   Perkins, C.L.; Trenary, M. Physical Review Letters. **1996**, 77, 1772-4775.

(18)   Pediaditakis, A.; Schroeder, M.; Sagawe, V.; Ludwig, T.; Hillebrecht, H. Inorg. Chem. **2010**, 49, 10882-10893.

(19)   Matkovich, V.I.; Economy, J. Acta Crystallogr. **1970**, B26, 616-621.

(20)   Will, V.G. Acta Crystallogr. **1969**, B25, 1219-1222.

(21)   Perrotta, A.J.; Townes, W.D.; Potenza, J.A. Acta Crystallogr. **1969**, B25, 1223-1229.

(22)   Meyer, F.D.; Hillebrecht, H. High Temperature Materials Chemistry, Pt. 1, **2000,** 161-164.

(23)   Roisnel, T.; Rodriguez-Carvajal, J. Materials-Science-Forum, **(1) 2010,** 118, 378-381.

(24)   Nonius Kappa CCD Program Package COLLECT, DENZO, SCALEPACK, SORTAV, Nonius Delft, The Netherlands, **1998**.

(25)   Sheldrick, G.M. SHELXS-97, Program for Crystal Structure Refinement University of
         Göttingen, Germany; Windows version by Mc Ardle, Natl. Univ. Ireland, Galway, **1997**.

(26)   Sheldrick, G.M. Acta Crystallogr. **2008, A64,** 112-122.

(27)   Farrugia, L.J. J. Appl. Crystallogr **1999**, 32, 837-838.

(28)   Johansson, A.; Ljung, H.; Westman, S. Acta Shem. Scand., **1968**, 22, 2743-2753.

(29)   Pu, Z.; Ito, K.; Schleyer, P.v.R.; Li, Q. Inorg. Chem. **2008**, 48, 10679-10686.

(30)   Rundqvist, S.; Pramatus, S. Acta Chemica Scandinavica **1967**, 21, 191-194.

(31)   Rogl, P. Borides with Boron Chains, in Inorganic Reactions and Methods: Formation of Bonds to Group-I, -II, and -IIIB Elements, Volume 13 (eds J. J. Zuckerman and A. P. Hagen), John Wiley & Sons, Inc., Hoboken, NJ, USA, 1991.

(32)   Ade, M.; Kotzot, D.; Hillebrecht, H.; Journal of Solid State Chemistry **2010**, 183, 1790-1797.

(34)   Rogl, P.; Nowotny, H. Monatsh. Chem. **1973**, 104, 1325-1332.

(35)   Kotzot, D.; Ade, M.; Hillebrecht, H. Solid State Science **2008**, 10, 291-302.

(36)   Moreau, J.M.; Paccard. D.; Parthé. E. Acta Crystallogr. **1974**, B30, 2583-2586.

(37)   Parthé, E.; Gelato, L.; Chabot, B.; Penzo, M.; Censual, K.; Gladyshevskii, R. TYPIX—Standardized Data and Crystal Chemical Characterization of Inorganic Structure Types, Berlin, Springer, **1994**.

Table1. Structural data for $Ni_{21}Zn_2B_{24}$

Alloy composition (at%)[b]	$Ni_{30}Zn_{40}B_{30}$
Ni:Zn atomic ratio, EPMA/refinement	91:9 / 91.2: 8.8
Formula from refinement	$Ni_{21}Zn_2B_{24}$
Structure type	$Ni_{21}Zn_2B_{24}$
Space group	*I4/mmm*; No. 139[a]
θ-range; sets; frames; time/frame	$2.85 < \theta < 36.27$; 7; 403; 200 sec
a [nm]	0.72103(1)
c [nm]	1.42842(5)
Volume (nm)	74.261(3)
Z	2
Data collection/ λ (nm)	MoK_α radiation/ 7.1073
Crystal size [μm]	20×30×45
Mosaicity	0.59
Reflections in refinement	493 $F_o > 4\sigma(F_o)$ of 561
Number of variables	34
$R_F{}^2 = \Sigma|F_0{}^2 - F_c{}^2|/\Sigma F_0{}^2$	0.017
R_{Int}	0.064
GOF	0.685
Extinction (Zachariasen)	0.00070(5)
Ni1 in 16*n* (0, *y*, *z*); Occ.	*y*=0.30020(5), *z*=0.10062(3); 1.00(1)
U_{11}[c]; U_{22}; U_{33}; U_{23}; $U_{13} = U_{12} = 0$	0.0042(2); 0.0059(2); 0.0063(2); -0.0010(1)
Ni2 in 8*j* (*x*, ½, 0); Occ.	*x*=0.24032(8); 1.00(1)
U_{11}; U_{22}; U_{33}; $U_{23} = U_{13} = U_{12} = 0$	0.0068(2); 0.0042(2); 0.0049(2)
Ni3 in 8*f* (¼, ¼, ¼); Occ.	1.00(1)
$U_{11} = U_{22}$; U_{33}; $U_{23} = U_{13}$; U_{12}	0.0113(2); 0.0053(2); -0.0003(1); 0.0051(2)
Ni4 in 4*d* (0,½,¼); Occ.	1.00(1)
$U_{11} = U_{22}$; U_{33}; $U_{23} = U_{13} = U_{12} = 0$	0.0048(2); 0.0043(3)
Ni5 in 2*a* (0, 0, 0); Occ.	1.00(1)
$U_{11} = U_{22}$; U_{33}; $U_{23} = U_{13} = U_{12} = 0$	0.0034(2); 0.007(4)
Ni6 in 4*e* (0,0,*z*); Occ.	*z*=0.36216(5); 1.00(1)
$U_{11} = U_{22}$; U_{33}; $U_{23} = U_{13} = U_{12} = 0$	0.0043(2); 0.0069(3)
Zn1 in 4*e* (0, 0, *z*); Occ.	*z*=0.19029(5); 1.00(1)
$U_{11} = U_{22}$; U_{33}; $U_{23} = U_{13} = U_{12} = 0$	0.0090(2); 0.0073(3)
B1 in 16*n* (0, *y*, *z*); Occ.; U_{iso}[d]	*y*=0.2984(4); *z*=0.3453(2) 1.00(1); 0.0061(5)
B2 in 16*m* (*x*, *x*, *z*); Occ.; U_{iso}	*x*=0.2929(3), *z*=0.1059(2) 1.00(1); 0.0052(5)
B3 in 16*l* (*x*, *x*, 0); Occ.; U_{iso}	*x*=0.2025(4); 1.00(1); 0.0052(6)
Residual electron density; max; min in [electrons/nm³] x1000	1.62; -1.02

[a]crystal structure data are standardized using the program Structure Tidy[37].
[b]nominal composition of the alloy from which a single crystal was isolated.
[c]anisotropic atomic displacement parameters U_{ij} in [10^2 nm²].
[d]isotropic atomic displacement parameters U_{iso} in [10^2 nm²].

Table 2. Structural data for $Ni_{12}ZnB_{8-x}$ (x=0.43).

Alloy composition (at%)[b]	$Ni_{58.34}Zn_{4.86}B_{36.79}$
Ni:Zn atomic ratio, EPMA/refinement	91.6: 8.4/ 92.3: 7.7
Formula from refinement	$Ni_{12}ZnB_{8-x}$ (x=0.43)
Structure type	$Ni_{12}AlB_8$
Space group	*Cmca*; No. 64 [a]
θ-range; sets; frames; time/frame	$2.77 < \theta < 34.99$; 7; 516; 200 sec/frame
a; b; c [nm]	1.05270(2); 1.45236(3); 1.45537(3)
Volume (nm)	222.511(8)
Z	1
Data collection/ λ (nm)	MoK_α radiation/ 7.1073
Crystal size [μm]	25×30×40
Mosaicity	0.48
Reflections in refinement	1823 $F_o >4\sigma(F_o)$ of 2554
Number of variables	129
$R_F^2 = \Sigma|F_0^2-F_c^2|/\Sigma F_0^2$	0.028
R_{Int}	0.060
GOF	1.037
Extinction (Zachariasen)	0.00017(1)
Ni1 in 8*f* (0, *y, z*); Occ. U_{11}; U_{22}; U_{33}; U_{23}; $U_{13}=U_{12}=0$	*y*=0.42251(4), *z*=0.08096(4); 1.00(1) 0.0083(3); 0.0102(3); 0.0092(3); -0.0022(2)
Ni2 in 16g (*x, y, z*); Occ.; U_{11}[c]; U_{22}; U_{33}; U_{23}; U_{13}; U_{12}	*x*=0.37254(5), *y*=0.06824(3), *z*=0.06440(3); 1.00(1) 0.0112(2); 0.0096(2); 0.0104(2); 0.0008(2); 0.0004(2); 0.0005(1)
Ni3 in 8*f* (0, *y, z*); Occ. U_{11}; U_{22}; U_{33}; U_{23}; $U_{13}=U_{12}=0$	*y*=0.13668(4), *z*=0.12413(4); 1.00(1) 0.0092(3); 0.0081(3); 0.0074(3); 0.0007(2)
Ni4 in 16g (*x, y, z*); Occ.; U_{11}; U_{22}; U_{33}; U_{23}; U_{13}; U_{12}	*x*=0.13373(4), *y*=0.42087(3), *z*=0.22086(3); 1.00(1) 0.0087(2); 0.0099(2); 0.0075(2); -0.0006(2); -0.0003(2); 0.0014(2)
Ni5 in 16g (*x, y, z*); Occ.; U_{11}; U_{22}; U_{33}; U_{23}; U_{13}; U_{12}	*x*=0.16955(4), *y*=0.00959(3), *z*=0.13227(3); 1.00(1) 0.0096(2); 0.0080(2); 0.0088(2); 0.0008(2); 0.0014(2); 0.0003(2)
Ni6 in 8*f* (0, *y, z*); Occ.; U_{11}; $U_{22}=U_{33}$; U_{23}; $U_{13}=U_{12}=0$	*y*=0.38296(4), *z*=0.36934(4); 1.00(1) 0.0089(3); 0.0078(3); -0.0002(2)
Ni7 in 16g (*x, y, z*); Occ.; $U_{11}=U_{22}$; U_{33}; U_{23}; U_{13}; U_{12}	*x*=0.16960(4), *y*=0.13245(3), *z*=0.00178(3); 1.00(1) 0.0096(2); 0.0088(2); 0.0017(2); 0.0005(2); 0.0015(2)
Ni8 in 16g (*x, y, z*); Occ.; U_{11}; U_{22}; U_{33}; U_{23}; U_{13}; U_{12}	*x*=0.13588(4), *y*=0.28315(3), *z*=0.08587(3); 1.00(1) 0.0089(2); 0.0079(2); 0.0106(2); -0.00003(15); -0.0011(2); -0.0002(2)
Ni9 in 16g (*x, y, z*); Occ. U_{11}; U_{22}; U_{33}; U_{23}; U_{13}; U_{12}	*x*=0.36810(4), *y*=0.23615(3), *z*=0.10344(3); 1.00(1) 0.0108(2); 0.0073(2); 0.0088(2); 0.0005(2); 0.0019(2); 0.0008(2)
Ni10 in 16*g* (*x, y, z*); Occ. U_{11}; U_{22}; U_{33}; U_{23}; U_{13}; U_{12}	*x*=0.13440(4), *y*=0.11128(3), *z*=0.26854(3); 1.00(1) 0.0120(2); 0.0093(2); 0.0081(2); -0.0004(2); 0.0005(2); -0.0016(2)
Ni11 in 8*e* (¼, *y*, ¼); Occ. U_{11}; U_{22}; U_{33}; U_{13}; $U_{23}=U_{12}=0$	*y*=0.26391(4); 1.00(1) 0.0090(3); 0.0075(3); 0.0078(3); 0.00058(2)
Zn1 in 8*f* (0, *y, z*); Occ. U_{11}; U_{22}; U_{33}; U_{23}; $U_{13}=U_{12}=0$	*y*=0.26794(4), *z*=0.23828(4); 1.00(1) 0.0098(3); 0.0111(3); 0.0117(3); -0.0025(2)
Zn2 in 4*a* (0, 0, 0); Occ. U_{11}; $U_{22}= U_{33}$; U_{23}; $U_{13}=U_{12}=0$	1.00(1) 0.0097(4); 0.0096(4); 0.0011(3)
B1 in 8*f* (0, *y, z*); Occ.; U_{iso}[d]	*y*=0.0249(4), *z*=0.3280(4); 1.00(1); 0.012(1)
B2 in 8*f* (0, *y, z*); Occ.; U_{iso}	*y*=0.0113(4), *z*=0.2053(4); 1.00(1); 0.0082(10)

110

B3 in 16g (*x, y, z*); Occ.; U_{iso}	*x*=0.1906(4), *y*=0.4256(3), *z*=0.0792(3); 1.00(1); 0.0093(7)
B4 in 8f (0, *y, z*); Occ.; U_{iso}	*y*=0.1727(4), *z*=0.4824(4); 1.00(1); 0.011(1)
B5 in 8f (0, *y, z*); Occ.; U_{iso}	*y*=0.2958(4), *z*=0.4969(4); 1.00(1); 0.010(1)
B6 in 16g (*x, y, z*); Occ.; U_{iso}	*x*=0.2987(4), *y*=0.3624(3), *z*=0.1514(3); 1.00(1); 0.0092(7)
B7 in 16g (*x, y, z*); Occ.; U_{iso}	*x*=0.2115(4), *y*=0.1546(3), *z*=0.1426(3); 1.00(1); 0.0121(8)
B8 in 8d (*x*, ½, 0); Occ.; U_{iso}	*x*=0.2722(7); 0.70(2); 0.007(2)
B9 in 8f (0, *y, z*); Occ.; U_{iso}	*y* =0.1428(6), *z*=0.3615(5); 0.65(2); 0.008(2)
Residual electron density; max; min in [electrons/nm³] x1000	2.01; -1.49

[a]crystal structure data are standardized using the program Structure Tidy[37].
[b]nominal composition of the alloy from which a single crystal was isolated.
[c]anisotropic atomic displacement parameters U_{ij} in $[10^2 \ nm^2]$
[d]isotropic atomic displacement parameters U_{iso} in $[10^2 \ nm^2]$.

Table 3. Crystal structure data for Ni_3ZnB_2

Alloy composition (at%)[b]	$Ni_{23}Zn_{67}B_{10}$
Ni:Zn atomic ratio, EPMA/refinement	75:25 / 75:25
Formula from refinement	$Ni_{50}Zn_{16.66}B_{33.34}$
Structure type	Ni_3ZnB_2
Space group	$C2/m$; No. 12 [a]
θ -Range [°]; sets; frames; time/frame	$2.46 < \theta < 35.60$; 6, 335, 335 sec
a [nm]	0.95101(4)
b [nm]	0.2892(4)
c [nm]	0.84366(3)
β [°]	101.097(3)
Volume (nm)	22.77(3)
Z	4
Data collection/ λ (nm)	MoK_α radiation/ 7.1073
Crystal size [μm]	25x35x40
Mosaicity	0.48
Reflections in refinement	527 $F_o > 4\sigma(F_o)$ of 593
Number of variables	34
$R_F^2 = \Sigma|F_0^2 - F_c^2|/\Sigma F_0^2$	0.020
R_{Int}	0.058
GOF	0.692
Extinction (Zachariasen)	0.0129(7)
Ni1 in $4i$ (x, 0, z); Occ.	x =0.21879(5), z=0.25127(6); 1.00(1)
U_{11}; U_{22}; U_{33}; U_{13}; $U_{23}=U_{12}=0$	0.0041(2); 0.0058(2); 0.0041(2); 0.0008(1)
Ni2 in $4i$ (x, 0, z); Occ.	x =0.49680(5), z=0.28968(6); 1.00(1)
U_{11}; U_{22}; U_{33}; U_{13}; $U_{23}=U_{12}=0$	0.0049(2); 0.0053(2); 0.0051(2); 0.0013(1)
Ni3 in $4i$ (x, 0, z); Occ.	x =0.63894(5), z=0.00305(6); 1.00(1)
U_{11}; U_{22}; U_{33}; U_{13}; $U_{23}=U_{12}=0$	0.0050(2); 0.0052(2); 0.0049(2); 0.0008(1)
Zn1 in $4i$ (x, 0, z); Occ.	x =0.13845(5), z=0.52534(5); 1.00(1)
U_{11}; U_{22}; U_{33}; U_{13}; $U_{23}=U_{12}=0$	0.0068(2); 0.0080(2); 0.0045(2); 0.0013(1)
B1 in $4i$ (x, 0, z); Occ.; U_{iso} [d]	x =0.1550(5), z=0.8151(5); 1.00(1); 0.0062(7)
B2 in $4i$ (x, 0, z); Occ.; U_{iso}	x =0.0145(5), z=0.1119(5); 1.00(1); 0.0069(7)
Residual electron density; max; min in [electrons/nm³] x1000	1.59; -1.33

[a] crystal structure data are standardized using the program Structure Tidy[37].
[b] nominal composition of the alloy from which a single crystal was isolated.
[c] anisotropic atomic displacement parameters U_{ij} in $[10^2 \ nm^2]$.
[d] isotropic atomic displacement parameters U_{iso} in $[10^2 \ nm^2]$.

The crystal structure of Ni-Zn co-doped
β boron $Ni_{0.19}Zn_{1.24}B_{34.22}$

7.1. Introduction

Elemental boron is well known to form a three-dimensional framework of covalently bonded boron clusters in the structure providing a series of voids which readily accommodate metal atoms [1]. Due to the strong covalent bonds, the so-called β-rhombohedral-boron high temperature modification ($T_m(ßB)$ = 2072°C [2]) and its solid solutions with transition metals exhibit high (Vickers) hardness around 40 GPa as well as high corrosion and acid resistance [3]. Selective occupation of transition metal atoms such as V, Cr, Co, Fe in various voids of the ßB-framework served as a tool to increase the conductivity and to render p-type ßB into n-type semiconducting behaviour [4]. A series of reports deal with (i) the crystal structure of ßB [5, 6, 7 8, 9, 10, 11], (ii) the electron counting rules [12,13], (iii) geometrical frustrations [14] and (iv) the charge self-compensation phenomenon of several solid solutions of metal atoms in β-rhombohedral boron [14]. One of the most detailed investigations of the crystal structure of pure β-rhombohedral boron is due to Slack et al. [9], who also coined the 'displacive' effect of doping in β-B by various metals [10]. A systematic catalogue with respect to size and coordination of voids in the boron framework, labelled as A_1, D, E, S_1, etc., is due to Lundström and co-workers [15, 16] and was later adopted by Slack et al. [9, 10]. Fig. 1 shows the arrangements of boron atoms around the void sites A_1, D, D_d and E. D_d was called "disordered void" as its atomic coordination varies with the type of dopant in ßB.
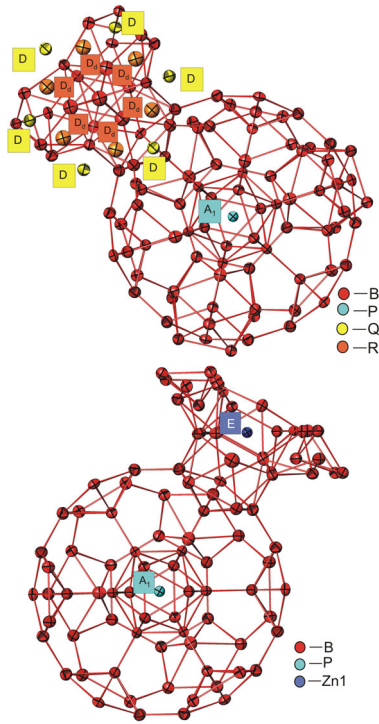
Figure 1. E, A_1, D, and D_d holes in β boron structure. E-void; Zn1 atoms, A_1-void; P atoms with a mix of 0.414Zn2 and 0.076Ni1. , D-void; Q atoms (0.254Zn3 and 0.047Ni2) and R (0.118Zn4 and 0.022Ni3).

The incorporation of Zn in the framework of ßB was studied by Kuzma et al. [17] and by Korsukova et al. [18], who claimed $ZnB_{\sim22}$ (~4.3 at.%Zn) as the solubility limit of Zn in βB in the temperature interval from 600 to 907 ºC. Below 600 ºC the solid solution was reported to terminate at ~3 at.% Zn with slightly reduced lattice parameters. The solid solution of Ni in β-rhombohedral boron $NiB_{48.5}$ was investigated by Lundström et al. [11] and Slack et al. [10], the latter paper comprising a detailed structural chemical study of the dopant incorporation in ßB for the compositions ScB_{80}, ScB_{64}, TiB_{52}, VB_{167}, VB_{63}, CrB_{95}, CrB_{69}, CrB_{67}, MnB_{135}, FeB_{89}, CoB_{65}, NiB_{137}, NiB_{112}, $NiB_{60,}$ CuB_{386}, CuB_{129}, ZrB_{143}, NbB_{200}, HfB_{240}, HfB_{50} and TaB_{96}.

As the multinary Mg-based alloy system Mg-Zn-Mn-RE (RE is a rare earth element) is of high importance in view of high strength lightweight alloys for automotive applications [19], we have recently focused on two quaternary systems, Ce-Ni-Zn-B and Ce-Ni-Zn-Si, because nothing is yet known on the influence of grain refining Ni, Si, B additions to the Mg-based alloy system. Whilst the small transition metal atoms readily dissolve in ßB, hitherto no solubility has been observed for the larger atoms such as the rare earth elements. For the system Ce-Ni-Zn-B we thus expect a significant combined

solubility of Ni and Zn in ßB. Consequently the present work intends to employ X-ray single crystal structure and EPM analyses in order to elucidate details on the site occupation and the void-filling mechanism of combined nickel and zinc in the solid solution of beta rhombohedral boron and the self-compensation of the solid solution of Ni-Zn co-doped β boron. Comparison will be made with the crystal structures of binary NiB_{60} [10], $NiB_{48.5}$ [11] and ZnB_{25} [17]. Particularly the high residual value of R=0.108 in the structure determination of ZnB_{25} [17] did not allow to detect all details of Zn incorporation and its impact on the ßB framework.

7.1. Experimental

Several alloys in a total amount of about 0.5 g each were prepared from Ni foil (Alfa Aesar, purity >99.9 mass%), zinc granules (Alfa Aesar, purity >99.9 mass%) and boron pieces (ChemPur, Karlsruhe, purity 98 mass%). Zinc drops were purified in an evacuated quartz tube by heating them below the boiling temperature of Zn (907°C). Intimate powder blends of an arc melted NiB_x master alloy and fine Zn-filings in proper compositional ratios were cold compacted in a steel die without lubricants, vacuum sealed in quartz tubes and heated up till melt and then annealed at 800 °C for 7 days and subsequently water quenched. In order to check on the incorporation of the Ni-homologues, Pd and Pt in ßB, we prepared two samples, Pd_8B_{92} and Pt_4B_{96} (in at. %) from powders of Pd (Alfa Aesar, purity >99.9 mass%), Pt (Alfa Aesar, purity >99.9 mass%) and crystalline boron of 99% purity (H.C. Starck). The powder blends were cold pressed and sintered in a W-heated high vacuum furnace at 1500°C for 12 hours and then cooled down to 1250°C and annealed at this temperature for 36 hours. A part of the sintered samples were argon arc melted on a water-cooled copper hearth. Again heating to 1500°C for 12 hours and annealing at 1250°C for 36 hours was performed in order to ensure the solubility of Pd and Pt in B.

X-ray powder diffraction data were collected from each alloy in as cast and annealed state employing a Guinier-Huber image plate system with monochromatic $CuK_{\alpha 1}$ radiation (8º<2θ<100º). Quantitative Rietveld refinements of the X-ray powder diffraction data were performed with the FULLPROF program [20]. Single crystals of NiZn-ßB were mechanically isolated from crushed specimens prepared and annealed as described above. Inspection on an AXS-GADDS texture goniometer assured crystal

quality, unit cell dimensions and Laue symmetry of the specimens prior to the X-ray intensity data collections on a four-circle Nonius Kappa diffractometer equipped with a CCD area detector employing graphite monochromated Mo Kα radiation (λ=0.071069 nm). Orientation matrices and unit cell parameters were derived using the program DENZO [21]. No additional absorption corrections were performed because of the rather regular crystal shapes, the small dimensions of the investigated specimens and the low linear absorption coefficient for Mo Kα radiation. The structure was solved by direct methods and was refined with the SHELXL-97 program [22, 23]within the Windows version WINGX [24].

The annealed samples were polished using standard procedures and microstructures and compositions were examined by light optical microscopy (LOM) and scanning electron microscopy (SEM) via Electron Probe Micro-Analyses (EPMA) on a Zeiss Supra 55 VP equipped with EDX and WDX systems operated at 20 kV. The binary compound Ni_2Zn_{11} at the Zn-rich boundary (15 at.% Ni) [25] served as EPMA standard to define the Ni : Zn ratio and pure Pt and Pd was used as a standard for PdB_x and PtB_x samples. The differences between measured and nominal compositions were found to be about ±1 at. %.

7.3. Results and Discussion

7.3.1. Structural Chemistry

X-ray single crystal structure of the Ni,Zn solid solution in β boron

A single crystal of prismatic shape was selected from the crushed regulus with nominal composition $Ni_{44.4}Zn_{11.2}B_{44.4}$ (in at.%). The X-ray diffraction pattern of the single crystal was fully indexed on the basis of a rhombohedral lattice with a_{hex}=1.10182(2) nm and c_{hex}=2.40534(5) nm. Systematic absences observed for reflections *hkil (–h+k+l=3n), hh$\overline{2h}$l (l=3n), h$\overline{h}$0 (h+l=3n), 000l (l=3n)* and *h$\overline{h}$0h (h=3n)* were consistent with the space group type of highest rhombohedral symmetry $R\overline{3}m$. Structure solution through direct methods in $R\overline{3}m$ prompted 15 positions for boron atoms and among them B13 and B15 with 64% and 81% occupancy (for atom labels in the ßB structure after standardization with program *Structure Tidy* [26], see below and Table 1a). Four metal atom positions have been located by the Patterson method and from difference Fourier

syntheses electron densities were assigned to atom positions considering their distances to the neighboring atoms. Refining occupancies this procedure converged for four partially occupied metal positions in the unit cell filling voids of the boron framework. From the previously determined crystal structures of ZnB_{25} [17], NiB_{60} [10] and $NiB_{48.5}$ [11] it was observed that Ni and Zn atoms reside in the A_1, D and D_d voids of β boron, whereas the large Zn atoms preferably enter the E void. Following this observation we assigned Zn atoms to the E-void. It should be noted here that Ni and Zn atoms differ only by 2 electrons and therefore X-ray diffraction techniques can hardly differentiate with certainty the two atom types, therefore a statistical mixture of Ni/Zn atoms was attributed to the remaining sites i.e. the voids in A_1, D and D_d. Taking the overall Ni/Zn ratio (13.43 : 86.57) as determined by EPMA of the ßB(Ni,Zn) solution phase, first refinements served to find the total occupancy levels for each of the metal sites starting from a Ni/Zn ratio of 1 : 5.89 for the metal mixture common to the voids of A_1, D and D_d. With a mild dependency of the occupancy level on the Ni/Zn-ratio only a few iterations were necessary to find the proper Ni/Zn ratio in the voids A_1, D and D_d to comply with the overall Ni/Zn ratio determined by EPMA. A final refinement of overall occupancies of the three sites (A_1, D and D_d) with the finally derived average Ni : Zn ratio (1:5.41) led to the occupancy values of 0.49, 0.30 and 0.14, respectively. Refinement resulted in occupancy value of 0.33 for Zn1 atoms in E void. High B_{iso} values for B15 and atoms at the 18f position (0.022(1) Ni3+0.118 Zn4) have been controlled by constraining the temperature factor of these positions as equivalent. In the following we labeled the mixed metal sites with their individual mixtures as P [0.414(1) Zn2+0.076(1) Ni1], Q [0.254(1) Zn3+0.047(1) Ni2] and R [0.118(1) Zn4+0.022(1) Ni3]. Structure refinement yielded the formula $Ni_{0.19}Zn_{1.24}B_{34.22}$ with $R_{F^2} = 0.057$ and residual electron densities ±2.27/$Å^3$. Data on the final atom positions (standardized with program *Structure Tidy* [26]), isotropic and anisotropic atom displacement parameters (ADPs) are summarized in Tables 1a,b. As standardization of crystal structures has led to different atom labels for framework boron atoms, Table 1b provides the standardized labels for the title compound but also provides a conversion list to the atom labels in the original publication of the related structures of pure ßB [9], $NiB_{48.5}$ [11], ZnB_{25} [17] and $Ni_{0.19}Zn_{1.24}B_{34.22}$ [this work] and the corresponding labels after standardization. The unit cell of the Ni, Zn co-doped ßB structure is depicted in Fig. 2. Interatomic distances are listed in Table 2 and the corresponding coordination figures for the four metal sites are

presented in Fig. 3. *Q* atoms have two *R* atoms in their coordination polyhedron with rather short distances $d_{Q\text{-}R}$=0.1386(1) nm. Rather distorted polyhedra for *R* atoms contain 5 B atoms and two *Q* and two *R* atoms (see Fig. 3).
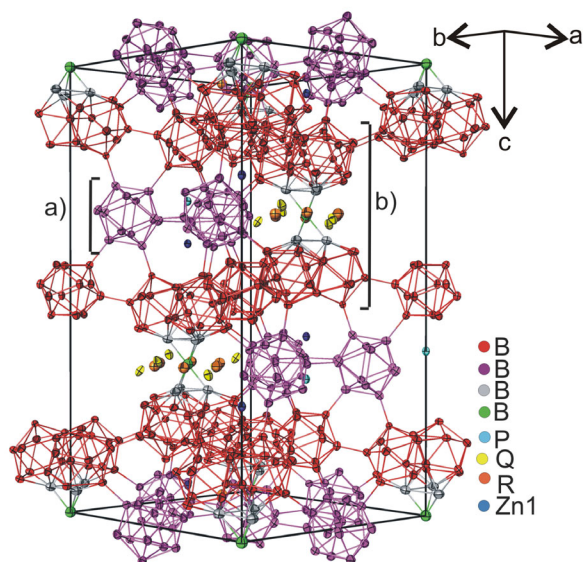
Figure 2. Unit cell for *β*-rhombohedral boron in perspective view. a) Interconnected B_{12} units along with Ni and Zn atoms. b) Boron network made of B_{28} units (three icosahedra sharing a common triangle of boron atoms). Zn1 atoms are residing in the E void, P (0.414Zn2 + 0.076Ni1) in A_1-void, Q (0.254Zn3 + 0.047Ni2) in D-void and R (0.118Zn4 + 0.022Ni3) in D_d-void.
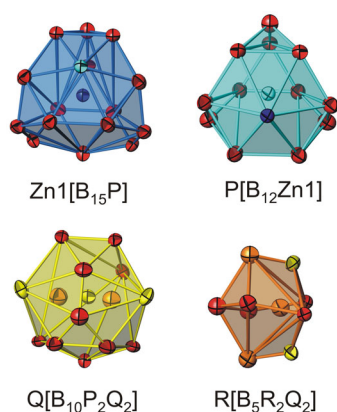
Figure 3. Coordination polyhedra for metal atoms in Ni,Zn *β*-boron. Two atoms R can be seen at $d_{Q\text{-}R}$=0.1386(1) within the polyhedron around Q atoms. B-atoms are drawn in red, Zn atoms in dark blue, and mixed atom positions are given in light blue (P site), in yellow (Q-site) and in orange for the R-site.

High values of B_{iso} have also been reported for two boron atoms, B15 [3a (0,0,0)], B16 [18h (0.2791,0.7209,0.0507)] and for Ni3 [18h (0.5169,0.4831,0.3111)] in NiB$_{48.5}$ [11] as well as for B15 [3a (0,0,0)], B13 [18h (0.6095,0.3905,0.2778)] and Zn4 [18f (0.1754,0,0)] in ZnB$_{25}$ [17]. This problem has been rectified in the present study by constraining equal isotropic temperature factors for B15 and the atoms at the 18f position (R). This part of unit cell is shown in Fig. 4.

The unit cell of pure β boron, as reported by Slack et al. [9], exhibits 20 sites for boron, out of which five have low occupancies: B16 (27%), B17 (9%), B18 (7%), B19 (7%), and B20 (4%) and are considered as non-framework atoms. The structure refinement of Ni, Zn co-doped ßB did not reveal these latter atom sites and attempts to introduce these positions in the NiZn-β boron crystal were unsuccessful due to the formation of negative occupancies at these sites. Thus the Ni,Zn co-doped ßB structure does not contain any extra boron atoms besides those forming the three dimensional framework of $B_{58}=(2B_{28})B15$ and B_{12} subunits as described for pure ßB [10]. In order to discuss the occupational mode in the voids of the boron framework we may recall the results on Ni- and Zn-doped binary ßB phases in the literature.

Figure 4. a) Three face-sharing B12 units resulting in a B28 unit: the atom B15 (green atom) is joining two B28 units [B$_{28}$-B15-B$_{28}$]. b) Surrounding of B15 forming a D-type void for Q [yellow atoms (0.254Zn3 + 0.047Ni2)] with 0.30 occupancy and

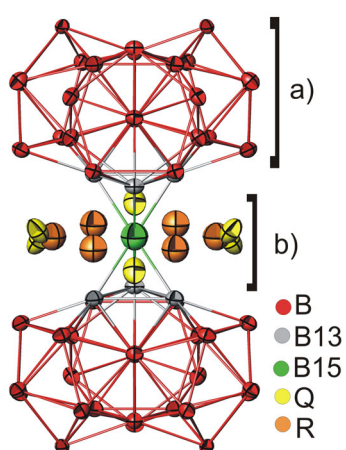Slight but significant differences in boron and metal atom sites are known from the structure determinations of $NiB_{48.5}$ [11] and NiB_{60} (Ni100) [10]. Nickel atoms in $NiB_{48.5}$ [11] were located in sites of type A_1 (Ni1), in D_d (Ni2 in 36i), in D (Ni3) and in a "new" type of voids (Ni4), whereby the distances between Ni2 and Ni2, Ni3, Ni4 are as low as 0.98 Å reflecting the low occupancies per unit cell of atoms not present simultaneously. For convenient comparison, Table 3 lists the Wyckoff position, atomic coordinates and corresponding void types for the Ni, Zn atoms in the structures of $NiB_{48.5}$ [11], ZnB_{25} [17] and $Ni_{0.19}Zn_{1.24}B_{34.22}$. It should be mentioned that besides a defect B13 site, $NiB_{48.5}$ [11] contained a full B15 and a defect B16 site, but no further boron atoms. Comparing Lundström's data on $NiB_{48.5}$ [11, 16] with Slack's structure model for NiB_{60} [10] (labelled as Ni100 containing 1.64 at. % Ni [10]), Ni atoms in NiB_{60} [10] were confirmed in voids i.e. A_1, D at slightly different occupancies of 37.6(2), 3.8(4)%, [10] but Ni3 (6.6(2)%) is found in site D_d with positional parameters different from Ni4 in $NiB_{48.5}$ [11]. In contrast to pure beta boron [9] there is no electron density at the site of B17, 7.3% at the site of for B17d, whereas B18 (16.2%) is present at slightly different positional parameters. In NiB_{60} [10] B17 is present at the 'distorted D' site D_d. In a discussion Slack argued that from the general structure-chemical behaviour of doped ßB-phases as well as taking the distances to the next-nearest neighbors into account, Ni3 and Ni4 atoms in $NiB_{48.5}$ should rather correspond to boron atoms B18 and B17d (disordered B17) [10]. The atomic coordinates of Q [this work], Ni3 [11], Zn2 [17] and Ni at the D position in NiB_{60} [10] seem to lie between those of B17 and B18 in pure ß boron (shown in table 3).

Considering Zn as dopant in ßB, it is evident from $ZnB_{\sim 25}$ [17] that Zn atoms enter four positions, 6c (Zn1 in void type A_1, 49%), 6c (Zn2, E, 34%), 18f (Zn4, undefined void type, 13%) and 18h (Zn3, D, 28%), out of which voids A_1 and D are also characteristic for smaller Ni as dopant. As typical for doped ßB structures, the defect sites B13 (64%) and B15 (78%) appear in $ZnB_{\sim 25}$ [17].

Following the size constraint only the large Zn atoms in ßB(Zn,Ni) have been observed in voids of type E, but the remaining three voids (A_1, D and D_d) all exhibit random mixtures of Ni and Zn atoms with a majority of Zn (see table 3). In comparison to the crystal structure of $NiB_{48.5}$ [11] one less boron position (B16) has

been observed in ßB(Zn,Ni), but mixtures Ni/Zn (P) in void A_1 (filled by Ni1 in $NiB_{48.5}$) and Ni/Zn (Q) in voids D (which corresponds to Ni3 in $NiB_{48.5}$) have been confirmed in this work. In the crystal $Ni_{0.19}Zn_{1.24}B_{34.22}$ metal atoms are neither observed in the "new site" (Ni4 in $NiB_{48.5}$), nor in the D_d sites ($36i$, Ni2 in $NiB_{48.5}$), but a Ni, Zn mixture (R) in site $18f$ (D_d) has been located. D_d is a so-called "disordered void" as its atomic coordination varies with the type of dopant in ßB. Such D and D_d voids have been reported by Slack et al. [10] only for Cu or Ni dopants in ß boron. Fig. 4 depicts the environment of site B15, which is surrounded by Q and R atoms along with a residual electron density of $\pm 2.27e^-/\text{Å}^3$. The short distances, $d_{B15-R}=0.1905(3)$ nm, $d_{R-R}=0.1905(6)$ nm and $d_{Q-R}=0.1386(1)$ nm, are only justified by the low occupancies of Q (30%) and R (14%), respectively. This fact is evident from the 3D difference Fourier map, which reveals a projection along c direction in Fig. 5. Adopting Slack's suggestion [10] for $NiB_{48.5}$ i.e. to replace the sites "Ni3" and "Ni4" in $NiB_{48.5}$ [11] by boron atoms (B17 and B18, as in pure β boron) results for ßB(Ni,Zn) in an occupancy of 2.48 and 1.24, respectively. From the occupancy values bigger than 1, it is prompted to keep metal atoms in the "Ni3" position (corresponding to Q in $Ni_{0.19}Zn_{1.24}B_{34.22}$) but possibly to replace "Ni4" (corresponding to R in $Ni_{0.19}Zn_{1.24}B_{34.22}$) by a boron atom: this attempt, however, led to $R_F^2 = 0.33$ with an unacceptably high temperature factor for "Ni4". It thus seems that both metal atom mixtures should be kept in voids D and D_d, as located originally from a Patterson analysis of our crystal data.
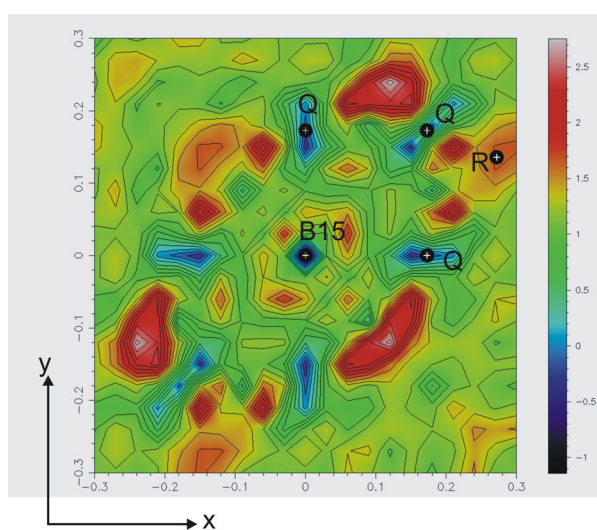
Figure 5. 3D Fourier map with F_0-F_c coefficient, (projection along c direction ranging from 0 to 0.5, x = y both range from –0.3 to 0.3) showing B15 surrounded by Q

(0.254Zn3 and 0.047Ni2) occupancy 0.30, R (0.118Zn4 and 0.022Ni3) occupancy 0.14 and a residual electron density of $+2.27e^-/Å^3$.

The short distance d_{R-R} is acceptable because of 14% occupancy for this site, which means that Q atom neighbors never exist all in one unit cell. Also Q, B15 and B13 in the vicinity of Q atoms are not fully occupied. As elemental boron may contain carbon as impurity, we attempted to refine the $18f$ (R) position for a carbon atom, however, the temperature factor turned to a negative value and the reliability factor increased to 16%. The average distance of Zn1 of ßB(Ni,Zn) in the A_1 void is 0.2176(3) nm from its neighboring boron atoms and compares well with the corresponding values in ZnB_{25} (0.2166(1) nm) [17]. In a thorough analysis of the influence of metal dopants on the void structure in ßB Slack et al [9]. have arrived at (i) a rather linear trend for the percentage occupancy of metal atoms in the A_1 voids versus the average distance to the 12 nearest boron neighbors (see Fig. 6), and (ii) a linear dependency of the fractional occupation of dopant metal atoms in site E versus the average distance to 15 neighbouring boron atoms (see Fig. 7). Zn atoms in ZnB_{25} [17] and the Ni/Zn mixture (P) in ßB(Ni,Zn) seem to follow both these relations (i) and (ii). For the sum of percentage occupancies of D and D_d sites Slack et al. [10] have formulated a relation $\Sigma_2 = P(D) + 2P(D_d)$. If the B13 site is occupied at 66.7% then the maximum value for Σ_2 can be 50% for NiB_{60} [10]. As in ßB(Ni,Zn) the D site is filled by 30% (Ni, Zn mixture-Q) and the D_d site is filled by 14% (Ni, Zn mixture-R), the sum Σ_2 in $Ni_{0.19}Zn_{1.24}B_{34.22}$ yields an occupancy of 58% but the B13 site shows a lower occupancy of 64%.

122
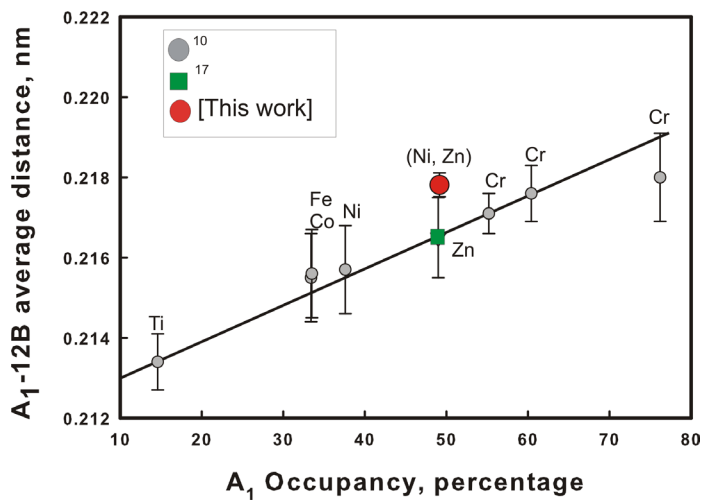
Figure 6. The percentage occupancy of the A_1 void versus the average distance from 12 neighboring boron atoms. Gray circles present the data from Slack et al. [10], the red circle represents the Ni, Zn mixture (P) at A_1 in $Ni_{0.19}Zn_{1.24}B_{34.22}$ [this work]; the green square represents data taken from [17] for Zn1 in ZnB_{25}.
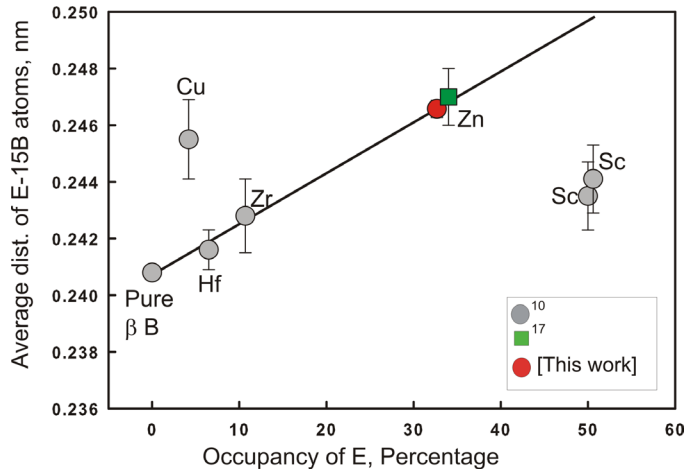
Figure 7. Percentage occupancy of the E site versus the average distance from 15 neighboring boron atoms: gray circles present data from Slack et al.[10], the red circle represents Zn1 in $Ni_{0.19}Zn_{1.24}B_{34.22}$ [this work] and the green square represents data taken from [17] for Zn3 of ZnB_{25}.

The R- atoms (Ni/Zn at 18f) are at a distance of 0.1386(1) nm from Q (Ni/Zn mixture at 18h) in the D void. From Fig. 3 we may conceive R in a distorted D void (called D_d) around the B15 atom which is linking the two B28 units. In the literature [10, 11] the D_d site has been assigned to a Wyckoff site 36i, but for this work and also for ZnB_{25} [17] Wyckoff position 18f was chosen. Ni4 in $NiB_{48.5}$ [11] was suggested to be in a new void type. However, from table 3 it is obvious that the positional parameters of the "new" site in $NiB_{48.5}$ [11] closely correspond to the 18f (R) parameters of this work and ZnB_{25} [17] (D_d site).

Lattice parameters and the unit cell volume depend almost linearly on dopant concentration as shown in Fig. 8 for pure β boron and Ni, Zn dopants.
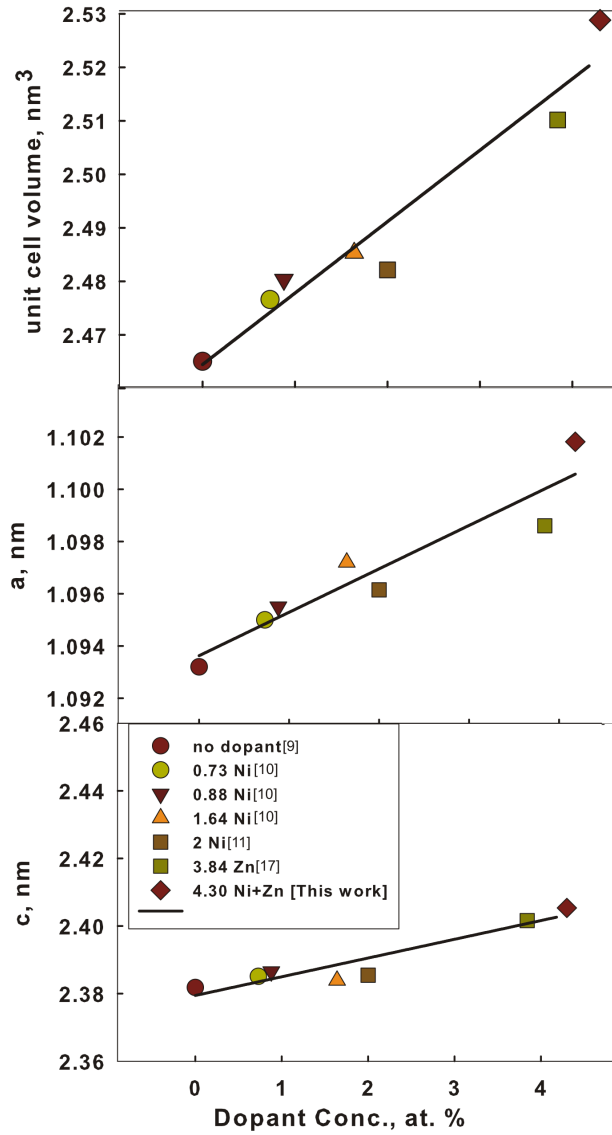
Figure 8. Correlation between lattice constants, cell volume and dopant concentration in pure β boron and in solid solutions with Ni and Zn and co-dopants (Ni, Zn).

The cell distortion parameter S was calculated from the unit cell dimensions by the following formula [10]

$$S = \left[1 - \frac{c}{2.1797\,a} \right] \times 10^{4} \,,$$

where 2.17978 is the c/a ratio of pure β boron as determined by Callmer [8]. Positive values of S correspond to a decrease in c/a and consequently in an increase of the rhombohedral angle α_{rhomb}. For the Ni-Zn co-doped solid solution of β boron ($Ni_{0.19}Zn_{1.24}B_{34.22}$) we calculated S = −15, which fits perfectly between the values of $S(ZnB_{25})$= −30 [17] and $S(NiB_{60})$=+32 [10] or $S(NiB_{48.5})$=+16 [11].

Refinement of the crystal structure of Ni,Zn β boron in space group R3

A marked anisotropy of unconstrained displacement parameters of the atom in the 18*f* Wyckoff position (x,0,0; x=0.1729(3)) and a pronounced maximum in the difference Fourier map of 2.27 e$^-$/Å^3 (in 36*i* (x=0.0634, y=0.8546, z=0.0002) at a distance 0.61 Å) (Fig. 5) suggested the possibility of disorder of this atom site, however the refinement of atoms on split 18*f* and 36*i* Wyckoff sites in space group $R\overline{3}m$ neither improved the reliability factor nor significantly reduced the residual electron density. Refinement was more successful in the space group $R3$ which offers two crystallographically nonequivalent atom sites for each metal atom in accordance with the group-subgroup relationships $R\overline{3}m \rightarrow R\overline{3} \rightarrow R3$. Further steps in refinement showed that only one Zn site of each pair is disordered, namely Zn2 and Zn4. While for Zn4 the order predominates exhibiting the occupancy ratio 27% Zn4 / 3.6% Zn44 (D void), the Zn2/Zn22 split sites (18*f* in $R\overline{3}m$, currently D$_d$, see above) are occupied almost equally (about 6% and 8% respectively). Despite the positional parameters of boron atoms refined in the $R3$ space group deviate only slightly from the corresponding atom positions in $R\overline{3}m$, the lower symmetry space group allowed to model disorder of Zn atoms. The refinement in space group $R3$ led to an improved value of reliability factor R$_F{}^2$=0.049 as compared to the refinement in $R\overline{3}m$ (R$_F{}^2$=0.057) and reduced the residual electron densities to +1.28/-1.67 e$^-$/Å^3. The positional and displacement parameters of atoms affected by Zn disorder (located within the 3.5 Å sphere around B36 in 3a; 0,0,z; z=0.000) as well as atoms in voids E and A$_1$ are given in Table 6. At the initial steps of refinement, partial substitutions of Zn by Ni have been tested for all metal sites and resulted in negative occupancy of Ni atoms in void D, negligible amount of Ni (less than 0.001%) in the atom position (Zn at 18*f*) while the void A$_1$ was found to accommodate Ni atoms randomly mixed with Zn. Further refinement considering partial occupancy for only the A$_1$ void rendered the formula Zn$_{1.24}$Ni$_{0.18}$B$_{34.20}$. To justify the accommodation of the Ni atoms, one may again recall the literature data: for the structure solution suggested in space group $R\overline{3}m$, void was reported to host Zn (E void, 6*c* 0,0,z; z=0.27012) while the remaining three sites [A$_1$ void in 6*c* (0, 0, z; z=0.36496)], [D in 18*h* (x, $\overline{x}$, z; x=0.53079, z=0.34807)] and [D$_d$ void in 18*f* (x,0,0; x=0.1729)] are favored by both Ni and Zn. However, comparing the positional parameters in the current structure of the atom in

D, it becomes obvious that this location is more inclined to Zn in the structure reported by Kuzma et al. [17] In good agreement with this behaviour, only the void A_1 was found to accommodate a statistical mixture Zn/Ni in space group $R3$ exhibiting different elemental ratios for the two atom sites $3a$ (Table 6). All atom sites were refined anisotropically except i) B4, B11; ii) B36, Zn1, Zn2, Zn22) and iii) Zn7/Ni1, Zn8/Ni2; the displacement parameters for atoms within these groups were refined to be equivalent.

7.3.2. Charge self-compensation in Ni,Zn β boron

Table 4 gives a comparison of the number of atoms and electrons in the unit cell of pure β boron [9], $NiB_{48.5}$ [11], $ZnB_{\sim 25}$ [17] and $Ni_{0.19}Zn_{1.24}B_{34.22}$ [this work]. Addition of transition metal atoms results in a decreased number of electrons available in the β boron solid solution for bonding as compared to that of the total electrons required in stabilizing the pure β boron structure (= 320 e/hex unit cell). Table 5 is showing somewhat higher values of residual electron densities at the intercluster bonds in $Ni_{0.19}Zn_{1.24}B_{34.22}$ as compared to that in NiB_{60} [10]. This higher electron number in the structural model $Ni_{0.19}Zn_{1.24}B_{34.22}$ is also obvious in Table 4. $Ni_{0.19}Zn_{1.24}B_{34.22}$ exhibits a dopant concentration of 4.01 at. %, which is higher than for many β boron solid solutions listed in table 4.

Following the argumentation by Ogitsu [14], the B13 site is a partially occupied site (POS) with an occupation of 52% [shown in Fig. 1b by Ogitsu [14]]. For a β boron crystal to be perfect without any defects and with 105 atoms in the unit cell, this site should be fully occupied.

7.3.3. On the solubility of Pd, Pt in ß boron

In order to check on the incorporation of the Ni-homologues, Pd and Pt in ßB, attempts were made to get good quality single crystals for solid solutions of Pd and Pt in β boron. Micrographs for Pd_8B_{92} and Pt_4B_{96} in Fig. 9 show the presence of Pd_2B and PtB_x, respectively, along with β boron.
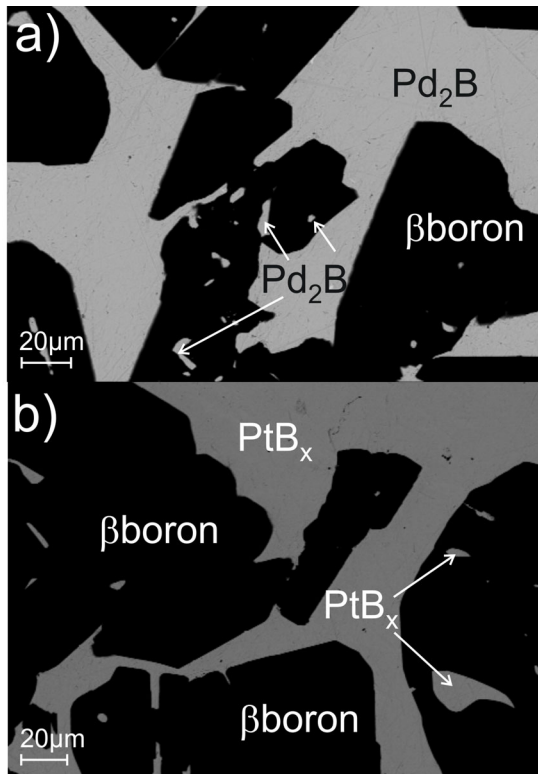
Figure 9 Micrograph for a) Pd_8B_{92} and b) Pt_4B_{96}, samples annealed at 1250°C for 36 hours, showing phase equilibria of practically pure ßB with Pd_2B and PtB_x, respectively.

The Pd_2B phase ($CaCl_2$ type) has been identified by x-ray powder diffraction. In case of Pt in β-B XPD showed a spectrum for which it was difficult to decide if it arises from $PtB_{0.67}$ (a=0.33532(4), b=0.58092(6), c=0.40924(1) nm, *Cmcm*, AlB_2 derivative) or PtB (a=0.335206(8), c=0.40910(1) nm, *P6₃/mmc*, NiAs type) [27]. EPMA of the samples showed that Pd has negligible solubility (0.13 at. %) in β boron at 1250°C while Pt has not any at this temperature. The low solubilities are in accord with earlier reports [28] and therefore do not encourage single crystal studies.

7.4. Conclusions

The crystal chemistry of a solid solution of Ni and Zn in β rhombohedral boron has been studied on a single crystal $Ni_{0.19}Zn_{1.24}B_{34.22}$ (*a* = 1.10182(2) nm, c = 2.40534(5) nm), the composition of which was defined by electron microprobe analyses (EPMA; ratio Ni/Zn=1:6.45). Keeping isotypism with the structure type of pure ßB, the structure solution in space group $R\bar{3}m$ prompted Zn atoms in the E void (occupancy of 33%) whilst random mixtures of Ni, Zn atoms (ratio 15.5:84.5) occupy the sites A_1,

D and D_d with a total occupation of 49, 30 and 14%, respectively. Although the R-value ($R_F{}^2$=0.057) and a residual electron density of $\pm2.27e^-/\text{Å}^3$ seems to be satisfactory, structure refinement in the lower symmetry space group $R3$ yields partial ordering of metal atom sites revealing a split of Zn atom sites in voids D and D_d, but a statistical mixture of Ni/Zn located in void A_1 ($R_F{}^2$=0.049 and a residual electron density of $\pm1.28e^-/\text{Å}^3$). As standardization of crystal structures has led to different atom labels for framework boron atoms a conversion table has been prepared comparing standardized atom site labels with those of the non-standardized settings in the original structures of pure ßB and doped ßB compounds.

7.6. References.

[1] T. Mori, D. Berthebaud, T. Nishimura, A. Nomura, T. Shishido, K. Nakajima, Dalton Trans. 39(2010) 1027–1030.

[2] T.B. Massalski, Binary Alloy Phase Diagrams, 2nd Ed., ASM International, Ohio, 1990.

[3] T. Mori, Handbook on the Physics and Chemsitry of Rare Earths, ed. K.A. Gschneidner Jr., J-C. Bunzli and V. Pecharsky, North-Holland, Amsterdam, 2008.

[4] T. Nakayma, J. Shimizu, K. Kimura. J Solid State Chem. 154 (2000) 13-19.

[5] R.E. Hughes, C.H.L. Kennard, D. Sullenger, H.A. Weakliem, D. Sands, J.L. Hoard. J. Am. Chem. Soc. 85 (1963) 361–362.

[6] J.L. Hoard, D.B. Sullenger, C.H.L. Kennard, R.E. Hughes, J. Solid State Chem. 1 (1970) 268-277.

[7] D. Geist, R. Kloss, H. Follner, Electron Technol 3 (1970) 109-118.

[8] B. Callmer, Acta Crystallogr. B33 (1977) 1951-1954.

[9] G.A. Slack, C-I. Hejna, M.F. Garbauskas, J.S. Kasper. J Solid State Chem. 76 (1988) 52-63.

[10] G.A. Slack, C-I. Hejna, M.F. Garbauskas, J.S. Kasper. J Solid State Chem. 76 (1988) 64-86.

[11] T. Lundström, L. Tergenius, Zeitschrift für Kristallogr. 167 (1984) 235-246.

[12] E.D. Jemmis, M.M. Balakrishnarajan, P.D. Pancharatna, J. Am. Chem. Soc 123 (2001) 4313-4323.

[13] E.D. Jemmis, M.M. Balakrishnarajan. J. Am. Chem. Soc. 123(2001) 4324-4330.

[14] T. Ogitsu, F. Gygi, J. Reed, Y. Motome, E. Schwegler, G.Galli, J. Am. Chem. Soc 131 (2009) 1903-1909.

[15] S. Andersson, B. Callmer, J Solid State Chem 10 (1974) 219.

[16] T.Lundström, AIP Conference Proc. 140 (1986)19.

[17] Y.B. Kuz'ma, V.N. Gurin, M.M. Korsukova, Akselrud L.G. Translated from Izvestiya Akademii Nak SSSR, Neorganicheskie Materialy. 23 (1987) 566-569.

[18] M.M. Korsukova, V.N. Gurin, Y.B. Kuz'ma, A.Y. Kiskachi, Solov'ev NE. Sov. Phys. Crystallogr 22 (1977) (6).

[19] J.F. Nie, B.C.Muddle, Scripta Mater. 37 (1997) 1473.

[20] T. Roisnel, J. Rodriguez-Carvalaj, Materials-Science-Forum 1:118 (2001) 378-381.

[21] Nonius Kappa CCD Program Package COLLECT, DENZO, SCALEPACK, SORTAV, Nonius Delft, The Netherlands, 1998.

[22] Sheldrick GM. SHELXS-97, Program for Crystal Structure Refinement University of Göttingen, Germany Windows version by McArdle, Natl. Univ. Ireland, Galway, 1997.

[23] G.M Sheldrick, Acta Crystallogr. A64 (2008) 112-122.

[24] L.J. Farrugia, J. Appl. Crystallogr. 32 (1999) 837-838.

[25] A. Jonnasson, H. Ljung, S. Westman, Acta Chemica Scandinavica 22 (1968) 2743-2753.

[26] E. Parthé, L. Gelato, B. Chabot, M. Penzo, K. Censual, Gladyshevskii R. TYPIX—Standardized Data and Crystal Chemical Characterization of Inorganic Structure Types. Berlin: Springer, 1994.

[27] P.Villars, K. Cenzual, Pearson's Crystal Data CD ROM, Release 2011/2012, ASM International, OH, USA.

[28] A.J. Crespo, L. Tergenius, T. Lundström, J Less Common Metals 77 (1981) 147-150.

Table 1a. Crystal structure data for β B-type $Ni_{0.19}Zn_{1.24}B_{34.22}$ (Nonius KappaCCD diffractometer, MoK_α radiation). Data on boron atoms are summarized in table 1b below

Compound	$Ni_{0.19}Zn_{1.24}B_{34.22}$
Nominal composition in [at.%] [d]	$Ni_{44.44}Zn_{11.12}B_{44.44}$
Space group	$R\bar{3}m$; No. 166
Ni: Zn ratio from EPMA	13.43 : 86.57
Formula from refinement	$Ni_{0.19}Zn_{1.24}B_{34.22}$
Structure type	β-B
θ Range [deg]	$3.70 < \theta < 33.47$
a [nm]	1.10182(2)
c [nm]	2.40534(5)
Crystal size [μm]	20x30x35
Mosaicity	0.45
Reflections in refinement	$917 F_o > 4\sigma(F_o)$ of 1148
Unit cell volume ($Å^3$)	2528.88(8)
Z, Calculated X-ray density (g/cm^3)	3, 2.70
Number of variables	115
$R_F^2 = \Sigma|F_0^2 - F_c^2|/\Sigma F_0^2$	0.057
R_{Int}	0.040
GOF	1.14
Extinction (Zachariasen)	0.0000(8)
Residual electron density; max; min in [electrons/nm^3] x1000	2.27; -1.17
Zn1 in $6c$ $(0, 0, z)$;Occ. $U_{11}{}^b = U_{22}$; U_{33}; $U_{23} = U_{13} = 0$; U_{12}	$z=0.27013(10)$; 0.33(1) 0.0080(8); 0.013(1); 0.0040(4)
$6c$ $(0, 0, z)$; Occ $U_{11}{}^b = U_{22}$; U_{33}; $U_{23} = U_{13} = 0$; U_{12}	$z=0.36495(5)$; 0.076(-)Ni1+0.414(-)Zn2 (P) 0.0049(4); 0.0066(6); 0.0024(2)
$18h$ $(x, \bar{x}, z)$; Occ. $U_{11}{}^b = U_{22}$; U_{33}; $U_{23} = -U_{13}$; U_{12}	$x=0.53080(7)$, $\bar{x}=0.46920(7)$, $z=0.34806(5)$; 0.047(-)Ni2+0.254(-)Zn3 (Q) 0.0103(5); 0.0138(7); 0.0021(2); 0.0050(5)
$18f$ $(x, 0,0)$;	$x=0.1729(3)$;
Occ; $U_{iso}{}^c$	0.022(-)Ni3+0.118(-)Zn4 (R); 0.0161(9)

[a] crystal structure data are standardized using the program Structure Tidy [26].
[b] Anisotropic atomic displacement parameters U_{ij} in $[10^2 \ nm^2]$.
[c] Isotropic atomic displacement parameters U_{iso} in $[10_2 \ nm_2]$.
[d] Nominal composition of the alloy from which a single crystal was isolated.

Table 1b. Boron atom labels and standardized atom positions for the structures Ni$_{0.19}$Zn$_{1.24}$B$_{34.22}$, NiB$_{48}$ [11] and ZnB$_{25}$ [17] in accordance with the standardized atom labels for ßB [9] described in TYPIX [26].

Atom # [a]- atom # [b] in NiB$_{48.5}$; Occ. [11]	Atom # [a]- atom # [b] in ZnB$_{25}$; Occ. [17]	Atom # [a]- atom # [b] in βB; Occ. [10]	+Atom # in [9] and [this work]	Ni$_{0.19}$Zn$_{1.24}$B$_{34.22}$ [This work]
B2^a-B2^b	B2^a-B2^b	B1^a-B2^b	B2 in 36i (x,y,z);	x=0.0141(2), y=0.3723(2), z=0.03844(9);
			Occ.	1.00(1)
			U$_{11}$^{b}; U$_{22}$; U$_{33}$; U$_{23}$; U$_{13}$; U$_{12}$	0.0062(9); 0.0059(9); 0.0054(9); 0.0005(7); 0.0002(7); 0.0030(7)
B3^a-B3^b	B3^a-B3^b	B2^a-B3^b	B3 in 36i ($x.y,z$);	x=0.0442(2), y=0.2620(2), z=0.08185(9);
			Occ.	1.00(1)
			U$_{11}$^{b}; U$_{22}$; U$_{33}$; U$_{23}$;U$_{13}$; U$_{12}$	0.0065(9); 0.0071(9); 0.0051(9); 0.0008(7); 0.0002(7) 0.0037(7)
B1^a-B1^b	B1-B1^b	B4-B1^b	B1 in 36i ($x.y,z$);	x=0.0017(2), y=0.1769(2), z=0.3238(1);
		With different y	Occ.	1.00(7)
			U$_{11}$^{b}; U$_{22}$; U$_{33}$;	0.0065(9); 0.0074(9); 0.0087(9);
			U$_{23}$; U$_{13}$; U$_{12}$	-0.0022(7); -0.0012(7); 0.0037(8)
B4^a-B4^b	B4^a-B4^b	B5^a-B4^b	B4 in 36i (x,y,z);	x=0.2519(2), y=0.0151(2), z=0.15343(9);
			Occ.	1.00(1)
			U$_{11}$^{b}; U$_{22}$; U$_{33}$; U$_{23}$; U$_{13}$; U$_{12}$	0.0066(9); 0.0057(9); 0.0066(9); -0.0005(7); -0.0013(7) 0.0028(7)
B6^a-B5^b	B5^a-B5^b	B7^a-B5^b	B5 in 18h ($x,\bar{x}$,z);	x=0.3878(2), $\bar{x}$=0.6122(2), z=0.1110(1);
			Occ.	1.00(1)
			U$_{11}$^{b}= U$_{22}$; U$_{33}$; U$_{23}$= -U$_{13}$; U$_{12}$	0.0055(9); 0.006(1); 0.0005(5);0.003(1)
B7^a-B6^b	B6^a-B6^b	B8^a-B6^b	B6 in 18h ($x,\bar{x}$,z);	x=0.4191(2), $\bar{x}$=0.5809(2), z=0.1798(1);
			Occ.	1.00(1)
			U$_{11}$^{b}= U$_{22}$; U$_{33}$; U$_{23}$= -U$_{13}$; U$_{12}$	0.0042(8); 0.008(1); 0.0003(5); 0.002(1)
B8^a-B7^b	B7^a-b7^b	B9^a-B7^b	B7 in 18h ($x,\bar{x}$,z);	x=0.4439(2), $\bar{x}$=0.5561(2), z=0.0543(1);
			Occ.	1.00(1)
			U$_{11}$^{b}= U$_{22}$; U$_{33}$; U$_{23}$= -U$_{13}$; U$_{12}$	0.0070(9); 0.006(1); 0.0001(5); 0.003(1)
B9^a-B8^b	B8^a-B8^b	B11^a-B8^b	B8 in 18h ($x,\bar{x}$,z);	x=0.5029(2), $\bar{x}$=0.4971(2), z=0.1942(1);
			Occ.	1.00(1)
			U$_{11}$^{b}= U$_{22}$; U$_{33}$; -U$_{23}$= U$_{13}$; U$_{12}$	0.0057(9); 0.005(1); 0.0002(5); 0.0028(9)
B10^a-B9^b	B9^a-B9^b	B13^a-B9^b	B9 in 18h ($x,\bar{x}$,z);	x=0.5372(2), $\bar{x}$=0.4628(2), z=0.0668(1);
			Occ. U$_{11}$^{b}= U$_{22}$; U$_{33}$; -U$_{23}$= U$_{13}$; U$_{12}$	1.00(1) 0.0065(9); 0.007(1); 0.0007(5); 0.003(1)
B11 ^{a}-B10^b	B10^a-B10^b	B14^a-B10^b	B10 in 18h ($x,\bar{x}$,z); Occ. U$_{11}$^{b}= U$_{22}$; U$_{33}$; -U$_{23}$= U$_{13}$; U$_{12}$	x=0.5649(2), $\bar{x}$=0.4351(2), z=0.1346(1); 1.00(1) 0.0062(9); 0.004(1); 0.00005(46); 0.004(1)
B12^a-B13^b; **0.67**	B11^a-B13^b; **0.64**	B16^a-B13^b; 0.**75**	B13 in 18h ($x,\bar{x}$,z); Occ. U$_{11}$^{b}= U$_{22}$; U$_{33}$; -U$_{23}$= U$_{13}$; U$_{12}$	x=0.6099(3), $\bar{x}$=0.3901(3), z=0.2767(2); 0.64(2) 0.009(2); 0.006(2); 0.0004(8); 0.005(2)
B13^a-B11^b	B12^a-B11 ^{b}	B17^a -B11^b	B11 in 18h ($x, \bar{x}$, z); Occ. U$_{11}$^{b}= U$_{22}$; U$_{33}$; -U$_{23}$= U$_{13}$; U$_{12}$	x=0.7235(2), $\bar{x}$=0.2765(2), z=), 0.1604(1); 1.00(1) 0.0057(9); 0.005(1); 0.00005(49); 0.002(1)
B14^a-B12^b	B13^a-B12^b	B18^a-12^b	B12 in 18h ($x, \bar{x}$, z);. Occ. U$_{11}$^{b}= U$_{22}$; U$_{33}$; -U$_{23}$= U$_{13}$; U$_{12}$	x=0.7567(2), $\bar{x}$=0.2434(2), z=0.2304(1); 1.00(1) 0.0053(9); 0.006(1); 0.0005(5); 0.003(1)

B15^a-B14^b	B14^a-B14^b	B19^a -B14^b	B14 in $6c$ $(0, 0, z)$; Occ. U_{11}^{b}= U_{22}; U_{33}; U_{23}= U_{13}=0; U_{12}	z=0.1152(2); 1.00(1) 0.006(1); 0.006(2); 0.0033(7)
B16^a-15^b	B15^a-B15^b; **0.78**	B20^a -B15^b	B15 in $3a$ $(0, 0, 0)$; Occ.;U_{iso}	0.81(3); 0.0159(9)

^{a} non standardised atom label;
^{b}standardised atom label,
+standardized boron atom labels in Slack et al [9]and [this work].

Table 2. Interatomic distances in $Ni_{0.19}Zn_{1.24}B_{34.22}$.

Atom	Distance (nm)	Atom	Distance (nm)	Atom	Distance (nm)
Zn1 – P	0.2281(3)	B3 – B2	0.1755(5)	B10 – B9	0.1714(4)
Zn1 –6B1	0.2330(3)	B3 – B8	0.1791(4)	B10 –2B11	0.1796(4)
Zn1 –3B9	0.2473(3)	B3 – B12	0.1798(5)	B10 –2B4	0.1858(3)
Zn1 –3B11	0.2577(4)	B3 – B4	0.1813(3)	B10 – B8	0.1859(4)
Zn1 –3B10	0.2592(3)	B3 – B13	0.1814(6)	B10 – Zn1	0.2592(3)
P – 3B5	0.2172(3)	B3 – B3	0.1913(7)	B11 – B14	0.1764(5)
P – 6B1	0.2179(3)	B3 – R	0.2145(3)	B11 –2B10	0.1796(4)
P – 3B7	0.2179(2)	B3 – Q	0.2391(4)	B11 – B12	0.1800(4)
P – Zn1	0.2281(3)	B4 – B4	0.1680(4)	B11 –2B4	0.1858(4)
Q – 4R	0.1386(1)	B4 – B8	0.1741(3)	B11 –2B11	0.1879(4)
Q – B13	0.2286(5)	B4 – B3	0.1813(3)	B11 – Zn1	0.2577(4)
Q – B12	0.2294(3)	B4 – B12	0.1855(4)	B12 – B14	0.1743(3)
Q – 2B1	0.2319(4)	B4 – B11	0.1858(4)	B12 –2B3	0.1798(5)
Q – 2B2	0.2353(4)	B4 – B10	0.1858(3)	B12 – B11	0.1800(4)
Q – 2B3	0.2391(4)	B5 – B7	0.1733(4)	B12 –2B4	0.1855(4)
Q – 2Q	0.2688(2)	B5 –3B6	0.1762(4)	B12 –2B13	0.1871(6)
R – 4R	0.1386(1)	B5 –2B5	0.1799(4)	B12 –2Q	0.2294(3)
R – 2B13	0.1755(6)	B5 –2P	0.2172(3)	B13 – B15	0.1740(5)
R – B15	0.1905(3)	B6 – B8	0.1636(3)	B13 –4R	0.1755(5)
R – 4R	0.1905(6)	B6 –2B6	0.1754(3)	B13 – B14	0.1778(6)
R – 2B3	0.2145(3)	B6 –3B5	0.1762(4)	B13 – 2B3	0.1813(3)
B1 – B2	0.1846(5)	B7 – B5	0.1733(4)	B13 – 2B12	0.1871(6)
B1 – B9	0.1850(4)	B7 –2B2	0.1796(5)	B13 – 2B13	0.1876(7)
B1 – B7	0.1858(4)	B7 – B9	0.1805(4)	B13 – Q	0.2286(5)
B1 – B2	0.1859(4)	B7 –2B1	0.1858(4)	B14 –3B12	0.1743(3)
B1 – B1	0.1913(5)	B7 –2P	0.2179(2)	B14 – 3B11	0.1764(5)
B1 – B1	0.1968(5)	B8 – B6	0.1636(3)	B14 – 3B13	0.1778(6)
B1 – P	0.2179(3)	B8 –2B4	0.1741(3)	B15–6B13	0.1740(5)
B1 – Zn1	0.2330(3)	B8 –2B3	0.1791(4)	B15–6R	0.1905(3)
B1 – Q	0.2319(4)	B8 – B10	0.1859(4)		
B2 – B3	0.1755(5)	B9 – B10	0.1714(4)		
B2 – B7	0.1796(5)	B9 – B7	0.1805(4)		
B2 – B9	0.1839(5)	B9 –2B2	0.1839(5)		
B2 – B1	0.1846(5)	B9 –2B1	0.1850(4)		
B2 – B1	0.1859(4)	B9 – Zn1	0.2473(3)		
B2 – B2	0.1869(3)				

Table 3. Site occupation of Ni and Zn atoms in voids of the β B-type boron framework in NiB_{60}, NiB_{48}, ZnB_{25} and in $Ni_{0.19}Zn_{1.24}B_{34.22}$.

Wyckoff position	Atomic coordinates			Void type	NiB_{60} ♠Occ. [10]	$NiB_{48.5}$ +Occ. [11]	ZnB_{25} ** Occ. [17]	$Ni_{0.19}Zn_{1.24}B_{34.22}$ *+ Occ. [This work]
	x	y	z					
$6c$	0	0	0.27012(10)*+	E	0		0.34(1) Zn3	0.33(-) Zn1
$6c$	0	0	0.36496(5) *+	A_1	0.38(2) Ni	0.44(1) Ni1	0.49(1) Zn1	0.076(-) Ni1 + 0.414(-) Zn2 (*P*)
$18h$	0.53079(7) *+	$\bar{x}$	0.34807(5) *+	D	0.4(4) Ni	0.18(2) Ni3	0.28(1) Zn2	0.047(-) Ni2 0.254(-) Zn3 (*Q*)
$18f$	0.1729(3) *+	0	0	D_d ♣			0.13(1) Zn4	0.022(-) Ni3 + 0.118(-) Zn4 (*R*)
$36i$	0.1744(6)+	0.1617(6) +	0.0247(2) +	D_d ("new")		0.006(2) Ni4		-
$36i$	0.2240(7)+	0.0789(7) +	0.00800(3) +	D_d		0.09(3) Ni2		-
$36i$	0.04167(1) ♠	0.15813(1) ♠	0.35823(1) ♠	D_d	0.7(2) Ni			-

+ ref. [11], ** ref. [17], ♠ ref. [10] and *+[This work].
♣ Environment for this position was not described in ref. [17].

Table 4. Electron count in pure β boron [9], NiB$_{48.5}$ [11], ZnB$_{\sim25}$ [17] and Ni$_{0.19}$Zn$_{1.24}$B$_{34.22}$ [this work].

Compound	# of B atoms in unit cell	# of Ni atoms in unit cell	# of Zn atoms in unit cell	# of electrons in the hexagonal unit cell
β Boron	106.66	-	-	320
NiB$_{48.5}$	104.1	2.14	-	316.58
ZnB$_{\sim25}$	103	-	4.12	317.24
Ni$_{0.19}$Zn$_{1.24}$B$_{34.22}$	102.65	0.561	3.719	316.51

If we assume electrons given by B, Ni and Zn to 3, 2 and 2, respectively in the unit cell [12].

Table 5. Electron densities (in [electrons/nm^3] x1000) between atoms connecting the boron clusters.

Standardized #	Bond						
	B1-B1	B2-B3	B4-B4	B5-B7	B6-B8	B9-B10	B13-B15
Ni$_{0.19}$Zn$_{1.24}$B$_{34.22}$ [This work]	-	0.34	-	0.39	0.49	0.64	0.32
NiB$_{60}$ [10]	0.29	0.36	0.56	0.39	0.36	0.39	-

Table 6. Positional[a] and displacement parameters of boron atoms within the 3.5 Å environment of B36 and metal atoms refined in the *R3* space group

Atom site / Void in $R\bar{3}m$	Atom in *R3*	$Ni_{0.19}Zn_{1.24}B_{34.22}$
B3	B3[a] in 9*b* (*x.y,z*); Occ. U_{11}[b]; U_{22}; U_{33}; U_{23}; U_{13}; U_{12}	*x*=0.4494(7), *y*= 0.0713(7), *z*=0.2525(5), 1.00 0.0069(7); 0.0086(8); 0.0064(4); -0.0006(7); -0.0011(7); 0.0047(7)
B3	B16[a] in 9*b* (*x.y,z*); Occ. U_{11}; U_{22}; U_{33}; U_{23}; U_{13}; U_{12}	*x*=0.4499(7), *y*=0.3773(7), *z*=0.2516(5), 1.00 0.0069(7); 0.0086(8); 0.0064(4); -0.0006(7); -0.0011(7); 0.0047(7)
B3	B20[a] in 9*b* (*x.y,z*); Occ. U_{11}; U_{22}; U_{33}; U_{23}; U_{13}; U_{12}	*x*=0.0442(7), *y*=0.2631(8), *z*=0.0821(5), 1.00 0.0069(7); 0.0086(8); 0.0064(4); -0.0006(7); -0.0011(7); 0.0047(7)
B3	B21[a] in 9*b* (*x.y,z*); Occ. U_{11}; U_{22}; U_{33}; U_{23}; U_{13}; U_{12}	*x*=0.2184(7), *y*=0.2619(7), *z*=0.0829(5); 1.00 0.0069(7); 0.0086(8); 0.0064(4); -0.0006(7); -0.0011(7); 0.0047(7)
B12	B7[a] in 9*b* (*x.y,z*); Occ. U_{11}=U_{22}; U_{33}; U_{23}; U_{13}; U_{12}	*x*=0.1796(7), *y*=0.0900(7), *z*= 0.1037(5), 1.00 0.0063(10); 0.0065(7); 0.0018(9); -0.0004(9); 0.0044(9)
B12	B15[a] in 9*b* (*x.y,z*); Occ. U_{11}=U_{22}; U_{33}; U_{23}; U_{13}; U_{12}	*x*=0.4858(7), *y*=0.2432(7), *z*=0.2312(5), 1.00 0.0063(10); 0.0065(7); 0.0018(9); -0.0004(9); 0.0044(9)
B14	B35[a] in 3*a* (0, 0,*z*); Occ. U_{11}=U_{22}; U_{33}; U_{23}=U_{13}=0; U_{12}	*z*=0.1140(11), 1.00 0.0064(7), 0.0048(13), 0.0032(4)
B14	B37[a] in 3*a* (0, 0,*z*); Occ. U_{11}=U_{22}; U_{33}; U_{23}=U_{13}=0; U_{12}	*z*=0.8838(2), 1.00 0.0064(7), 0.0048(13), 0.0032(4)
B13	B4[a] in 9*b* (*x.y,z*); Occ.; U_{iso}[c]	*x*=0.6104(1), *y*=0.2211(1), *z*=0.2783(6); 0.57(2); 0.0076(8)
B13	B11[a] in 9*b* (*x.y,z*); Occ.; U_{iso}	*x*=0.0569(10), y=0.1145(10), z=0.0578(6); 0.70(2), 0.0076(8)
B15	B36[a] in 3*a* (0, 0,*z*); Occ.; U_{iso}	*z*=0.0000[d], 0.78(1); 0.0088(5)
18*f*	Zn1[a] in 9*b* (*x.y,z*); Occ.; U_{iso}	*x*=0.1722(4), *y*=0.1719(4), *z*=0.0009(4), 0.144(2); 0.0088(5)
18*f*	Zn2[a] in 9*b* (*x.y,z*); Occ., U_{iso}	*x*=0.0331(10), *y*=0.1920(8), *z*=0.0010(5), 0.062(2); 0.0088(5)
18*f*	Zn22[a] in 9*b* (*x.y,z*); Occ.; U_{iso}	*x*=0.1845(8), *y*=0.0209(7), *z*=0.0012(5), 0.082(2); 0.0088(5)
D, 18*h*	Zn3[a] in 9*b* (*x.y,z*); Occ. U_{11}; U_{22}; U_{33}; U_{23}; U_{13}; U_{12}	*x*=0.2716(3), *y*=0.1360(3), *z*=0.0153(4), 0.306(2) 0.0087(5); 0.0116(5); 0.0112(4); -0.0016(5); 0.0029(4); 0.0045(5)
D, 18*h*	Zn4[a] in 9*b* (*x.y,z*); Occ. U_{11}; U_{22}; U_{33}; U_{23}; U_{13}; U_{12}	*x*=0.3939(3), *y*=0.1967(3), *z*=0.3189(4), 0.270(2) 0.0087(5), 0.0116(5), 0.0112(4); -0.0016(5), 0.0029(4), 0.0045(5)
D, 18*h*	Zn44[a] in 9*b* (*x.y,z*); Occ. U_{11}; U_{22}; U_{33};	*x*=0.1272(17), *y*=0.2322(13), *z*=0.0017(8), 0.036(2) 0.0087(5); 0.0116(5); 0.0112(4);

	U$_{23}$; U$_{13}$; U$_{12}$	-0.0016(5); 0.0029(4); 0.0045(5)
E, 6c	Zn5^a in 3a *(0,0,z)*; Occ.	z=0.7302(16); 0.288(4)
	U$_{11}$=U$_{22}$; U$_{33}$; U$_{23}$=U$_{13}$; U$_{12}$	0.0087(4), 0.0138(6); 0.0043(2)
E, 6c	Zn6^a in 3a *(0,0,z)*; Occ.	z=0.2704(16), 0.288(4)
	U$_{11}$=U$_{22}$; U$_{33}$; U$_{23}$=U$_{13}$; U$_{12}$	0.0087(4); 0.0138(6), 0.0043(2)
A$_1$, 6c	Zn7+Ni1^a in 3a *(0,0,z)*; Occ.	z=0.6356(16), 0.111(4) Zn+0.389(4) Ni
	U$_{iso}$	0.0053(2)
A$_1$, 6c	Zn8+Ni2^a in 3a *(0,0,z)*; Occ.	z=0.3656(16), 0.359(4) Zn+0.141(4) Ni
	U$_{iso}$	0.0053(2)

^{a}crystal structure data are standardized using the program Structure Tidy [26].

^{b}Anisotropic atomic displacement parameters U$_{ij}$ in [10^2 nm^2].

^{c}Isotropic atomic displacement parameters Uiso in [10^2 nm^2].

^{b} fixed atom coordinate.

Physical Properties of the Ternary Borides
$Ni_{21}Zn_2B_{20}$ and Ni_3ZnB_2

8.1. Introduction

Reaction of boron with Ni and Zn leads to the formation of phases with complex structures e.g., $Ni_{21}Zn_2B_{20}$ is a unique structure[1] with isolated B_{20} cages and a Ni_6-octahedron nested within each B_{20}-unit [1]. In contrast to this interleaved metal-boron clusters in $Ni_{21}Zn_2B_{20}$, the compound Ni_3ZnB_2 contains four-membered fragments of boron zigzag chains [1]. As both structure types in addition contain infinite nets of metal atoms, interesting physical properties may arise from the combination of typical metal features with the covalently bonded and more ceramic like boron aggregations. Therefore the aim of this study is to analyze the mechanical, electrical and magnetic properties of the compounds $Ni_{21}Zn_2B_{20}$ and Ni_3ZnB_2, which reveal a rather different boron-boron aggregation due to their different boron/metal ratio.

8.2. Experimental

Starting materials for alloy synthesis were Ni foil (Alfa Aesar, purity >99.8 mass%), zinc granules (Alfa Aesar, purity >99.9 mass%), boron pieces (ChemPur, Karlsruhe, purity 98 mass%) and nickel powder (-100 mesh; 99.9 mass%; PCR Inc. USA). Zinc drops were purified in an evacuated quartz tube by heating them 50°C below the boiling point of Zn (907°C). Samples of about 5g each were prepared from intimate blends of powders (40μm) of arc melted NiB_x master alloys and fine Zn-filings in proper compositional ratio. Hand milling of the NiB_x master alloy to a particle size below 40 μm (in a WC-mortar) was found to be necessary for a proper diffusion among Zn and NiB_x grains in order to achieve single-phase material. The powder blends were cold compacted in a steel die without lubricants,

---

[1] In our previous study we have reported on the crystal structure of $Ni_{21}Zn_2B_{24}$. [1]. However, the boron positions were incorrectly summed up and thus the correct chemical formula is $Ni_{21}Zn_2B_{20}$.

vacuum-sealed in quartz tubes, were heated up till 800°C and then annealed at this temperature for 4 days and subsequently water quenched. Then the specimens were hand milled in a WC-mortar within an argon filled glove box in which the powders were finally loaded into a 10 mm diameter graphite die for hot pressing under Ar in an uniaxial hot press system (HP W 200/250-2200-200-KS) at 800°C for 1 hour employing a pressure of 56 MPa. After removing a 0.5 mm thick surface layer (grinding at an Al_2O_3-wheel), a 1 mm slice of the hot pressed cylinders (~9 mm diameter and 8 mm height was polished using standard procedures in order to inspect microstructure and composition by light optical microscopy (LOM) and scanning electron microscopy (SEM) via Electron Probe Micro-Analyses (EPMA) on a Zeiss Supra 55 VP equipped with an EDX system operated at 20 kV. For Ni:Zn ratios the binary compound Ni_2Zn_{11} at the Zn-rich boundary (defined at 15.0 at.% Ni [2]) was used as EPMA standard. The differences between measured and nominal compositions were found to be less than 1 at. %.

Percentage porosities were calculated from the differences between the calculated X-ray densities of $Ni_{21}Zn_2B_{20}$, Ni_3ZnB_2 [1] and the densities of the samples measured in distilled water using Archimedes' principle. X-ray powder diffraction data were collected from the alloys before and after hot pressing employing a Guinier-Huber image plate system with monochromatic $CuK_{\alpha1}$ radiation (8°<2θ<100°). For both sample specimens quantitative Rietveld refinements of the X-ray powder diffraction data with the FULLPROF program [3] based on the atom parameters derived from the single crystal studies of $Ni_{21}Zn_2B_{20}$ and Ni_3ZnB_2 [1] confirm the structure types and assured single-phase condition for Ni_3ZnB_2 but traces of Ni_2Zn_{11} as a secondary phase in $Ni_{21}Zn_2B_{20}$ (see Fig. 1).

Thermal expansion from 4.2 to 300 K was measured in a miniature capacitance dilatometer [4], using the tilted plate principle [5, 6]. For the measurement the sample is placed in a hole of the lower ring-like silver capacitance plate, which is separated from the silver upper capacitor plate by two needle bearings. This equipment can also be used under magnetic fields up to 9 Tesla.

The Vickers hardness (HV) was measured under the load of 0.98, 1.47 and 1.96 N (corresponding to loads of 100, 150 and 200 ponds) sustained for 10 seconds in an Anton Paar MHT 4 micro-hardness tester, which is mounted on a Reichert POLYVAR optical microscope. The micro-hardness HV (Vickers hardness) was computed from the relation:

$$HV = \frac{2F\sin\frac{136°}{2}}{d^2} \qquad (1)$$

where F is the load applied and d is the length of the diagonal left by the Vickers diamond indenter in the sample. For resonant ultrasonic spectroscopy (RUS) measurements at the University of Vienna (RUS2), the cylindrical samples were mounted edge-to-edge between the two piezo-transducers and excited via a network analyser in the frequency range from 25 kHz to 500 kHz.
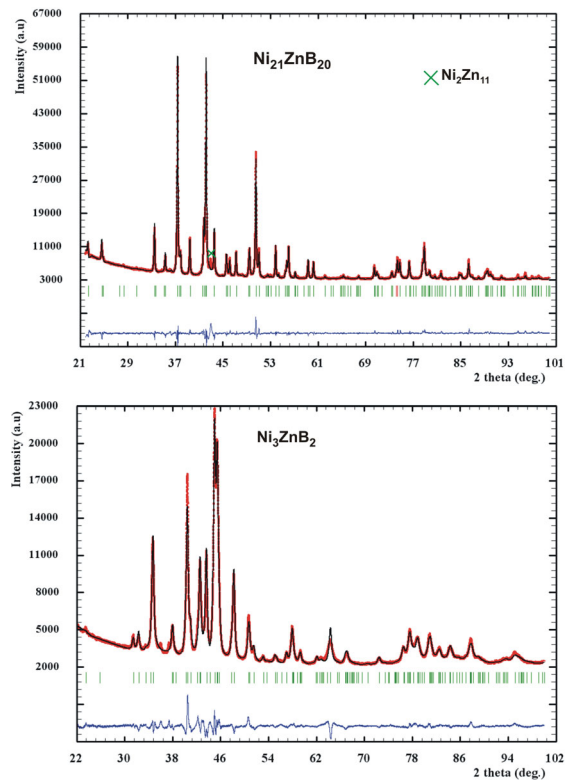

Figure 1. Rietveld refinement of X-ray powder data of $Ni_{21}Zn_2B_{20}$ and Ni_3ZnB_2.

Electrical resistivity measurements in a temperature range from 4.2 to 300 K were carried out in a He4 cryostat, using a home made equipment (four point technique). At temperatures above 300 K the electrical resistivity and the Seebeck coefficient were measured simultaneously in a commercial equipment (model ZEM-3, ULVAC, Japan; for details see ref. [7]). For magnetic measurements a SQUID susceptometer was used.

The specific heat experiments were performed with a commercial physical property measurement system (PPMS) in the temperature range of 2 to 300 K and in a 3He/4He-dilution refrigerator down to a base temperature of 60 mK employing a standard relaxation method [8].

8.3. Results and Discussion.

8.3.1. Physical properties

8.3.1.1. Elastic properties

Resonant Ultrasound Spectroscopy was used to determine elastic properties via the eigenfrequencies of the samples and knowledge of sample mass and dimensions. The RUS theory [9, 10] establishes the relation between kinetic energy and elastic energy and hence makes it possible to calculate the eigenfrequencies of a sample based on its mass, dimensions and a set of elastic constants. A least squares fit is carried out by minimizing the sum of the squared differences between the measured and the calculated eigenfrequencies to derive the elastic properties. The parameters of this fit were the elastic constants or moduli (i.e. in this case the Young's modulus and the Poisson's ratio as the average elastic symmetry of the polycrystalline samples is isotropic). The independent variables were the first 25 eigenfrequencies of the respective sample and they were fitted via the Nelder-Mead method [11]. Shear modulus and bulk modulus were calculated by equations:

$$G = \frac{E}{2(1+\upsilon)} \qquad\qquad (2)$$

$$B = \frac{E}{2(1-2\upsilon)} \qquad\qquad (3)$$

The elastic properties derived for $Ni_{21}Zn_2B_{20}$ and Ni_3ZnB_2 are summarized in Table 1. Dependencies of elastic modulus values upon density for $Ni_{21}Zn_2B_{20}$ and Ni_3ZnB_2 are shown in Fig. 2. A linear extrapolation to 100% density yields Young's moduli of 263 and 225 GPa for $Ni_{21}Zn_2B_{20}$ and Ni_3ZnB_2, respectively.

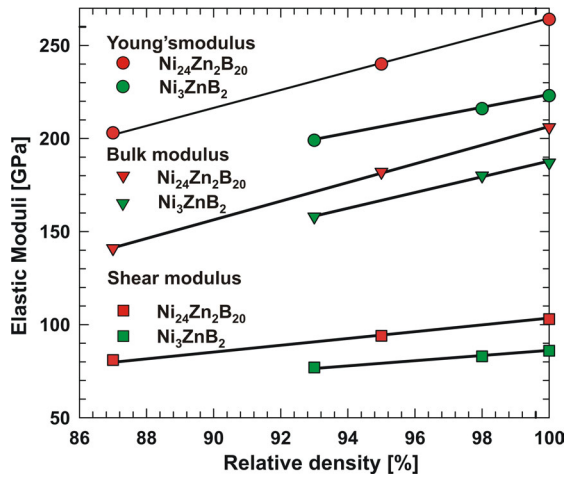Figure 2. Elastic moduli vs. relative density for $Ni_{21}Zn_2B_{20}$ and Ni_3ZnB_2, extrapolated to 100% density: E (Young's Modulus) 264 and 223 GPa, B (Bulk Modulus) 206 and 187 GPa and G (Shear Modulus) to 103 and 86 GPa, respectively.

8.3.1.2. Hardness

Hardness of NiB, $Ni_{21}Zn_2B_{20}$ and Ni_3ZnB_2 was measured on as cast samples with big grains of the phases under investigation in order to ensure the measurement of intrinsic hardness of materials. Hardness values decrease with increasing force from 0.98 to 1.47 N, but saturate from 1.47 N to 1.96 N for all three compounds as shown in Fig. 3 and Table 1. The hardness value reported for NiB is 15.3 GPa (as measured for a load of 50 g) [12]. It corresponds well to that investigated in this work. Due to the low symmetry of Ni_3ZnB_2 the vertical (d_1) and transverse (d_{11}) diameters of indentation differ within an averaged d_1/ d_{11} ratio of 1.46. Figure 3 clearly shows the dependency of the hardness upon the boron content and the boron-boron aggregation in the structure of the compounds investigated. NiB with infinite boron chains has a hardness superior to $Ni_{21}Zn_2B_{20}$ with Ni-octahedra nested $B_{20}Ni_6$ cages and superior to Ni_3ZnB_2 with B_4-chain fragments. This trend is also seen in the mechanical properties where $Ni_{21}Zn_2B_{20}$ exhibits higher elastic moduli than boron-poor Ni_3ZnB_2 (see Table 1).
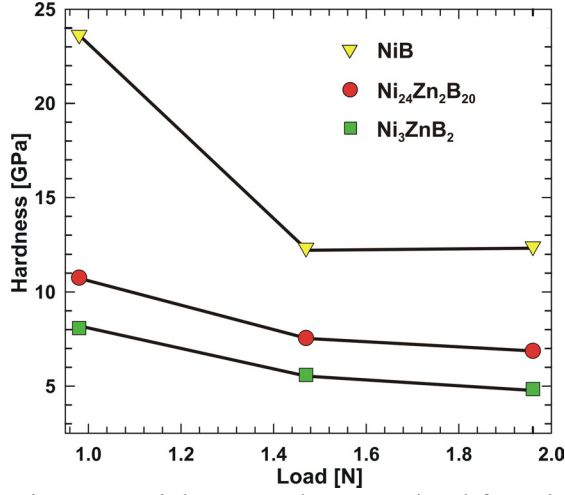
Figure 3. Vickers Hardness vs. load for NiB, $Ni_{21}Zn_2B_{20}$ and Ni_3ZnB_2.

8.3.1.3. Thermal expansion

Figure 4 shows the thermal expansion $\Delta l/l_0$ of $Ni_{21}Zn_2B_{20}$ and Ni_3ZnB_2 as a function of temperature. It is obvious that $\Delta l/l_0$ decreases almost linearly from room temperature to about 150 K. The thermal expansion coefficient α follows from a temperature derivative of the length change, i.e.,

$$\alpha = \frac{\partial \Delta l}{\partial T}\frac{1}{l_0} \tag{4}$$

$\alpha = 8*10^{-6}$ and $10.4*10^{-6}$ K^{-1} was derived for $Ni_{21}Zn_2B_{20}$ and Ni_3ZnB_2 in the temperature range from 150 – 250 K, respectively. The temperature dependent thermal expansion was analysed following a semi-classical treatment by Mukherjee (details are described in ref. [13]) taking into account three- and four-phonon interactions and considering an anharmonic potential, using both the Debye model for the acoustic phonons, and the Einstein approximation for the optical modes. The length change $\Delta l/l$ (T_0) is given by

$$\frac{\Delta l}{l(T_0)} = \frac{\langle x\rangle_T - \langle x\rangle_{T_0}}{x_0} \qquad \langle x\rangle_T = \frac{\gamma}{2}T^2 + \frac{3g}{4c^2}\left[\varepsilon - G\varepsilon^2 - F\varepsilon^3\right]$$

$$\varepsilon = \left\{\left(\frac{3}{p}\right)3k_B T\left(\frac{T}{\theta_D}\right)^3 \int_0^{\frac{\theta_D}{T}}\frac{z^3 dz}{e^z - 1} + \left(\frac{p-3}{p}\right)\frac{k_B\theta_E}{e^{\theta_E/T} - 1}\right\} \tag{5}$$

where γ is the electronic contribution to the average lattice displacement, θ_D is the Debye temperature, θ_E is the Einstein temperature, and p is the average number of phonon branches actually excited over the temperature range. G, F, c, and g are further material dependent constants. Debye (θ_D) temperatures obtained from least square fits of equations

144

(5) to the experimental data of $Ni_{21}Zn_2B_{20}$ and Ni_3ZnB_2 reveal θ_D = 349 K and 346 K respectively.

Magnetostriction measurements carried out at 4.2 K with magnetic fields up to 9 Tesla did not indicate any field induced ordering phenomena.
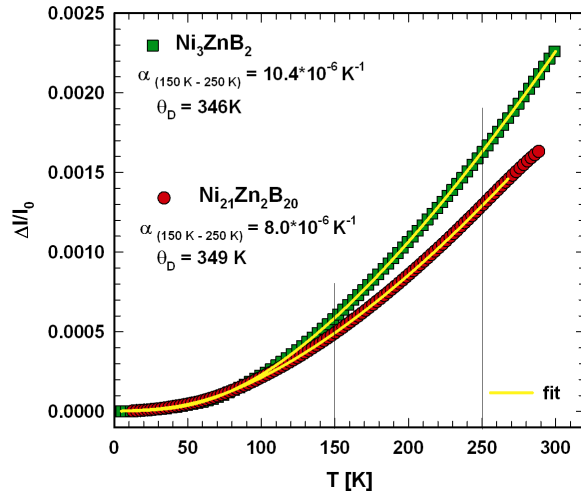

Figure 4. Thermal expansion vs. temperature for $Ni_{21}Zn_2B_{20}$ and Ni_3ZnB_2.

8.3.1.4. Specific Heat

Temperature dependent zero-field specific heat measurements, C/T vs. T, for $Ni_{21}Zn_2B_{20}$ and Ni_3ZnB_2 are displayed in Figs. 5a, b respectively. For a closer view on the low temperature data the inserts of Figs. 5 a, b show the corresponding C/T vs. T^2 graphs revealing for Ni_3ZnB_2 below 10 K a simple $C(T) = \gamma T + \beta T^3$ behavior with γ = 7 mJmol^{-1}K^{-2} and β= 8.7*10^{-5} Jmol^{-1}K^{-4} as typical for a simple Pauli-paramagnetic metal. The β coefficient refers to a low temperature Debye temperature of 510 K. For $Ni_{21}Zn_2B_{20}$, however, a distinctly different behavior with a small low temperature upturn and significant non-linearity in C/T vs. T^2 is observed. Instead of a T-linear electronic contribution there is a contribution, which is presumably of magnetic origin dominating the low temperature heat capacity. At elevated temperatures, the specific heat of both compounds, $Ni_{21}Zn_2B_{20}$ and Ni_3ZnB_2, is clearly dominated by the lattice contribution, which is analyzed in terms of Debye and Einstein contributions yielding the lattice heat capacity as

$$C_{ph}(T) = c_0 \frac{3R}{\omega_D^3} \int_0^{\omega_D} \frac{\omega^2 \left(\frac{\omega}{2T}\right)^2}{\sinh^2\left(\frac{\omega}{2T}\right)} d\omega + \sum_i c_i R \frac{\left(\frac{\omega_i}{2T}\right)^2}{\sinh^2\left(\frac{\omega_i}{2T}\right)} \qquad (6)$$

where R is the gas constant, ω_D and ω_i are Debye and Einstein frequencies and c_0 and c_i are the corresponding spectral weights. When excluding the low temperature data below 10 K, the specific heat of $Ni_{21}Zn_2B_{20}$ in Fig. 5a is acceptably approximated by a lattice heat capacity C_{ph} which consists of one Debye and two Einstein contributions with $\omega_D = 251$ K and $c_0 = 30$, $\omega_1 = 306$ K and $c_1 = 36$ as well as $\omega_2 = 761$ K and $c_2 = 63$. The corresponding fit is displayed as solid line in Fig. 5a.
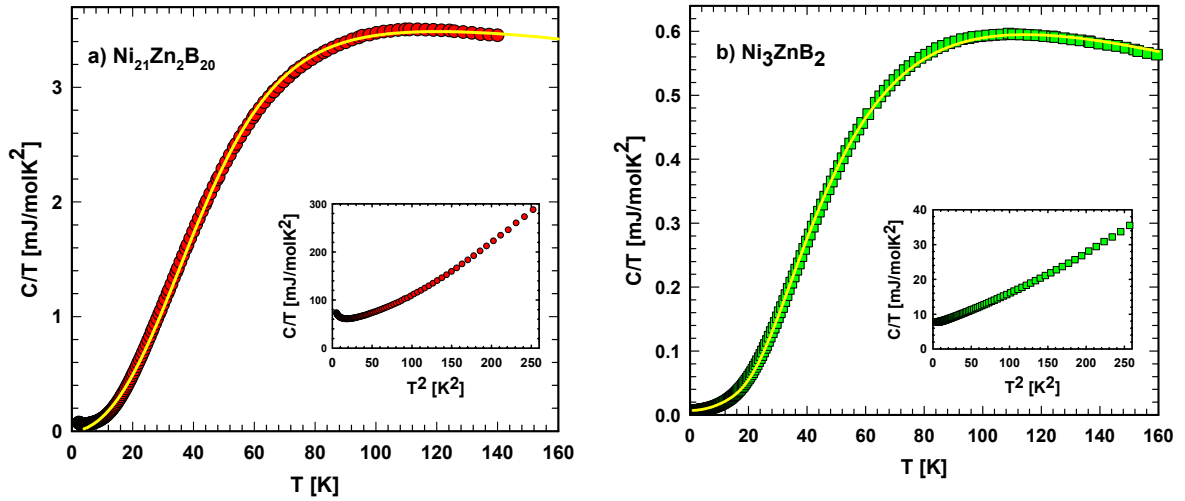

Figure 5. Specific heat Cp/T vs. T and T^2 of $Ni_{21}Zn_2B_{20}$ (a) and Ni_3ZnB_2 (b) the yellow solid lines are fits in terms of Debye and Einstein models (see text).

Introducing a third Einstein frequency by splitting the spectral weight c_2 essentially reproduces this result (ω_3 remains near 750 K). In the case of Ni_3ZnB_2 (Fig. 5b) the specific heat data (from 2 K to 180 K) are rather well accounted for by a lattice heat capacity consisting of Debye and three Einstein contributions with $\omega_D = 269$ K and $c_0 = 3$, $\omega_1 = 191$ K and $c_1 = 3$, $\omega_2 = 348$ K and $c_2 = 6$ and $\omega_3 = 714$ K with $c_3 = 6$; an electronic contribution with $\gamma = 7$ mJ mol^{-1} K^{-2} was added (see the solid line in figure 4b).

This analysis of the lattice heat capacity indicates that the boron related high energy Einstein modes display at similar energies in these two compounds with spectral weights being in clear correspondence with the boron stoichiometries of $Ni_{21}Zn_2B_{20}$ and Ni_3ZnB_2.

8.3.1.5. Magnetic properties

The temperature dependent magnetization measurements displayed in Fig. 6 reveal a paramagnetic behavior of $Ni_{21}Zn_2B_{20}$ as well as Ni_3ZnB_2 suggesting almost filled 3d states of Ni by contributions from B and Zn valence electrons. There is some discrepancy with respect to the expected paramagnetic linear scaling of the 0.1 T and 3 T data, which is attributed to the presence of a small amount of Ni_2Zn_{11} impurities in particular in Ni_3ZnB_2 as indicated by a very little peak in the powder pattern. The temperature dependent susceptibility, $M(T)/H$, of $Ni_{21}Zn_2B_{20}$ is clearly dominated by a Curie-Weiss like paramagnetic susceptibility, $\chi(T)=C/(T-\theta)$. A fit of the $M(T, 3 T)/H$ data (see Fig. 6a) results in a Curie constant $C = 0.48*10^{-4}$ emu K g^{-1} and a paramagnetic Curie temperature $\theta = -5$ K yielding a rather small effective moment $\mu_{eff}= 0.17$ μ_B/Ni atom. Any temperature independent Pauli paramagnetic like contribution is rather small, i.e. $\chi_0 \sim 7*10^{-8}$ emu g^{-1} may define an upper limit. In the case of Ni_3ZnB_2 shown in Fig. 6b, the susceptibility is clearly dominated (in particular at temperatures above 50 K) by a weakly temperature dependent Pauli susceptibility, $\chi(T) = \chi_0 (1-aT^2)$, yielding $\chi_0 = 2.26*10^{-6}$ emu g^{-1} and $a = 2.84*10^{-6}$ K^{-2} when analyzing the 3 T data in Fig. 6b. A Curie like contribution due to paramagnetic impurities yields $C= 0.91*10^{-4}$ emu K g^{-1} and $\theta \sim -8$ K. The effective paramagnetic moment per Ni atom is of similar magnitude for both compounds and might relate to paramagnetic impurities and possibly also to an intrinsic localization of moments near structural defects.
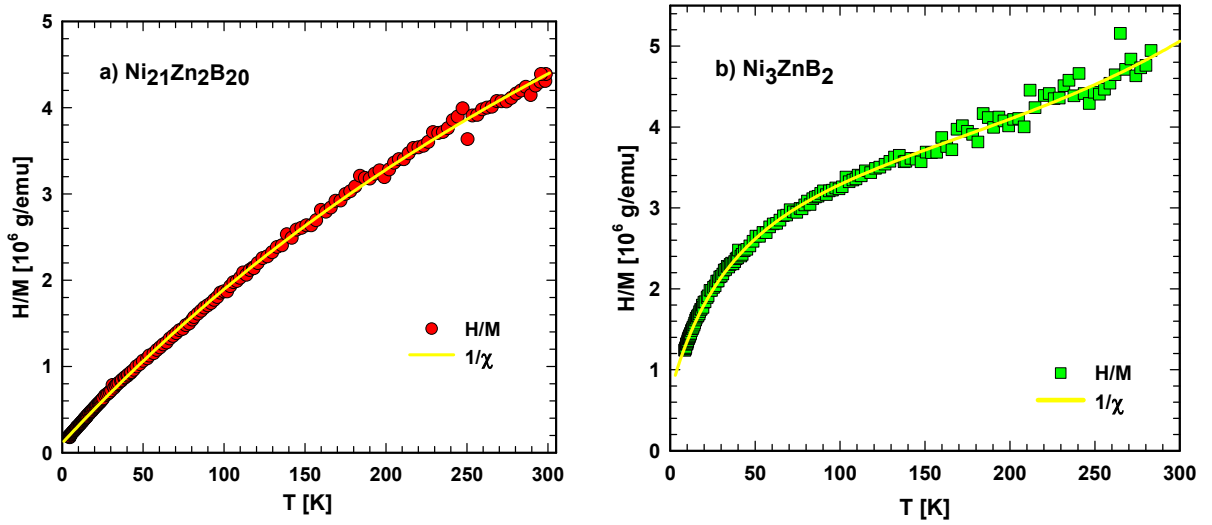
Figure 6. Temperature dependent inverse susceptibility, *H/M*, of $Ni_{21}Zn_2B_{20}$ (a) and Ni_3ZnB_2 (b) measured at 3 T. Solid lines represent fits as explained in the text.

8.3.1.6. Electrical Resistivity and Seebeck Coefficient

The temperature dependent electrical resistivity ρ of $Ni_{21}Zn_2B_{20}$ and Ni_3ZnB_2 is shown in Figs. 7a and 7b. While the former exhibits a pronounced curvature of $\rho(T)$ in the entire temperature range up to 900 K, the latter is characterized by an almost linear temperature dependence for T > 50 K. Similar residual resistivities refer to similar sample qualities of both ternary compounds. Furthermore, the inset of Fig. 7a shows a tiny increase of the electrical resistivity upon cooling (about 1 $\mu\Omega$cm) below 20 K for $Ni_{21}Zn_2B_{20}$. Since the material is non-magnetic, this feature is supposed to be caused by small amounts of Ni being statistically dispersed in the otherwise non-magnetic host $Ni_{21}Zn_2B_{20}$, triggering Kondo type of interactions between the conduction electrons and the magnetic moments of Ni. Note that the Kondo effect occurs already on an impurity level of several *ppm* in a host metal. The much larger overall variation of the electrical resistivity of $Ni_{21}Zn_2B_{20}$ compared to Ni_3ZnB_2 might be a consequence of a much stronger electron-phonon interaction in the former.
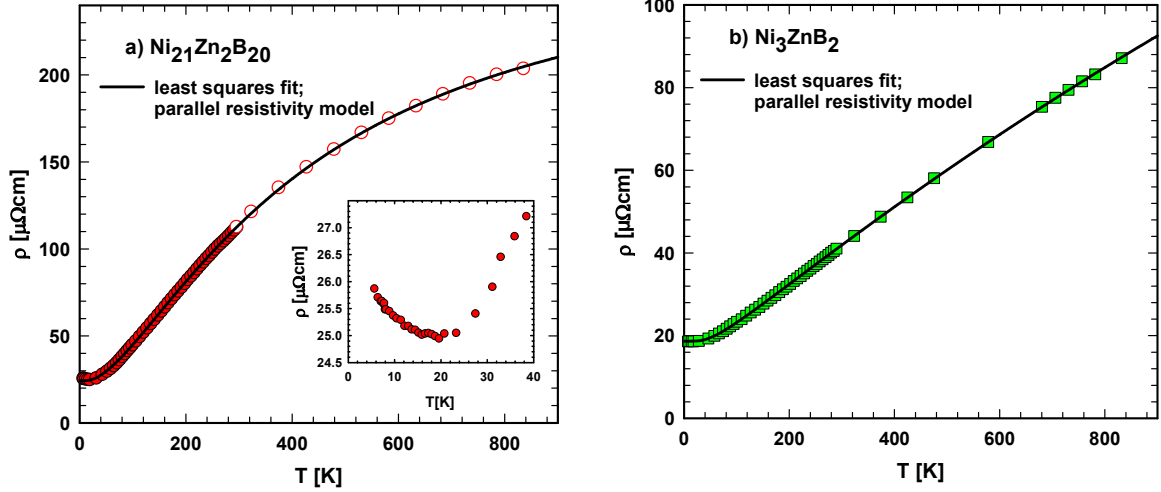
148

Figure 7. Temperature dependent resistivity ρ of $Ni_{21}Zn_2B_{20}$ (a) and Ni_3ZnB_2 (b). The inset in panel (a) shows low temperature details of $\rho(T)$.

In order to quantitatively account for the temperature dependence of both data sets with the very same model, the parallel resistivity model is selected. Systems with resistivities of the order of several hundred $\mu\Omega$cm are prone to reach the saturation limit at high temperatures, once the electronic mean free path becomes comparable to interatomic distances. In such a case, the parallel resistance model [14] can be used, i.e.,

$$1/\rho = 1/\rho_i + 1/\rho_s, \tag{7}$$

where ρ_i is the ideal resistivity, represented by a proper model able to account for the electron-phonon interaction. ρ_s is a shunt resistivity near to the saturation value. Least squares fits employing the Bloch-Grüneisen formula as a representative of $1/\rho_i$ fail to describe the entire temperature range of $Ni_{21}Zn_2B_{20}$. It turns out that a model developed by Hellman and Hartford [15] is best suited to be used in Eqn. 7. When the mean free path of electrons in a metal is short, the momentum dependence of scattering can be ignored and the resistivity is simply proportional to the weighted integral over the phonon density [15]. This model involves essentially two parameters T_{m1} and T_{m2}, which confine a flat band of bosons. Least squares fits (solid lines in Figs. 7a,b) reveal $T_{m1} = 50$ and $T_{m2} = 2300$ K for $Ni_{21}Zn_2B_{20}$ as well as $T_{m1} = 140$ and $T_{m2} = 165$ K for Ni_3ZnB_2. These distinctly different scales refer to significantly different phonon dynamics in both compounds. Different phonon spectra were concluded already from heat capacity measurements.

Least squares fits below 300 K can be carried out employing the standard Bloch-Grüneisen model. In both cases the Debye temperature is of the order of 310 K, but the electron-phonon interaction constant is more than 4 times larger in the case of $Ni_{21}Zn_2B_{20}$ compared to Ni_3ZnB_2. A similarity of the Debye temperature was derived from the specific heat data, too.

In view of the dominant metallic behaviour of $Ni_{21}Zn_2B_{20}$ and Ni_3ZnB_2 Seebeck coefficients (S) for both compounds are expected to be small and negative. In fact, both Ni based compounds vary in the range of a few μV/K (see Fig.8) and the negative sign of the thermopower refers to electrons as the majority charge carriers. These low values make the thermoelectric power factor S^2/ρ small (maximum values: about 0.012 W/mK^2 @ 600 K for $Ni_{21}Zn_2B_{20}$ and 0.04 W/mK^2 @ 300 K for Ni_3ZnB_2).
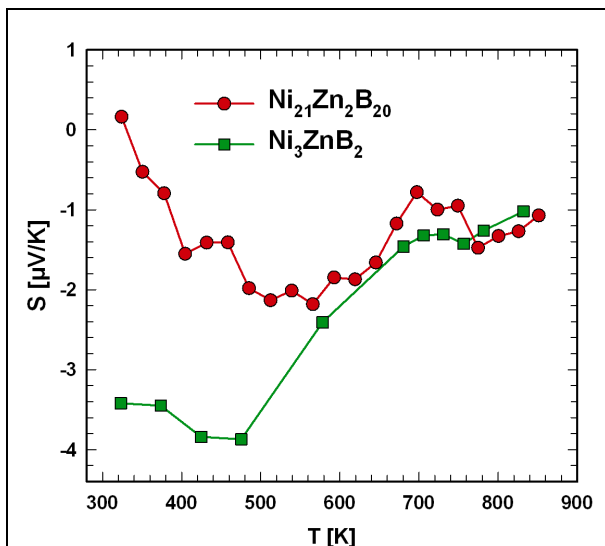
Figure 8.Seebeck coefficient S vs. temperature for $Ni_{21}Zn_2B_{20}$ and Ni_3ZnB_2.

8.4. Conclusion

The investigation of physical properties (mechanical, electrical and magnetic) revealed significant differences for the compounds $Ni_{21}Zn_2B_{20}$ and Ni_3ZnB_2, which differ in boron-boron aggregation and bonding due to their different boron/metal ratio. The higher the boron/metal ratio the higher the elastic moduli, the higher Vickers hardness but the smaller are the thermal expansion coefficients. At elevated temperatures, the specific heat C_p of both compounds is clearly dominated by the lattice contribution and the boron related high energy Einstein modes are at similar energies with spectral weights being in

clear correspondence with the boron stoichiometries of both borides. Temperature dependent magnetization measurements reveal a paramagnetic behavior for both compounds suggesting almost filled 3d states of Ni by contributions from B and Zn valence electrons. Electrical resistivities attest a dominant metallic behaviour for both $Ni_{21}Zn_2B_{20}$ and Ni_3ZnB_2 yielding negative Seebeck coefficients (electrons as the majority charge carriers) in the range of a few $\mu V/K$.

The metallic state of both compounds prevents a significant thermoelectric performance, although the complex crystal structure formed by boron rings might favour promising thermoelectric properties. Reducing the electron density by proper doping the ternary materials will be a future task.

8.5. References

[1]   Z.P. Malik, O. Sologub, A. Grytsiv, G. Giester, P. Rogl, Inorg. Chem 50 (2011) 7669-7675

[2]   A. Johansson, H. Ljung, S. Westman, Acta Chem. Scand 22 1968 2743-2753.

[3]   T. Roisnel, J. Rodriguez-Carvajal, Materials-Science-Forum (1) 118 2010 378-381.

[4]   M. Rotter, H. Müller, E. Gratz, M. Doerr, M. Löewenhaupt, Rev. Sci. Instrum 69(7) (1998) p. 2742.

[5]   G. Brändli, R. Griessen, Cryogenics 13 (1973) 299.

[6]   J. Genossar, M. Steinitz, Rev. Sci. Instrum 61 (1990)2469.

[7]   G. Rogl, A. Grytsiv, E. Bauer, P. Rogl, M. Zehetbauer, Intermetallics, **18**, 57-60 (2010)

[8]   R. Bachmann et al, Rev. Sci. Instrum. 43 (1972) 205.

[9]   B.J. Zadler, J.H. Le Rousseau, J.A. Scales, M.L. Smith, Geophys. J. Int 156 (2004) 1254-169.

[10]   A. Migliori, J.L. Sarrao, Resonant Ultrasound Spectroscopy: applications to physics, materials measurements and non destructive evaluation. John Wiley & Sons. Inc., New York (1997).

[11]   J.A. Nelder, R. Mead, Comput J 7 (1965) 308–313.

[12]   A.S. Sobolev, A.S. Fedorov: 'Phase Diagram of the Nickel-Boron System', Izv. Akad. Navk. SSSR, Neorg. Meter 3(4) (1967) 723-727.

[13]   G.D. Mukherjee, C. Bansal, A. Chatterjee, Phys. Rev. Lett 76(11) (1996) 1876.

[14]   M. Calandra, O. Gunnarsson, Phys. Rev. B 66 (2002) 205105.

[15]   E.S. Hellman and E.H. Hartford, Jr., Phys. Rev B 47 (1993) 11346.

Table 1. Nominal compositions, (d) density, (ν) Poisson's ratio, (E) Young's modulus, (B) Bulk Modulus, (G) Shear modulus, (θ_D) Debye temperature, (ρ_o) residual resistivity for hotpressed samples of $Ni_{21}Zn_2B_{20}$ and Ni_3ZnB_2. Vickers microhardness was measured for a load of 1.96 N sustained for 10s on melted bulk alloys.

Nominal composition Ni-Zn-B at. %	Compound	NiB_x grain size , μm	d %	ν (±0.01)	E GPa (±1)	B GPa	G GPa	θ_D K Resistivity	θ_D K Thermal expansion	θ_D K Specific heat (low T)	ρ_o μΩcm	Hardness GPa Bulk alloy
44-6-50	$Ni_{21}Zn_2B_{20}$	20	95	0.28	240	182	94	315	349	-	26	-
44-6-50	$Ni_{21}Zn_2B_{20}$	40	87	0.26	203	141	81	-	-	-	-	6.87
50-16-34	Ni_3ZnB_2	20	98	0.30	216	180	83	320	346	510	20	-
50-16-34	Ni_3ZnB_2	40	93	0.29	199	158	77	-	-	-	-	4.99
50-0-50	NiB	>100										12.41

Phase Equilibria and Crystal Structures in the System Ce-Zn-Si

9.1. Introduction

Zinc-based alloys with rare-earth metals are used in several engineering applications and are employed to replace cast iron because of similar properties and higher machinability [1]. Rare earths (RE) improve the mechanical performance, tensile strength, hardness and also the corrosion resistance by removing impurities from the grain boundaries of their alloys with zinc [2]. Silicides may find applications as contact materials or in optoelectronic devices or simply as grain refiners [3]. As far as high strength lightweight alloys for automotive applications are concerned [4], the Ce-Zn system is an important part of the multinary Mg-based alloy system Mg-Zn-Mn-RE-(Si). Besides the compound CeZnSi, which has been reported [5] to be paramagnetic within the temperature range of 77-300K, no phase diagram has yet been reported for the system Ce-Zn-Si. Therefore the present work intends to provide detailed information on phase equilibria and crystal structures in the Ce-Zn-Si system. The formation of $BaAl_4$-type structures has been investigation along the sections, $La(Ni_{1-x}Zn_x)_2Si_2$ and $Ce(Ni_{1-x}Zn_x)_2Si_2$.

9.2. Experimental

Samples were prepared from cerium ingots (Alfa Aesar, purity >99.9 mass%), lanthanum ingots (Auer Remy, 99.9 mass %) zinc granules (Alfa Aesar, >99.9 mass%), Ni foil (Alfa Aesar, >99.8 mass%) and silicon pieces (Alfa Aesar, 6N). Zinc

drops were purified in an evacuated quartz tube by heating them at ~750°C, below the boiling point of Zn (907°C). Cerium and lanthanum ingots were mechanically surface cleaned before use.

Samples for ternary phase analysis were prepared from intimate blends of powders of arc melted master alloys $CeSi_x$ (varius x; powdered under cyclohexane) and fine Zn-filings in proper compositional ratios. These blends were cold compacted in a steel die without lubricants, vacuum-sealed in quartz tubes, heated from 420°C to 800°C at the rate of 1°C/min and then annealed at his temperature for 4 days. After water quenching the samples were re-powderized under cyclohexane in order to ensure homogeneity. The samples were once again cold compacted and annealed at 800°C for 7 days and subsequently water quenched. Ce-Ni-Si samples have been prepared by direct arc melting of the elements in an Ar atmosphere on a water-cooled Cu hearth and were then subjected to annealing at 800°C after sealing in quartz tubes under vacuum. Polycrystalline quaternary samples $\{La,Ce\}(Ni_{1-x}Zn_x)_2Si_2$ were prepared from intimate blends of powders of arc melted master alloys $\{La,Ce\}Ni_xSi_2$ and fine Zn-filings in proper compositional ratios. The cold compacts were treated as described above, but annealed for 7 days prior to quenching in cold water.

X-ray powder diffraction data were collected from each alloy in as cast and annealed state employing a Guinier-Huber image plate system with monochromatic $CuK_{\alpha 1}$ radiation (8°<2θ<100°). Precise lattice parameters were calculated by least squares fits to the indexed 2θ values calibrated with Ge as internal standard (a_{Ge} =0.565791 nm). Quantitative Rietveld refinements of the X-ray powder diffraction data were performed with the FULLPROF program [6].

Single crystals were picked either from crushed reguli or from the residue of the flux syntheses. Quaternary single crystals were grown from Zn flux starting from a cold

compacted pellet ($Ce_2Ni_4Si_8$ + Zn-filings = $Ce_2Ni_4Si_8Zn_{86}$ (in at. %)), which was heated to 900 °C at the rate of 1°C/min and then cooled to 800°C at the same rate. After annealing for 4 days at this temperature the sample was subsequently quenched in water and then boiled with 15% aqueous solution of HCl in a water bath in order to dissolve the extra Zn. Crystals were washed many times with distilled water and dried. Inspections on an AXS-GADDS texture goniometer assured high crystal quality, unit cell dimensions and Laue symmetry of the specimens prior to the X-ray intensity data collections on a four-circle Nonius Kappa diffractometer equipped with a CCD area detector employing graphite monochromated MoKα radiation (λ=0.071069 nm). Orientation matrices and unit cell parameters were derived using the program DENZO [7]. No special absorption corrections were performed because of the rather regular crystal shapes and small dimensions of the investigated specimens. The structures were solved by direct methods and were refined with the SHELXL-97 program [8, 9] within the Windows version WINGX [10].

After reaction during annealing the samples had almost powder-like consistency, too soft to be polished by standard procedures. This problem was overcome by casting the sample powder along with conducting glue into a cylindrical mould of ~5mm diameter. After hardening several of the powder cylinders were hot compacted in conductive resin and were ground and polished under glycerin instead of water in order to avoid oxidation of the samples. Microstructures and compositions were examined by light optical microscopy (LOM) and scanning electron microscopy (SEM) via Electron Probe Micro-Analyses (EPMA) on a Zeiss Supra 55 VP equipped with an EDX system operated at 20 kV.

9.3. Results and Discussion.

9.3.1. Binary Boundary Systems

The binary system Ce-Zn was recently reinvestigated by the authors [11]. The latest experimentally established phase diagram of the system Ce-Si was reported by Bulanova et al. [12]. Additional phases, however, have been described such as Ce_2Si_{3-x}, x=0.3 [13] and the high-pressure phases $CeSi_5$ and Ce_2Si_7 [14]. The Zn-Si system (degenerate eutectic) was taken from [15]. All crystal data relevant to the unary and binary boundary phases in the Ce-Zn-Si system are compiled in Table 1.

9.3.2. The System Ce-Zn-Si

9.3.2.1. Structural Chemistry

9.3.2.1.1. *The crystal structure of a novel cerium zinc silicide $Ce_7Zn_{21}(Zn_{1-x}Si_x)_2$, x=0.28*

A single crystal of prismatic shape was selected from the crushed regulus with nominal composition $Ce_{25}Zn_{60}Si_{15}$ (in at.%). The X-ray diffraction pattern of the single crystal was fully indexed with orthorhombic symmetry (a=1.55722(3), b=1.71942(3), c=0.44772(1) nm). Systematic absences for *h0l, h=2n+1, 0kl, k=2n+1* proved consistency with the space group types *Pbam* and *Pba*2. Direct methods employing the centrosymmetric space group: *Pbam* yielded an atom arrangement of 12 Zn atoms of which one showed smaller electron density due to a possibly partial occupation by Si atoms. Results of the refinement for the new structure type $Ce_7Zn_{21}(Zn_{1-x}Si_x)_2$ (x=0.28), which converged to R_{F^2}=0.029 with anisotropic atom displacement parameters (ADPs) and with residual electron densities smaller than $\pm3.02e^-/Å^3$, are summarized in Tables 2, 3 including interatomic distances. The residual electron density peak appears in the structure as a ripple near the heavy Ce-

157

atom at a distance 0.60 Å. With the Zn/Si-substitution in one site, the composition calculated from the refinement ($Ce_{23.3}Zn_{74.8}Si_{1.9}$ in at.%) is in good agreement with the composition $Ce_{24.1}Zn_{73}Si_{2.9}$ found from EPMA.
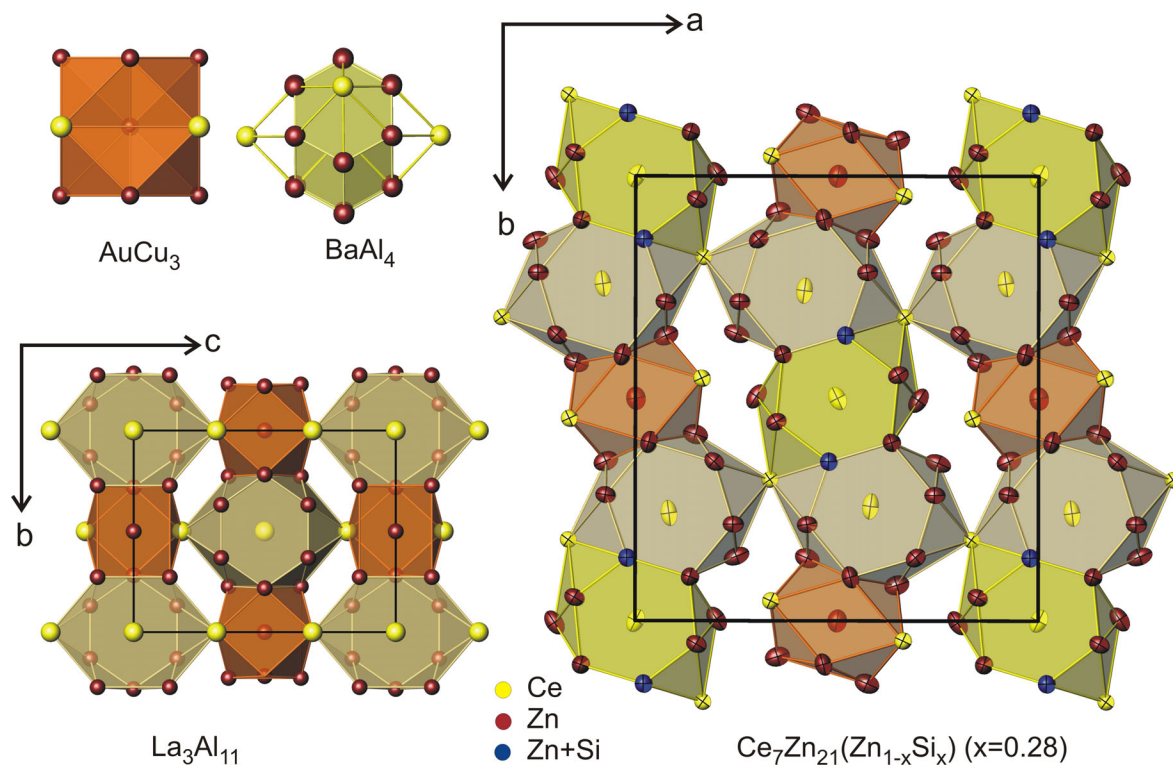
Figure 1. The crystal structure of $Ce_7Zn_{21}(Zn_{1-x}Si_x)_2$ (x=0.28) projected on the *ab* plane and the relationship with the structure of La_3Al_{11} as well as the structural units $AuCu_3$ and $BaAl_4$. Atoms are presented with anisotropic atom displacement parameters from single crystal refinement.

The structure of $Ce_7Zn_{21}(Zn_{1-x}Si_x)_2$ is shown in Fig. 1 in a projection on the *ab* plane. Coordination polyhedra of all atoms are presented in Fig. 2. The nearest neighbor shells around Ce-atoms are essentially formed by Zn-atoms and comprise a total of 17 or 16 atoms, respectively (for details see Fig. 2). Coordination polyhedra for the Zn-atoms are made up of 9 or 12 atoms, among which Zn atoms in almost all cases occupy more than 50% of the vertices. The structure of $Ce_7Zn_{21}(Zn_{1-x}Si_x)_2$ can be considered as an arrangement of slightly distorted building blocks of Cu_3Au-type

(Zn1[Ce$_4$Zn$_8$]) and BaAl$_4$-type (Ce3[Ce$_2$Zn$_{10}$M$_4$] and Ce4[Ce$_2$Zn$_{13}$M$_2$]. The arrangement of these building blocks is a zig-zag string of face-connected units…Cu$_3$Au-BaAl$_4$-BaAl$_4$-BaAl$_4$-Cu$_3$Au… running parallel to the *b*-axis. A simpler and linear arrangement of more regular face-connected units …Cu$_3$Au-BaAl$_4$-Cu$_3$Au… is known from the closely related structure type of La$_3$Al$_{11}$ [16] (see Fig. 1). Interatomic distances in the Ce-polyhedra are consistent with the sum of metal radii of Ce and Zn (d$_{Ce-Zn}$= 0.316 nm) except for Ce2, Ce3 and Ce4 polyhedra, which are capped by two Ce atoms each at a long distance of 0.411 nm from the central atom. For the polyhedra around the Zn-atoms we found Zn-Zn and Ce-Zn distances in the range of 0.2526-0.2975 nm and 0.3113-0.3385 nm, respectively, whereas the actual sum of atomic radii [17] for Zn-Zn and Ce-Zn is 0.278 nm and 0.322 nm. Rietveld refinements of the X-ray powder spectra for the phase Ce$_7$Zn$_{21}$(Zn$_{1-x}$Si$_x$)$_2$ confirmed the atom arrangement and the mixed Zn/Si-site (4g-site; M-site in Table 2), which at the Si-rich end of the homogeneity range, Ce$_7$Zn$_{21}$(Zn$_{1-x}$Si$_x$)$_2$, 0.28<x<0.98, leads to an almost complete replacement of Zn by Si atoms. As only a small amount of about 2 at.% Si is necessary to stabilize the compound Ce$_7$Zn$_{21}$(Zn$_{1-x}$Si$_x$)$_2$ at 800°C, we can conclude on a small degree of instability for a hypothetical binary phase "Ce$_7$Zn$_{23}$".
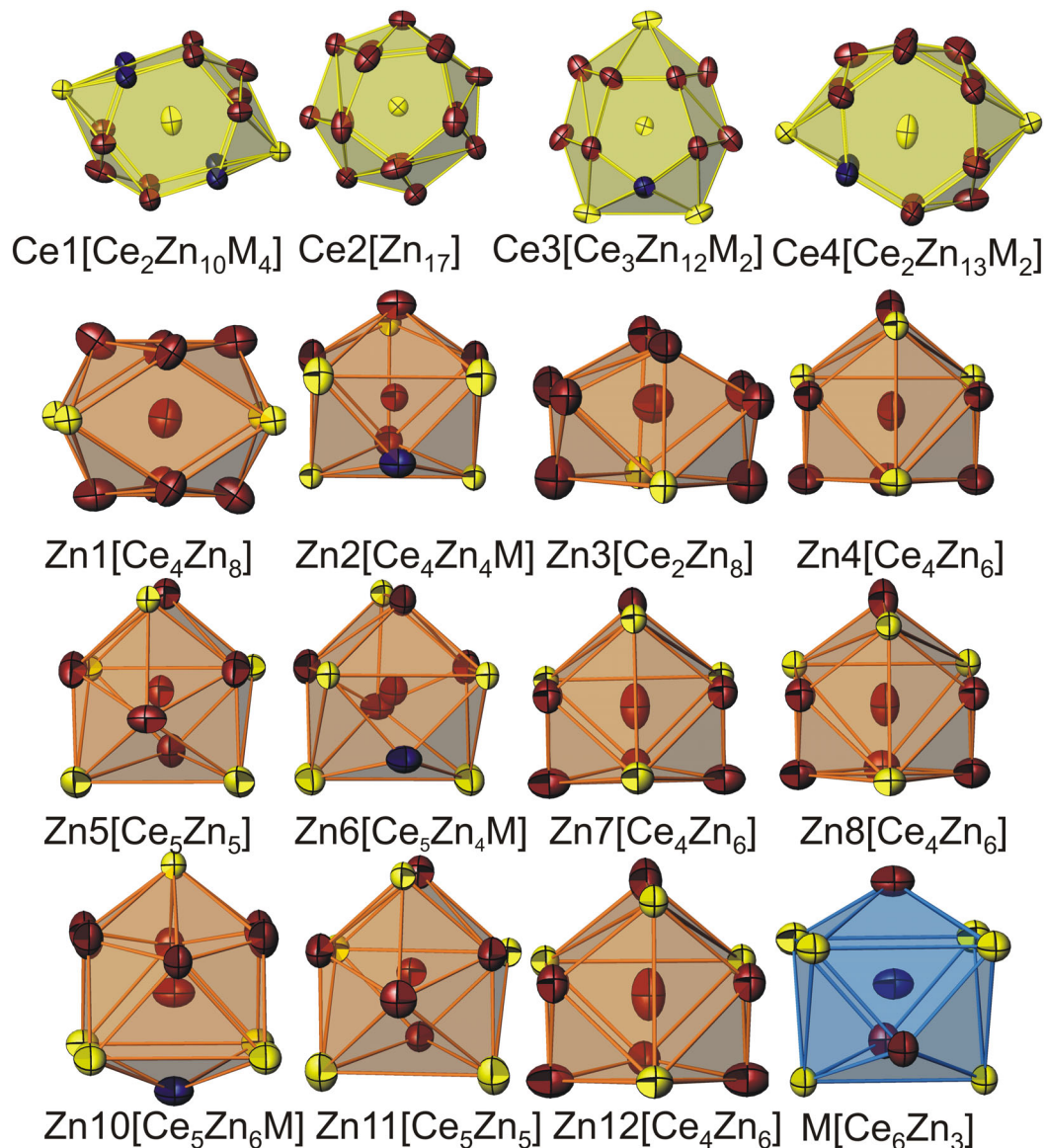
Figure 2. Coordination polyhedra for the independent crystallographic sites in $Ce_7Zn_{21}(Zn_{1-x}Si_x)_2$.

Stabilization of a corresponding phase $La_7Zn_{21}(Zn_{1-x}Si_x)_2$ has also been attempted in the system La-Zn-Si. XPD in combination with EPM analysis of the alloy with composition $La_{23}Zn_{73}Si_4$ (at. %) annealed at 800°C revealed the phase $La_7Zn_{21}(Zn_{1-x}Si_x)_2$ (x=0.41) suggesting isotypic with the structure type of $Ce_7Zn_{21}(Zn_{1-x}Si_x)_2$ ($La_{23.7}Zn_{73.5}Si_{2.8}$ (at. %); *Pbam*; a=1.569(1) nm, b=1.7311(6) nm, c=0.4514(1) nm).

9.3.2.1.2. *The crystal structure of Ce(Zn$_x$Si$_{1-x}$)$_2$, x=0.44, with AlB$_2$-type*

A single crystal suitable for X-ray structure analysis was selected from a crushed sample with nominal composition Ce$_{33}$Zn$_{27}$Si$_{40}$ (in at. %). Complete indexation of the hexagonal diffraction pattern (a=0.41827(2) nm, c=0.42747(2) nm) and analysis of systematic extinctions led to the space group types *P6/mmm*, *P$\bar{6}$2m*, *P$\bar{6}$m2*, *P622*, *P6/m*, *P$\bar{6}$* and *P6*. Refinement in the highest symmetry space group *P6/mmm* quickly converged to the formula Ce(Zn$_x$Si$_{1-x}$)$_2$ x=0.44 with $R_{F^2} = 0.009$ and residual electron densities smaller than ±1.84e$^-$/Å^3 with a fully occupied Ce site and a mixed 2*d* site for Zn and Si with occupancies 44% and 56%, respectively. The phase has been confirmed by X-ray powder diffraction and EPMA with a large homogeneity range at 800°C, Ce(Zn$_x$Si$_{1-x}$)$_2$, 0.41<x<0.75. Crystal data along with the ADPs are summarized in Table 4. Unit cell, crystal symmetry and atom positions confirm isotypism with the AlB$_2$ type. XPD and EPM analyses of the alloy, La$_{33}$Zn$_{42}$Si$_{25}$ (at. %) annealed at 800°C suggest corresponding La(Zn$_x$Si$_{1-x}$)$_2$, x=0.56, to be an isostructural compound in equilibrium with La(Zn$_{0.95}$Si$_{0.05}$)$_2$, CeCu$_2$-type. Crystal structure data for La(Zn$_x$Si$_{1-x}$)$_2$, x=0.56 are presented in Table 4 and Rietveld refinement data are given in Fig. 3.
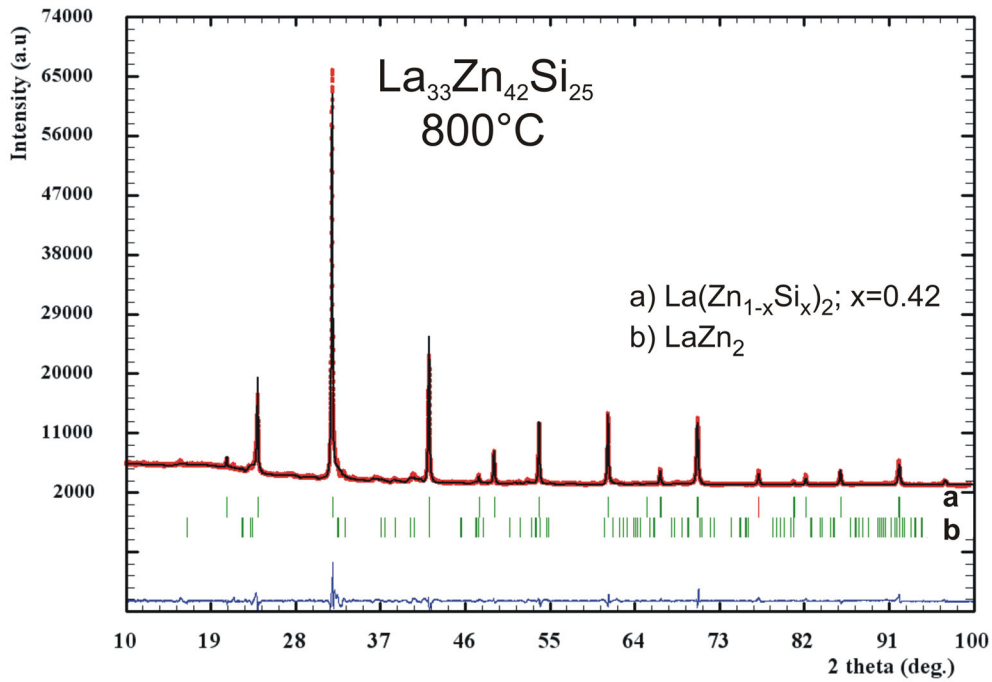
Figure 3. Rietveld refinement of the XPD pattern of the alloy La$_{33}$Zn$_{42}$Si$_{25}$ (at. %), annealed at 800°C. The main phase is La(Zn$_{1-x}$Si$_x$)$_2$, x=0.42, AlB$_2$–type. The secondary phase is La(Zn$_{0.95}$Si$_{0.05}$)$_2$, CeCu$_2$-type.

9.3.2.2. The system Ce-Zn-Si: isothermal section at 800°C

About sixty samples have been analyzed by electron microprobe analysis and x-ray powder diffraction in order to establish the isothermal phase equilibria for the system Ce-Zn-Si at 800°C shown in Fig. 4. Data for tie-lines and the vertices of three-phase triangles have been summarized in Table 5 for selected alloys. The system is characterized by the presence of 4 ternary compounds, most of which form extended homogeneity regions: τ_1-Ce$_7$Zn$_{21}$(Zn$_{1-x}$Si$_x$)$_2$, 0.28<x<0.98, τ_2-Ce(Zn$_x$Si$_{1-x}$)$_2$, 0.36<x<0.75, τ_3-Ce(Zn$_x$Si$_{1-x}$), 0.17<x<0.23, and τ_4-Ce$_{40}$Zn$_{37}$Si$_{23}$ (in at. %). Whereas solubility of Si in cerium zinc phases CeZn$_x$ is negligible for x>2, and in general less than a few percent of Zn can dissolve in cerium silicides (for details see Fig.5 and

162

Table 5), the section $CeSi_2$ – $CeZn_2$ contains a series of compounds with extensive

Zn/Si substitution at a constant Ce-content.

1 $CeZn_3$
2 Ce_3Zn_{11}
3 $Ce_{13}Zn_{58}$
4 $CeZn_5$
5 Ce_3Zn_{22}
6 Ce_2Zn_{17}
7 $CeZn_{11}$

Ce-Zn-Si 800°C

τ_1 $Ce_7Zn_{21}(Zn_{1-x}Si_x)_2$
τ_2 $Ce(Zn_xSi_{1-x})_2$
τ_3 $Ce_{50}Zn_{8.5-12.2}Si_{41.5-38.8}$
τ_4 $Ce_{40}Zn_{37}Si_{23}$
τ_5 $Ce_{25}Zn_{41.2-37.1}Si_{33.8-38}$

$CeSi_2$
α-$ThSi_2$

$CeSi_2$
α-$GdSi_2$

$Ce_2Si_{2.7}$
CeSi
Ce_5Si_4
Ce_3Si_2
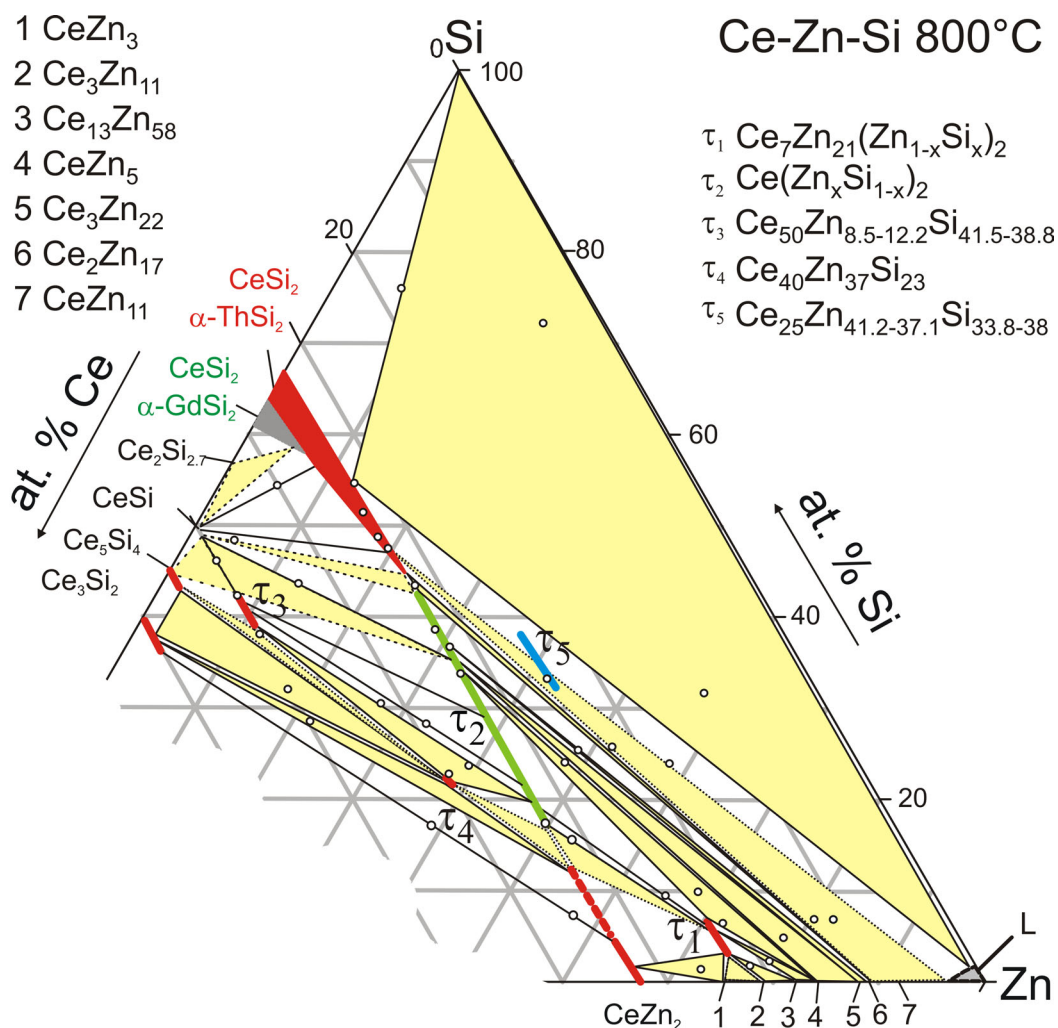
Figure 4. System Ce-Zn-Si; isothermal section at 800°C.The ternary phases τ_5 only

exists at lower temperature; its homogeneity region at 600°C is outlined.

The sequence of the structurally closely related structure types of α$ThSi_2$-type

($Ce(Zn_xSi_{1-x})_2$; $0<x<0.32$) , AlB_2-type (τ_2-$Ce(Zn_xSi_{1-x})_2$; $0.36<x<0.75$) and $CeCu_2$-

type ($Ce(Zn_xSi_{1-x})_2$; $0<x<0.07$) is well known for many ternary systems such as Ce-

Cu-Si [18, 19], Ce-Ag-Si [20] or Ce-Ag-Ge [21]. Fig. 5 shows the volume/per atom

versus Zn-content along the section $CeSi_2$-$CeZn_2$. Whereas the structure types of

α$ThSi_2$ and AlB_2 are closely related by an atom shift and thus yield a linear and

163

monotonic increase of the average volume per atom with increasing Zn-content, the drop in the volume/atom for $Ce(Zn_{1-x}Si_x)_2$ with $CeCu_2$-type indicates a change in bond type and a better space filling in the latter phase.
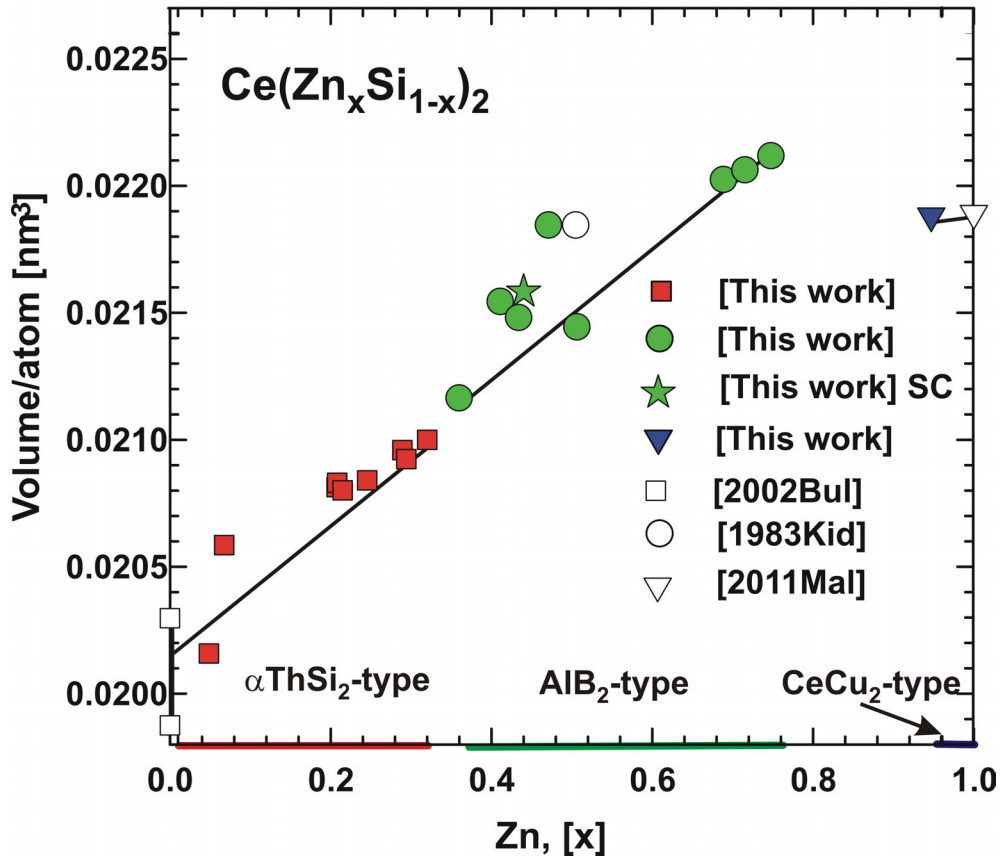
Figure 5. Volume per atom vs. Zn-content in $Ce(Zn_xSi_{1-x})_x$ phases along the section $CeSi_2$ - $CeZn_2$.

A series of three-phase equilibria at 800°C such as $\tau_1+Ce_3Zn_{11}+Ce_{13}Zn_{58}$ (Fig. 6a), $Ce_2Zn_{17}+CeSi_2+Ce_3Zn_{22}$ (Fig. 6b) and $\tau_1+CeZn_5+\tau_2$ (Fig. 6c) are presented in the respective micrographs and their related lattice parameters and qualitative EPM analysis data are summarized in Table 5. EPMA and XPD confirm for the alloy with composition $Ce_{35}Zn_{58}Si_7$ the phase equilibrium $Ce(Zn_{1-x}Si_x)_2$ + $Ce_3(Zn_xSi_{1-x})_2$ (see micrograph 6d and Table 5): for this tie-line we are sure about the presence of $Ce(Zn_{1-x}Si_x)_2$ (x=0.07) with $CeCu_2$-type structure.

Narrow phase triangles $Ce(Zn_{1-x}Si_x)_2 + Ce_3(Zn_xSi_{1-x})_2 + \tau_4$ (see Fig. 6e), $Ce_3(Zn_xSi_{1-x})_2 + Ce_5(Zn_xSi_{1-x})_4 + \tau_4$ and $\tau_3 + \tau_4 + \tau_2$ have been observed from the samples $Ce_{50}Zn_{22}Si_{28}$, $Ce_{52}Zn_{32}Si_{16}$ and $Ce_{37}Zn_{40}Si_{23}$ (at. %), respectively. XPD was not able to unambiguously determine the structure for the $Ce(Zn_{1-x}Si_x)_2$ phase ($CeCu_2$- or AlB_2-type ?) for which EPMA defined the composition $Ce_{50}Zn_{22}Si_{28}$ (at. %) (see micrograph Fig. 6e); therefore the Si-rich region of the $Ce(Zn_{1-x}Si_x)_2$ phase is shown by a dashed line in Fig. 5. The phase τ_3 forms a two-phase equilibrium with CeSi and ranges from 8 to 11 at. % Zn at 50 at.% Ce. For $Ce_2Si_{2.7}$ and $CeSi_2$ with $\alpha GdSi_2$-type a rather small solubility of Zn is suggested, as these phases did not appear in alloys with Zn-contents above 5 at.% Zn. The sample with composition $Ce_{18}Zn_{58}Si_{24}$ (in at. %), annealed at 800°C mainly showed the $\alpha ThSi_2$–type phase $Ce(Zn_xSi_{1-x})_2$ with small grains of a novel phase τ_5 formed during quenching (see micrograph Fig 6f). EPM analysis indicated a composition $Ce_{25.3}Zn_{40.8}Si_{33.9}$ (in at. %) for the τ_5 phase. Although τ_5 is not present in alloys annealed at 800°C, the amount of τ_5 significantly increased after annealing at 600°C. From alloys $Ce_{11}Zn_{82}Si_7$ and $Ce_{25}Zn_{42}Si_{33}$ (in at. %, annealed at 600°C) a homogeneity range was defined by EPMA: $Ce_{25}Zn_{41.2-37.1}Si_{33.8-38}$ (at. %) suggesting a formula $Ce(Zn_{1-x}Si_x)_3$.
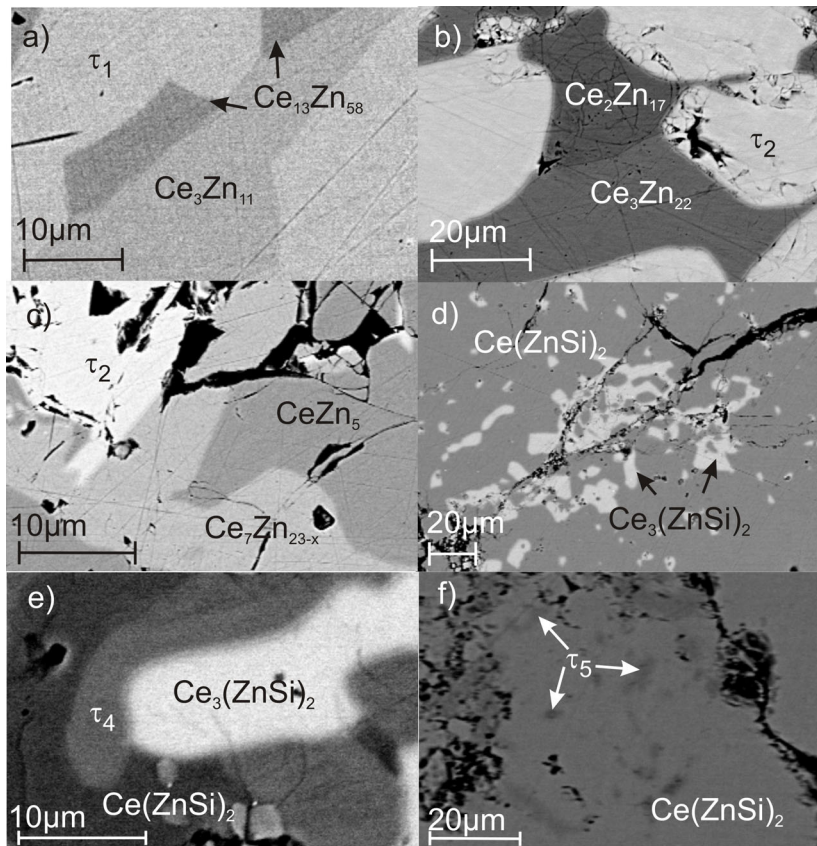
Figure 6. Selected micrographs for Ce-Zn-Si samples annealed at 800°C a) $Ce_{22}Zn_{76}Si_2$, b) $Ce_{25}Zn_{48}Si_{26}$, c) $Ce_{22}Zn_{72}Si_6$ d) $Ce_{35}Zn_{58}Si_7$, e) $Ce_{50}Zn_{22}Si_{28}$ and f) $Ce_{18}Zn_{58}Si_{24}$ (all compositions given in at. %).

9.3.3. The isopleths La(Ni$_{1-x}$Zn$_x$)$_2$Si$_2$ and Ce(Ni$_{1-x}$Zn$_x$)$_2$Si$_2$

$CeNi_2Si_2$ has been reported by Bodak and coworkers [22] to crystallize with the $ThCr_2Si_2$-type. The same group of authors [23, 24, 25] showed this phase at a point composition in the Ce-Ni-Si isothermal section at 800°C. Our re-inspection of alloys with compositions $Ce_{20}Ni_{40}Si_{40}$ and $La_{20}Ni_{40}Si_{40}$ (at. %; both as cast and annealed at 800°C for 4 days) by means of X-ray powder and EPMA proved consistency with the body-centered tetragonal $ThCr_2Si_2$-type. Rietveld refinement data for both compounds are summarized in Table 6. Although the 800°C section Ce-Ni-Si showed the $ThCr_2Si_2$-phase in equilibrium with $CeNi_{~4}Si$ (structure unknown), XPD and EPMA analysis of an as cast sample $Ce_{20}Ni_{60}Si_{20}$ (at. %) revealed a new phase $Ce_{20}Ni_{46.6}Si_{33.4}$

with identical unit cell but with a primitive tetragonal pattern, suggesting the CaBe$_2$Ge$_2$-type.
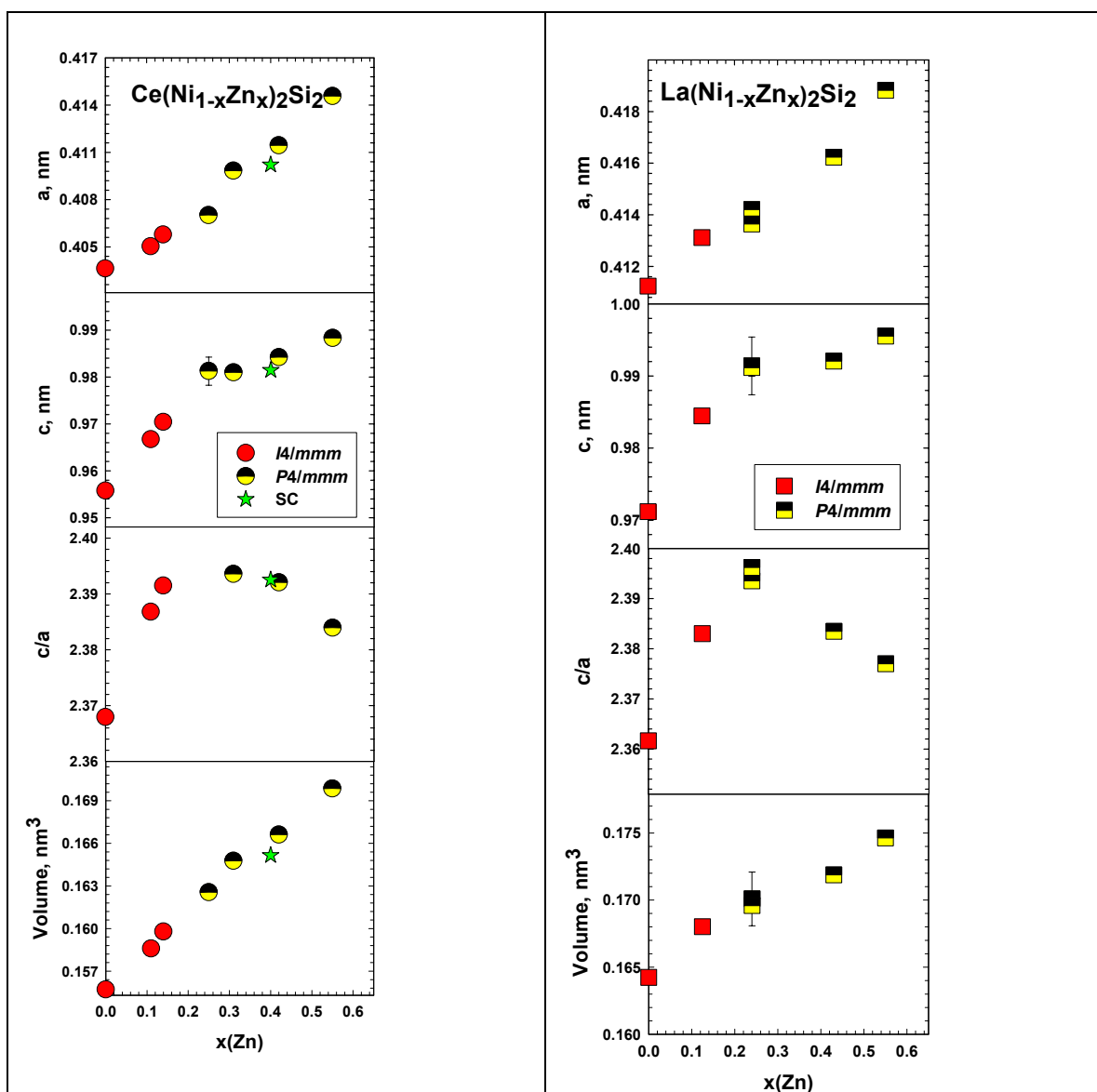
Figure 7. Unit cell parameters vs. Zn-content in the phases {La,Ce}[Ni$_{1-x}$Zn$_x$]$_2$Si$_2$ revealing the transition from body centered to primitive symmetry as a consequence of Ni/Zn substitution (compositions from EPMA).

9.3.3.1. The crystal structure of CeNi$_2$(Ni$_x$Si$_{1-x}$)$_2$, x=0.14 with CaBe$_2$Ge$_2$–type

The X-ray intensity pattern of a single crystal, extracted from an arc-melted alloy Ce$_{20}$Ni$_{60}$Si$_{20}$, was fully indexed on the basis of a primitive tetragonal unit cell (a= 0.40150(2) and c=0.95210(2) nm). Systematic extinctions were consistent with space group type *P4/nmm* for the highest crystal symmetry. Direct methods prompted Ce, Ni, Si atoms in positions typical for the CaBe$_2$Ge$_2$–type. Refinement with anisotropic atom displacement parameters (ADPs) converged to $R_{F^2} = 0.011$ and residual electron densities smaller than ±0.82 e$^-$/Å^3 with fully occupied metal sites but for a statistical occupation of 0.72Ni+0.28Si in site 2a of *P4/nmm*. Thus, a structure formula CeNi$_2$(Ni$_x$Si$_{1-x}$)$_2$, x=0.14, results, which corresponds to a composition Ce$_{20}$Ni$_{46.6}$Si$_{33.4}$ close to the ThCr$_2$Si$_2$-type phase, but in between CeNi$_2$Si$_2$+CeNi$_4$Si. Crystal data for CeNi$_2$(Ni$_x$Si$_{1-x}$)$_2$ along with the ADPs have been summarized in Table 6.

Combined XPD and EPMA defined the homogeneity range for the CaBe$_2$Ge$_2$-type phase at 800°C as CeNi$_2$(Ni$_{1+x}$Si$_{1-x}$)$_2$, 0.14<x<0.5, whilst the homogeneity range for the ThCr$_2$Si$_2$-type phase extends at lower Ni-concentrations around the stoichiometric composition 1:2:2, i.e. for -0.13<x<0.14. Obviously the substitution of Ni by Si in the 2a site results in a structural change from a body centered to a primitive atom arrangement in terms of a group-subgroup relation.

9.3.3.2. The crystal structure of Ce(Ni$_{1-x}$Zn$_x$)$_2$Si$_2$, x=0.39

From the phase relations in the isothermal section Ce-Zn-Si at 800°C it is obvious that no ThCr$_2$Si$_2$ type phase forms. In order to explore the maximal substitution of Ni by Zn, the section Ce(Ni$_{1-x}$Zn$_x$)$_2$Si$_2$ was studied starting from stoichiometric CeNi$_2$Si$_2$ with ThCr$_2$Si$_2$-type. In single-phase alloys Ce(Ni$_{1-x}$Zn$_x$)$_2$Si$_2$, annealed at 800°C, the crystal structure remains body centered up to a Zn-content of x=0.15. For higher Zn-contents additional but

weak reflections start to appear in the X-ray powder spectra, which are clearly visible in the range $0.22<x<0.55$ and could be all indexed on a primitive unit cell. At Zn-concentrations $x>0.55$ the X-ray spectra get multiphase indicating that the solubility limit has been reached. All Zn-contents were obtained from EPMA data in combination with X-ray powder data analyses. As seen from Fig. 7, Zn addition is linearly associated with an increase in lattice parameters, c/a ratio and volume of the unit cell.

In order to get details on the primitive unit cell a single crystal has been selected from the flux residuals of an alloy with composition $Ce_2Ni_4Si_8Zn_{86}$ (at.%), slowly cooled from 900°C. A SEM analysis performed directly on the crystals separated out of the flux (shown in Fig. 8), defined the composition as $Ce_{19}Ni_{25}Zn_{16}Si_{41}$ (at. %).
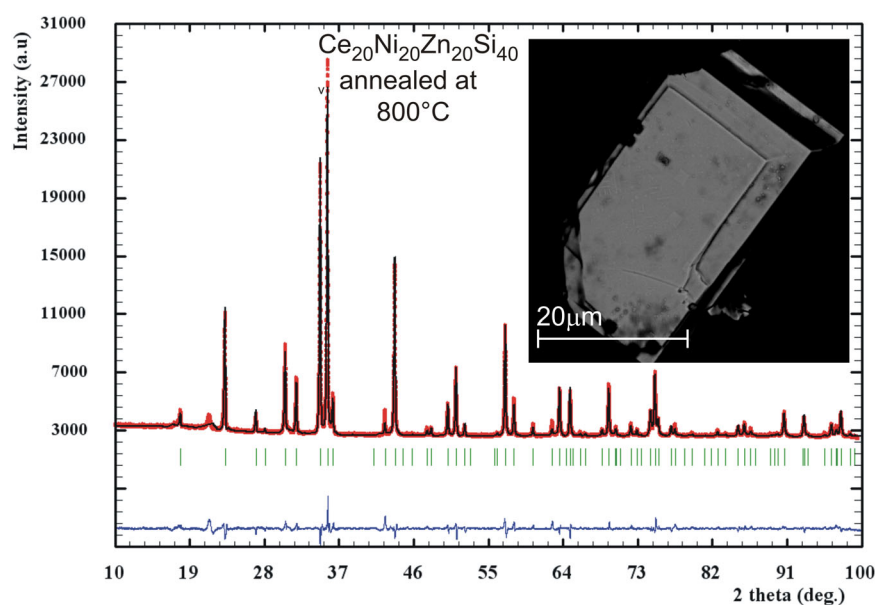
Figure 8. Rietveld refinement of the alloy with composition $Ce_{20}Ni_{20}Zn_{20}Si_{40}$ at.% showing $Ce(Ni_{1-x}Zn_x)_2Si_2$ with $CaBe_2Ge_2$-type (space group $P4/nmm$) and the micrograph of the single crystal obtained from Zn flux (from sample $Ce_2Ni_4Si_8Zn_{86}$).

Unit cell, systematic extinctions (indicating $P4/nmm$ as the space group type of highest symmetry) as well as the X-ray intensity pattern confirmed a structure solution in terms of the $CaBe_2Ge_2$-type. Refinement converged to $R_F{}^2= 0.012$ and residual electron densities less

then ±0.96 electrons/Å^3 for three metal and two Si positions with a Wyckoff sequence *abc*^{3}.

Fixing the Ni/Zn-ratio from the EPMA resulted in the structure formula *Ce(Ni$_{1-x}$Zn$_x$)$_2$Si$_2$,* *x=0.39* (i.e. Ce$_{20}$Ni$_{24.4}$Zn$_{15.6}$Si$_{40}$). It should be mentioned, however, that six reflections; violated the space group extinction rules: (010), (210), ($2\bar{1}0$), ($3\bar{2}0$), (320) and (340). In comparison to the highest intensity observed (~12000), the (210), ($2\bar{1}0$), ($3\bar{2}0$), (320) reflection intensities are below 2 and can be disregarded, whereas the (010) intensity (below 7) may stem from a 'Renninger enhancement' effect. Crystal data for Ce(Ni$_{1-x}$Zn$_x$)$_2$Si$_2$, x=0.39, with the CaBe$_2$Ge$_2$-type along with the ADPs are summarized in Table 7; coordination polyhedra for all atom sites and a three-dimensional view on the crystal structure are presented in Fig. 9. In analogy to the Ce-section phase relations have also been explored for the isopleth La(Ni$_{1-x}$Zn$_x$)$_2$Si$_2$ (see Fig. 7). Combined EPM and X-ray powder intensity data analyses revealed a solid solution with the ThCr$_2$Si$_2$-type for 0<x<0.15, followed by a change to a primitive tetragonal symmetry typical for the CaBe$_2$Ge$_2$-type for 0.2<x<0.56. The solid solution terminates at x=0.56 as for higher Zn-concentrations multiphase X-ray spectra were observed. Rietveld refinement data for La(Ni$_{0.56}$Zn$_{0.44}$)$_2$Si$_2$ are summarized in Table 7 and Figure 10.
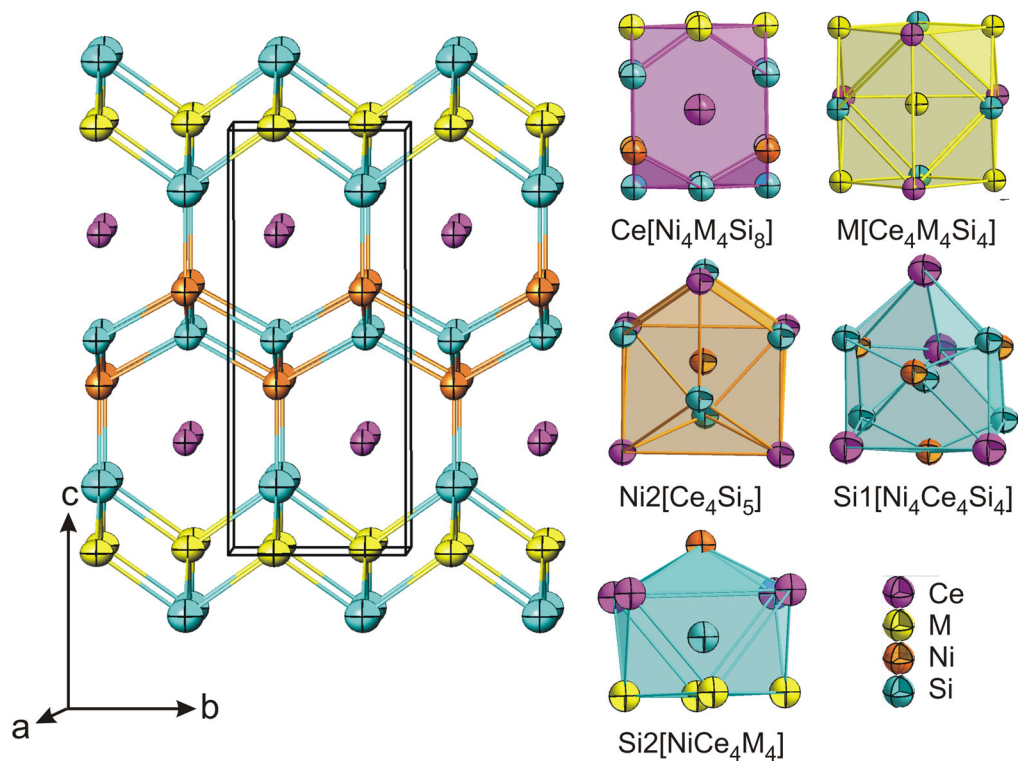
Figure 9. The crystal structure and coordination polyhedra of Ce$(Ni_{1-x}Zn_x)_2Si_2$, x=0.39.
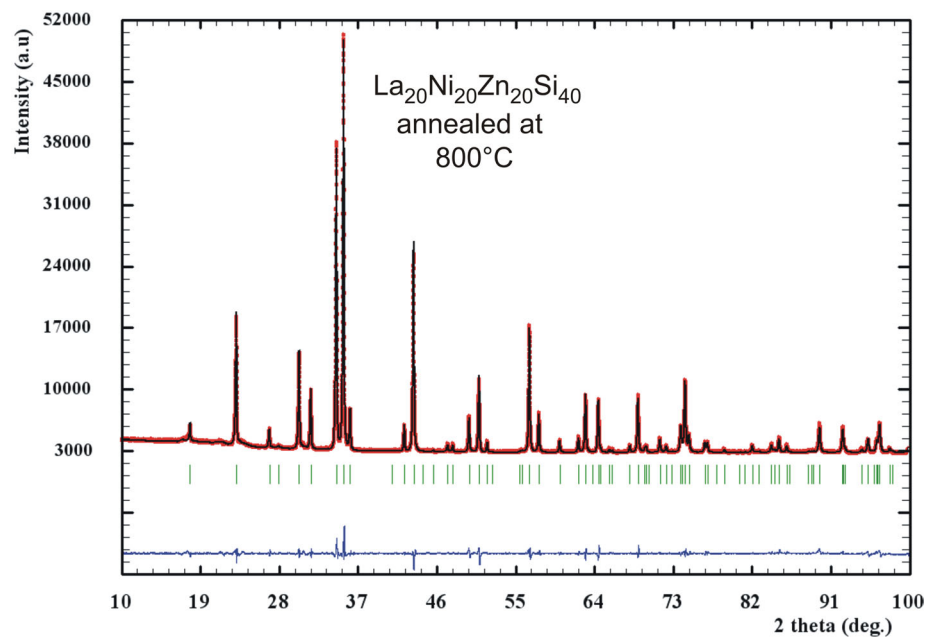
Figure 10. Rietveld refinement of single phase La$(Ni_{1-x}Zn_x)_2Si_2$; x=0.44 (CaBe$_2$Ge$_2$-type, space group $P4/nmm$) from the alloy with composition La$_{20}$Ni$_{20}$Zn$_{20}$Si$_{40}$ (at.%), annealed at 800°C.

9.4. Conclusions

With EDX electron microprobe analysis and x-ray powder diffraction we have derived the isothermal section for the system Ce-Zn-Si at 800°C. The section is characterized by the presence of four ternary compounds in some cases with extended homogeneity regions at constant Ce-content (Zn/Si exchange). Extended solid solutions along the section $CeSi_2$-$CeZn_2$ form a structurally related sequence of structure types: $Ce(Zn_xSi_{1-x})_2$, $0<x<0.32$ ($\alpha ThSi_2$-type), τ_2- $Ce(Zn_xSi_{1-x})_2$, $0.36<x<0.75$ (AlB_2-type) and $Ce(Zn_{1-x}Si_x)_2$, $0<x<0.07$ ($CeCu_2$-type). Silicon stabilizes the ternary compound τ_1-$Ce_7Zn_{21}(Zn_{1-x}Si_x)_2$, $0.28<x<0.98$, for which the crystal structure has been derived from X-ray single crystal diffraction data ($Ce_7Zn_{21}(Zn_{1-x}Si_x)_2$, $x=0.28$; unique structure type, *Pbam*; a=1.55722(3) nm, b=1.71942(3) nm, c= 0.44772(1) nm). Lanthanum forms a compound $La_7Zn_{21}(Zn_{1-x}Si_x)_2$ at $x=0.41$ (assumed $Ce_7Zn_{21}(Zn_{1-x}Si_x)_2$-type; *Pbam*; a=1.569(1) nm, b=1.7311(6) nm, c=0.4514(1) nm). The structure types of the two ternary compounds existing at 800°C: τ_3-$Ce(Zn_xSi_{1-x})$, $0.17<x<0.23$ and τ_4- $Ce_{40}Zn_{37}Si_{23}$ at. % are still unknown. Although the ternary systems {La,Ce}-Zn-Si at 800°C do not contain a compound "{La, Ce}Zn_2Si_2", solid solutions exist starting from $CeNi_2Si_2$ on substitution of Ni by Zn. Combined XPD and EPMA defined the homogeneity range at 800°C {La,Ce}$(Ni_{1-x}Zn_x)_2Si_2$ with a maximum Zn-content of $x=0.55$. The crystal structure remains body centered up to a Zn-content of $x=0.15$. For higher Zn-contents additional but weak reflections start to appear in the X-ray powder spectra, which are clearly visible in the range $0.22<x<0.55$ and could be all indexed on a primitive unit cell. Obviously the substitution of Ni by Zn in the 2a site results in a structural change from a body centered to a primitive atom arrangement in terms of a group-subgroup relation. The symmetry reduction is documented by single crystal X-ray diffraction data for $Ce(Ni_{0.61}Zn_{0.39})_2Si_2$ (CaB_2Ge_2-type; *P4/nmm*; a=0.41022(1) nm, c=0.98146(4) nm). A compound τ_5, stable below 800°C, has been observed with a considerable homogeneity

region at 600°C: $Ce_{25}Zn_{41.2-37.1}Si_{33.8-38}$ (at. %). As a characteristic of the solid solutions with $CaBe_2Ge_2$-type Ni/Si and Ni/Zn substitutions appear in 2a site.

9.5. References

[1]   Murphy S. Wear 1984;98:151-161.
[2]   Tao X. Wenguan G. Pinlin G. Zhongguo Xitu Xuebao 1998;16(3):230-233.
[3]   Duboz J.Y. Badoz P.-A. Perio A. Oberlin J.C. Arund d'Avitaya F. Campidelli Y. Chroboczek J.A. Appl.Surf.Sci. 1989; 38:171.
[4]   I.J. Polmear, Light Alloys, 3rd ed., Arnold London, 1995.
[5]   Kido H. Hoshikawa T. Shimada M. Koizumi M. Phys. Stat. Sol. 1983;(a) 80:601-605.
[6]   Rodríguez-Carvajal J. Satellite Meeting on Powder Diffraction of the XV IUCr Congress 1990:127.

[7]   Nonius Kappa CCD Program Package COLLECT, DENZO, SCALEPACK, SORTAV, Nonius Delft, The Netherlands, 1998.
[8]   Sheldrick G.M. Acta Crystallogr. 2008:A64:112-122.
[9]   Sheldrick G.M. SHELXS-97, Program for Crystal Structure Refinement University of Göttingen, Germany Windows version by McArdle, Natl. Univ. Ireland, Galway, 1997.
[10]   Farrugia L.J. J. Appl. Crystallogr. 1999;32:837-838.
[11]   Malik Z. Sologub O. Giester G. Rogl P. J. Solid State Chem. 2011;184:2840–2848.
[12]   Bulanova M.V. Zheltov P.N. Meleshevich K.A. Saltykov P.A., Effenberg G.J. of Alloys Compounds 2002; 345:110-145.
[14]   Wosylus A. Meier K. Prots Y. Schnelle W. Rosner H. Schwarz U. Grin Y., Angewandte Chemie, 2010;122:9187-9191.
[13]   Schobinger P. P. Buschow K.H.J. J. Alloys Compd. 1993; 198:47-50.
[16]   Gomes de Mesquita A.H. Buschow K.H.J. Acta Crystallogr. 1967;22:497-501.
[17]   Teatum E. Gschneidner K. Waber J. LA-2345, U.S. Department of Commerce: Washington D.C.; 1960.
[18]   Bodak O.I. M Kalychak Y. Gladyshevskii E.I. *Inorg. Mater. (Engl. Trans.)*, 1974;10(3):388-391.
[19]   Braun H.F. Jorda J.L. *Physica B/C* 1985;135(1-3): 72-75.
[20]   Cordruwisch E. Kaczorowski D. Saccone A. Rogl P.Ferro R.; J. Alloys Compd 2001;320:308-319..
[21]   E.Cordruwisch, D.Kaczorowski, A.Saccone, P.Rogl and R.Ferro; J. Phase Equilibria, 20(4), 407-422 (1999).
[22]   Bodak O.I. Gladyshevskii E.I. Krypyakevych P.I. Inorg. Mater. 1966;2:1861–1864.
[25]   Mis'kiv M.G. Tyvanchuk A.T. Kharchenko O.I. Inorg. Mater. 1973;**9:**777–779.
[23]   Bodak O.I. Gladyshevskii E.I. Dopov. Akad. Nauk Ukr. RSR, 1969; Ser. A:1125–1129.
[24]   Bodak O.I. Gladyshevskii E.I. Inorg. Mater. 1969;**5:**1754–1758.
[15]   Massalski T.B. Binary Alloy Phase Diagrams, second ed., ASM International, Materials Park, OH, 1990.
[26]   Celotti G. Nobili D. Ostoja P. J. Mater. Sci. 1974;9:821,828.

[27]   Villars P. Cenzual K. Pearson's Crystal Data CD ROM, ASM International, OH, USA, Release 2011/2012
[28]   Piao S. Gomez C.P. Lidin S. Z. Kristallogr. 2006; 221:391-401.
[30]   Kripyakevich P.I. Kuz'ma Y.B. Ugrin N.S. Journal of Structural Chemistry, Translated from Zhurnal Strukturnoi Khimii 1967;8:632-633.
[31]   Iandelli A. Palenzona A. J. Less-Common Metals 1967;12:333-343.
[32]   Zelinska O. Conrad M. Harbrecht B. Z. Kristallogr. NCS 2004;219:357-358.
[33]   Parthé E. Gelato L. Chabot B. Penzo M. Censual K. Gladyshevskii R., TYPIX—Standardized Data and Crystal Chemical Characterization of Inorganic Structure Types, Berlin, Springer, 1994.
[29]   Lott B.G. Chiotti P. Acta Crystallogr.1966;20;733,738

Table 1. Crystallographic data of unary and binary boundary solid phases of the system Ce–Zn–Si

Phase, Temperature range (ºC)	Space group, Prototype	Lattice parameters (nm)			Comments
		a	b	c	
(δCe) 798-700 [15]	$Im\overline{3}m$ W	0.412	-	-	[15] -
(γCe) <726 [15]	$Fm\overline{3}m$ Cu	0.51610	-	-	[15] -
(Zn) <420	$P6_3/mmc$	0.2665	-	0.4947	[15] -
(Si) <1414°C	$Fd\overline{3}m$ C (*Diamond*)	0.543110	-	-	[26] -
CeSi$_2$ <1725°C [12]	*Imma* α GdSi$_2$		-	0.4109(1)	Ce$_{37.4}$Si$_{62.6}$[a] [12]
CeSi$_2$ ~1575°C [12] Ce(Zn$_x$Si$_{1-x}$)$_2$	*I4$_1$/amd O2* α ThSi$_2$	0.4192(1) 0.4201(1)	-	1.3913(5) 1.4312(7)	Ce$_{33.3}$Si$_{66.7}$[a] [12] (0≤x≤0.32) [This work] x=0.32 [This work]
CeSi <1630°C [12]	*Pnma* FeB		-	0.3961(2)	Ce$_{49.9}$Si$_{50.1}$[a] [12]
Ce$_5$Si$_4$ <1500°C [12]	*P4$_1$2$_1$2* Zr$_5$Si$_4$	0.7936(1)	-	1.5029(5)	Ce$_{55.6}$Si$_{44.4}$[a] [12]
Ce$_3$Si$_2$ <1335°C [12]	*P4/mbm* U$_3$Si$_2$	0.7780(6)	-	0.4367(6)	[12]
Ce$_5$Si$_3$ <1260°C [12]	*I4/mcm* Cr$_5$B$_3$	0.7878(4) -	- -	1.067(1) -	[12] -
Ce$_2$Si$_{3-x}$	*Cmcm* V$_2$B$_3$	- -	2.48389	0.39517	x=0.3 [13] -
CeSi$_5$ <827°C	*Immm* LaGe$_5$	- -	0.60189(4)	0.92979(6)	[14] high pressure phase; 10GPa
Ce$_2$Si$_7$ <1127°C	*Cmmm* Ce$_2$Si$_7$	- -	0.99644(7)	0.44868(4) -	[14] high pressure phase; 10GPa
CeZn <825 [15]	$Pm\overline{3}m$ CsCl	0.3704(1) 0.37059(2)	- -	- -	[27] [11]
CeZn$_2$ <875 [15] Ce(Zn$_{1-x}$Si$_x$)$_2$	*Immm* CeCu$_2$	0.4633(5) 0.46393(8) 0.46119(3)	0.7538(5) 0.7544(1) 0.7551(4)	0.7499(5) 0.7506(1) 0.754(4)	[27] [11] (0<x<0.07) [This work] x=0.07 [This work]
CeZn$_3$ <820 [15]	*Cmcm* CeZn$_3$	0.4620(5) 0.46324(5)	1.0440(5) 1.0452(1)	0.6640(5) 0.66557(6)	[27] [11]
Ce$_3$Zn$_{11}$ <840 [15]	*Immm* La$_3$Al$_{11}$	0.45215 0.45242(2)	0.88855 0.88942(3)	1.3463 1.34754(4)	[27] SC [11]
Ce$_{13}$Zn$_{58}$ <870 [15]	*P6$_3$/mmc* Gd$_{13}$Zn$_{58}$	1.4638(1) 1.4616(1)	- -	1.4158(1) 1.4173(1)	[28] [11]
CeZn$_5$ <885 [15] CeZn$_{5+y}$	*P6/mmm* CaCu$_5$	0.54163(5) 0.54082(1) 0.54163(5)	- - -	0.42647(5) 0.42798(1) 0.42647(5)	[27] [11] 0.017≤y≤0.046 <885°C [29]
Ce$_3$Zn$_{22}$ <960 [15]	*I4$_1$/amd* Ce$_3$Zn$_{22}$	0.897(1) 0.8936(2)	- -	2.133(5) 2.1380(5)	[30] SC [11]
β Ce$_2$Zn$_{17}$ <980 [15] 980-~750 [11]	$R\overline{3}m$ Th$_2$Zn$_{17}$	0.9090(5) 0.90916(4)	- -	1.32844(7) 1.32861(1)	[27] [11]
α Ce$_2$Zn$_{17}$ αCe$_{1+x}$Zn$_{5+2x}$ <~750 [11]	*P6$_3$/mmc* TbCu$_7$	0.9088(4) 0.52402(2) -	- - -	0.8856(5) 0.44257(1) -	[31] x=0.33 [11] -
CeZn$_{11}$ <795 [15]	*I4$_1$/amd* BaCd$_{11}$	1.0658(6) 1.06630(1)	- -	0.6862(8) 0.686644(7)	[32] [11]
τ_1-Ce$_7$Zn$_{21}$(Zn$_{1-x}$Si$_x$)$_2$	*Pbam* Ce$_7$Zn$_{21}$(Zn$_{1-x}$Si$_x$)$_2$ -	1.71942(3)	0.44772(1)	x=0.28 [This work] SC (0.28<x<0.98) [This work]
τ_2-Ce(Zn$_{1-x}$Si$_x$)$_2$ - - -	*P6/mmm* AlB$_2$ -	0.4223 0.41827(2) - 0.41315(7) 0.4416(1)	- - - - -	0.4238 0.42747(2) - 0.4295(2) 0.3929(1)	[5] [This work] SC at x=0.56 (0.36≤x<0.75) [This work] x=0.36 [This work] x=0.75 [This work]
τ_3-Ce(Zn$_x$Si$_{1-x}$)	unknown	-	-	-	(0.17<x<0.23) [This work]
τ_4- Ce$_{40}$Zn$_{37}$Si$_{23}$	unknown	-	-	-	at. % [This work]

175

τ_5- $Ce_{25.3}Zn_{40.8}Si_{33.9}$	unknown	-	-	-	at. %, stable < 800°C [This work]

Table 2. X-ray single crystal data[a,b] for $Ce_7Zn_{21}(Zn_{1-x}Si_x)_2$, x=0.28 (MoK$_\alpha$ radiation)

Compound	$Ce_7Zn_{21}(Zn_{1-x}Si_x)_2$, x=0.28
EPMA composition [at. %]	$Ce_{24.1}Zn_{73}Si_{2.93}$
Refinement composition [at. %]	$Ce_{23.3}Zn_{74.8}Si_{1.9}$
Structure type	$Ce_7Zn_{21}(Zn_{1-x}Si_x)_2$
θ Range [deg]	$2.37 < \theta < 36.24$
Space group	*Pbam*; No. 55
Crystal size	35x40x35
a [nm]	1.55722(3)
b [nm]	1.71942(3)
c [nm]	0.44772(1)
Reflections in refinement	2414 $F_o > 4\sigma(F_o)$ of 3119
Mosaicity	0.55
Number of variables	102
$R_F^2 = \Sigma|F_0^2 - F_c^2|/\Sigma F_0^2$	0.029
R_{Int}	0.066
GOF	1.018
Extinction (Zachariasen)	0.00011(6)
Ce1 in 2*b* (0,0, ½); Occ.	1.00(1)
U_{11}^b; U_{22}; U_{33}; $U_{23}=U_{13}=0$; U_{12}	0.0142(2); 0.0217(2); 0.0146(2); -0.0048(2)
Ce2 in 4*g* (*x, y*, 0); Occ.	*x*=0.16411(2), *y*=0.45496(2); 1.00(1)
U_{11}^b; U_{22}; U_{33}; $U_{23}=U_{13}=0$; U_{12}	0.0112(1); 0.0119(1); 0.0088(1); 0.0005(1)
Ce3 in 4*h* (*x, y*, ½); Occ.	*x*=0.16711(2), *y*=0.18202(2);1.00(1)
U_{11}^b; U_{22}; U_{33}; $U_{23}=U_{13}=0$; U_{12}	0.0116(1); 0.0113(1); 0.0091(1); 0.0005(1)
Ce4 in 4*h* (*x, y*, ½); Occ.	*x*=0.41764(2), *y*=0.25774(2);1.00(1)
U_{11}^b; U_{22}; U_{33}; $U_{23}=U_{13}=0$; U_{12}	0.0114(2); 0.0280(2); 0.0146(2); -0.0023(1)
Zn1 in 2*d* (0, ½, ½); Occ.	1.00(1)
U_{11}^b; U_{22}; U_{33}; $U_{23}=U_{13}=0$; U_{12}	0.0159(5); 0.0219(5); 0.0181(5); 0.0010(4)
Zn2 in 4*g* (*x, y*, 0); Occ.	*x*=0.15113(5), *y*=0.05238(4); 1.00(1)
U_{11}^b; U_{22}; U_{33}; $U_{23}=U_{13}=0$; U_{12}	0.0157(3); 0.0131(3); 0.0119(3); 0.0022(2)
Zn3 in 4*g* (*x, y*, 0); Occ.	*x*=0.46676(4), *y*=0.09813(4); 1.00(1)
U_{11}^b; U_{22}; U_{33}; $U_{23}=U_{13}=0$; U_{12}	0.0117(3); 0.0201(3); 0.0187(3); -0.0026(3)
Zn4 in 4*h* (*x, y*, ½); Occ.	*x*=0.35208(5), *y*=0.08045(4);1.00(1)
U_{11}^b; U_{22}; U_{33}; $U_{23}=U_{13}=0$; U_{12}	0.0255(4); 0.0166(3); 0.0122(3); 0.0031(3)
Zn5 in 4*g* (*x, y*, 0); Occ.	*x*=0.25777(5), *y*=0.28255(4); 1.00(1)
U_{11}^b; U_{22}; U_{33}; $U_{23}=U_{13}=0$; U_{12}	0.0168(3); 0.0116(3); 0.0112(3); 0.00001(23)
Zn6 in 4*g* (*x, y*, 0); Occ.	*x*=0.07430(5), *y*=0.28324(4); 1.00(1)
U_{11}^b; U_{22}; U_{33}; $U_{23}=U_{13}=0$; U_{12}	0.0163(3); 0.0119(3); 0.0125(3); 0.0008(2)
Zn7 in 4*h* (*x, y*, ½); Occ.	*x*=0.29902(5), *y*=0.49551(4);1.00(1)
U_{11}^b; U_{22}; U_{33}; $U_{23}=U_{13}=0$; U_{12}	0.0174(4); 0.0238(3); 0.0118(3); -0.0078(3)
Zn8 in 4*h* (*x, y*, ½); Occ.	*x*=0.07423(5), *y*=0.35896(4);1.00(1)
U_{11}^b; U_{22}; U_{33}; $U_{23}=U_{13}=0$; U_{12}	0.0250(4); 0.0169(3); 0.0116(3); -0.0042(3)
Zn10 in 4*g* (*x, y*, 0); Occ.	*x*=0.36494(5), *y*=0.40099(4); 1.00(1)
U_{11}^b; U_{22}; U_{33}; $U_{23}=U_{13}=0$; U_{12}	0.0124(3); 0.0139(3); 0.0243(3); 0.0006(2)
Zn11 in 4*g* (*x, y*, 0); Occ.	*x*=0.30487(5), *y*=0.14196(4); 1.00(1)
U_{11}^b; U_{22}; U_{33}; $U_{23}=U_{13}=0$; U_{12}	0.0153(3); 0.0146(3); 0.0125(3); 0.0035(2)
Zn12 in 4*h* (*x, y*, ½); Occ.	*x*=0.24993(6), *y*=0.35461(4);1.00(1)
U_{11}^b; U_{22}; U_{33}; $U_{23}=U_{13}=0$; U_{12}	0.0272(4); 0.0147(3); 0.0122(3); 0.0060(3)
M in 4*g* (*x, y*, 0); Occ.	*x*=0.02066(6), *y*=0.14166(5); 0.72(1) Zn9+0.28 Si1
U_{11}^b; U_{22}; U_{33}; $U_{23}=U_{13}=0$; U_{12}	0.0119(4); 0.0139(4); 0.0210(4); -0.0000(3)
Residual electron density; max; min in [electrons/nm³] x10³	3.02; -2.27

[a]crystal structure data are standardized using the program Structure Tidy [33].
[b]anisotropic atomic displacement parameters U_{ij} in [10^2 nm²].

Table 3. Interatomic distances for $Ce_7Zn_{21}(Zn_{1-x}Si_x)_2$, x=0.28.

Bonds	Distance (nm)	Bonds	Distance (nm)	Bonds	Distance (nm)
Ce1 – 2Zn7	0.31307(8)	Zn2 – M	0.25464(12)	Zn8 – 2Zn6	0.25897(5)
Ce1 – 4M	0.3238(6)	Zn2 – 2Zn7	0.25632(5)	Zn8 – Zn1	0.26865(7)
Ce1 – 4Zn2	0.33706(6)	Zn2 – Zn10	0.26150(10)	Zn8 – Zn12	0.27371(11)
Ce1 – 4Zn10	0.35118(6)	Zn2 – Zn11	0.28468(11)	Zn8 – 2Zn3	0.28908(6)
Ce1 – 4Ce2	0.40702(3)	Zn2 – 2Ce2	0.31689(5)	Zn8 – 2Ce1	0.31137(6)
		Zn2 – Ce1	0.33292(8)	Zn8 – Ce4	0.31579(8)
Ce2 – 2Zn8	0.31137(6)	Zn2 – 2Ce3	0.33706(6)	Zn8 – Ce2	0.33686(8)
Ce2 – 2Zn4	0.31194(5)				
Ce2 – 2Zn12	0.31264(6)	Zn3 – Zn11	0.26312(10)	Zn10 – M	0.25334(12)
Ce2 – 2Zn7	0.31482(6)	Zn3 – Zn6	0.26391(10)	Zn10 – Zn2	0.26150(10)
Ce2 – Zn3	0.31958(7)	Zn3 – 2Zn1	0.28506(4)	Zn10 – Zn5	0.26329(10)
Ce2 – Zn3	0.32059(7)	Zn3 – 2Zn4	0.28797(6)	Zn10– 2Zn7	0.29507(7)
Ce2 – Zn11	0.32514(8)	Zn3 – 2Zn8	0.28908(6)	Zn10– 2Zn12	0.29757(7)
Ce2 – Zn10	0.32621(8)	Zn3 – Ce1	0.31958(7)	Zn10 – Ce1	0.32621(8)
Ce2 – Zn6	0.32671(8)	Zn3 – Ce1	0.32059(7)	Zn10 – 2Ce4	0.34281(6)
Ce2 – Zn5	0.33038(8)			Zn10 – 2Ce3	0.35118(6)
Ce2 – Zn2	0.33292(7)	Zn4 – 2Zn11	0.25827(5)		
Ce2 – 2Zn1	0.34845(3)	Zn4 – Zn1	0.26869(8)		
		Zn4 – Zn7	0.27694(11)	Zn11 – Zn5	0.25262(10)
Ce3 – 2Zn5	0.31611(6)	Zn4 – 2Zn3	0.28797(6)	Zn11 – 2Zn4	0.25827(5)
Ce3 – 2Zn2	0.31689(5)	Zn4 – 2Ce1	0.31194(5)	Zn11– Zn3	0.25827(5)
Ce3 – 2Zn11	0.31761(6)	Zn4 – Ce4	0.32148(8)	Zn11– Zn2	0.28468(11)
Ce3 – 2Zn6	0.31826(6)	Zn4 – Ce2	0.336858)	Zn11 – 2Ce2	0.31761(6)
Ce3 – Zn12	0.32357(8)			Zn11– Ce1	0.32514(8)
Ce3 – Zn7	0.32500(8)	Zn5 – Zn11	0.25262(10)	Zn11– 2Ce4	0.34725(6)
Ce3 – 2M	0.32701(7)	Zn5 – 2Zn12	0.25615(5)		
Ce3 – Zn4	0.33685(8)	Zn5 – Zn10	0.26329(10)	Zn12 – Zn7	0.25404(10)
Ce3 – Zn8	0.33686(8)	Zn5 – Zn6	0.28571(11)	Zn12 – 2Zn5	0.25615(5)
Ce3 – Ce4	0.40205(5)	Zn5 – 2Ce2	0.31611(6)	Zn12 – Zn8	0.27371(11)
Ce3 – Ce3	0.40702(3)	Zn5 – Ce1	0.33038(8)	Zn12 – 2Zn10	0.29757(7)
Ce3 – Ce4	0.41128(5)	Zn5 – 2Ce4	0.33751(6)	Zn12– Ce4	0.30975(8)
				Zn12– 2Ce1	0.31264(6)
Ce4 – Zn12	0.30975(8)	Zn6 – M	0.25737(11)	Zn12– Ce2	0.32357(8)
Ce4 – Zn8	0.31579(8)	Zn6 – 2Zn8	0.25897(5)		
Ce4 – Zn4	0.32148(8)	Zn6 – Zn3	0.26391(10)		
Ce4 – 2M	0.32522(7)	Zn6 – Zn5	0.28571(11)	M – Zn10	0.25334(12)
Ce4 – 2Zn5	0.33751(6)	Zn6 – 2Ce2	0.31826(6)	M – Zn2	0.25464(12)
Ce4 – 2Zn6	0.33851(6)	Zn6 – Ce1	0.32671(8)	M – Zn6	0.25737(11)
Ce4 – 2Zn10	0.34281(6)	Zn6 – 2Ce4	0.33851(6)	M – 2Ce4	0.32522(7)
Ce4 – 2Zn11	0.34725(6)			M – 2Ce2	0.32701(7)
Ce4 – 2Zn3	0.36233(6)	Zn7 – Zn12	0.25404(10)	M – 2Ce3	0.33238(6)
Ce4 – 2Ce2	0.41128(5)	Zn7 – 2Zn2	0.25632(5)		
		Zn7 – Zn4	0.27694(11)		
Zn1 – 2Zn8	0.26865(7)	Zn7 – 2Zn10	0.29507(7)		
Zn1 – 2Zn4	0.26869(8)	Zn7 – Ce3	0.31307(8)		
Zn1 – 4Zn3	0.28506(4)	Zn7 – 2Ce1	0.31482(6)		
Zn1 – 4Ce1	0.34845(3)	Zn7 – Ce2	0.32500(8)		

Table 4. X-ray single crystal data[a,b] for the compound Ce(Zn$_x$Si$_{1-x}$)$_2$, x=0.44 and Rietveld XPD data for isotypic La(Zn$_x$Si$_{1-x}$)$_2$, x=0.56

Compound	Ce(Zn$_x$Si$_{1-x}$)$_2$, x=0.44	La(Zn$_x$Si$_{1-x}$)$_2$, x=0.56
EPMA composition [at. %]	Ce$_{33.7}$Zn$_{29.34}$Si$_{36.96}$	La$_{33.52}$Zn$_{37.42}$Si$_{29}$
Composition from refinement	Ce$_{33.33}$Zn$_{29.33}$Si$_{37.33}$	La$_{33.52}$Zn$_{37.43}$Si$_{29.05}$
Space group	$P6/mmm$; No. 191	$P6/mmm$; No. 191
Structure type	AlB$_2$	AlB$_2$
Radiation used	MoK$_\alpha$	CuK$_\alpha$
2θ Range [deg]°	$9.54 < \theta < 70.78$	$8 < \theta < 100$
Crystal size [µm]	35x30x40	-
a [nm]	0.41827(2)	0.42775(4)[c]
c [nm]	0.42747(2)	0.42832(4)[c]
Reflections in refinement	84 F$_o$ > 4σ(F$_o$) of 84	28
Mosaicity	0.57	-
Number of variables	9	18
R$_F^2$ = Σ|F$_0^2$-F$_c^2$|/ΣF$_0^2$	0.0095	R$_F$=0.0515
R$_{Int}$	0.064	R$_I$=0.0661
GOF	1.33	χ^2=7.64
Extinction (Zachariasen)	0.039(3)	-
RE in 1a (0, 0, 0); Occ.	Ce; 1.00(1)	La; 1.00 (1)
U$_{11}$[b]= U$_{22}$; U$_{33}$; U$_{23}$=U$_{13}$=0; U$_{12}$	0.0070(2); 0.0058(2); 0.0035(1)	B$_{iso}$=0.57(13)
M in 2d (⅓, ⅔, ½); Occ.	0.44(1) Zn + 0.56 Si	0.56(2) Zn + 0.44 Si
U$_{11}$[b]= U$_{22}$; U$_{33}$; U$_{23}$=U$_{13}$=0; U$_{12}$	0.0060(3); 0.0157(4); 0.0030(1)	B$_{iso}$=0.71(30)
Residual electron density; max; min in [electrons/nm^3] x10^3	1.84; -1.19	-

[a]crystal structure data are standardized using the program Structure Tidy [33].
[b]anisotropic atomic displacement parameters U$_{ij}$ and isotropic B$_{iso}$ in [10^2 nm^2].
[c]Ge standard.

Table 5. Ce- Zn - Si system: Phase equilibria and Lattice Parameters of alloys annealed at 800°C

Phase regions	Phase	Structure Type	EPMA Composition, at. %			Lattice Parameters, nm		
			Ce	Zn	Si	a	b	c
τ_1+ Ce_3Zn_{11}+ $Ce_{13}Zn_{58}$ Fig. 6a	τ_1	$Ce_7Zn_{21}(Zn_{1-x}Si_x)_2$	23.1	74	2.9	-	-	-
	Ce_3Zn_{11}	La_3Al_{11}	22.8	76.8	0.4	0.45175(6)	0.8894(1)	1.3447(2)
	$Ce_{13}Zn_{58}$	$Gd_{13}Zn_{58}$	19.4	80.2	0.4	1.4635(5)		1.4176(5)
Ce_2Zn_{17}+ τ_2+Ce_3Zn_{22}	Ce_2Zn_{17}	Th_2Zn_{17}	11	88.8	0.2	0.9091(4)	-	1.3286(1)
Fig. 6b	Ce_3Zn_{22}	Ce_3Zn_{22}	12.3	87.4	0.3	0.897(1)	-	2.133(5)
	τ_2	AlB_2	33.9	28.6	37.5	0.41707(3)	-	0.42779(7)
τ_1+$CeZn_5$+τ_2	τ_1	$Ce_7Zn_{21}(Zn_{1-x}Si_x)_2$	23.3	70.3	6.4	-	-	-
Fig. 6c	$CeZn_5$	$CaCu_5$	16.5	83.4	0.1	0.5408(1)		0.4280(1)
	τ_2	AlB_2	33.3	33.3	33.4	0.41648(3)	-	0.42829(3)
$CeSi_2$+τ_2+Ce_2Zn_{17}	$Ce(Zn, Si)_2$	$\alpha ThSi_2$	33.4	21.3	45.3	0.4201(1)		1.4312(7)
	τ_2	AlB_2	33.4	24	42.6	0.4132(1)		0.4295(2)
	Ce_2Zn_{17}	Th_2Zn_{17}	11	88.8	0.2	-	-	-
$CeSi$+$CeSi_2$	$Ce(Zn, Si)_2$	$\alpha ThSi_2$	33.9	27.3	38.8	0.42013(2)	-	1.3995(1)
	$CeSi$	FeB	49.9	0.8	49.3	-	-	-
$CeZn_2$+Ce_3Si_2	$CeZn_2$	$CeCu_2$	33.2	62.5	4.3	0.461(1)	0.7551(4)	0.754(4)
Fig. 6d	$Ce_3(Zn, Si)_2$	U_3Si_2	59.5	3.2	37.3	-	-	-
τ_2/$CeZn_2$+Ce_3Si_2+ τ_4	$Ce(Zn,Si)_2$	AlB_2/ $CeCu_2$	33.8	52.9	13.3	-	-	-
Fig. 6e	$Ce_3(Zn, Si)_2$	U_3Si_2	58.4	2.1	39.5	-	-	-
	τ_4	-	40	38	22	-	-	-
Ce_3Si_2+Ce_5Si_4+ τ_4	$Ce_5(Zn, Si)_4$	Zr_5Si_4	42.8	2	55.2	-	-	-
	$Ce_3(Zn, Si)_2$	U_3Si_2	58.4	2.1	39.5	-	-	-
	τ_4	-	40	38	22	-	-	-
τ_3+τ_4+τ_2	τ_3	-	49.6	11.7	38.7	-	-	-
	τ_4	-	40.7	36.6	22.7	-	-	-

	τ₂	AlB₂	33.9	45.4	20.7	-	-	-
CeSi+τ₃	CeSi	FeB	50.8	1.1	48.1	-	-	-
	τ₃	-	49.7	8.3	42	-	-	-

Table 6. X-ray single crystal data[a] for $CeNi_2(Ni_xSi_{1-x})_2$, x=0.14 and X-ray powder diffraction data for $CeNi_2Si_2$ and $LaNi_2Si_2$ (samples annealed at 800°C).

Compound	$CeNi_2(Ni_xSi_{1-x})_2$, x=0.14	$CeNi_2Si_2$	$LaNi_2Si_2$
EMPA composition [at. %]	$Ce_{20.1}Ni_{46.5}Si_{33.4}$	$Ce_{20.4}Ni_{38}Si_{41.6}$	$La_{20.3}Ni_{37.9}Si_{41.8}$
Refinement composition [at. %]	$Ce_{20}Ni_{45.6}Si_{34.4}$	$Ce_{20.6}Ni_{39.4}Si_{40}$	$La_{20.6}Ni_{39.2}Si_{40.7}$
Space group	$P4/nmm$; No. 129, origin at centre	$I4/mmm$, No. 139	$I4/mmm$, No. 139
Structure type	$CaBe_2Ge_2$	$ThCr_2Si_2$	$ThCr_2Si_2$
Data collection	Nonius KappaCCD	Guinier Image Plate	Guinier Image Plate
Radiation	MoK_α	$CuK_{\alpha 1}$	$CuK_{\alpha 1}$
2θ range	$2.14 < 2\theta < 36.16$	$10 < 2\theta < 100$	$10 < 2\theta < 100$
Crystal size [μm]	40x50x50	-	-
a [nm]	0.40150(2)	0.4037(1)	0.411237(2)
c [nm]	0.95210(2)	0.9571(1)	0.971184(8)
Reflections in refinement	266 $F_o > 4\sigma(F_o)$ of 262	38	39
Z, volume [nm³]	2, 153.5(1)	2, 0.156(1)	2, 0.164(1)
Number of variables	16	22	22
$R_F^2 = \Sigma|F_0^2 - F_c^2|/\Sigma F_0^2$	0.011	$R_F = 0.024$	$R_F = 0.024$
R_{Int}	0.014	$R_B = 0.029$	$R_B = 0.028$
GOF	0.927	$\chi^2 = 1.35$	$\chi^2 = 2.16$
Extinction (Zachariasen)	0.036(1)	$R_{wp} = 2.63$	$R_{wp} = 2.74$
RE Occ.; $B_{iso.}$ $U_{11}{}^b = U_{22}; U_{33}; U_{23} = U_{13}; U_{12} = 0$	Ce in $2c$ (¼, ¼, z); z=0.75072(2); 1.00(1) 0.0054(1); 0.0065(1)	Ce in $2a$ (0, 0, 0) 1.00(1); 0.14(2)	La in $2a$ (0, 0, 0) 1.00(1); 0.95(2)
Ni Occ.; $B_{iso.}$ $U_{11}{}^b = U_{22}; U_{33}; U_{23} = U_{13}; U_{12} = 0$	Ni2 in $2b$ (¾, ¼, , ½); 1.00(1) 0.0083(1); 0.0073(2)	Ni in $4d$ (0, ½, ¼) 1.00(2); 0.60(5)	Ni in $4d$ (0, ½, ¼) 0.95(2); 0.19(3)
M Occ. $U_{11}{}^b = U_{22}; U_{33}; U_{23} = U_{13} = U_{12} = 0$	M in $2a$ (¾, ¼, 0); 0.28(1) Ni1+0.72 Si2 0.0134(4); 0.0066(4)		
Si Occ.; $B_{iso.}$ $U_{11}{}^b = U_{22}; U_{33}; U_{23} = U_{13}; U_{12} = 0$	Si1 in $2c$ (¼, ¼, z); z=0.3717(1); 1.00(1) 0.0055(3); 0.0077(4)	Si in $4e$ (0, 0, z); z=0.3804(3); 1.00(1); 0.26(7)	Si in $4e$ (0, 0, z); z=0.3684(2); 1.00(1); 0.49(5)
M Occ. $U_{11}{}^b = U_{22}; U_{33}; U_{23} = U_{13} = U_{12} = 0$	Ni1 in $2c$ (¼, ¼, z); z=0.12643(6); 1.00(1) 0.0130(2); 0.0116(3)		
Residual electron density; max; min in [electrons/nm³] x 1000	0.67; -0.82	-	-

[a] crystal structure data are standardized using the program Structure Tidy [33].
[b] anisotropic atomic displacement parameters U_{ij} and isotropic B_{iso} in $[10^2 \ nm^2]$.

Table 7. X-ray single crystal data for Ce(Ni$_{1-x}$Zn$_x$)$_2$Si$_2$, x=0.39 and Rietveld XPD data for La(Ni$_{1-x}$Zn$_x$)$_2$Si$_2$; x=0.44 (space group *P4/nmm*; No. 129, origin at centre)[a]

Compound	Ce(Ni$_{1-x}$Zn$_x$)$_2$Si$_2$, x=0.39	La(Ni$_{1-x}$Zn$_x$)$_2$Si$_2$; x=0.44
EMPA composition [at. %]	Ce$_{19.4}$Ni$_{25.3}$Zn$_{16.1}$Si$_{39.2}$	La$_{19.9}$Ni$_{22.3}$Zn$_{17.2}$Si$_{40.7}$
Refinement composition [at. %]	Ce$_{20}$Ni$_{24.4}$Zn$_{15.6}$Si$_{40}$	La$_{20}$Ni$_{22.6}$Zn$_{17.4}$Si$_{40}$
Structure type	CaBe$_2$Ge$_2$	CaBe$_2$Ge$_2$
Data collection	Nonius KappaCCD	Guinier-Huber IP
Radiation	MoK$_\alpha$	CuK$_\alpha$
2θ range	$2.08 < 2\theta < 36.05$	$8 < 2\theta < 100$
Crystal size [μm]	40x50x50	
a [nm]	0.41022(1)	0.41615(6)[c]
c [nm]	0.98146(4)	0.99213(7)[c]
Reflections in refinement	266 F$_o$ >4σ(F$_o$) of 272	72
Mosaicity	0.65	
Z, density [gm/Cm^3]	2, 6.44	2, 6.022
Number of variables	20	26
R$_F^2$ = Σ|F$_0^2$-F$_c^2$|/ΣF$_0^2$	0.012	R$_F$=0.0435
R$_{Int}$	0.058	R$_I$=0.024
GOF	0.806	χ^2=2.78
Extinction (Zachariasen)	0.024(1)	R$_w$=2.75
RE in 2*c* (¼, ¼, *z*); Occ. B$_{iso}$ U$_{11}$[b]=U$_{22}$; U$_{33}$; U$_{23}$=U$_{13}$;U$_{12}$ = 0	*z*=0.73977(2); 1.00(1) 0.0052(1); 0.0060(1)	*z*=0.73833(7); 1.00(1); B$_{iso}$=0.52(1)
M in 2*a* (¾, ¼, 0); Occ. U$_{11}$[b]=U$_{22}$; U$_{33}$; U$_{23}$=U$_{13}$=U$_{12}$=0	0.78(1) Zn1+0.22 Ni1 0.0095(1); 0.0063(2)	0.87(1) Zn1+0.13 Ni1 B$_{iso}$=0.26(3)
Ni2 in 2*c* (¼, ¼, *z*); Occ. U$_{11}$[b]=U$_{22}$; U$_{33}$; U$_{23}$=U$_{13}$;U$_{12}$ = 0	*z*=0.38511(6); 1.00(1) 0.0067(2); 0.0071(2)	*z*=0.3883(1); 1.00(1); B$_{iso}$=0.36(4)
Si1 in 2*b* (¾, ¼, , ½); Occ. U$_{11}$[b]=U$_{22}$; U$_{33}$; U$_{23}$=U$_{13}$=U$_{12}$=0	1.00(1) 0.0063(3); 0.0062(4)	1.00(1); B$_{iso}$=0.54(6)
Si2 in 2*c* (¼, ¼, *z*); Occ. U$_{11}$[b]=U$_{22}$; U$_{33}$; U$_{23}$=U$_{13}$;U$_{12}$ = 0	*z*=0.1472(1); 1.00(1) 0.0111(3); 0.0095(5)	*z*=0.1537(3); 1.00(1); B$_{iso}$=0.68(7)
Residual electron density; max; min in [electrons/nm^3] x 1000	1.22; -0.98	

[a]crystal structure data are standardized using the program Structure Tidy [33].
[b]anisotropic atomic displacement parameters U$_{ij}$ and isotropic B$_{iso}$ in [10^2 nm^2].
[c] Ge standard

Table 8. Interatomic distances for $Ce(Ni_{1-x}Zn_x)_2Si_2$, x=0.39 ($P4/nmm$; No. 129).

Bonds	Distances	Bonds	Distances
Ce – 4Si1	0.31044(1)	Si1– 4Ni	0.23405(1)
Ce – 4Si2	0.31217(1)	Si1– 4Ce	0.31217(1)
Ce – 4Ni	0.31492(1)	Si1– 4Si1	0.29007(1)
Ce – 4Zn	0.32756(1)		
		Si2– Ni	0.23320(1)
M – 4Si2	0.25108(1)	Si2– 4Zn	0.25108(1)
M – 4Zn	0.29007(1)	Si2– 4Ce	0.31044(1)
M – 4Ce	0.32756(1)		
Ni – Si2	0.23320(1)		
Ni – 4Si1	0.23405(1)		
Ni – 4Ce	0.31492(1)		

Summary

Zn-based alloys with rare-earth metals are an important part of the high strength lightweight multinary Mg-based alloy system Mg-Zn-Mn(Ni)-RE for automotive applications. Rare earths (RE) improve the mechanical performance, tensile strength, hardness and also the corrosion resistance by removing impurities from the grain boundaries of their alloys with zinc. The present work provides detailed information on phase relations and crystal structures in the quaternary systems Ce-Ni-Zn-(B,Si) at 800°C backed by light optical microscopy, electron microprobe analysis and x-ray powder and single crystal diffraction.

The isothermal sections at 800°C have been established for the systems Ce-Zn-B, Ni-Zn-B, Ce-Ni-Zn and Ce-Zn-Si. In the system Ni-Zn-B six ternary compounds were found, which in some cases exhibit considerable mutual solid solubilities mostly as an exchange of Ni-Zn at constant B-content, but in the case of the so-called τ-phase τ_1-$(Ni_{1-x}Zn_x)_{21}[Zn_{1-y-z}\square_y(B_4)_z]_2B_6$ (1.5<x<2.25, 0.07<y<0.53, 0<z<0.3) also with Zn/B substitution. Whereas Ni/Zn exchange (at constant B-content) ranges at about 4 to 5 at. % for τ_4-Ni_3ZnB_2 and τ_5-$Ni_{48}Zn_{32}B_{20}$, it is below 3 at. % for τ_2-$Ni_{12}ZnB_{8-x}$ (x=0.43), τ_3-$Ni_{21}Zn_2B_{20}$ and τ_6-$Ni_{47}Zn_{23}B_{30}$. Phase relations in the system Ce-Ni-Zn are characterized by a large region for the liquid phase in the Ce-rich part and a continuous solution of the phase $Ce(Ni_{1-x}Zn_x)_5$ with $CaCu_5$-type through the entire section for the full temperature region from 400 to 800°C. Zn/Ni substitution has found to stabilize the structure of $CeZn_{11}$ at 800°C appearing as a ternary solution phase $Ce(Zn_{1-x}Ni_x)_{11}$(0.03≤x≤0.22) and a rather extended solution of $Ce_2(Ni_xZn_{1-x})_{17}$(0≤x≤0.53). No ternary compound exists in the ternary system Ce-Zn-B and no significant mutual solid solubilities of binary phases have been observed. For the low temperature modification $\alpha CeZn_7$ ($Ce_{1-x}Zn_{5+2x}$; x~0.33) up to 750°C the $TbCu_7$-type could be assigned in this work.

X-ray single crystal and x-ray powder diffraction were employed to study the precise site occupation and site preferences in the crystal structures of more than 18 compounds. The crystal chemistry of the rhombohedral β boron solid solution co-doped by Ni,Zn metal atoms has been studied on a $Ni_{0.19}Zn_{1.24}B_{34.22}$ single crystal. Zn atoms were found in the E void (occupancy of 28%) whilst random mixtures of Ni, Zn atoms (ratio 15.5:84.5) occupy the sites A_1, D and D_d. Among the new crystal structures determined a new boron-metal cluster was found in $Ni_{21}Zn_2B_{20}$ (*I4/mmm*)

185

with characteristic isolated B_{20}- cages nesting six nickel atoms in the form of an octahedron. Ni_3ZnB_2 (*C2/m*) was found to form B_4 zigzag chains, $Ce_7Zn_{23-x}Si_x$, x=0.14 (*Pbam*) consists of $AuCu_3$ and disordered $BaAl_4$ structural units and $Ce(Ni_{1-x}Zn_x)_2Si_2$, x=0.39 (Pnmm) is $CaBe_2Ge_2$-type.

Physical properties including thermal expansion, hardness, elastic properties, resistivity, specific heat and magnetization were studied for the borides $Ni_{21}Zn_2B_{20}$ and Ni_3ZnB_2.

Publication List

1. The System Ce-Zn-B at 800°C
   Z. Malik, O. Sologub, G. Giester and P. Rogl,
   J. of Solid State Chem. 184 (2011) 2840–2848.

2. Crystal Structure of Novel Ni-Zn Borides; First Observation of a Boron–Metal Nested Cage Unit: $B_{20}Ni_6$
   Zahida P. Malik, Oksana Sologub, Andriy Grytsiv, Gerald Giester and Peter F. Rogl,
   Inorg. Chem. 50 (2011) 7669-7675.

3. Phase relations and crystal structures in the system Ce-Ni-Zn at 800°C
   Z. Malik, A. Grytsiv, P. Rogl and G. Giester,
   J. of Solid State Chem. (2012) (Accepted).

4. The crystal structure of Ni-Zn co-doped β boron $Ni_{0.19}Zn_{1.24}B_{34.22}$
   Z. Malik, O. Sologub, G. Giester and P. Rogl,
   J. Alloys and Compounds (Submitted).

5. Physical Properties of the Ternary Borides $Ni_{21}Zn_2B_{20}$ and Ni_3ZnB_2,
   Z. Malik, H. Michor, A. Grytsiv, G. Rogl, S. Puchegger, H. Müller,
   M. Kriegisch, E. Bauer, C. Eisenmenger-Sittner, P. Rogl,
   J Alloys and Compounds (submitted).

6. Phase Relations and Structure Chemistry in the System Ni-Zn-B
   Z. Malik, A. Grytsiv, P. Rogl, G. Giester and J. Bursik,
   J. of Solid State Chem. (to be submitted).

7. Phase Equilibria and Crystal Structures in the System Ce-Zn-Si

Z. Malik, A. Grytsiv, P. Rogl and G. Giester,

Intermetallics (to be submitted).

8. On the Quaternary Systems Ce-Ni-Zn-(B, Si),

   Z. Malik, A. Grytsiv, O. Sologub and P. Rogl,

   18th International Conference on Solid Compounds of Transition Elements"

   Lisbon University, Lisbon, Portugal (2012).

9. The System Ce-Ni-Zn-B,

   Z. Malik, O. Sologub and P. Rogl,

   17th International Symposium on Boron, Borides and Related Materials,

   Istanbul, Turkey, (2011).

Curriculum vitae

MALIK, Zahida Parveen

Father's Name: MALIK, Sakhawat Hussain.

Nationality: Pakistani.

Date of Birth: 12-02-1976

Educational Background:

2008-2012:   PhD candidate, Institute of Physical Chemistry,

            University of Vienna, Austria.

2000-2002:   M.Phil (Physical Chemistry), Institute of Physical Chemistry,

            Quaid-e-Azam University, Islamabad, Pakistan.

M.Phil research topic: Investigation of Preferential Solvation of Ni and
              Co salts in Aqueous Solutions of Higher Alcohols.

1998-2000:   M.Sc (Physical Chemistry), Department of Chemistry,
            University of Agriculture Faisalabad, Pakistan.

M.Sc research topic: Extraction of Allelopahthic Compounds from
              Sorghum Stem and their affect on wheat seedlings growth.

2004-1998:   BSc (Chemistry, Botany, Zoology), University of Punjab, Lahore, Pakistan.